ABSTRACT

Differential Production Cross-Section of Heavy-Flavor Electrons in $\sqrt{s} = 2.76$ TeV pp collisions at the LHC with the ALICE detector

Bernard Richard Hicks

Yale University

2013

Recent results at RHIC seem to confirm T.D.Lee's hypothesis that a new form of matter, the quark-gluon plasma (QGP), could be formed in heavy-ion collisions at high energies. Heavy quarks, being formed in the early stages of heavy-ion collisions, form a good probe for the properties of the QGP. The energy loss of heavy quarks as they traverse the medium is predicted to be less than that of the lighter quarks. However, previous measurements of the nuclear modification factor at RHIC indicate that the energy loss of heavy and light quarks is comparable. Thus measurements of the in-medium energy loss of heavy-quarks are of particular interest. In this thesis, a measurement of the differential production cross-section of electrons from the semi-leptonic decay of heavy-flavor quarks in $\sqrt{s} = 2.76$ TeV pp is presented. This provides a stringent test of perturbative QCD in a new energy regime, and forms a crucial baseline for Pb-Pb collisions where the in-medium energy loss mechanism can be studied.

Differential Production Cross-Section of Heavy-Flavor Electrons in $\sqrt{s} = 2.76$ TeV *pp* collisions at the LHC with the ALICE detector

A Dissertation
Presented to the Faculty of the Graduate School
of
Yale University
in Candidacy for the Degree of
Doctor of Philosophy

by
Bernard Richard Hicks

Dissertation Director: Helen Caines

November 18, 2013

Contents

List of Figures **vi**

List of Tables **xvii**

1 Introduction **1**

1.1 The Standard Model and QCD 1

1.2 The Quark Gluon Plasma (QGP) 5

1.3 Relativistic Heavy-ion Collisions 8

1.4 Signatures of the QGP 12

1.4.1 Debye Screening and J/ψ Suppression 12

1.4.2 Strangeness Production and Hadronic Yields 13

1.4.3 Anisotropic Flow 14

1.4.4 Hanbury-Brown-Twiss Interferometry 16

1.4.5 Jet Tomography 19

1.4.6 High p_T suppression of hadrons, R_{AA} 21

1.5 Heavy-Flavor and the QGP 23

1.5.1 Heavy-Quark Production in pp collisions 24

1.5.2 Heavy-Ion Collisions and Energy-Loss Mechanisms 31

2 ALICE experiment **37**

2.1 The Large Hadron Collider 37

2.1.1 Performance and Luminosity 43

2.1.2 Bunching and Filling Schemes 45

2.2 The ALICE detector 46

2.2.1 The Central Barrel 47

2.2.1.1 The Time Projection Chamber (TPC) 47

2.2.1.2 The Inner Tracking System (ITS) 53

2.2.2 The Transition Radiation Detector (TRD) 57
2.2.3 Time of flight detector (TOF) 58
2.2.4 High momentum particle identification detector (HMPID) 59
2.2.5 Photon Spectrometer (PHOS) 60
2.2.6 Electromagnetic Calorimeter (EMCal) 62
2.2.7 The Muon Spectrometer 65
2.2.8 ACORDE 66
2.2.9 Forward and Trigger Detectors 67
2.2.9.1 Zero Degree Calorimeter (ZDC) 67
2.2.9.2 Photon Multiplicity Detector (PMD) 68
2.2.9.3 Forward Multiplicity Detector (FMD) 68
2.2.9.4 V0 detector 69
2.2.9.5 T0 detector 70
2.2.10 The ALICE Trigger 70

3 Data Set and Event Selection **74**
3.1 Description of Data and Run Conditions 74
3.2 Event Selection 77
3.3 Data Quality Assurance 85
3.4 Brief Overview of the Analysis Methodology 88

4 Tracking **89**
4.1 Tracking in ALICE 89
4.2 Track Selection and Quality Assurance 91
4.3 Tracking Efficiency 98
4.4 Momentum Resolution and Bremsstrahlung Unfolding 100
4.5 Systematic Uncertainties 104
4.5.1 Systematic Uncertainty Associated with the Tracking Efficiency 104
4.5.2 Systematic Uncertainty Associated with Unfolding 105

5 Electron Identification **109**
5.1 Electron PID Optimization and Strategy 110
5.2 Determination of the PID Efficiency and Purity 115
5.2.1 TPC Method of Purity and Efficiency Estimation 116

5.2.2 EMCal Method of Purity Estimation 120
5.2.3 Results 124
5.3 Systematic Uncertainty 126

6 The EMCal Trigger **129**
6.1 Description of the Trigger 129
6.2 L0 Trigger Bias Correction 131
6.2.1 Electron Trigger Efficiency 132
6.2.2 EMCal Trigger Simulation 134
6.2.3 Trigger Efficiency Correction 136
6.2.4 Systematic Uncertainty Associated with the Trigger Correction 139

7 Non-Heavy-Flavor Cocktail **141**
7.1 Cocktail Components 143
7.1.1 The Light Mesons 144
7.1.2 $\mathrm{K_{e3}} \rightarrow \mathrm{e}^{+/-}\pi^{-/+}\nu$ decays 147
7.1.3 Heavy Quarkonia 147
7.1.4 Direct Photons 148
7.1.5 Other Possible Background Sources 148
7.2 Systematic Uncertainty 148

8 Results **151**
8.1 Inclusive Electron Cross-Section 151
8.2 Heavy-Flavor Electron Cross-Section 156
8.3 Disentanglement of b/c Contributions 158
8.4 pQCD $\sqrt{s}$-Scaling of the Measurement at $\sqrt{s} = 7$ TeV 161
8.5 Measurement of Heavy-Flavor Electron R_{AA} 163
8.6 Looking Forward 164

Appendices **165**
A The ALICE Coordinate System 166
B The Effective Signal 167
C Additional PID plots 169
C.1 PID optimization 169
C.2 High p_T PID Efficiency Toy Model 171

D Trigger Efficiency Formulae 173
    D.1 Trigger Efficiency from MB and EMCal Triggered Spectra 173
    D.2 High p_T trigger efficiency 173

References **177**

List of Figures

1.1.1 Fundamental particles within the standard model [1] 2

1.1.2 QCD strong coupling constant as a function of energy [2] 4

1.2.1 Schematic of the QCD phase diagram as presently understood. The approximate regions of phase space explored by the FAIR experiment, experiments at RHIC and the ALICE experiment are indicated on the diagram. The chiral-symmetry breaking transition is assumed to coincide with the hadron-plasma transition as suggested by lattice QCD calculations [3, 4] 6

1.2.2 Equation of state of hadronic matter at zero baryon chemical potential as determined using lattice QCD by the HotQCD collaboration [5] 7

1.3.1 Schematic of the evolution of a heavy-ion collision 9

1.3.2 Space-time evolution of a heavy-ion collision with (right) and without (left) QGP formation [6] 9

1.3.3 Illustration of a heavy-ion collision with some finite impact parameter, b. A b-dependent fraction of the incident nucleons will interact, with the remaining non-interacting nucleons being known as spectators. The Glauber model enables a connection to be made between the measured multiplicity and the impact parameter b 10

1.4.1 In-medium free-energy of a $q\bar{q}$ pair at a variety of temperatures around the QGP phase transition (the temperatures are in units of T_c) as calculated in lattice QCD [7]. At low temperatures the free energy approaches that in free space (black line). The plot demonstrates the temperature dependence of the $q\bar{q}$ color potential and hints at J/ψ suppression as a possible signature of the QGP 13

1.4.2 Hadronic yield ratios measured in $\sqrt{s} = 200$ GeV Au-Au collisions at RHIC compared to theoretical predictions assuming chemical equilibrium[8] 14

1.4.3 Illustration of a non-central nucleus-nucleus collision highlighting the asymmetry in the overlap region 15

1.4.4 Elliptic flow (v_2) as measured by a number of experiments including STAR at RHIC and ALICE at the LHC [9] 16

1.4.5 Top: Comparison of measurements of v_2 at RHIC [10] to perfect hydrodynamical calculations with and without QGP formation. At low p_T the results suggest the formation of the QGP with near zero shear viscosity. At higher p_T the agreement is not as convincing, and effects of viscosity have to be included. Bottom: Comparison of measurements of v_2 at ALICE and STAR with hydrodynamical calculations that incorporate finite shear viscosity and a phase transition to non-hydrodynamical behavior for the hadronic gas phase [11] 17

1.4.6 Illustration of the source of interference in HBT interferometry. Particles emitted from sources a and b can proceed to detectors A and B along either of the paths drawn which results in an interference in the resultant amplitude 17

1.4.7 Left: Comparison of measurements of the ratio R_{out}/R_{side} made at STAR to hydrodynamic models assuming zero viscosity [12]. Right: R_{out}/R_{side} as measured by ALICE (red points) and STAR (blue circles) compared to various hydrodynamic models [13] 18

1.4.8 Measurements of system size as parameterized by $R_{out}R_{side}R_{long}$ (left) and system decoupling time (right) as a function of particle multiplicity (a proxy for energy density) [13] 19

1.4.9 Feynman diagram of a simple process calculable in perturbative QCD at high energy 20

1.4.10 Feynman diagrams illustrating mechanisms of partonic energy loss in the QGP. Radiative energy losses are expected to dominate [14] 20

1.4.11 Schematic comparison of pp collisions with no in-medium energy loss, and heavy-ion collisions with path-dependent energy loss 21

1.4.12 Left: Di-hadron correlations as measured in STAR in central d-Au, pp and Au+Au collisions [12]. The striking suppression of the away-side jet in Au+Au provided strong evidence for in-medium jet modification. Right: Early 2D di-hadron correlation results from ALICE, where jet away-side jet modification is also apparent [15] 22

1.4.13 Left: R_{AuAu} of charged hadron yields in central Au-Au collisions at $\sqrt{s} = 200$ GeV and R_{dAu} in central and peripheral d-Au collisions at $\sqrt{s} = 200$ GeV as measured by STAR [16]. The high p_T hadronic suppression is apparent in Au+Au collisions. Right: R_{AA} of charged hadron yields in $\sqrt{s} = 2.76$ TeV Pb-Pb collisions for three different centralities as measured by ALICE [17]. High p_T hadron suppression is evident at all centralities, though greatest for most central collisions (0-5%) 23

1.5.1 Schematic of the various approaches to probing heavy-flavor in relativistic heavy-ion physics: (i) Measurement of J/ψ production via decays to electrons and muons (ii) Exploiting the large lifetime of B-hadrons and their unique decay topology for identification via displaced secondary vertices. These 'b-tagging' approaches can be implemented at the particle or the jet level (iii) Reconstruction of charm and bottom mesons via complete identification of their decay products and subsequent calculation of the invariant mass (iv) Identification of electrons or muons as a proxy for the parent B/D mesons. This methodology requires careful subtraction of background electrons from other sources, and by itself only allows for total heavy-flavor cross-section measurements to be performed. It is this procedure that is employed in this thesis 27

1.5.2 Differential cross-section of $J/\psi \to \mu^+\mu^-$ as measured by the CDF collaboration in $\sqrt{s} = 1.96$ TeV pp collisions [18] 28

1.5.3 Left: Invariant yield of electrons from semi-leptonic decays of heavy-flavor hadrons as measured by PHENIX with a comparison to FONLL predictions [19] Right: The invariant yield of electrons from semi-leptonic decays of heavy-flavor hadrons as measured by STAR with a comparison to FONLL predictions [20]. The blue points arise from a previous flawed measurement, that was later improved resulting in the red points (the agreement with FONLL is better with the latter result) 29

1.5.4 Left: Differential production cross-section of J/ψ in $\sqrt{s} = 2.76$ TeV and $\sqrt{s} = 7$ TeV pp collisions as measured by ALICE [21, 22] Right: Comparison of differential production cross-section of electrons from heavy-flavor decays as measured in ALICE and ATLAS with FONLL predictions [23] 30

1.5.5 Differential production cross-section for D mesons in $\sqrt{s} = 2.76$ TeV pp collisions as measured by the ALICE experiment [24] 31

1.5.6 Comparison of the nuclear modification factor of pions in $\sqrt{s_{NN}} = 200$ GeV Au-Au collisions as measured by the PHENIX collaboration with the predictions of various energy loss models [25]. Radiative energy loss models have been successful in replicating the experimentally observed energy loss for light flavors 33

1.5.7 Comparison of the R_{AA} of electrons from the decays of heavy-flavor hadrons as measured by PHENIX compared to a number of models. On the left the result is compared to DGLV predictions with (green band) and without (yellow band) collisional energy losses, and BDMPS predictions (thick dotted green line). On the right the result is compared to the results from two models employing a thermal approach to the energy loss: the Van Hees model and the Moore/Teaney model [26] 34

1.5.8 90% confidence level contours for R_{AA} of high p_T electrons ($p_T > 5$ GeV) from D-meson and B-meson decays compared to some model predictions[27] 35

1.5.9 R_{AA} of D meson production in Pb-Pb collisions at $\sqrt{s} = 2.76$ compared to a sample of different model predictions [28] 35

2.1.1 The development of high-energy accelerators (known as Livingston plots). The figure on the left shows the development of the equivalent energy of a fixed target accelerator for various types of particle detectors as a function of time, whereas the figure on the right shows the development of the center of mass energy of specific particle detectors and when they began operation [29]. 38

2.1.2 CERN's accelerator complex [30] 39

2.1.3 Schematic layout of the LHC [30] 41

2.1.4 Principle of RF acceleration 45

2.2.1 Simulation of the pseudorapidity distribution for central diffractive pp events in ALICE with the pseudorapidity acceptance of each detector subsystem overlayed. . 47

2.2.2 Schematic of the ALICE detector [31] 48

2.2.3 ALICE detector cross section during data taking in 2010 (a), 2011 (b), and 2012 (c). The data used for this analysis was recorded during March 2011 when the detector was in configuration (b) [31] 48

2.2.4 Diagram of the ALICE TPC indicating the major components. The drift principle is also illustrated: from a collision at the origin a track leaves an ionization trail (orange). At each point these *clusters* slowly drift towards the readout chamber (the dotted blue line indicates the drift trajectory of one such cluster) [32] 49

2.2.5 Illustration of a typical multi-wire-proportional-chamber (MWPC), that which provides readout in the ALICE TPC at the endcaps of the TPC. A charged particle within the drift volume ionizes the gas, and leaves a trail of *clusters*. These slowly drift towards the endcaps, whereupon they pass through a gating grid and cathode plane and subsequently form avalanches around the anode wires. The image of the ions produced in the avalanches constitutes the signal on the cathode read out pad [33] 50

2.2.6 p_T resolution of the tracking system in the data set used for this analysis [34] . . . 52

2.2.7 Figure (a) shows the dE/dx distribution for all tracks and (b) shows the dE/dx resolution for pions, electrons and protons in the data used for this analysis. For the resolution plot, pions and electrons are identified using the TOF detector and protons are identified from lambda decays [31] 53

2.2.8 Layout of the ALICE ITS detector: (a) Schematic of the detector where geometrical position of the 6 layers can be seen with respect to the ALICE coordinate system (see Appendix A) [35] (b) Cross-section of the ALICE detector as defined by the (x,y) distributions of gamma conversion points in 7 TeV *pp* collisions [31] 54

2.2.9 Vertex resolution in 7 TeV *pp* collisions as measured by the width of the vertex position distributions 56

2.2.10 ITS performance: (a) is the impact parameter resolution as estimated from the width of DCA distributions in 7 TeV *pp* collisions [31] (b) is the dE/dx distribution of all tracks in 2.76 TeV Pb-Pb collisions using the ITS as a standalone detector [31] 57

2.2.11 β for different particle species as measured by TOF in $\sqrt{s}$ = 2.76 TeV Pb-Pb collisions [31] 59

2.2.12 Photograph of an individual EMCal module comprising four towers. The Shashlik WLS fibers that penetrate the module longitudinally are visible [36] 63

2.2.13 Illustration and dimensions of a single module (right) and depiction of strip module assembly from 12 modules (left) [37] 64

2.2.14 Illustration of the construction of a supermodule from the individual strip modules [37] 64

2.2.15 Diagram of the ALICE EMCal as it is installed in ALICE. Note the structure of the 10 full and two half supermodules [36] 65

2.2.16 Illustration of positioning of the V0, T0 and FMD detectors in ALICE [38] 69

3.1.1 LHC delivered luminosity at the four interaction points during 2011 74

3.2.1 Illustration of the rejection of beam gas using V0 timing information. In case (b) a beam gas event occurs within the detector which results in a signal in only one of the V0 detectors; these are rejected by requiring a signal in both V0 detectors. In beam-beam collisions, and in beam-gas events similar in nature to case (a), a signal is seen in both V0 detectors. Timing information can be used to reject beam-gas events like those in case (a) by demanding that the collision time occurs before signals are recorded in the V0 detectors. 78

3.2.2 Correlation of the number of SPD clusters and the number of generated tracklets without (left) and with (right) physics selection. Only V0 timing information is used to remove beam-gas background 78

3.2.3 Illustration of the construction of tracklets in the SPD 79

3.2.4 Cut efficiency after physics selection for various event quality criteria for MB and EMCal trigger data 80

3.2.5 z coordinate of the reconstructed vertex for EMCal Trigger data, MB data and simulation (lhc11b10b) 81

3.2.6 (x, y) coordinates of the reconstructed vertex for the MB data 82

3.2.7 (x, y) coordinates of the reconstructed vertex for the EMCal trigger data 82

3.2.8 Number of towers with an energy above 100 MeV in each super module for the first 13 runs (left) and the last 3 runs (right) in MB data. The lines indicate the LED event rejection criteria. 83

3.2.9 Trigger Mask employed during data taking for lhc11a/pass2 EMCal triggered events. The white regions are not triggered on, while the red regions are allowed to be triggered on 84

3.2.10 Cluster multiplicity (left) and track multiplicity (right) for MB and EMCal trigger data sets 84

3.3.1 Firing frequency of the ≈12000 towers in the EMCal. The distribution is fitted with a Gaussian and those towers 5 standard deviations above the mean are deemed as hot towers and are removed from the analysis 86

3.3.2 $d\eta$ (left) and $d\phi$ (right) distributions of matched track-cluster pairs in MB and EMCal trigger data. The dased lines represent the matching cuts placed in this data analysis 87

3.3.3 Cluster positions in MB (left) and EMCal trigger (right) data sets for clusters with an energy above 1 GeV. 87

4.1.1 Illustration of the combinatorial seed generation procedure (from [39]) 90

4.2.1 (η, ϕ) position of tracks with 4 ITS hits in lhc11a/pass2. Since the SDD layers are not active, this can only occur when both SPD layers have hits. The gaps in acceptance due to the faulty cooling system are clearly observed 92

4.2.2 η distribution of accepted tracks for all tracks (left) and high p_T tracks (right). In both sets the distribution is approximately uniform at low p_T but a characteristic enhancement is observed for high p_T tracks in the EMCal triggered data set. The red lines indicate the imposed track cut 93

4.2.3 ϕ distribution of tracks passing all track quality cuts with (left) and without (right) requiring 3 ITS hits. The distribution of tracks is approximately uniform for the MB data set as one would expect, however requiring 3 ITS hits introduces inhomogeneity due to the non-uniform response of the SPD 94

4.2.4 Track p_T distribution for the MB and EMCal triggered data sets 94

4.2.5 Cumulative track cut efficiency as a function of the track cut being applied for the MB and EMCal trigger data 95

4.2.6 DCA$_{xy}$ (left) and DCA$_z$ (right) distributions of all tracks that *pass all other cuts* except the DCA$_{xy}$ (left) and DCA$_z$ (right) cuts in MB and EMCal trigger data. The red lines indicate the cut placement 96

4.2.7 Number of ITS (left) and TPC (right) clusters possessed by tracks that *pass all other cuts* except the ITS (left)/TPC (right) cluster cuts. The red line indicates the cut placement 97

4.2.8 χ^2 distribution of tracks that *pass all other cuts* except the χ^2 cut in MB and EMCal trigger data. The red line indicates the cut criteria 97

4.3.1 Tracking efficiency of pions and electrons in simulation (lhc11b10b) 100

4.4.1 Apparent momentum resolution for electrons (left) and pions (right) in simulations 101

4.5.1 Ratio of reconstructed spectrum with normal tracking cuts to the reconstructed spectra with loose and hard tracking cuts in MB (left) and EMCal trigger data (right). The red line indicates the assigned systematic uncertainty 105

4.5.2 Ratio of the reconstructed spectrum for various unfolding algorithms and iterations to the reconstructed spectrum for the 'default algorithm' (Bayesian) with the optimal iteration parameter (5) 106

4.5.3 Comparison of the result of various unfolding algorithms when the MB and EMCal trigger spectra are first combined before unfolding. The lower panel shows the ratio of the spectrum obtained from some of the unfolding algorithms (those used for estimating the systematic uncertainty) to that obtained with the default algorithm (Bayesian with iteration parameter 5) 107

5.1.1 $\frac{dE}{dx}$ as a function of momentum, p, for 2.76 TeV pp EMCal triggered (left) and MB (right) events. The solid lines are tuned Bethe-Bloch parameterization curves for different species 110

5.1.2 E/p distributions of electrons (black) and hadrons (blue). The inlay is the same plot with a logarithmic y-axis 111

5.1.3 $n\sigma_e$ vs $\frac{E}{p}$ for the EMCal triggered data integrated over all $p_T > 4$ GeV/c 112

5.1.4 $n\sigma_e$ vs $\frac{E}{p}$ for the EMCal triggered data integrated over all p_T illustrating the PID optimization method. A test ellipse is drawn followed by a mirror of this ellipse about the peak position of the electron distribution in $n\sigma_e$ space. The highlighted regions are used to calculate the signal (S) and background (B) as described in the text 113

5.1.5 Effective Signal of various PID selection criteria in MB (left) and EMCal triggered data (right) 114

5.1.6 p_T independent optimized cut choices in MB (left) and EMCal triggered data (right) 115

5.2.1 $n\sigma_e$ distribution of all tracks which pass the $\frac{E}{p}$ cut and have $5 < p_T < 6$ GeV/c in EMCal triggered data 116

5.2.2 $n\sigma_e$ distribution of all tracks with $5 < p_T < 6$ GeV/c (left), and all tracks that pass the $\frac{E}{p}$ cut (right) in EMCal triggered data 118

5.2.3 $n\sigma_e$ vs p_T with the Bethe-Bloch parameterizations (solid curves) for each particle species and the mean of the gaussian fitted to the $n\sigma_e$ distributions (circular points) for MB data (left) and EMCal triggered data (right). The error bars represent the sigma of the fitted gaussian 119

5.2.4 Estimated PID efficiency in the toy model for various background scenarios as a function of the purity cut 120

5.2.5 Estimated PID efficiency as a function of the purity cut in EMCal triggered data. Each histogram represents a different p_T bin in GeV/c 121

5.2.6 $\frac{E}{p}$ signal in simulation (lhc11b10b) for tracks with $4 < p_T < 5$. The curves are fits used to estimate the PID purity 122

5.2.7 The estimated purity in EMCal data using the TPC method and the EMCal method. Within error bars, the results are consistent 124

5.2.8 Estimated efficiency and purity in the MB data (left) and EMCal data (right) . . . 125

5.3.1 Ratio of reconstructed spectrum with normal PID cuts to the reconstructed spectra with loose and hard PID cuts in EMCal trigger data. The red line indicates the assigned systematic uncertainty 127

5.3.2 The reconstructed spectrum in the EMCal triggered data using the maximal, minimal and standard PID efficiency and purity. The gray lines indicate the spectra calculated with the maximum and minimum PID efficiency and purity corrections, and the deviation between the gray lines and the black points represents the second component of the associated systematic uncertainty in the PID efficiency and purity correction 128

6.1.1 Schematic of the trigger electronics of the ALICE EMCal (from [40]). SMA/Ci refers to supermodule number i on the A/C side of the detector (see Appendix A for more information on the detector orientation and labelling). The Summary Trigger Unit (STU) collects and aggregates the information from the individual trigger units (TRUs) to generate the global L0 trigger decision 130

6.1.2 Depiction of the different trigger algorithm patch sizes over a single supermodule. From [40] 131

6.2.1 Schematic of a hypothetical cluster energy distribution obtained from a MB trigger and an L0 EMCal trigger 131

6.2.2 Comparison of the ratio of PID electron track p_T in EMCal triggered to PID electron track p_T in MB data to the ratio of inclusive cluster energy in EMCal triggered to inclusive cluster energy in MB data 133

6.2.3 Ratio of the cluster energy spectrum in EMCal data to that in MB data separated by supermodule 134

6.2.4 Ratio of the triggered cluster energy spectrum to the inclusive cluster energy spectrum in EMCal trigger data 136

6.2.5 Ratio of the triggered cluster energy spectrum in EMCal data to the inclusive cluster energy spectrum in MB data 137
6.2.6 Comparison of the trigger efficiency for all clusters measured in data, to that obtained from the described trigger simulation. The red lines indicate the upper and lower uncertainty bands on the simulation 138
6.2.7 Comparison of the trigger efficiency for all clusters (in energy) to electrons (in track p_T) 138
6.2.8 Applied trigger correction incorporating the trigger efficiency and the rejection factor. The blue lines indicate the error bounds used in assigning the systematic error 139

7.1.1 Invariant differential cross-section of π^0 production in $\sqrt{s} = 2.76$ TeV *pp* collisions as measured by ALICE. The left-hand size is the cross-section with a Tsallis fit, and the right-hand side is the ratio of the data points to the fit 145
7.1.2 Invariant differential cross-section of η production in $\sqrt{s} = 2.76$ TeV *pp* collisions as measured by ALICE. The left-hand size is the cross-section with a Tsallis fit, and the right-hand side is the ratio of the data points to the fit 145
7.1.3 Invariant yield of background electrons from the various sources included in the background electron cocktail 149
7.2.1 The magnitudes of the systematic error introduced in the background cocktail from various sources 150

8.1.1 Illustration of the effect of an exponentially decaying spectrum on the average bin position. The FONLL prediction for the heavy-flavor cross-section was taken as the assumed functional form. This bin-shifting effect was incorporated into the application of the various efficiency and purity corrections 154
8.1.2 Inclusive electron cross-section obtained by unfolding the MB and EMCal separately and subsequently merging. The boxes present the systematic uncertainty and the error bars represent the statistical uncertainty 155
8.1.3 Inclusive electron cross-section obtained by merging the MB and EMCal trigger spectra before applying the unfolding procedure. The boxes present the systematic uncertainty and the error bars represent the statistical uncertainty 155
8.1.4 Systematic error from various source in the inclusive electron cross-section and the heavy-flavor electron cross-section. The heavy-flavor electron cross-section includes the systematic uncertainty associated with the cocktail 156

8.2.1 Heavy-flavor electron cross-section in $\sqrt{s}$ = 2.76 TeV pp collisions compared to FONLL, GM-VFNS and k_T-factorization models 157

8.3.1 Measurement of the ratio of the yield of electrons from the decays of b-hadrons to the yield of electrons from heavy-flavor hadrons by ALICE, with comparison to other experiments (left) and FONLL (right) [41] 160

8.3.2 Measured of the charm and beauty electron cross-sections obtained by combining the result of this analysis with the result of a correlation analysis by ALICE [31] . 160

8.4.1 Comparison of the heavy-flavor electron production cross-section measured in $\sqrt{s}$ = 2.76 TeV pp collisions for this thesis to the heavy-flavor electron production cross-section measured in $\sqrt{s}$ = 7 TeV pp collisions scaled to $\sqrt{s}$ = 2.76 TeV collision energies using a pQCD based scaling [31] 162

8.5.1 Heavy-flavor electron R_{AA} as measured by ALICE in $\sqrt{s}$ = 2.76 TeV Pb-Pb collisions for most central events (0-10%) compared to the heavy-flavor electron R_{AA} measured by PHENIX in $\sqrt{s}$ = 200 GeV Au-Au collisions [31, 42]. The results are consistent where they overlap. Note that for $p_T < 8$ GeV/c the the scaled $\sqrt{s}$ = 7 TeV pp cross-section was used as a reference, while above $p_T = 8$ GeV/c the FONLL prediction for pp collisions was used as a reference 163

A.1 The coordinate system of the ALICE detector. Adapted from [43, 44] 166

B.1 A real-life example of the measurement that comprises some signal, S, and background B. In this case it is the measurement of the bottom baryon resonance, Λ_b^0, by the CDF collaboration [45] 167

C.1 $n\sigma_e$ vs $\frac{E}{p}$ distributions in p_T slices for HT data 169

C.2 $n\sigma_e$ vs $\frac{E}{p}$ distributions in p_T slices for MB data 170

C.3 Illustration of toy model employed to study the effects of varying the 'purity cut' on the determination of the PID efficiency 171

C.4 Estimated PID efficiency in the toy model for various background scenarios as a function of the purity cut 172

List of Tables

2.1.1 Various beam parameters at injection and collision at the LHC at peak luminosity for proton beams [46] 44
2.2.1 Characteristics of the ITS detector subsystems [47] 54
2.2.2 The minimum bias trigger class definitions 72

3.2.1 Event selection efficiency for various event cuts placed after physics selection 84

4.2.1 Track quality cut efficiencies for MB and EMCal trigger data. Four efficiencies are listed: 'final' refers to the efficiency of the cut once all other cuts have been applied; 'sequential' (Seq.) refers to the efficiency of the cut when applied in the order the cuts are listed in the table; 'cumulative' (Cum.) refers to the total track efficiency of all tracks cuts applied sequentially in the order the cuts are listed in the table; and 'sole' refers to the efficiency of the cut when no other cuts have been applied. It is the cumulative efficiency that is visually represented in Figure 4.2.5 95
4.4.1 Selected iteration parameters for the different unfolding algorithms and data sets . . 104
4.5.1 The three set of track cuts used for determining the systematic uncertainty in the estimation of the tracking efficiency and response matrix. 105
4.5.2 Summary of the estimated systematic uncertainties associated with the tracking efficiency and unfolding corrections. In the final cross-section the 'Tracking Efficiency + Response Matrix' uncertainty is combined in quadrature with the 'Unfolding Algorithm' uncertainty 108

5.1.1 Electron PID cuts used in this analysis 115
5.3.1 The three set of track cuts used for determining the systematic uncertainty in the estimation of the PID efficiency and purity 126

7.1.1 Sources of electrons included in the background cocktail simulation, their decay modes, and respective branching ratios [48] 144

7.1.2 Ratio of various meson to π^0 yields at $p_T = 5$ GeV/c used in the m_T-scaling procedure146

1

Introduction

1.1 The Standard Model and QCD

Although considered by many to be incomplete [49, 50, 51], the standard model of particle physics provides the best available description of the fundamental particles and their interactions. Since its inception in the 1970's a plethora of different experiments have provided experimental validation of the standard model. Measurement of the anomalous magnetic moment of the electron (g) to better than 1 part in 10^{13}, measurement of the value of the strong coupling constant (α_s) along with it's variation with energy (asymptotic freedom), and the discovery of the predicted $W^{\pm}$ and Z^0 bosons (and the connection between their masses) are among the diverse experimental verifications of the standard model [2, 52, 53, 54].

The standard model is formulated within the framework of quantum field theory. The primitive entities are 'fields', excitations of which represent particles; 'quantum', in the sense that the analogous classical fields are promoted to operators with a specified algebra (see for example [55, 56]). The fundamental particles can be delineated as 'leptons', 'quarks' or 'gauge-bosons' (see Figure 1.1.1). The gauge-bosons act as force mediators for the four fundamental interactions in the theory: the electromagnetic, weak, strong and gravitational interactions (though as yet there is no known way to incorporate gravity in the present framework [57]).

The standard model is also a 'gauge field theory', where the form of the interactions is determined by demanding local invariance under some symmetry transformation. The underlying symmetry group of the standard model in its entirety is SU(3)⊗SU(2)⊗U(1). The SU(3) part of the standard model is known as quantum chromodynamics (QCD), which describes how the fundamental particles interact via the strong force. Only the quarks interact via the strong force along with the mediating gauge boson, the gluon.

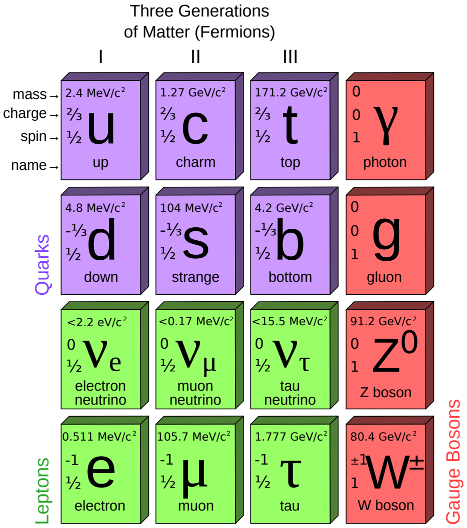

Figure 1.1.1: Fundamental particles within the standard model [1]

The quark model arose from an attempt to understand the large number and diversity of hadronic states [48] which began to be observed in the 1940's. Such a vast multiplicity strongly suggested that the newly observed hadrons were not fundamental. Indeed, the quark model provided a description of the hadronic spectrum in terms of six fundamental quarks [58, 59, 60]. To satisfy the Pauli exclusion principle, quarks were hypothesized to possess another quantum number known as *color*. The predication of the confinement hypothesis, that hadronic states must be colorless, was used to explain why free quarks were hitherto unobserved. Subsequent experiments, such as the measurement of the ratio of the $\sigma(\mathrm{e}^+\mathrm{e}^- \rightarrow \mathrm{hadrons})$ and $\sigma(\mathrm{e}^+\mathrm{e}^- \rightarrow \mu^+\mu^-)$ cross-sections, lent credence to the quark model [61]. The observation of 3 distinct colors, and the fact that quarks and anti-quarks are distinct states (so real lie group representations are excluded) suggests that SU(3) should form the basic symmetry group of QCD [62].

In theory, to describe all physical processes involving the strong force one only needs the Lagrangian of QCD:

$$\mathcal{L}_{\mathrm{QCD}} = \bar{\psi}_i(i\gamma^\mu\partial_\mu - m)\psi_i - gG^a_\mu\bar{\psi}_i\gamma^\mu T^a_{ij}\psi_j - \frac{1}{4}G^a_{\mu\nu}G^{\mu\nu}_a \tag{1.1}$$

where $\psi_i(x)$ is the quark field, $G^a_\mu(x)$ are the gluon fields, γ^μ are the Dirac matrices, and T^a_{ij} are the generators connecting the fundamental, anti-fundamental and adjoint representations of the SU(3) gauge group. $G^a_{\mu\nu}$ is the gluonic field strength tensor given by:

$$G^a_{\mu\nu} = \partial_\mu G^a_\nu - \partial_\nu G^a_\mu - g f^{abc} G^b_\mu G^c_\nu \tag{1.2}$$

where f^{abc} are the structure constants of SU(3). Calculational difficulties limit the predictive power to particular regimes however. Like the standard model as a whole, perturbation theory is the primary tool for making quantitative predictions. One of the unsettling features of the standard model, and of quantum field theories in general (at least those that correspond to observed physical processes), are UV divergences in calculable quantities. The commonly accepted resolution to these divergences is the method of renormalization. We acknowledge that our theory is some low energy approximation to a complete theory, but are also aware of the common separation of scales that appears in physics: in order to study the motion of a tennis ball we need not invoke quantum mechanics, which is only relevant at roughly atomic scales. We thus parameterize our ignorance by absorbing the divergences into the definitions of the coupling constants and masses. The masses and couplings that appear in the Lagrangian are thus 'bare' masses, not representative of what is measured. This renormalization procedure leads to a variation of the coupling constants with energy (for a discussion of the theory of renormalization see [63]). This variation in the coupling constant as a function of energy (or the renormalization scale) is described by the renormalization group [55, 56]. Since the perturbation theory of such theories is typically a series expansion involving progressively higher orders of the coupling constant, this scale variation has the capacity to limit the efficacy of perturbation theory. In particular, the QCD coupling constant, α_s, exhibits *asymptotic freedom*: the coupling constant decreases logarithmically at high energies. To leading order in perturbation theory the functional dependence of the coupling constant on the energy scale is given by:

$$\alpha_s(Q^2) = \frac{4\pi}{(11 - \frac{2}{3}n_f)\log Q^2/\Lambda^2_{QCD}} \tag{1.3}$$

where Q^2 is the momentum transfer of the process under consideration, n_f is the number of 'active' quark flavors, and Λ_{QCD} can be thought of as the momentum scale where non-perturbative effects start to become significant. Thus at high energy scales the theory is amenable to perturbative approaches, but at low energy scales perturbation theory fails and other (non-perturbative) techniques have to be employed.

The cross-over between the perturbative and non-perturbative regimes occurs at $\approx$ 200 MeV, and above this energy scale predictive power is provided by perturbative methods. Although in QCD

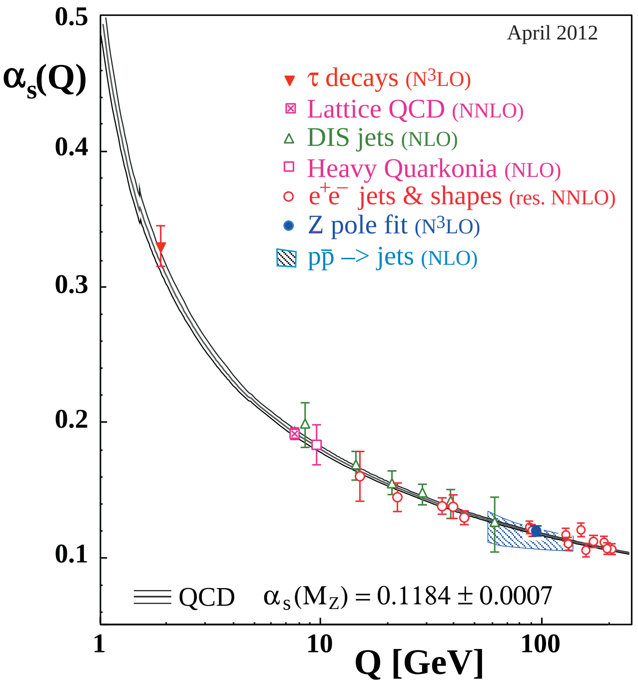

Figure 1.1.2: QCD strong coupling constant as a function of energy [2]

there is no analog of the remarkable measurement of the anomalous magnetic moment in QED, perturbative QCD has been tested in a plethora of different experimental conditions. Observation of scaling violations of the proton structure function, measurement of quarkonium decay rates, and the determination of jet properties in processes such as $e^+e^- \rightarrow q\bar{q}$ are among the diverse experimental verifications of QCD in the perturbative regime [64, 65]. Perhaps the most direct quantitative test is the scaling of α_s with Q^2. Figure 1.1.2 shows the value of the strong coupling constant (α_s) as measured by a number of different experiments that convincingly demonstrate the expected logarithmic variation of the coupling constant with energy [2]. In many experimental tests of QCD, both perturbative and non-perturbative effects play a role. Critical to the ability to make quantitative predictions then, are a number of *factorization theorems*. These allow for the separation (factorization) of the perturbative, and calculable, part of a process from the non-perturbative parts (for instance hadronization which necessarily involves long-distance behavior). The latter can then be accommodated with further measurements of parton distribution functions and fragmentation functions. However, the long-distance behavior is of interest in it's own right, and it is non-perturbative calculations that hint at the possibility of forming a state of matter known as the quark-gluon-plasma.

1.2 The Quark Gluon Plasma (QGP)

Various approaches have been employed to study the features of QCD at low energy, with each approach capable of exploring different aspects of the theory. These techniques include the MIT bag model, QCD sum rules, Nambu-Jona-Lasinio models and effective theories such as chiral perturbation theory [66]. Perhaps the best established approach is *lattice QCD* [48, 67, 68]. Lattice gauge theory is an approach to quantum field theories where space and time is discretized on a 'lattice'. This provides a natural method of renormalization since there is a natural cut-off at the lattice space-time dimension, but more importantly for this discussion, it allows for predictions in the non-perturbative regime. Calculations proceed via the path integral approach, with fermion fields defined on lattice points and gluon fields defined on the links between lattice points. In practice these calculations proceed numerically with the aid of supercomputers. In order to make a connection to continuum QCD, calculations are repeated at different lattice spacings and extrapolated to the continuum limit. Lattice QCD allows for non-perturbative calculations of a medley of interesting parameters such as the masses of the hadrons (the hadron spectrum), form factors of various semileptonic decays (e.g. $B \to \pi l \nu$) and decay constants of a variety of mesons and hadrons [48]. Confinement has also been demonstrated in the continuum limit with lattice QCD by showing the inter-quark potential can be parameterized by:

$$V(r) = -\frac{A}{r} + \sigma r + V_0 \tag{1.4}$$

where A, σ, and V_0 are parameters of the fit, and r is the quark-quark separation. Thus the attractive force increases with separation, seemingly without bound. In reality at some point the formation of a $q\bar{q}$ pair becomes more energetically favorable and confinement is maintained with the production of two new colorless mesons. Of most relevance to this thesis however, is the elucidation of the QCD phase diagram provided by lattice QCD.

Although the idea that hadronic matter may undergo a phase transition at high densities and temperatures was already being discussed [69, 70, 71], Cabbibo and Parisi were the first to draw a phase diagram of hadronic matter akin to what is commonly accepted today [72]. Hagedorn developed the so-called statistical bootstrap model, where he showed that the spectrum of hadronic states increased without bound, and in fact diverged at some critical temperature [73]. This was suggested as an indication of a limiting temperature beyond which hadronic matter could not exist. Based on this idea, Cabbibo and Parisi went further to hypothesize a second a order phase transition both at high temperatures and high densities; Figure 1.2.1 shows a schematic of the hypothesized phase diagram of QCD in it's contemporary formulation. The physical basis for the idea of a phase transition is easily understood intuitively within the bag model of hadrons [74, 75, 76]. In it's simplest guise, the bag model of hadrons describes a colorless baryon (meson) as a collection of 3 (2) *valence* quarks, some number of $q\bar{q}$ pairs (from the vacuum) and some number of gluons all confined within a boundary that phenomenologically incorporates non-perturbative effects (confinement) with some finite *bag pressure*, B. Simple thermodynamic arguments lead one to expect the following equation of state for a modeled hadron [76]:

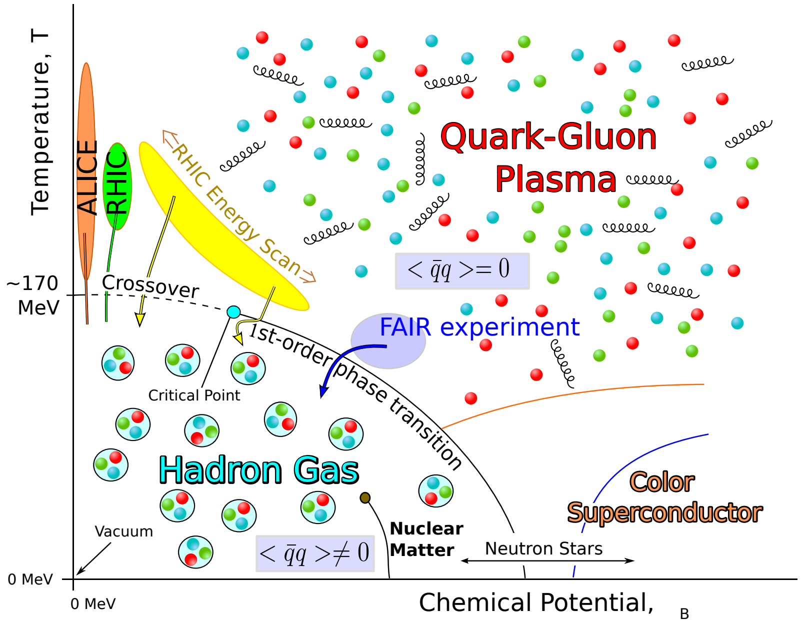

Figure 1.2.1: Schematic of the QCD phase diagram as presently understood. The approximate regions of phase space explored by the FAIR experiment, experiments at RHIC and the ALICE experiment are indicated on the diagram. The chiral-symmetry breaking transition is assumed to coincide with the hadron-plasma transition as suggested by lattice QCD calculations [3, 4]

$$P = 37\frac{\pi^2}{90}T^4 \tag{1.5}$$

Thus the finite bag pressure, which can be estimated by solving the Dirac equation for fermions in a spherical cavity, will be overcome at some critical temperature, T_c, and one may expect that a deconfined state of matter may be produced. Likewise, since the pressure scales as $P \sim \mu_B^4$, one may expect the formation of a deconfined state at high enough densities. This deconfined state is known as the quark-gluon plasma (QGP). These intuitive ideas suggesting the possibility of a deconfined state have been placed on firmer footing by lattice QCD.

At zero baryon chemical potential, which is approximately satisfied in the experimental conditions created at RHIC and the LHC, lattice QCD has successfully determined the equation of state of hadronic matter, identifying a cross-over between hadronic gas and the QGP at ~ 175 MeV (see also Figure 1.2.2). At finite chemical potential a difficulty known as the 'sign problem' prevents direct

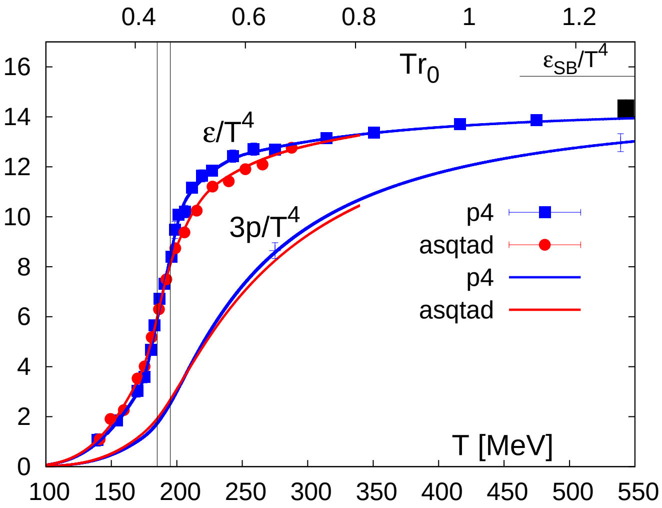

Figure 1.2.2: Equation of state of hadronic matter at zero baryon chemical potential as determined using lattice QCD by the HotQCD collaboration [5]

application of lattice QCD [77]. However, much progress has recently been made to overcome the sign problem and several approximate calculations have demonstrated that the transition temperature indeed decreases as a function of chemical potential [78, 79, 80]. Moreover, in agreement with chiral effective theories, lattice QCD suggests that at sufficiently high chemical potential the cross-over becomes a first order phase transition, with disputably a critical point at a chemical potential of ~ 240 MeV [81, 82, 83]. Lattice QCD has also shed light on the so called *chiral symmetry breaking*. In the massless limit, QCD exhibits chiral symmetry, an invariance of the Lagrangian under the transformation $\psi \rightarrow e^{i\alpha\gamma^5}\psi$. Typically this symmetry is spontaneously broken, that fact being manifest in a non-zero vacuum expectation value of the field, $\angle q\bar{q}\rangle \neq 0$. Hence, a chiral phase transition may be expected at high temperatures as the massless limit becomes a better approximation to reality. A priori, the chiral symmetry breaking transition and the confinement-deconfinement transition are unrelated. However, lattice QCD has shown that at the very least the transition temperatures are exceptionally close, and it hypothesized that they may be coincident [3, 4]. Although not accessible with lattice QCD, the QCD phase diagram has also been theoretically explored at high densities and low energies. An interesting result of these studies is the prediction of a color superconductor at sufficiently high densities. The fermionic nature of quarks implies that at high enough densities a collection of quarks will form a Fermi surface. Then in analogy to the corresponding situation for electrons in certain solids, a bosonic condensate of pairs of quarks can form in the presence of an attractive interaction [84, 85].

The existence of the quark-gluon plasma is not solely a theoretical possibility. The high energy densities that are expected to have existed soon after the Big Bang indicate that all matter would have existed in the form of the QGP until $\sim 10^{-5}s$ after the big bang [75]. Moreover, the density of matter is sufficiently high in neutron stars that a high density QGP is expected to exist [75]. Most relevant for this thesis are the efforts to recreate the QGP in the laboratory. By colliding heavy nuclei in particle accelerators it is possible to achieve sufficiently high temperatures and densities to form a QGP [75].

1.3 Relativistic Heavy-ion Collisions

The observation of high energy nuclear collisions dates back to the genesis of particle physics, with experiments studying cosmic rays using nuclear emulsions [86]. Although experiments involving collisions of relativistic nuclei had already taken place in the 1970's at Lawrence Berkeley National Lab (LBNL) in the USA and at the Joint Institute of Nuclear Research (JINR) in the USSR [86], the first investigations of relativistic heavy ion collisions that were motivated by the hypothesis of QGP formation were the experiments at Brookhaven National Laboratory (BNL) in the USA and at the European Organization for Nuclear Research (CERN) near Geneva, Switzerland. Experiments utilizing both the alternating gradient synchrotron (AGS) with $\sqrt{s_{NN}} \sim 5$ GeV at BNL, and the super-proton-synchrotron (SPS) with $\sqrt{s_{NN}} \sim 17$ GeV at CERN, provided tantalizing evidence of the production of a QGP [87, 88, 89, 90, 91]. However, unambiguous evidence of the quark-hadron phase transition was first provided at the relativistic heavy-ion collider (RHIC) [87, 91, 92] at BNL, and subsequently at the large hadron collider (LHC) at CERN [93] in a new energy regime ($\sqrt{s_{NN}} = 200$ MeV at RHIC and $\sqrt{s_{NN}} = 2.75$ TeV at the LHC). A discussion of some of the general features of heavy-ion collisions is relevant to all of these experiments, including that relevant for this thesis: the ALICE experiment at the LHC.

In a typical heavy-ion experiment, heavy-ions stripped of their valence electrons are accelerated to high energies for collision. Although the AGS utilized fixed target experiments, the greater energy available for particle production (or QGP formation) when both particles are accelerated towards one another motivates the use of colliders in modern heavy-ion experiments such as those at RHIC and the LHC. Typically, the coordinate system is chosen such that the collision takes place along the z-axis, with the relevant kinematic variables being the transverse momentum, $p_T = \sqrt{p_x^2 + p_y^2}$, the rapidity, $y = \frac{1}{2}\ln\left(\frac{E+p_z c}{E-p_z c}\right)$, the pseudo-rapidity, $\eta = \frac{1}{2}\ln\left(\frac{p+p_z}{p-p_z}\right)$, and the transverse mass, $m_T =$

$\sqrt{p_T^2 + c^2}$. More details concerning the exact coordinate system utilized in ALICE are to be found in Appendix A. A simplified picture of the evolution of a heavy-ion collision in the center-of-mass frame is presented in Figure 1.3.1 In the initial state, the heavy-ions are accelerated to an ultra-relativistic domain such that the dimension along the direction of motion is highly Lorentz contracted; the resulting collision can be visualized as the collision of 2 very thin discs. In Figure 1.3.1 the collision is drawn as a head-on collision, with no transversal displacement between incident nuclei. However, in real collisions the relative position of the particle beams is not able to be controlled with sufficient precision to guarantee that this picture holds, and it is clear that the collisional geometry is of great significance. In fact, the *centrality* of a collision is a parameter of critical importance in characterizing

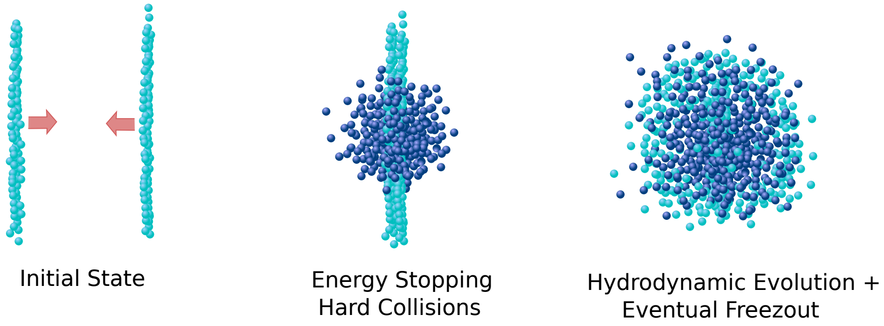

Figure 1.3.1: Schematic of the evolution of a heavy-ion collision

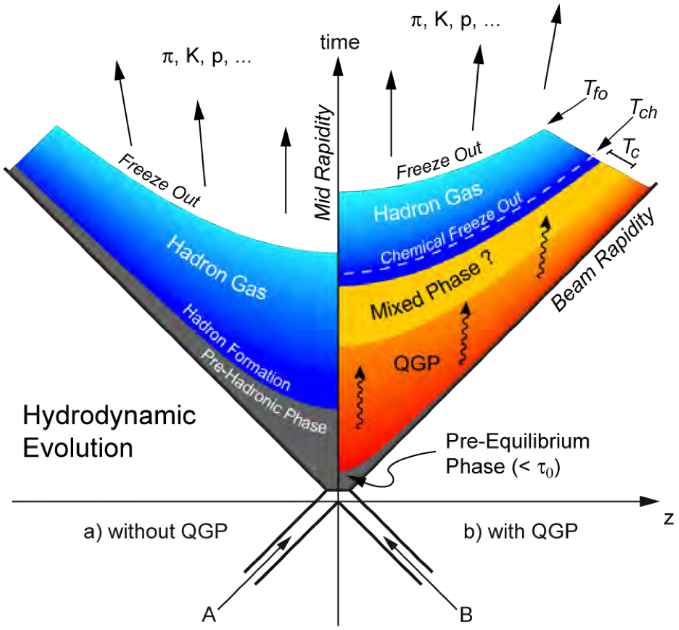

Figure 1.3.2: Space-time evolution of a heavy-ion collision with (right) and without (left) QGP formation [6]

heavy-ion collisions. For head-on collisions, which are designated *central* collisions, a larger fraction of the impingent partons are involved in the collision than in *peripheral* collisions where the colliding nuclei are not aligned. Thus, the energy density, the probability of QGP formation, and the size of the QGP formed are highly dependent on the centrality. In practice the centrality is correlated with the multiplicity, the number of particles produced in a collision in some predefined pseudo-rapidity window, and the multiplicity serves as a measure of centrality. The correlation between the multiplicity and the centrality (as characterized theoretically by the number of participant partons) is typically determined through simulations based on the Glauber model [94, 95].

The Glauber model provides a simple semi-classical picture of the collisional geometry of a heavy-ion collision. To first approximation, the possibility of secondary particle production and excitation of incident nucleons is ignored; a heavy-ion collision is treated as a number of independent hard collisions between the constituent baryons. Dependent upon the impact parameter, b, the number of *participant* and *spectator* nucleons will vary (see Figure 1.3.3). The position of the incident nucleons is determined stochastically according to the well known Woods-Saxon distribution that phenomenologically characterizes the nuclear charge densities from low energy electron-nucleus scattering experiments [96, 97]:

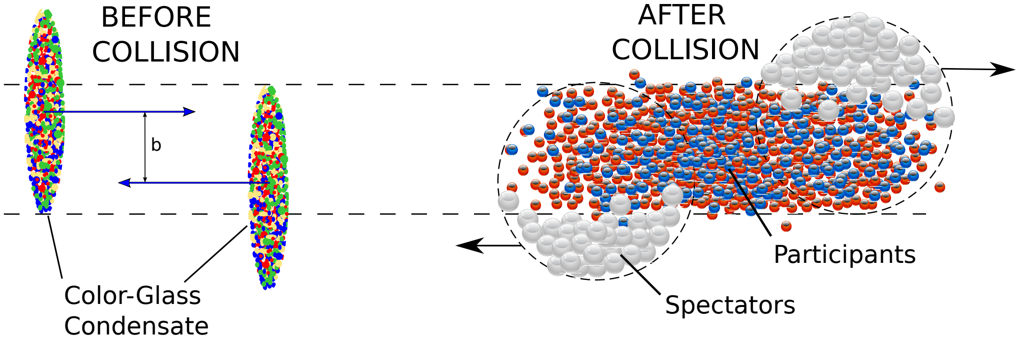

Figure 1.3.3: Illustration of a heavy-ion collision with some finite impact parameter, b. A b-dependent fraction of the incident nucleons will interact, with the remaining non-interacting nucleons being known as spectators. The Glauber model enables a connection to be made between the measured multiplicity and the impact parameter b

$$\rho(r) = \rho_0 \frac{1 + w(r/R)^2}{1 + e^{\frac{r-R}{a}}} \tag{1.6}$$

where w parameterizes non-sphericity, R is the nuclear radius, ρ_0 is the nucleon density at the center of the nucleus, and a is a parameter known as the 'skin depth'. Assuming independent binary collisions between these probabilistically positioned nucleons, the Glauber model enables calculation of the number of participants and number of binary collisions as a function of the impact parameter which can in turn be related to the measured centrality [94].

Although the Glauber model serves as a useful tool to correlate measured centrality to the unmeasured number of binary collisions and the impact parameter, in reality the collision of heavy-ions will involve both nucleon excitation and particle production. There are several models which define the initial condition for collision and describe the immediate particle production mechanisms. This pre-equilibrium phase can be described incoherently with perturbative QCD based models, or coherently with models involving color-strings or the color-glass condensate, see for instance [75, 76]. In the former, hard or semi-hard parton scatterings in the initial collision create multiple *mini-jets* which form the seeds of the QGP [98]. In string models, the strong force between constituent quarks is phenomenologically visualized as flux tubes ("color strings"), which are stretched as the incident nuclei pass one another; at some point it becomes energetically favorable to generate $q\bar{q}$ pairs, and thus the breaking of these strings acts as a source of the QGP. The color-glass-condensate is a state of matter hypothesized to exist in baryons accelerated or probed to extreme relativistic domains [99, 100]. At high energies, the fraction of the baryon momenta carried by gluons drastically increases and the baryon can be visualized as a dense saturated sea of overlapping and highly correlated gluons. The decoherence to the QGP takes place via *glasma* formation [101, 102, 103, 104].

Some of the first experimental data from RHIC indicated that the QGP formed a nearly inviscid fluid with the initial state quickly thermalizing unexpectedly quickly, well within $\tau_0 \sim 1$ fm/c [12, 105, 106]. The subsequent evolution of the thermalized QGP was shown to be well described by relativistic hydrodynamics [12], though true agreement was only evident in central collisions of large nuclei [107]. More recent work has indicated that the resolution of the discrepancies in more peripheral collisions resides in the fact that QGP is best described by relativistic hydrodynamics only in the initial stages, and dissipative effects can not be ignored for the entire evolution [107, 108].

As the plasma expands and cools, the system eventually approaches the hadron-plasma phase transition, at which point the quarks and gluons begin to condense into hadrons. Depending on the nature of the phase transition, there may be an interval of coexistence of the QGP with a hadronic gas, but eventually the system fully transitions to the hadronic gas phase (see Figure 1.3.1 for an illustration of the described space-time evolution of the system with and without QGP formation). Initially, when the mean-free path of the hadronic gas is larger than the scale of the system, the hadronic gas evolution can too be described hydrodynamically (though recent results indicate that that the hadronic phase may be too dissipative to be described hydrodynamically [9, 109]) . Eventually however, chemical equilibrium can no longer be maintained and chemical *freeze-out* is reached. Subsequent to chemical freeze-out is thermal freeze-out, where kinetic equilibirum is no longer maintained. Particle multiplicities can be well described assuming thermalization within *statistical hadronization models* where hadronization takes place statistically in local 'clusters' or 'fireballs' [12, 110]. From the final state particles that form the remnants of this evolution, experiments such as those at RHIC and the LHC are forced to play detective to reconstruct the entire process and try to understand the properties of the QGP.

1.4 Signatures of the QGP

Part of the inevitable detective work is distinguishing between scenario (a) or scenario (b) (with reference to Figure 1.3.2), and thus searching for unique measurable characteristics of the QGP phase. Though there is no unique signal that would provide unambiguous evidence for formation of the QGP, there are a plethora of different signatures that collectively can provide strong evidence for its creation in the laboratory. A few of these diagnostic tools are summarized here, but more complete reviews can be found in the references (for instance, see [12, 75, 76, 111]).

1.4.1 Debye Screening and J/ψ Suppression[1]

In analogy to familiar Debye screening in electrodynamics, in the QGP the abundance of quarks and gluons present in the system may lead to a screening of the color charge of quarks and gluons as first suggested by Matsui and Satz [76, 112]. This suggestion has been confirmed in lattice QCD simulations, where the in-medium potential between two quarks is highly dependent on the temperature of the medium (see Figure 1.4.1). In combination with the inherent deconfinement in the QGP, this can lead to the dissociation of J/ψ particles in the medium. The large mass of charm quarks indicates that J/ψ mesons are most prolifically produced by hard scatterings in the initial collision, and thus suppression of the J/ψ yield is a characteristic signature of QGP formation.

Experimentally, success of utilizing this probe has been mixed. J/ψ suppression was indeed observed at SPS [113], but similar levels of suppression were observed at RHIC [114] and the LHC [115, 116, 117]. This fact, combined with the observed suppression in both $p-$A and d-A collisions suggests that cold-nuclear-matter effects must play a part in the observed suppression. Another possible effect being considered is the *J/ψ enhancement* due to in-medium charm-quark recombination [116, 117, 118]. In all, the J/ψ suppression signal has not experimentally provided unambiguous evidence for QGP formation thus far.

---

[1] Here J/ψ is taken as the model example, but the same applies to all quarkonia

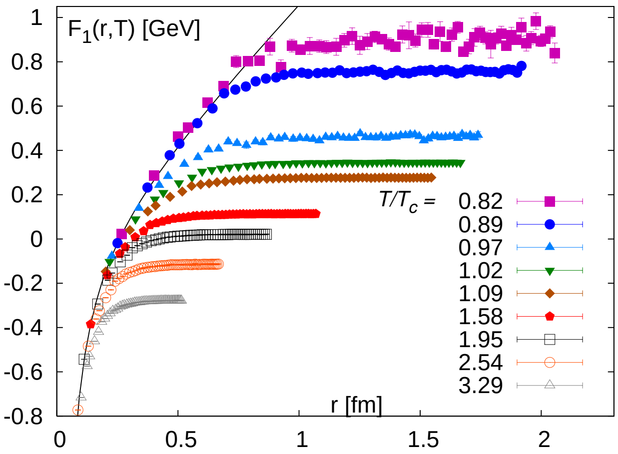

Figure 1.4.1: In-medium free-energy of a $q\bar{q}$ pair at a variety of temperatures around the QGP phase transition (the temperatures are in units of T_c) as calculated in lattice QCD [7]. At low temperatures the free energy approaches that in free space (black line). The plot demonstrates the temperature dependence of the $q\bar{q}$ color potential and hints at J/ψ suppression as a possible signature of the QGP

1.4.2 Strangeness Production and Hadronic Yields

In heavy-ion collisions $q\bar{q}$ pairs can be created by hard collisions. The cross-section for such processes exhibits an inverse relationship to the quark mass; heavy-quarks are energetically suppressed due to their large masses. In fact, even $s\bar{s}$ pair yields are only a fraction of $u\bar{u}$ or $d\bar{d}$ yields ($\sim 10-20\%$ according to references [75, 119]). Moreover, in hot hadronic matter strangeness production is only moderately enhanced since the cross-section for strange particle production from non-strange particles is very small [75]. On the other hand, in the QGP $q\bar{q}$ pairs are copiously produced via gluon fusion ($gg \rightarrow q\bar{q}$) [120, 121], a process which is far more probable in the gluon rich environment of the QGP than in a hot hadronic gas [122, 123]. Thus, one characteristic of QGP formation is the relative enhancement of strange particle production.

At both RHIC and SPS, the statistical hadronization model has been successful in describing hadron yield ratios including those of strange particles [8, 124, 125, 126]. Assuming chemical equilibrium, the particle number density, n_i, is given by [75, 126]:

$$n_i = d_i \int \frac{d^3p}{(2\pi)^3} \frac{1}{\exp\left[\left(E_i - \mu\right)/T\right] \pm 1} \tag{1.7}$$

where d_i is the spin degeneracy, p is the momentum, E_i is the total energy, μ_B is the baryon chemical potential and T is the temperature. Since strange quarks are primarily produced in the medium, it is possible that strangeness chemical equilibrium occurs subsequent to general chemical freeze-out, a fact which is incorporated with the inclusion of a strangeness saturation factor, γ_s, which reaches 1

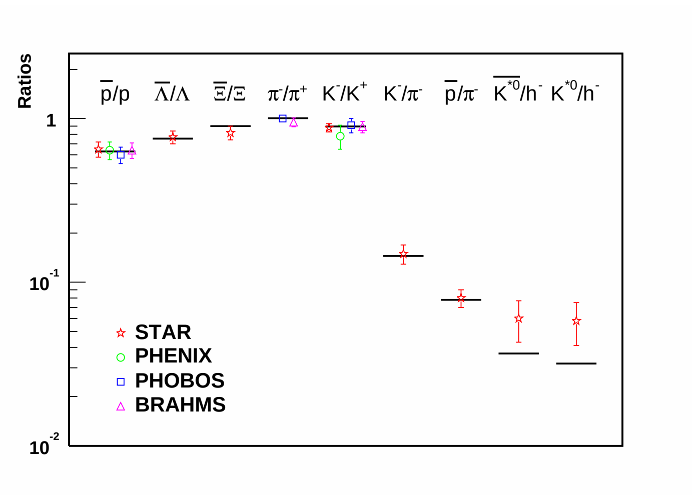

Figure 1.4.2: Hadronic yield ratios measured in $\sqrt{s} = 200$ GeV Au-Au collisions at RHIC compared to theoretical predictions assuming chemical equilibrium[8]

for chemical equilibrium [125] (results at RHIC indicate that at RHIC energies chemical equilibrium is reached for strange particles and $\gamma_s \sim 1$ [12]). The temperature, T, the baryon chemical potential, μ_B, and the saturation factor, γ_s, are free parameters used to fit to the data. Figure 1.4.2 shows some of the measured hadronic yields at RHIC compared to statistical predictions (black line), which indicate that the temperature at chemical equilibrium is of the order of 160 MeV. The results are consistent with expectations of the statistical hadronization model, and thus confirm results obtained at SPS. In addition, in line with expectations of QGP formation, the yields of multi-strange baryon production are enhanced at RHIC energies as compared to SPS energies [12, 126].

1.4.3 Anisotropic Flow

If a thermalized QGP is formed in a relativistic heavy-ion collision, then it is expected that the behavior (at least in the initial stages) can be modeled using relativistic hydrodynamics. The collective hydrodynamic behavior is known as *flow*, evidence for which is expected to be an observable signature of the quark-gluon plasma [9, 75]. In particular, for non-central collisions the so-called *anisotropic* or *elliptic flow* is of great interest. In peripheral collisions, the geometry is such that the overlap region is ellipsoidal (see Figure 1.4.3) with a resulting pressure gradient that is highly anisotropic. This initial state anisotropy should be reflected in an azimuthal anisotropy of the momenta of produced particles as pressure gradients boost the momenta of particles within those gradients [9, 127].

Experimentally, this elliptic flow is often characterized by harmonic coefficients, v_n. The impact parameter vector, $\vec{b}$, and the beam axis (see Figure 1.4.3) define the *reaction plane*, which

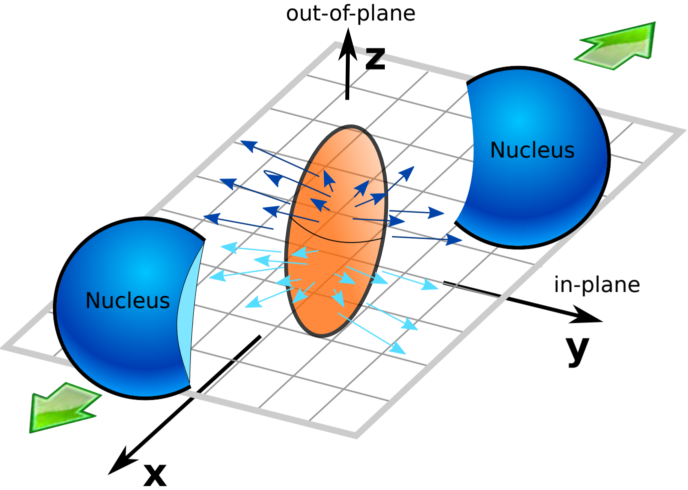

Figure 1.4.3: Illustration of a non-central nucleus-nucleus collision highlighting the asymmetry in the overlap region

is experimentally estimated on an event-by-event basis from the particle azimuthal distribution [127, 128, 129]. The particle azimuthal distribution with respect to the reaction plane can be expanded in a Fourier series [127]:

$$E\frac{d^3N}{d^3p} = \frac{1}{2\pi p_T}\frac{d^2N}{dp_T dy}\left(1 + 2\sum_{n=1}^{\infty} v_n \cos\left[n(\phi - \Psi_{RP})\right]\right) \tag{1.8}$$

where Ψ_{RP} is the azimuth of the reaction plane, ϕ is the particle azimuthal angle distribution, y is the rapidity, p_T is the transverse momentum, and the harmonic coefficients, v_n, are used to quantify the anisotropy of the distribution. v_1 is known as the *directed flow* and v_2 is referred to as the *elliptic flow*. The magnitude of v_2 (more generally v_n, though v_2 is the largest coefficient and thus the first to be studied) depends on the shear viscosity of the fluid, and thus can provide evidence for collective hydrodynamic behavior of the QGP. Figure 1.4.4 shows the integrated elliptic flow as measured by a number of experiments at different collision energies. The magnitude of v_2 increases by $\sim 30\%$ from RHIC to the LHC, as was predicted by hydrodynamic models that provided successful descriptions of flow at RHIC [9, 130].

One of the most striking initial results to emerge from RHIC was the observation that the QGP behaves like an almost perfect liquid [106]. Although perfect hydrodynamics provides quantitative agreement in some collision systems and some momentum ranges (see the left-hand side of Figure 1.4.5), it is now understood that complete quantitative agreement requires the incorporation of the effects of finite viscosity [9], as well as a more realistic approach to the evolution of the dissipative hadronic phase [9, 109]. Figure 1.4.5 shows measurements of v_2 by ALICE and STAR with

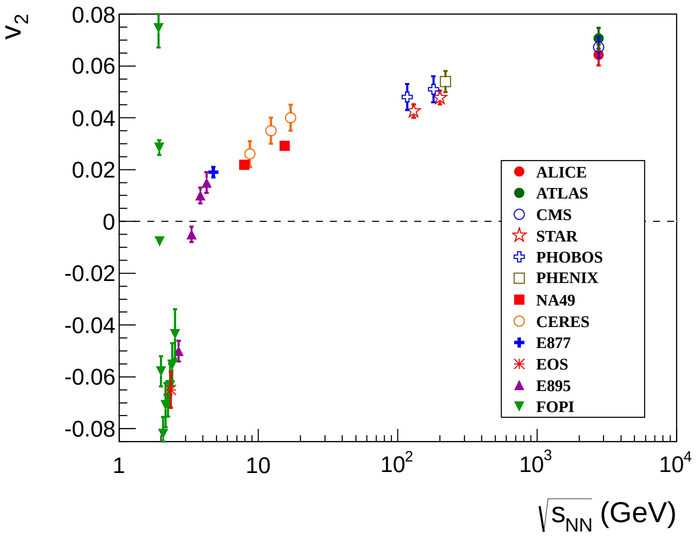

Figure 1.4.4: Elliptic flow (v_2) as measured by a number of experiments including STAR at RHIC and ALICE at the LHC [9]

comparisons to various hydrodynamic models incorporating shear viscosity (models with zero viscosity predict higher v_2 than observed at intermediate and high p_T). The importance of initial state fluctuations to measurements of elliptic flow has also become apparent in recent years [9].

1.4.4 Hanbury-Brown-Twiss Interferometry

The effects of interference arising from the wave-like nature of light are well known from elementary optics. For instance, the interference pattern observed in Young's double slit experiment can be explained in terms of the interference of the amplitudes of waves scattered from the two slits [131]. With the advent of quantum mechanics the phenomena of interference became much more widely applicable as quantum mechanical amplitudes exhibit similar interference behavior [132]. Intensity interferometry first appeared in the context of astronomy, where Hanbury Brown and Twiss used it to estimate the angular diameter of stellar objects [133, 134]. Goldhaber independently applied intensity interferometry to two-pion correlations in the context of hadronic physics to estimate the size of the annihilation fireball in pp and $p\bar{p}$ collisions. The intensity interferometry results from an indefiniteness in the path between the source and detection (see Figure 1.4.6) combined with the effects of Bose-Einstein statistics. If two identical bosons are emitted simultaneously from position a and position b in an extended source, there are two possible paths the particles can take to reach detection at points A and B. If the particles are described by plane waves then the amplitude for

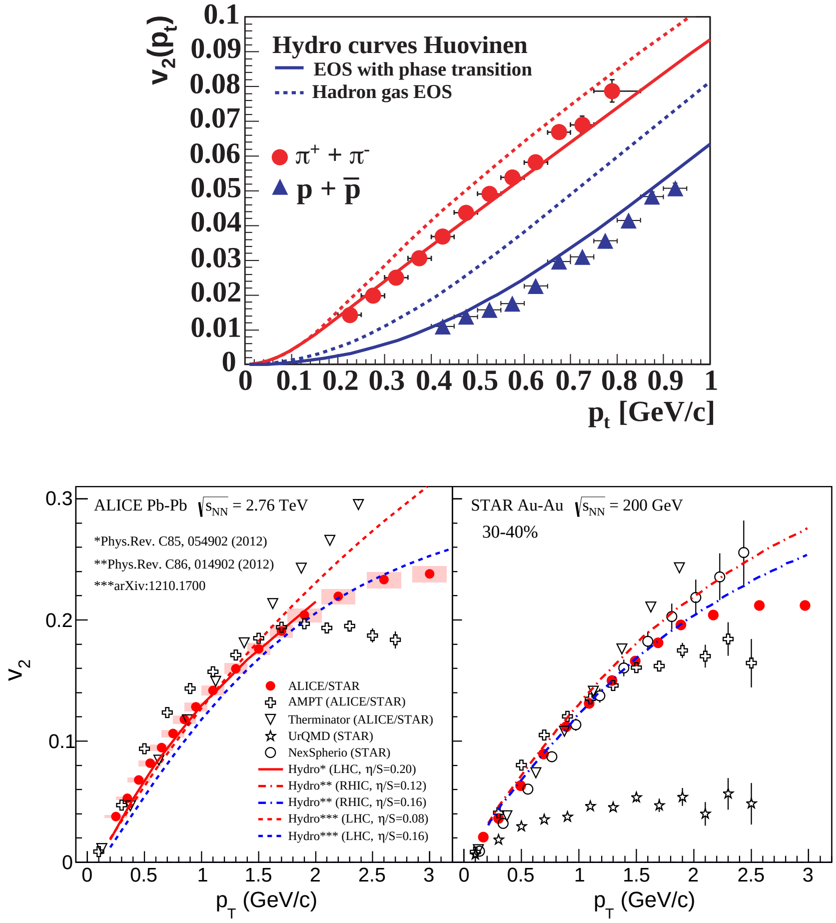

Figure 1.4.5: Top: Comparison of measurements of v_2 at RHIC [10] to perfect hydrodynamical calculations with and without QGP formation. At low p_T the results suggest the formation of the QGP with near zero shear viscosity. At higher p_T the agreement is not as convincing, and effects of viscosity have to be included. Bottom: Comparison of measurements of v_2 at ALICE and STAR with hydrodynamical calculations that incorporate finite shear viscosity and a phase transition to non-hydrodynamical behavior for the hadronic gas phase [11]

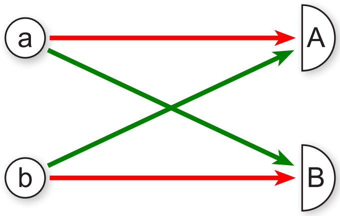

Figure 1.4.6: Illustration of the source of interference in HBT interferometry. Particles emitted from sources a and b can proceed to detectors A and B along either of the paths drawn which results in an interference in the resultant amplitude

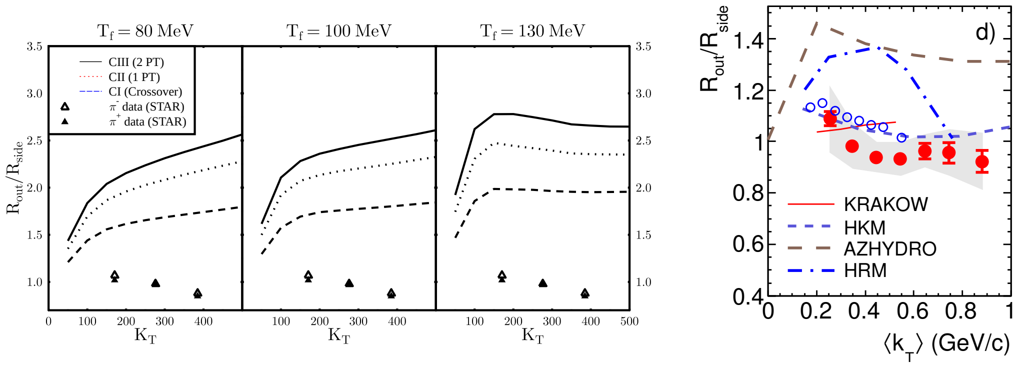

Figure 1.4.7: Left: Comparison of measurements of the ratio R_{out}/R_{side} made at STAR to hydrodynamic models assuming zero viscosity [12]. Right: R_{out}/R_{side} as measured by ALICE (red points) and STAR (blue circles) compared to various hydrodynamic models [13]

detecting a two-particle state at A and B is given by [86]:

$$A(\vec{k_A}, \vec{k_B}) = \frac{1}{\sqrt{2}} \left[e^{i\vec{k_A}(\vec{r_A}-\vec{r_a})} e^{i\vec{k_B}(\vec{r_B}-\vec{r_b})} + e^{i\vec{k_A}(\vec{r_A}-\vec{r_b})} e^{i\vec{k_B}(\vec{r_B}-\vec{r_a})} \right] \tag{1.9}$$

The summation in the expression, which arises from indistinguishably and Bose-Einstein statistics, makes explicit the ambiguity in the path taken in each particle. The interference arises from cross-terms which are generated when the square of this expression is taken in calculations of probabilities.

In practice, HBT correlations are probed with the two-particle correlation function, $C(\mathbf{p}_1, \mathbf{p}_2)$:

$$C(\mathbf{p}_1, \mathbf{p}_2) = \frac{E_1 E_2 dN/(d^3p_1 d^3p_2)}{(E_1 dN/d^3p_1)(E_2 dN/d^3p_2)} \tag{1.10}$$

The distribution of the two-particle correlation is maximal at $\Delta\mathbf{p} = \mathbf{p}_1 - \mathbf{p}_2 \sim 0$ due to Bose-Einstein statistics, with the width providing a quantitative measure of the source dimensions [75, 133]. By measuring the two-particle correlation in 3 independent directions, information about the geometry of the source can be deduced. In particular, the ratio of the dimension along the direction defined by the emitted particles, R_{out}, to the dimension perpendicular to the plane defined by the direction of the emitted particles and the beam axis, R_{side}, is a sensitive probe of the duration of QGP formation and a large value of R_{out}/R_{side} would be indicative of QGP formation [12, 135]. In the context of heavy-ion collisions then, Hanbury-Brown-Twiss (HBT) interferometry provides a signature for QGP formation and enables estimation of the size of the system. Early results from AGS and SPS using HBT interferometry provided insight into various aspects of collision dynamics and evolution. Measurements of the system size scaled as one would expect with increasing center of mass energy and with differing system composition, thus providing unambiguous evidence that HBT

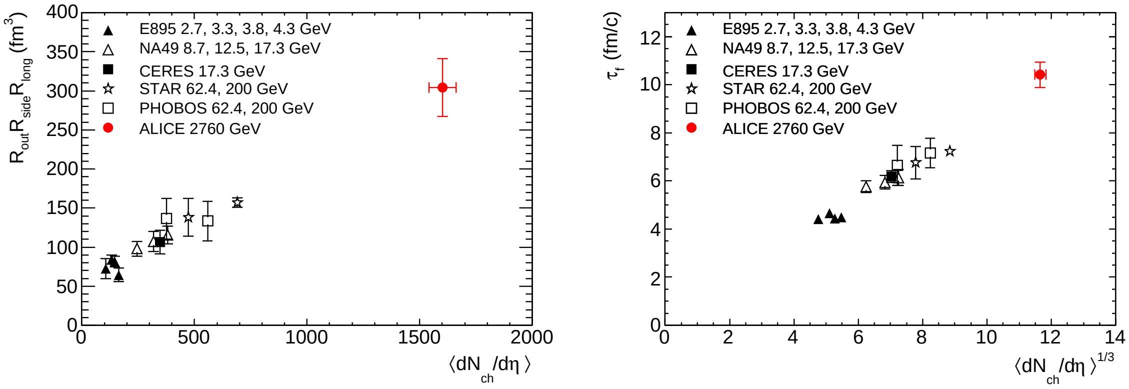

Figure 1.4.8: Measurements of system size as parameterized by $R_{out}R_{side}R_{long}$ (left) and system decoupling time (right) as a function of particle multiplicity (a proxy for energy density) [13]

interferometry does indeed provide ability to probe the system size [133]. Differences between the source radii for Kaon and pion correlations hinted at differing freeze-out times for each species, and thus proffered aspects of the space-time evolution [75, 136]. At SPS, the $\langle k_T \rangle$ ($\langle k_T \rangle = |\mathbf{p}_1 + \mathbf{p}_2|/2$) dependence of the source dimensions was used as evidence for collective expansion, though the R_{out}/R_{side} ratio was not indicative of hydrodynamic behavior [75, 135]. Despite the apparent success of ideal hydrodynamic models in describing elliptic flow when data first emerged from RHIC, ideal hydrodynamic models clearly over predicted R_{out}/R_{side} measured at STAR [12] (see the left hand-side of Figure 1.4.7), though consistency was later obtained by incorporating finite viscosity and pre-thermalized collective flow [137]. Combining HBT measurements from the LHC, RHIC and earlier experiments demonstrates the expected scaling of system size and lifetime with energy (see Figure 1.4.8).

1.4.5 Jet Tomography

From the early days of QCD it was realized that experimental tests of the theory may involve complications not present in QED. Since the QCD coupling constant becomes large at low energies, non-perturbative phenomena are likely to always play a role even in high-energy experiments. Fortunately, various factorization theorems enable the separation of the calculable perturbative components from the non-perturbative components which are parameterized with parton distribution functions and factorization functions. At the level of perturbative QCD, the cross-section of a simple hard process such as that of Figure 1.4.9 can be easily calculated. However, even in this perturbative regime the observed final state particles bear little resemblance to the Feynman diagram; confinement dictates that any quarks and gluons will hadronize into colorless baryons and mesons

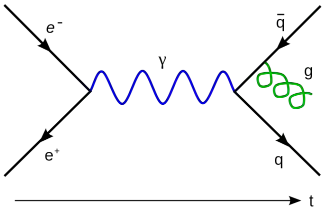

Figure 1.4.9: Feynman diagram of a simple process calculable in perturbative QCD at high energy

in the final state. Thus in a process such as this, which in fact provided one of the early success of QCD [55], what is observed in the final state are *jets*, collections of hadrons with small angular separation the average direction of which presumably corresponds to that of the initial state scattering parton. Experimentally, identification of jets can be a challenge, especially in the high-multiplicity environment of heavy-ion collisions. There is no one best method of jet identification and a variety of jet-finding algorithms have been developed over the years [138]. Some of the most prominent are the 'cone' algorithms like SIScone[139], and 'sequential recombination' algorithms like the k_T [140] and anti-k_T algorithms [141].

The significance of jets in the context of heavy-ion collisions stems from the potential in-medium modification of their properties, and thus their ability to serve as a diagnostic tool to probe the QGP. In free space, fast partons produced in a hard collision lose energy primarily via non-perturbative effects which can be phenomenologically described with color flux tube models [75]. However, in the presence of the QGP fast partons can interact with the medium and collisional and radiative energy losses can also contribute (see Figure 1.4.10); in fact, radiative energy loss is expected to be the dominant energy loss mechanism. As far back as 1982 [142] it was suggested that a signature of the QGP could be *jet quenching*: if the radiative and collisional energy losses are sufficiently large then

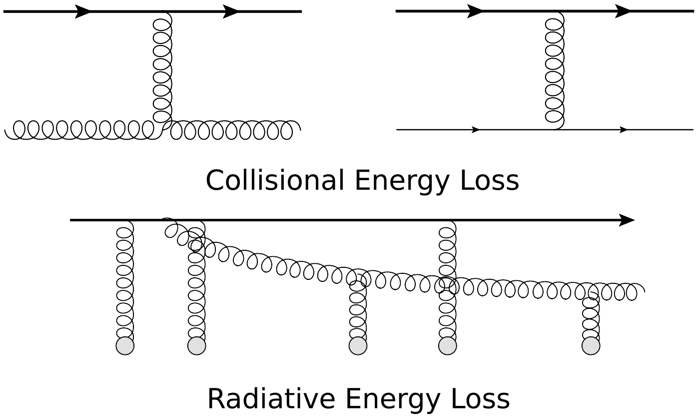

Figure 1.4.10: Feynman diagrams illustrating mechanisms of partonic energy loss in the QGP. Radiative energy losses are expected to dominate [14]

the observable characteristics of a jet may be eliminated (a uniform distribution of soft hadrons as opposed to a hard collimated jet of particles). Moreover, the degree of jet quenching would exhibit a strong path dependence (see Figure 1.4.11) which would manifest itself in an azimuthal dependence of the jet energy loss in peripheral collisions (where the system's geometry is asymmetric). Thus, *jet tomography* can aid in revealing the spatial and temporal structure of the QGP.

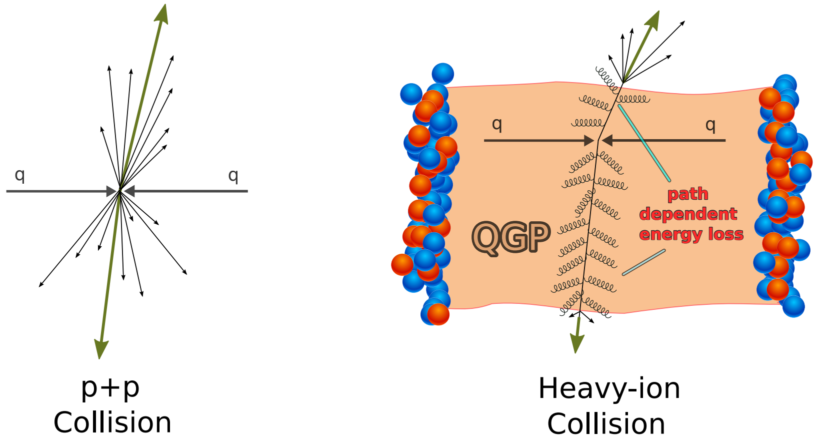

Figure 1.4.11: Schematic comparison of *pp* collisions with no in-medium energy loss, and heavy-ion collisions with path-dependent energy loss

Although jet quenching was not observed at AGS or SPS, observations of jet quenching was one of the major successes of the experimental programs at RHIC. One way jet quenching was explored experimentally was by studying two-particle azimuthal correlations. The particle in the final state with the greatest p_T typically aligns closely with the direction of one of the outgoing partons. In the original hard scattering, momentum conservation implies that the two hard scattering partons should lie approximately 'back-to-back' with an azimuthal angular separation of $\Delta\phi \sim 180°$ (see Figure 1.4.11). One therefore expects to observe jets with a similar angular separation ($\sim 180°$), and thus a characteristic double-peak structure in the two-particle azimuthal angular correlation distribution is expected. Indeed, this is exactly what is observed in *pp* collisions (see Figure 1.4.12). However, consistent with expectations of jet quenching, in Au+Au collisions the 'away-side' peak in the two-particle azimuthal angular correlation distribution is completely absent. Similar jet modification has been observed at the LHC (see Figure 1.4.12).

1.4.6 High p_T suppression of hadrons, R_{AA}

Particles with high p_T ($\gtrsim 2 - 3$ GeV/c) are thought to arise from initial state hard-scattering processes, as opposed to low p_T particles for which thermal production can be dominant. At these energy scales, the typical distances probed ($\Delta\mathbf{r} \sim 1/p_T \lesssim 0.1$ fm) are significantly smaller than

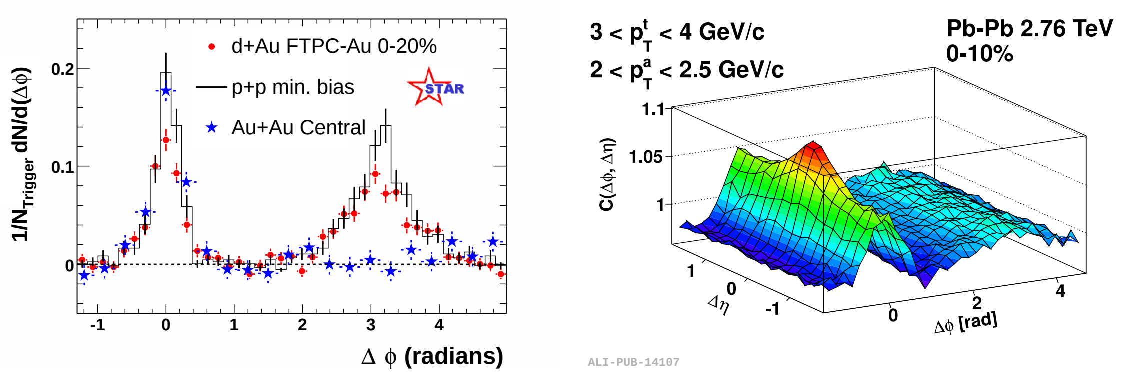

Figure 1.4.12: Left: Di-hadron correlations as measured in STAR in central d-Au, *pp* and Au+Au collisions [12]. The striking suppression of the away-side jet in Au+Au provided strong evidence for in-medium jet modification. Right: Early 2D di-hadron correlation results from ALICE, where jet away-side jet modification is also apparent [15]

nucleonic dimensions and thus the interactions can be considered as 'point-like'. In this regime then, consistent with expectations of the Glauber model, one would anticipate that the yield of high p_T particles would scale with the number of elementary binary collisions, $\langle N_{binary}\rangle$. This expectation is manifest in the *Cronin effect*: high p_T hadron production is enhanced in pA collisions as compared to *pp* collisions due to multiple elastic collisions in the initial state [75, 143, 144]. However, in the presence of the QGP the same energy loss mechanisms responsible for the in-medium modification of jet structure can also result in suppression of high p_T hadron production [86, 145]. Given the expected scaling property of collisions with no QGP formation, a measure of this suppression is provided by the *nuclear modification factor*, R_{AA}:

$$R_{AA} = \frac{1}{\langle N_{binary}\rangle}\frac{d^2N^{AA}/dp_Td\eta}{d^2N^{pp}/dp_Td\eta} \tag{1.11}$$

where $d^2N^{AA}/dp_Td\eta$ is the yield in nucleus-nucleus collisions and $d^2N^{pp}/dp_Td\eta$ is the yield in *pp* collisions. The subscript/superscript AA here is used to mean 'nucleus-nucleus' collisions but other notations can be used for specific collision systems (for instance R_{CuCu}, R_{dAu} or R_{AuAu}). In particular, an important quantity often used as an alternative to the comparison to a *pp* baseline is R_{CP}, the ratio of yields in central and peripheral collisions for a given centrality class:

$$R_{CP} = \frac{\langle N_{binary}^{peripheral}\rangle}{\langle N_{binary}^{central}\rangle}\frac{d^2N^{Central}/dp_Td\eta}{d^2N^{Peripheral}/dp_Td\eta} \tag{1.12}$$

where $\langle N_{binary}^{central}\rangle$ is the number of binary scatterings in central collisions in the given centrality class, $\langle N_{binary}^{peripheral}\rangle$ is the number of binary scatterings in peripheral collisions in the given centrality class,

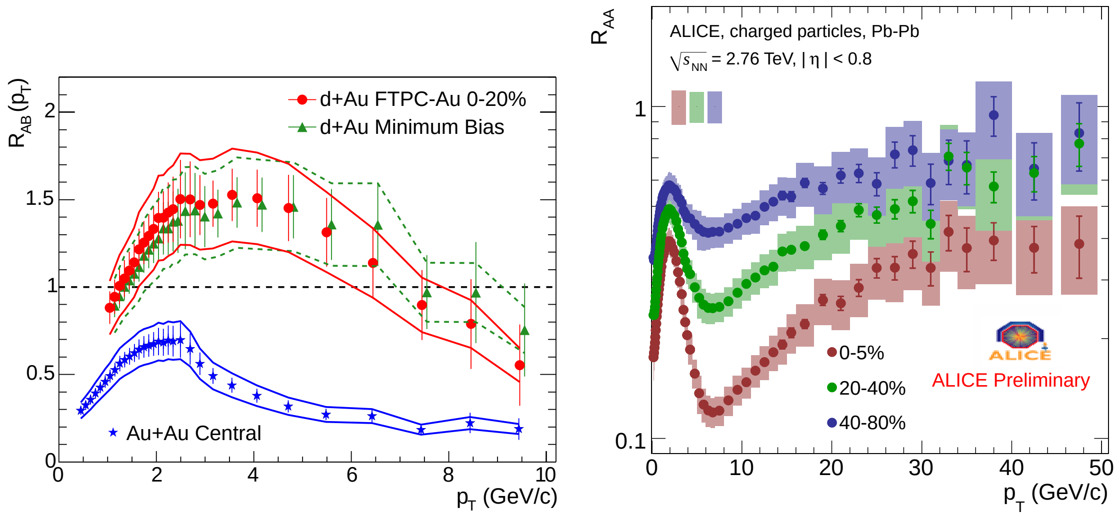

Figure 1.4.13: Left: R_{AuAu} of charged hadron yields in central Au-Au collisions at $\sqrt{s} = 200$ GeV and R_{dAu} in central and peripheral d-Au collisions at $\sqrt{s} = 200$ GeV as measured by STAR [16]. The high p_T hadronic suppression is apparent in Au+Au collisions. Right: R_{AA} of charged hadron yields in $\sqrt{s} = 2.76$ TeV Pb-Pb collisions for three different centralities as measured by ALICE [17]. High p_T hadron suppression is evident at all centralities, though greatest for most central collisions (0-5%)

$d^2N^{Peripheral}/dp_Td\eta$ is the yield in peripheral collisions and $d^2N^{Central}/dp_Td\eta$ is the yield in central collisions in the given centrality class.

Given the naive binary scaling expected of the high p_T yield, a value of $R_{AA} = 1$ would be anticipated at high p_T if no QGP was present. However, since at low p_T soft production processes dominate, one would actually expect the yield to scale with the number of participants in this region and R_{AA} not to be an appropriate variable to measure suppression. Hence, the characteristic signal of QGP formation is the *suppression* of hadronic yields at high p_T, with $R_{AA} \lesssim 1$. Since photons do not interact with the QGP, photons should not suffer in medium energy loss and thus the nuclear modification factor of direct photons is often used as a non-interacting baseline when considering R_{AA} measurements. Although such suppression was not a feature of the data at AGS and SPS, it was unambiguously observed both at RHIC and the LHC (see Figure 1.4.13).

1.5 Heavy-Flavor and the QGP

The subject of heavy-flavor is a broad field, with potential implications far beyond fundamental tests of the standard model [146]. The large masses ($m_c = (1.27^{+0.07}_{-0.09})\mathrm{GeV}/c^2$ and $m_b = (4.19^{+0.18}_{-0.06})\mathrm{GeV}/c^2$ [48]) of heavy quarks (heavy-flavor quarks are defined as b and c quarks, with t possessing it's own phenomenology [146, 147]) indicate that even simple processes involving these quarks necessarily probe a large physical domain; QCD, QED, weak interactions, Higgs interactions, and even potentially physics beyond the standard model can all be relevant [146, 148]. Precision measurements in this realm may be sensitive to supersymmetric particles in loop diagrams [146, 148, 149], and heavy-flavor measurements can shed light on quark mixing [149, 150], CP violation via the CKM matrix [149, 150], and thus aid in understanding the observed matter-antimatter asymmetry in the universe [146, 148, 151]. In the context of relativistic heavy-ion physics, measurements involving heavy-quarks are relevant in a variety of contexts. Suppression of J/ψ production (a $c\bar{c}$ bound state) was one of the early suggested signatures of the QGP. In pp collisions, the large quark masses provide a large energy scale that enables perturbative QCD (pQCD) to be applied even at low momenta [14]. Thus measurements of heavy-flavor production in pp collisions can provide stringent tests of pQCD calculations [152]. Since their masses greatly exceed the temperature scale of the QGP [14, 153], even in heavy-ion collisions they are expected to be produced primarily in the initial hard scatterings with negligible thermal production [14]. Combined with the fact that the thermalization time of heavy-quarks is expected to be of the same order as the lifetime of the QGP [154, 155], heavy-quarks can provide probes of the QGP for the entire evolution. In-medium energy loss of quarks is also expected to exhibit a strong mass dependence [14, 156], which makes the measurement of the energy loss of heavy-flavors in particular of great theoretical interest. Here a review of some aspects of heavy-flavor phenomenology relevant to relativistic heavy-ion physics is presented, in addition to some highlights of experimental heavy-flavor results from RHIC and the LHC.

1.5.1 Heavy-Quark Production in *pp* collisions

One of the most interesting tests of QCD dynamics at RHIC and the LHC are measurements of charm and bottom production. Their large masses enable the use of perturbative calculations down to low momenta, and indicate that their production are dominated by the initial hard scatterings even in the presence of the QGP [14]. Moreover, although measurements of bottom quark production at SPS agreed with next-to-leading (NLO) order QCD calculations [157, 158, 159], some of the first measurements of bottom production at the Tevatron seemed to indicate rates of bottom production $\sim 2-3$ times greater than those predicted by NLO QCD calculations [157, 160, 161, 162]. Since that time, improvements in theoretical calculations, in particular the so called "fixed order + next-to-leading log" (FONLL) framework, demonstrated that heavy-flavor measurements at the Tevatron and RHIC can well be described by QCD [14, 152]. Despite these successes, comparison of predictions of QCD to measurements in the new energy regime at the LHC, where new calculational techniques may need to be exploited [152], are of particular interest.

Modulo photoproduction, the approach of perturbative QCD to heavy-quark production proceeds via factorization that can be divided into three elements [14]:

- The non-perturbative initial conditions typically parameterized by the parton distribution functions.
- The partonic hard-scattering cross-section, which is calculable in pQCD.
- Non-perturbative hadronization as described by the fragmentation functions. From the standpoint of this thesis, what is relevant is the hadronization to *open heavy flavor* hadrons (hadrons with one c or b quark), though the $1-2\%$ of cases where charmonium and bottonium are produced are also of relevance in heavy-ion physics.

The ability to partition the calculation in this way relies on the factorization theorems of QCD, proven somewhat rigorously in free-space and less than rigorously (but typically assumed to hold true) in presence of the QGP [163]. Various approaches have been taken to heavy-quark production in pQCD, though they can be divided into two main classes: ‘pure’ perturbative approaches such as FONLL and GM-VFNS, and approaches that incorporate MC generators like POWHEG [164], PYTHIA [165], HERWIG [166] and MC@NLO [167]. The former utilize strictly perturbative calculations and enable the prediction of *exclusive* observables that do not necessarily incorporate all aspects of the final state, while the latter match NLO perturbative calculations with parton shower Monte Carlos (PSMCs) [168] and can predict inclusive as well as exclusive variables. The latter are of great importance throughout high energy physics, and in fact PYTHIA is heavily utilized in this thesis. However, an exclusive measurement is presented for this thesis and a comparison is only made to approaches of the former type. The various purely perturbative approaches differ primarily in the details of how the hard-scattering cross-section is calculated [169]. Three prominent approaches to this calculation that are compared to the measurement undertaken for this thesis are FONLL, GM-VFNS and ‘k_T-factorization’.

The “fixed-order + next-to-leading log” (FONLL) framework utilizes next-to-leading order (NLO) QCD calculations with resummation of large logs to next-to-leading log (NLL) accuracy in the limit $\frac{p_T}{m} \gg 1$ [170, 171, 172]. The ZM-VFNS (zero-mass variable flavor number scheme) calculation is similar in nature to the FONLL calculation but deals with the collinear singularities by instead absorbing them into the fragmentation functions (FF’s) for the produced hadrons, and the parton distribution functions (PDFs) for the incoming hadrons. The description ‘variable flavor number scheme' serves to contrast the calculation with FFNS (fixed-flavor number scheme) calculations where the number of flavors in the initial state is fixed to 3(4) for charm (bottom) production. In ZM-VFNS, the number of active quark flavors changes as a function of momentum and thus enables predictions where $p_T \sim m$. GM-VFNS (general-mass variable-flavor scheme) calculations extend ZM-VFNS calculations by allowing the heavy quark mass to be non-zero, whereas in ZM-VFNS the heavy-quark is assumed to be massless. GM-VFNS thus incorporates virtues of both the FFNS approach and the ZM-VFNS approach [173, 174, 175, 176, 177]. Both GM-VFNS and FONLL in some way employ the DGLAP (Dokshitzer-Gribov-Lipatov-Altarelli-Parisi) evolution equations to perform the resummation of leading logarithms. The k_T-factorization calculations differ from GM-VFNS calculations in that they employ an alternative approach for the PDF evolution, namely the BFKL (Balitsky-Fadin-Kuraev-Lipatov) equations. In theory, the DGLAP evolution equations are more appropriate at lower energies, while the BFKL equations are more suitable at high energies. [178, 179, 180, 181, 182, 183].

The measurement of heavy-flavor cross-sections for comparison to any of these theoretical approaches is a difficult task. First and foremost, quarks are not directly observable and they are thus indirectly detected via their hadronization products. Moreover, these hadronization products (such as J/ψ, Υ and D mesons) have very short lifetimes ($\sim 10^{-12}s$)[48], and correspondingly very short mean path lengths; even for the b-hadrons that have the longest lifetimes, the mean path length is expected to be $\sim 500\mu$m [184]. The longer lifetime of the b-hadrons is large enough that secondary vertex identification is feasible at current and past experiments [185, 186], but short enough that the measurement of these hadrons inevitably proceeds via identification of their decay products. Without being fully inclusive, the experimental approaches to the measurement of heavy-flavor production can be broadly categorized according to Figure 1.5.1; namely the measurement of electrons and muons from the decays of heavy-flavor hadrons, the full reconstruction of D-meson hadronic decays, the full reconstruction of B-meson hadronic decays, the measurement of displaced J/ψ from B decays, and b-tagging techniques.

Historically, the first observation of open heavy flavor hadron production was via the measurement of high p_T electrons at ISR [187], though at the time the origin of these electrons was not understood. Experiments at Sp$\bar{\text{p}}$S provided the first direct confrontation of theory with experiment by measuring the production cross-section of muons from the decays of heavy flavor hadrons. Within significant experimental and theoretical uncertainties, these measurements provided some of the first successes of pQCD in predicting heavy-flavor production cross-sections [188]. However, as has already been alluded to, comparisons of NLO pQCD to results from the Tevatron were not

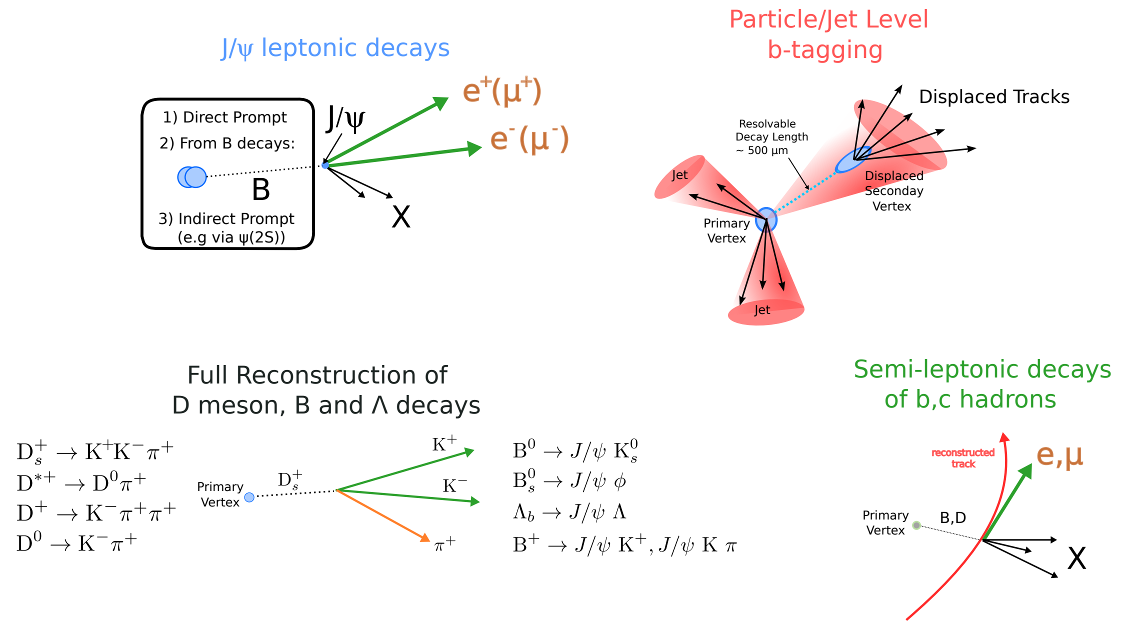

Figure 1.5.1: Schematic of the various approaches to probing heavy-flavor in relativistic heavy-ion physics: (i) Measurement of J/ψ production via decays to electrons and muons (ii) Exploiting the large lifetime of B-hadrons and their unique decay topology for identification via displaced secondary vertices. These 'b-tagging' approaches can be implemented at the particle or the jet level (iii) Reconstruction of charm and bottom mesons via complete identification of their decay products and subsequent calculation of the invariant mass (iv) Identification of electrons or muons as a proxy for the parent B/D mesons. This methodology requires careful subtraction of background electrons from other sources, and by itself only allows for total heavy-flavor cross-section measurements to be performed. It is this procedure that is employed in this thesis

as promising [14]. Measurements of B mesons via semi-leptonic decay channels to electrons and muons, in addition to full reconstruction of B mesons via $B^{\pm} \to J/\psi K^{\pm}$, seemed to suggest that the yield of b-quarks was significantly greater than that predicted by NLO pQCD [157, 158]. However, improvements in theoretical calculations (in particular the FONLL approach hitherto briefly described), and an improved displaced vertex trigger allowed for the demonstration of the agreement of pQCD with heavy-flavor production cross-section measurements (for instance see Figure 1.5.2).

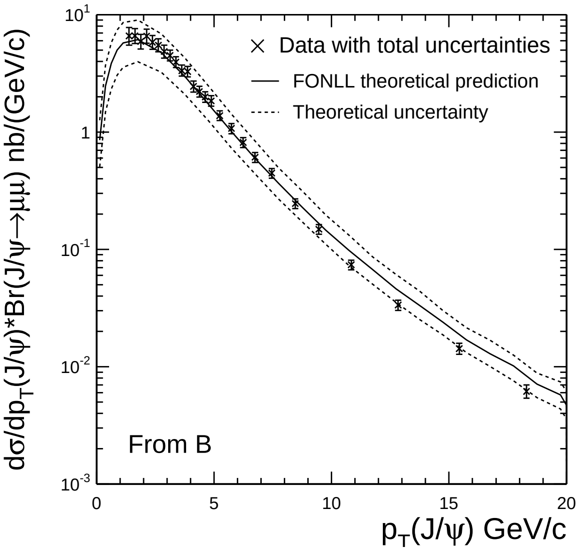

Figure 1.5.2: Differential cross-section of $J/\psi \to \mu^+\mu^-$ as measured by the CDF collaboration in $\sqrt{s} = 1.96$ TeV pp collisions [18]

The exploration of the heavy-flavor sector, in particular in the domain of heavy-ion collisions, was much expanded with the advent of RHIC. STAR performed full reconstruction of the decays $D^0 \to K^-\pi^+$ and $D^{*+} \to D^0\pi^+$ in pp collisions [189], both PHENIX and STAR measured heavy-flavor hadron yields via their decays to electrons and muons [19, 20, 190, 191, 192], and measurements of J/ψ and Υ yields were measured via their decay to electrons [193]. In addition, the disentanglement of the relative contribution of b and c hadrons to the total heavy-flavor yield was determined using electron-hadron correlation measurements [194]. In all of these measurements in pp collisions, FONLL was found to provide a satisfactory description of the data [14]. For instance, the good agreement of the cross-section of electrons from open heavy-flavor decays in pp collisions can be seen in Figure 1.5.3.

At the LHC, the exploration of heavy-flavor production has continued into a new energy regime. The LHCb experiment [195] is in fact designed to probe heavy-flavor physics, in particular the

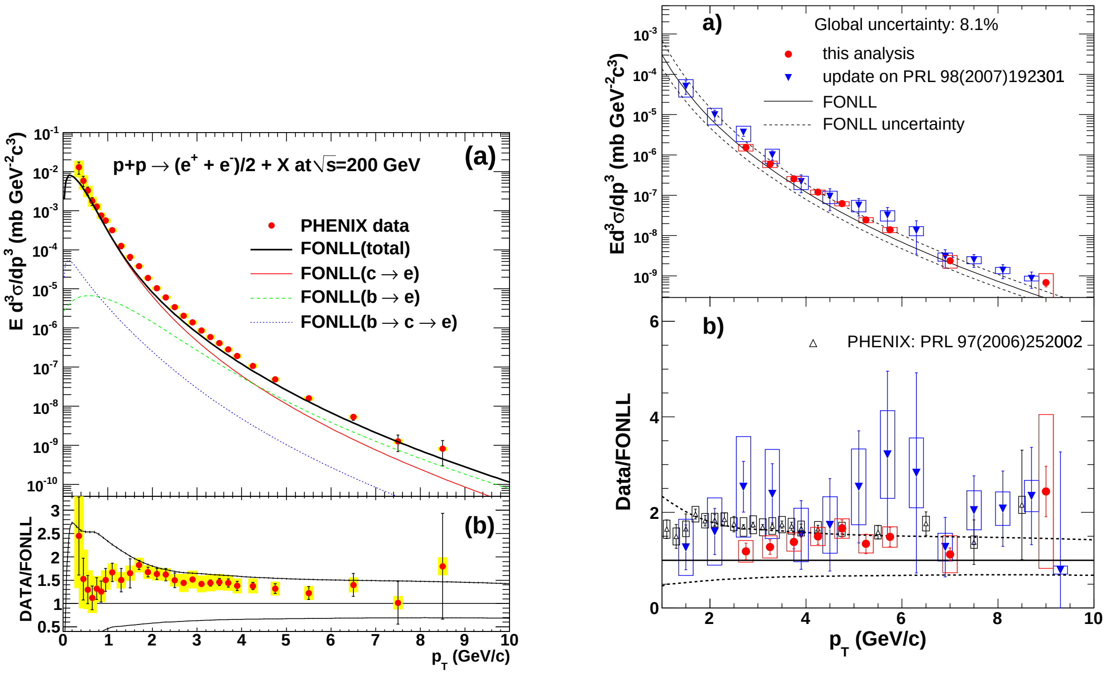

Figure 1.5.3: Left: Invariant yield of electrons from semi-leptonic decays of heavy-flavor hadrons as measured by PHENIX with a comparison to FONLL predictions [19] Right: The invariant yield of electrons from semi-leptonic decays of heavy-flavor hadrons as measured by STAR with a comparison to FONLL predictions [20]. The blue points arise from a previous flawed measurement, that was later improved resulting in the red points (the agreement with FONLL is better with the latter result)

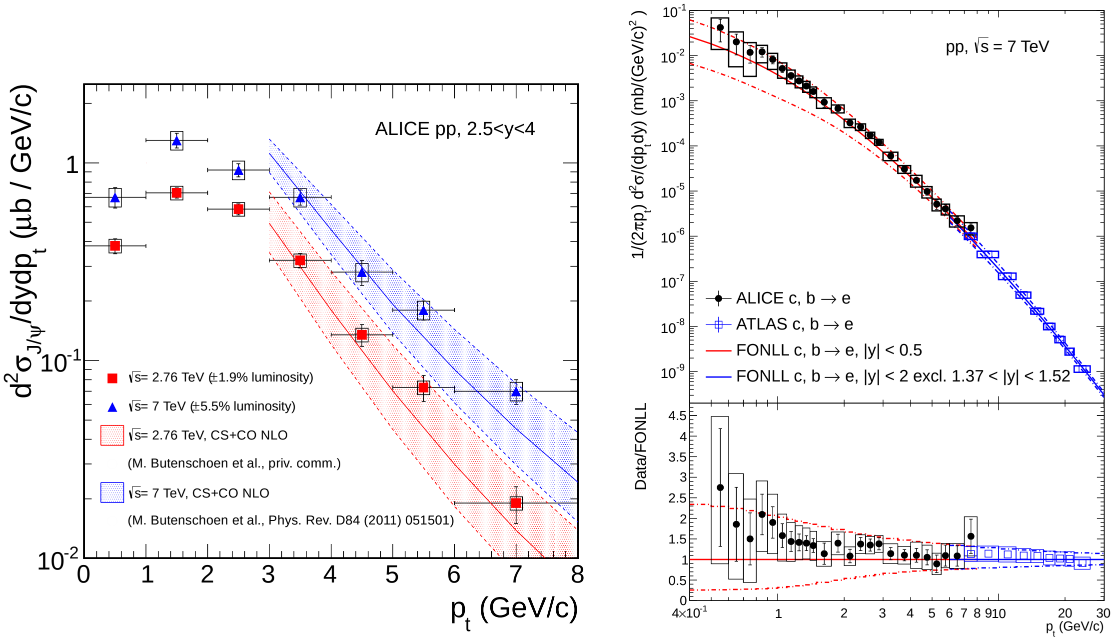

Figure 1.5.4: Left: Differential production cross-section of J/ψ in $\sqrt{s} = 2.76$ TeV and $\sqrt{s} = 7$ TeV *pp* collisions as measured by ALICE [21, 22] Right: Comparison of differential production cross-section of electrons from heavy-flavor decays as measured in ALICE and ATLAS with FONLL predictions [23]

measurement of CP violation in B hadrons which has already provided strong constraints on supersymmetric extensions to the standard model [196]. Heavy-quark production in *pp* has been probed with a variety of measurements at ALICE [35], CMS [197, 198, 199, 200] and ATLAS [198, 199, 201]. J/ψ production cross-sections have been measured in $\sqrt{s} = 2.76$ TeV and $\sqrt{s} = 7$ TeV *pp* collisions at CMS [202, 203], ALICE [21, 22] and ATLAS [204, 205] (see the left side of Figure 1.5.4), where good agreement was found with FONLL predictions. In addition, ATLAS measured the $\Upsilon(1S)$ production cross-section in $\sqrt{s} = 7$ TeV *pp* collisions, finding that the measured yield exceeded FONLL predictions to some degree, though the need for higher order corrections could explain the discrepancy [206]. Full reconstruction of $B^{\pm}$, B^0 and B^0_s mesons was undertaken by CMS in the decay channels $B^{\pm} \to J/\psi K^{\pm}$, $B^0 \to J/\psi K^0_s$ and $B^0_s \to J/\psi \phi$ where the total and differential production cross-sections were found to be consistent with MC@NLO within systematic uncertainties [207]. Similarly, full reconstruction of the decays of D^0, D^+ and D^{*+} have been measured in $\sqrt{s} = 7$ TeV and $\sqrt{s} = 2.76$ TeV by ALICE (see Figure 1.5.5) and were found to be consistent with FONLL and GM-VFNS predictions [24]. At ALICE and ATLAS, the differential production cross-section of electrons from heavy-flavor decays has been measured in $\sqrt{s} = 7$ TeV collisions [23] (see the right side of Figure 1.5.4). ALICE has performed similar measurements in $\sqrt{s} = 2.76$ TeV *pp* collisions utiliz-

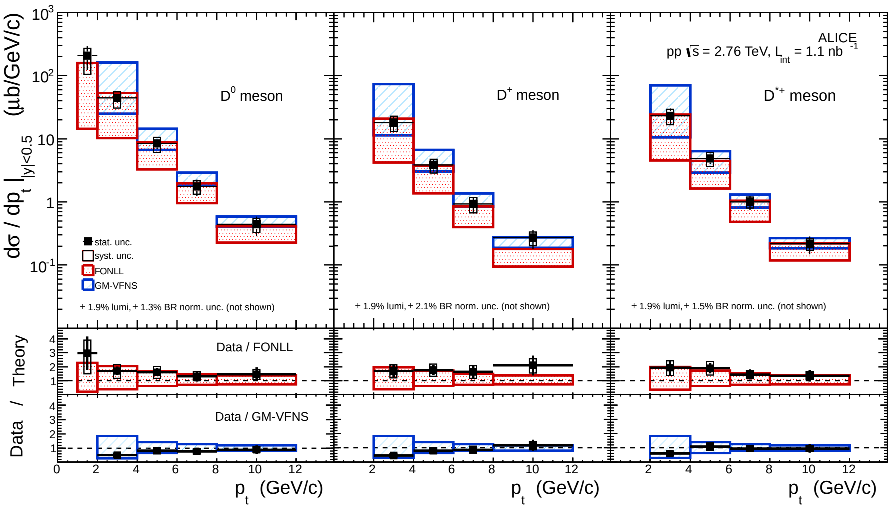

Figure 1.5.5: Differential production cross-section for D mesons in $\sqrt{s}$ = 2.76 TeV *pp* collisions as measured by the ALICE experiment [24]

ing the decays of heavy-flavor hadrons to muons (as opposed to electrons) at forward rapidity with the dedicated muon spectrometer [208, 209]. Both CMS and ALICE, though CMS at the jet-level and ALICE at the particle level, have also utilized b-tagging methodologies to measure production cross-sections of B-hadrons, and production cross-sections of electrons from beauty-hadron decays respectively [185, 186]. In both cases good agreement with FONLL predictions was noted. As a whole, pQCD has been highly successful in predicting the heavy-flavor production cross-sections in a variety of contexts in *pp* collisions at the LHC both at $\sqrt{s}$ = 7 TeV and $\sqrt{s}$ = 2.76 TeV. In fact, though this short review only touches on the large body of heavy-flavor results already accumulated at the LHC (see the references for more comprehensive summaries [198, 199, 200, 210, 211, 212, 213]), a number of other measurements have been successfully described by pQCD at the LHC.

For this thesis, the measurement of the differential production cross-section of electrons from semi-leptonic decays of heavy-flavor hadrons in $\sqrt{s}$ = 2.76 TeV *pp* collisions is presented. In addition to providing an important test for pQCD in a new domain, such a measurement provides a crucial baseline for comparison to $\sqrt{s}$ = 2.76 TeV Pb-Pb collisions. The QGP is only expected to be produced in Pb-Pb collisions, and thus to identify any possible in-medium modifications of heavy-quark energy loss a corresponding reference in *pp* collisions is required.

1.5.2 Heavy-Ion Collisions and Energy-Loss Mechanisms

Some of the highlights of the experiments at RHIC have already been described; the outcome is the unambiguous evidence for the production of a strongly coupled medium known as the quark-gluon-plasma. Some of the expected signals of this novel medium have already been discussed. In the light of results from RHIC, one of the most interesting of these signals is the predicted energy loss of quarks traversing the medium. Observation of jet-quenching at RHIC provided clear evidence of this expected energy loss, but the outcomes of detailed measurements of high p_T suppression were somewhat unexpected.

Due to their large masses, the production of heavy-quarks is expected to be dominated by the initial hard scatterings and thus is calculable within pQCD. As hard remnants of these scatterings traverse the QGP, they undergo energy loss via a number of mechanisms (see Figure 1.4.10). Before the data from RHIC emerged it was thought that induced radiative energy losses would be the dominant mechanism of in-medium energy loss, and it is still thought to be so for light quarks [14]. Moreover, the induced radiative energy loss exhibits a mass dependence due to the *dead cone* effect [214]. Intuitively, the large heavy-quark mass corresponds to velocities significantly smaller than the speed of light (relative to the light quarks) which in turn prevents gluon emission at small angles [163]. The result is a $[1 + (m/E)\theta^{-2}]^{-2}$ suppression factor for radiative energy losses [163, 214], which given the purported dominance of this energy loss mechanism, should result in heavy-quarks exhibiting significantly reduced in-medium energy loss. However, results from RHIC seem to indicate that the energy loss of heavy-quarks is similar to that of lighter quarks, which called into question this picture [14]. Thus measurements of the energy-loss of heavy-flavor quarks are of particular importance to better understand the in-medium energy loss mechanisms.

A number of phenomenological approaches have been developed to predict the energy loss of partons traversing the medium. They can be broadly classified into five main categories: radiative energy loss models, Langevin transport models, collisional energy models, hadronic energy loss models, and AdS/CFT-based energy loss models. In all such schemes the calculation is assumed to be factorizable, with a separation of the perturbatively tractable production cross section, $\frac{d\sigma_{ab\to cX}}{d\hat{t}}$, the initial state nuclear structure functions, $G_b^A(x_a), G_b^B(x_b)$, and a *medium-modified* fragmentation function, $\tilde{D}_c^h(z)$ [25]:

$$\frac{d^2\sigma^h}{dyd^2p_T} = \frac{1}{\pi}\int dx_a \int dx_b G_b^A(x_a) G_b^B(x_b) \frac{d\sigma_{ab\to cX}}{d\hat{t}} \frac{\tilde{D}_c^h(z)}{z} \tag{1.13}$$

In radiative energy loss models, the energy loss is assumed to be dominated by induced gluon emission which is modeled as interactions with scattering centers in the medium. Among these approaches are the BDMPS models [215] where energy loss takes place in a series of soft medium induced gluon emissions at these scattering centers, and the DGLV model [216] where a smaller number of hard scatterings take place. Although these models were successful at describing the high p_T suppression of light flavors (see Figure 1.5.6), in light of the RHIC data it has become clear that collisional

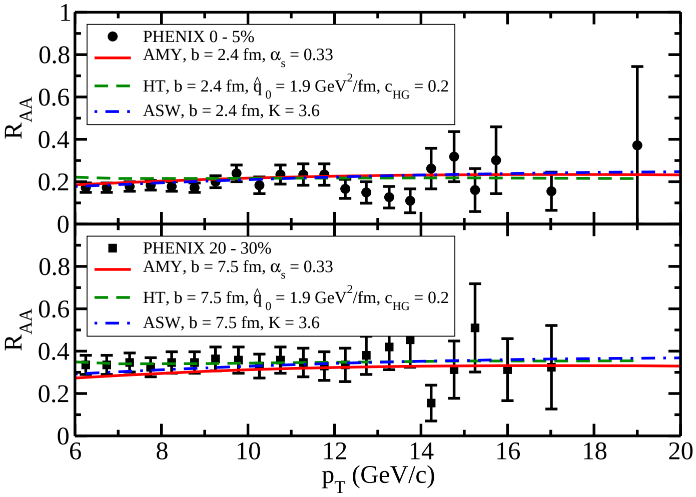

Figure 1.5.6: Comparison of the nuclear modification factor of pions in $\sqrt{s_{NN}}$ = 200 GeV Au-Au collisions as measured by the PHENIX collaboration with the predictions of various energy loss models [25]. Radiative energy loss models have been successful in replicating the experimentally observed energy loss for light flavors

energy loss may be at least as significant as radiative energy loss for heavy quarks, and now these models incorporate collisional energy loss alongside radiative energy losses [14]. Collisional energy loss models describe the process as predominantly due to elastic scatterings in the QGP. In this class is the model of Gossiaux and Aichelin [217] who utilize a running coupling constant and use a novel infrared regulator to describe the interaction with the plasma. The Langevin transport models adopt a thermal approach utilizing finite temperature field theory [218, 218]; a heavy-quark is placed into a hot medium with the quark-medium interaction being described by uncorrelated in-medium collisions the magnitude of which is defined by the diffusion constant (in this sense the Langevin transport models are collisional, but are characterized by the thermal approach). Hadronic energy loss models, like the collisional dissociation model [219], allow for the sequential formation and dissociation of heavy-flavor hadrons and the resulting effective energy loss. Finally, the AdS/CFT-based energy loss models employ a far reaching relationship between conformal field theories and string theories in Anti-de-Sitter space [220]. This enables calculational tools of string theory to be employed in quantum field theories. An interesting outcome of this endeavor is the hypothesized bound on the ratio of the shear viscosity to the volume density of entropy, $\eta/s = 1/4\pi$, for all relativistic thermal field theories [220]. The prescribed classification of the models may serve to elucidate some of the ideas underlying the different models, but in practice any individual model may employ both collisional and radiative energy losses, and may or may not allow for the hadronization

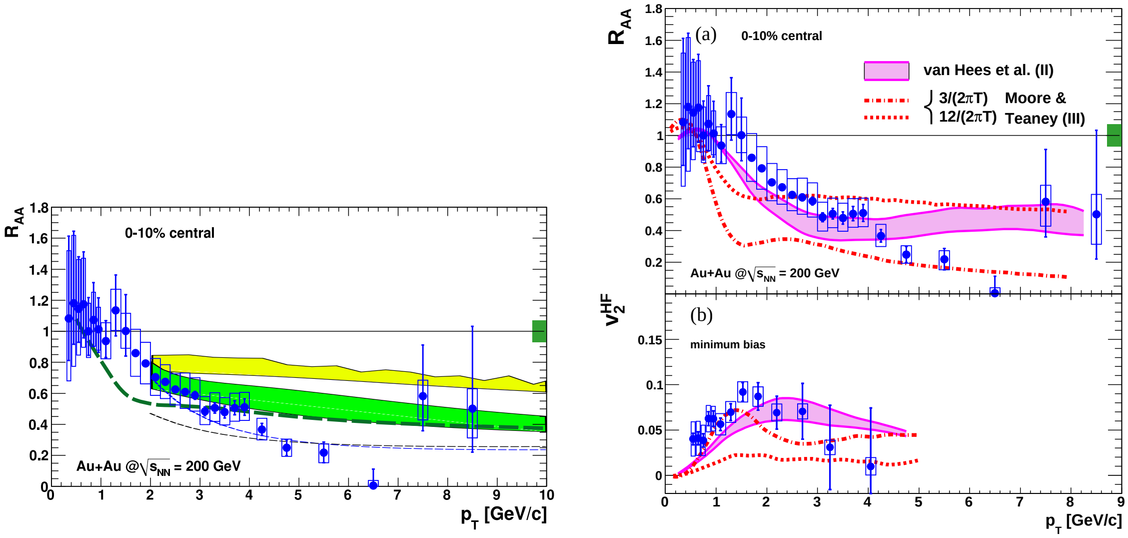

Figure 1.5.7: Comparison of the R_{AA} of electrons from the decays of heavy-flavor hadrons as measured by PHENIX compared to a number of models. On the left the result is compared to DGLV predictions with (green band) and without (yellow band) collisional energy losses, and BDMPS predictions (thick dotted green line). On the right the result is compared to the results from two models employing a thermal approach to the energy loss: the Van Hees model and the Moore/Teaney model [26]

and dissociation of heavy-flavor hadrons.

In contrast to the success of pQCD in *pp* collisions, models of in-medium energy loss have not on the whole been successful in describing the high p_T suppression observed at RHIC. The radiative energy loss models were in good agreement with the R_{AA} of light hadrons, and thus in describing the energy loss of light-flavor quarks (see Figure 1.5.6). At both STAR and PHENIX, the combinatorial background for D-meson measurements in Au-Au collisions was too large to make useful quantitative conclusions concerning D-meson suppression at high momenta [14]. Although upgrades to both STAR and PHENIX hope to remedy that deficiency, the energy loss of heavy-flavor quarks has thus far primarily been probed via measurements of the R_{AA} of electrons from the decays of heavy-flavor quarks. Figure 1.5.7 shows the R_{AA} of electrons from the decays of heavy-flavor quarks as measured by the PHENIX collaboration with a comparison to a number of models. In the general, the agreement is far from perfect, a fact highlighted by the confidence interval plot in Figure 1.5.8. Radiative energy losses models are not consistent with both the light and heavy flavor R_{AA} measurements, though the thermal model of Van Hees that allows for hadronization and dissociation, and the collisional model of Sharma incorporating cold nuclear matter effects and also allows for hadronization and dissociation show greater consistency. As a whole, the data pose more questions than they answer, and the exact energy loss mechanism of quarks in the QGP is not completely understood. Data emerging from the LHC that may shed light on the exact energy loss

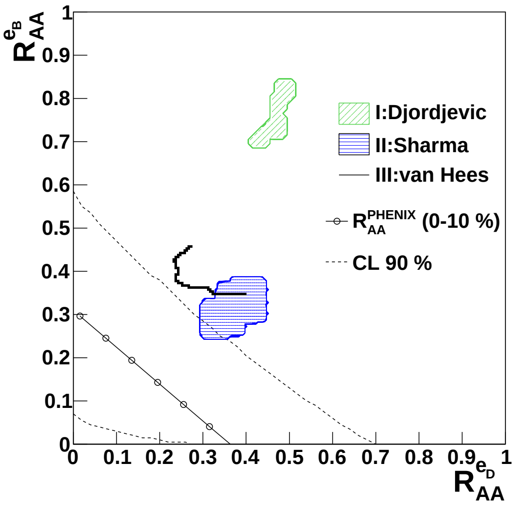

Figure 1.5.8: 90% confidence level contours for R_{AA} of high p_T electrons ($p_T > 5$ GeV) from D-meson and B-meson decays compared to some model predictions[27]

mechanism is thus of great theoretical interest.

In contrast to STAR and PHENIX, experiments at the LHC are capable of making measurements of D-meson production and suppression from the outset. Indeed, the measurement of D-meson suppression in Pb-Pb collisions was the first result concerning heavy-flavor suppression to emerge from the LHC [14] (see Figure 1.5.9). Radiative energy loss models supplemented with repeated

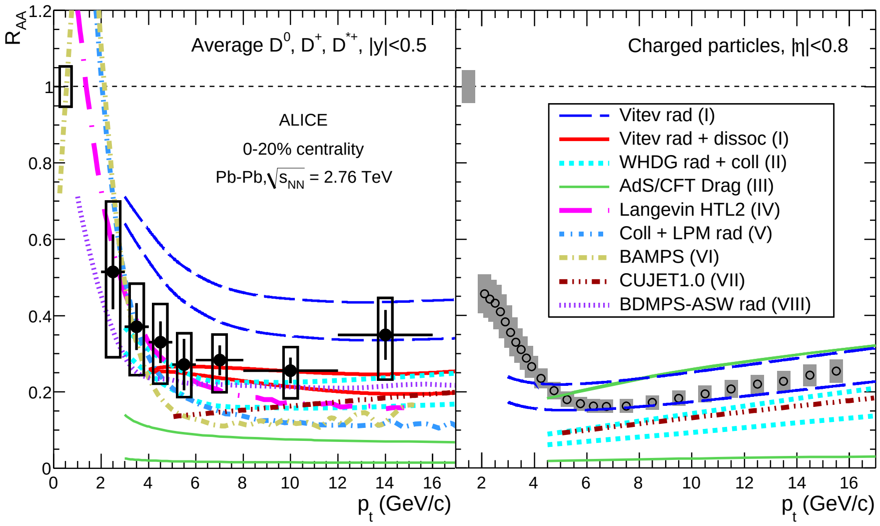

Figure 1.5.9: R_{AA} of D meson production in Pb-Pb collisions at $\sqrt{s} = 2.76$ compared to a sample of different model predictions [28]

hadronization and dissociation (Vitev radiative + dissociation) or collisional energy loss (WHDG) describe the data reasonably well. However, this is only the inception of what should be a highly fruitful period for heavy-flavor physics and relativistic ion physics as a whole. Measurements of b-jet suppression at CMS [221], R_{AA} of electrons from the decays of heavy-flavor hadrons [222], in addition to the R_{AA} of electrons from the decays of B-hadrons at ALICE are all results soon to emerge from the LHC.

Finally, it is also important to note the significance of initial state effects such as the Cronin effect and nuclear shadowing. Although most of the energy loss models do incorporate some of these effects, upcoming results from p-Pb collisions at the LHC are an extremely important tool to disentangle possible initial and final state effects in the data observed so far.

2

ALICE experiment

2.1 The Large Hadron Collider

An examination of the history of particle physics [29, 69, 70, 223] quickly reveals a historical trend towards conducting experiments at higher and higher collision energies. This fact is not surprising; the de Broglie relation, $\lambda = \frac{h}{p}$, and Einstein's mass-energy equivalence, $E = mc^2$, indicate that to probe smaller length scales or to produce particles of greater mass one needs to generate collisions of higher energy. In fact, the collision energy of particle accelerators has increased almost exponentially since the inception of field in a manner reminiscent of Moore's law in computer science [224] (see Figure 2.1.1). The first accelerators were the simplest conceivable: linear accelerators where some accelerating potential difference is applied in straight accelerating regions. As the need for higher energies was recognized, the space advantage of circular accelerators where accelerating potentials can be applied multiple times in many revolutions, led to the development of the cyclotron, the betatron, the synchrocyclotron and finally the synchrotron [223]. As accelerators move into the realm of TeV center of mass energy the effects of synchrotron radiation are such that some speculate the future of accelerators lies once again in linear accelerators [225]. Currently the highest center of mass energy collisions are achieved in a synchrotron accelerator called the large hadron collider (LHC).

The LHC is located on the Swiss-Franco border near Geneva, Switzerland The site had previously been used for a number of experiments, and the complex (the CERN laboratory, founded in 1954) in fact comprises a number of accelerators, many of which are currently used as an injector for the LHC. The LHC is situated within a tunnel of circumference 26.7 km, with a depth ranging from

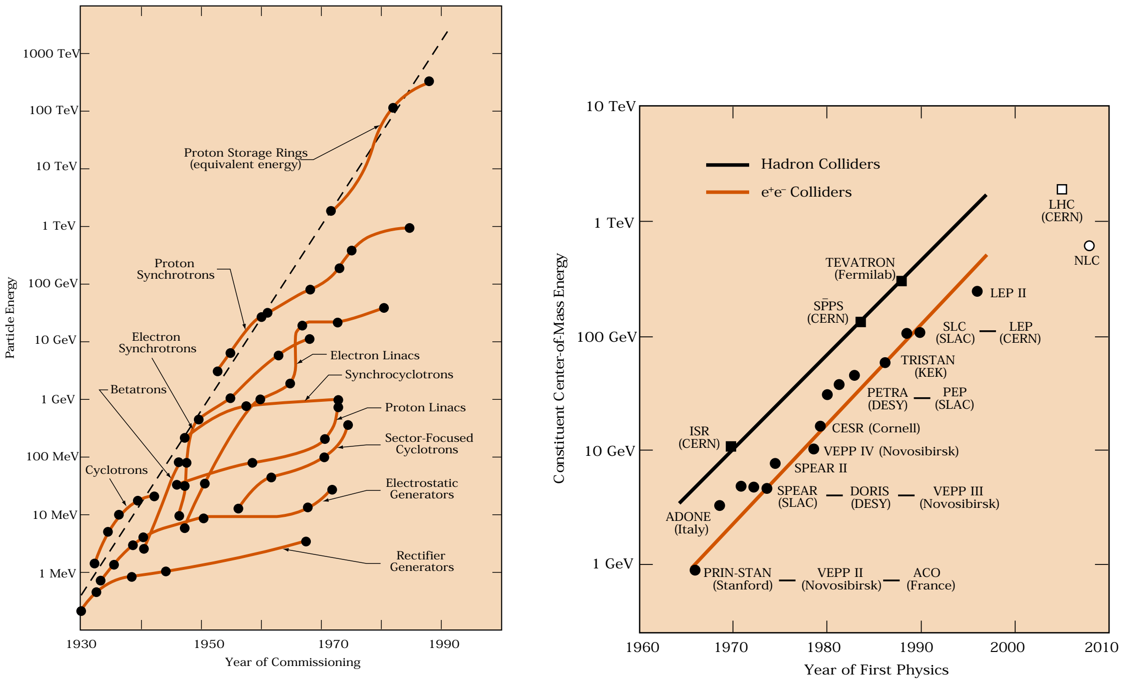

Figure 2.1.1: The development of high-energy accelerators (known as Livingston plots). The figure on the left shows the development of the equivalent energy of a fixed target accelerator for various types of particle detectors as a function of time, whereas the figure on the right shows the development of the center of mass energy of specific particle detectors and when they began operation [29].

50m to 175m. The tunnel was built between 1984 and 1989 for a previous accelerator, the large electron-positron collider (LEP), but it was in 1998 that work began on the construction of the LHC. The CERN accelerator complex is used to accelerate protons and lead ions to injection energies of $\sqrt{s}$ =450 GeV and $\sqrt{s}$ =177 GeV per nucleon respectively, whereupon the LHC provides further acceleration to reach proton-proton collisions with nominal center of mass energies of $\sqrt{s}$ =14 TeV, and lead-lead collisions with a nominal center of mass energy per nucleon-pair of $\sqrt{s_{NN}} = 2.76$ TeV.

A schematic of the injection chain is shown in Figure 2.1.2 The initial stages of injection are

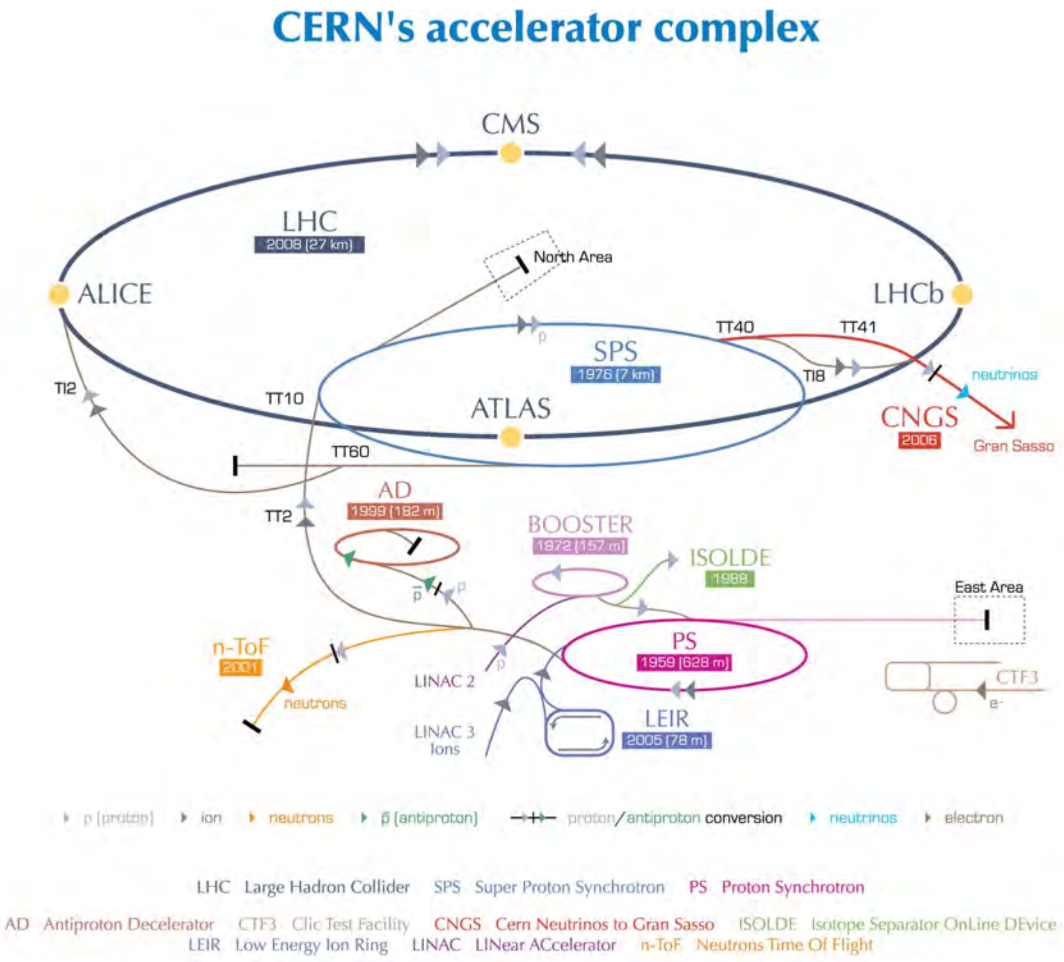

Figure 2.1.2: CERN's accelerator complex [30]

different for protons and lead ions. In *pp* collisions, a duoplasmatron source provides protons stripped from hydrogen gas with an energy of 92 keV which are promptly focused and accelerated to an energy of 750 keV by a 1m long radio frequency (RF) quadrupole for injection into LINAC2. LINAC2, a preexisting linear accelerator, provides acceleration to beam energies of 50 MeV, whereupon the PSB booster synchrotron accelerates the protons to an energy of 1.4 GeV for injection into the proton synchrotron (PS). The beginning of the injection chain for lead ions incorporates some more recently constructed accelerators: LINAC3 which was specially adapted for this purpose, and LEIR which was a new accelerator built in existing facilities used by the low-energy anti-proton ring (LEAR) accelerator. The lead-ion source is an electron cyclotron resonance (ECR) source where a sample of isotropically pure Pb_{208} is ionized in a microwave heated plasma. It provides a 200 μA beam of Pb_{208}^{27+} ions at an energy of 2.5 keV per nucleon. After a 135° spectrometer separates the ion species, they are accelerated by a long RF quadrupole to an energy of 250 keV per nucleon before being injected into LINAC3. LINAC3 is another linear accelerator which accelerates the ion beam to an energy of 4.2 MeV per nucleon whereupon the ions are stripped to produce a 20-24 μA Pb_{208}^{54+} ion beam which is injected into the low energy ion ring (LEIR). The circular LEIR accelerator finally provides acceleration to an extraction energy of 72.2 MeV per nucleon for injection into the PS accelerator. From this point on, lead ions and protons follow the same path (though under different conditions) through the CERN accelerator complex.

The CERN proton synchrotron (PS) was the first synchrotron to be built at CERN and was put into operation in 1959. From it's beginnings as the world's highest energy collider (for 7-8 months before being surpassed by the AGS at Brookhaven) it has since functioned as a injector for the intersecting storage ring (ISR) accelerator, the super proton synchrotron (as a stand-alone accelerator) and most recently for the LHC. 12 RF cavities accelerate protons to an energy of 25 GeV, and lead ions to an energy of 5.9 GeV per nucleon, whereupon they are injected into the super proton synchrotron (SPS) accelerator. The LHC bunch spacing (nominal proton bunch spacing of 25ns) is also established in the PS accelerator. The lead ions are stripped with an Aluminum stripper just before this stage, generating a beam of Pb^{82+} ions. The SPS is the final accelerator in the injection chain before injection into the LHC. It was built in 1976 and a slew of experiments have utilized the accelerator since its construction, among the many highlights being the discovery of the W and Z bosons in 1983 [226, 227, 228, 229]. The 7 km circumference ring utilizes four RF cavities for acceleration and 1425 non-superconducting magnets of 30 different types for beam control (including 744 dipoles and 216 quadrupoles); the SPS is in fact the world's largest accelerator utilizing warm (non-superconducting) magnets. Protons are extracted from the SPS with energies of 450 GeV and lead ions are extracted with energies of 177 GeV per nucleon. At this stage the beam is finally injected into the LHC for acceleration to nominal energies.

The layout of the LHC is depicted in Figure 2.1.3. The LHC tunnel is comprised of 8 circular arcs ($\approx$2.8km) connected by 8 500m straight sections labeled 'point' 1-8. Unlike the intersecting storage ring accelerator (ISR) at CERN (which operated from 1971 to 1984), the tunnel was not large

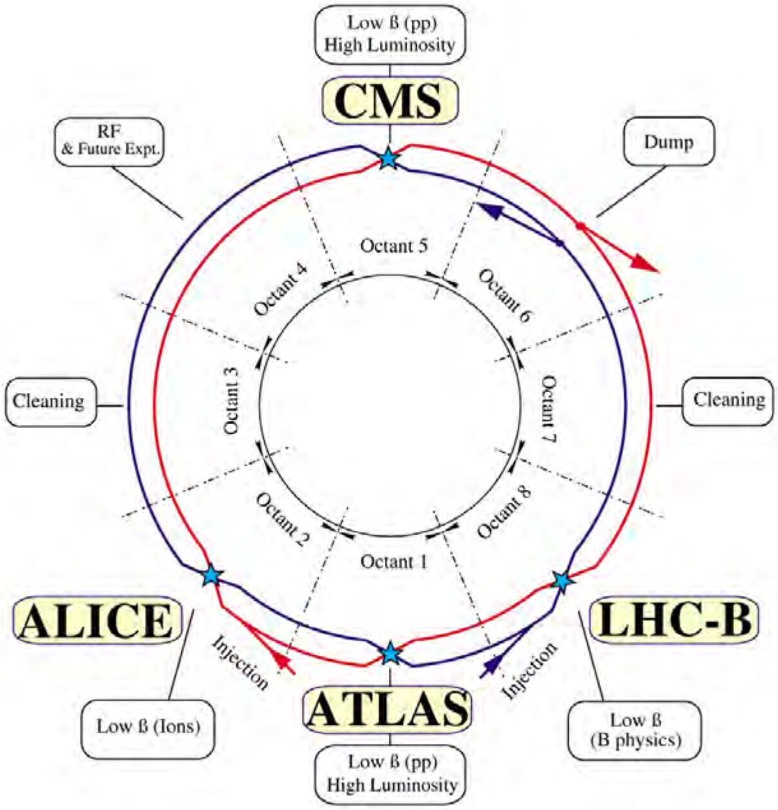

Figure 2.1.3: Schematic layout of the LHC [30]

enough to contain two separate beam pipes; to achieve the high magnetic fields required to maintain a particle's trajectory at these energies requires the use of superconductors, and superconductors occupy a large amount of space due to the cooling requirements. Hence the LHC utilizes two beam pipes of diameter 56mm which are separated by 194mm and are both enclosed within a common yoke and cryostat. There are four collision points (points 1, 2, 5 and 8) where the two beam pipes cross and the counter-circulating beams cross and collide. At four of these points are located detectors which form the basis of four of the experiments currently being conducted at the LHC: the ALICE detector, the ATLAS detector, the LHCb detector and the CMS detector. There are also the TOTEM, the LHCf and the MoEDAL experiments which utilize the LHC. The analysis in this thesis utilizes data from recorded with the ALICE detector, which was specifically designed to study the high-density nuclear matter produced in lead-lead collisions, and is located at point 2. Point 2 also houses the injection elements for ring 1 (clockwise ring), which lie at the end of the 2.6km connecting tunnel (TI2) from the SPS to the LHC. Point 8 houses the injection elements for ring 2 (counterclockwise ring) ending the 2.4km connecting tunnel, TI8.

Points 3 and 7 are used for beam 'cleaning'. Even when operating under ideal conditions the beam will not be constrained exactly within the ideal beam profile. Despite being held under vacuum, the beam will contain some residual gas that beam particles may collide with. In addition, intra-nuclear scattering, remnants of collisions at the interaction points, RF noise and other effects [230, 231] result in a 'beam halo'. This can produce unwanted background for the experiments, and could induce a quench (transition of the magnets out of a superconducting state due to a temperature rise) whereupon the beam is lost. Beam collimation, or beam cleaning, is used to intercept this beam halo as far as possible. Points 3 and 7 contain the adjustable beam collimation systems utilized by the LHC.

Point 4 houses the RF acceleration system. There are two independent 4 cavity 400MHz RF systems for each beam, the size of which demands a greater separation of the two beam pipes (420mm vs 194mm). Two pairs of dipole magnets are used to separate and coalesce the beams along the diverging and converging beam pipes. Like the magnets that are utilized in the LHC, the RF cavities are superconducting operating at 4.5K. This provides for a significant power saving (resistive losses) and allows for more flexibility in other aspects of the RF cavity design [226]. This choice also minimizes beam loading effects that can induce displacement of the collisions points [232, 233].

Within each of these points, and in the sections of tunnel between them, the complex array of magnets and RF control systems at the LHC allow for precise control of the transverse size of the beam and the beam luminosity which in turn determines the interaction rate observed at the collisions points.

2.1.1 Performance and Luminosity

The most important performance characteristics of any accelerator are the center of mass energy and the provided luminosity. The concepts of luminosity, cross-section and the reaction rate are intimately related. Experimentally the interesting parameter is the reaction rate, the number of collisions per unit time (or the number of a specific type of collision or interaction per unit time). Naturally one expects that this will comprise two elements: the intrinsic probability for the chosen interaction to occur, and properties of the colliding beams such as the particle density. The former is characterized by the cross-section, σ, and the latter is characterized by the luminosity, $\mathcal{L}$, with the interaction rate given by:

$$\frac{dN}{dt} = \mathcal{L}\sigma \tag{2.1}$$

The cross-section can be seen as an effective cross-sectional area for interaction. The luminosity is given by the rate of particle crossings (not necessarily interactions, but potential interactions) divided by the total effective crossing area. In the simplest case of two beams with circular cross-sectional area the luminosity is given by:

$$\mathcal{L} = \frac{N_1 N_2 f}{A_{eff}} \tag{2.2}$$

where A_{eff} is the effective crossing area, f is the bunch crossing frequency, N_1 is the number of particles per bunch in beam 1 and N_2 is the number of particles per bunch in beam 2 (beam bunching is described in the following section). In the more general case of non-uniform beam density the luminosity is given by the overlap integral:

$$\mathcal{L} = N_1 N_2 f_{rev} N_b K \int\int\int\int_{-\infty}^{\infty} \rho_1(x, y, s, -s_0)\rho_2(x, y, s, s_0) dx dy ds ds_0 \tag{2.3}$$

where f_{rev} is the beam revolution frequency, N_b is the number of bunches per beam, ρ_1 and ρ_2 are time-dependent distribution functions of the two beams. K is the relativistic Moller-factor[234] which accounts for the the relative speed of the beam:

$$K = \sqrt{(\mathbf{v}_1 - \mathbf{v}_2)^2 - \frac{(\mathbf{v}_1 \times \mathbf{v}_2)^2}{c^2}} \tag{2.4}$$

In the collinear limit (and in the non-relativistic limit), this reduces to what one would intuitively expect: $K = |\mathbf{v}_1 - \mathbf{v}_2|$.

Table 2.1.1: Various beam parameters at injection and collision at the LHC at peak luminosity for proton beams [46]

Beam Parameter	Injection	Collision
Proton Energy (GeV)	450	7000
γ_r	479.6	7461
No. of particles per bunch	1.15×10^{11}	1.15×10^{11}
Number of Bunches	2800	2800
Bunch spacing	25 ns	25 ns
β^* at IP1/IP5	18 m	0.55 m
β^* at IP2	10 m	0.5 m for Pb-Pb and 10 m for *pp*
β^* at IP8	10 m	$1 \rightarrow 50$ (IP8)
Transverse Emittance, ε	3.5 μm rad	3.75 μm rad

At the LHC the collisions take place at finite crossing angles [235]. The bunch spacing and the length of the interaction 'points' are such that multiple bunches can theoretically overlap within the interaction point. To remove these long range (parasitic) interactions, the beams cross at a finite crossing angle. This alters the luminosity by a multiplicative factor, F [236]:

$$F = \frac{1}{\sqrt{1+\left(\frac{\sigma_x}{\sigma_s}\tan\frac{\phi}{2}\right)^2}}\frac{1}{\sqrt{1+\left(\frac{\sigma_s}{\sigma_x}\tan\frac{\phi}{2}\right)^2}} \tag{2.5}$$

where σ_s is the bunch length, and ϕ is the crossing angle. At the interaction points in the LHC $\sigma_{x/y} \approx 17\mu$m, $\sigma_s = 7.7$cm and $\phi \approx 300\mu$rad. In this case we can therefore take the reasonable limits $\sigma_s \gg \sigma_{x/y}$ and $\tan\frac{\phi}{2} \approx \frac{\phi}{2}$ and F becomes:

$$F = \frac{1}{\sqrt{1+\left(\frac{\phi\sigma_s}{2\sigma_x}\right)^2}} \tag{2.6}$$

Utilizing the expressions for the RMS beam widths in terms of β and ε, and assuming a symmetric beam we obtain the following formula for the luminosity quoted in [46].

$$\mathcal{L} = \frac{N_1 N_2 f_{rev} N_b}{4\pi\varepsilon\beta}F \tag{2.7}$$

The LHC aims for a peak luminosity of 10^{24}cm^{2}s. Table 2.1.1 shows the LHC beam parameters for injection and collision at peak luminosity. The instantaneous luminosity varies considerably during a typical operation cycle. From injection at 450 GeV with a β^* of 10/11 m (11m at IP1, IP5 and 10 m at IP2 and IP8), the beam energy is first 'ramped' to 7 TeV. To prepare for collision the beam is subsequently 'squeezed' reducing β^* and thus increasing the luminosity. Once peak luminosity is reached, a gradual decay of luminosity occurs due to collisional beam loss, beam-beam interactions, beam-gas interactions and other effects [46] before the beam is dumped. The entire cycle takes about 75 minutes in addition to 5-10 hours of collisions.

There is also intentional variation of luminosity at the various collision points. The peak design luminosity for proton-proton collisions is only requested by the CMS and ATLAS experiments at IP1 and IP8. For instance, the ALICE experiment goal luminosity is 10^{30} cm^{2}s for protons and 10^{27} cm^{2}s for heavy-ions. Thus the luminosity is carefully controlled around the beam pipe, primarily by reducing or increasing the β^* value (i.e the transverse dimensions of the beam). For a nominal *pp* run $\beta^* = 10$ m for ALICE but only 0.55 m for ATLAS/CMS. For ALICE, this request for lower luminosity is a result of the slow readout time of the TPC which is 100 μs; maximum luminosity would result in too much pile-up.

2.1.2 Bunching and Filling Schemes

In modern accelerators the accelerating potential difference is typically supplied by an AC source with a sinusoidal wave form. This overcomes the problem of maintaining high potential differences that DC accelerators had in the early days of particle physics. Radio-Frequency RF accelerators apply a sinusoidal AC voltage across multiple cavities in sequence to accelerate particles. A consequence of RF acceleration is that the beams are not continuous but are segmented into bunches; Figure 2.1.4 illustrates the principle. When a particle arrives late it will receive a larger voltage and when it arrives early it will receive a smaller voltage, and thus the particles tend to form bunches. Of course the success of this scheme will depend on the RF operating frequency relative to the revolution frequency; the RF frequency needs to be a multiple of the revolution frequency. For the LHC the RF operating frequency is 400.8 MHz, and the revolution frequency is 11.245 kHz giving 35640 stable positions called buckets. When these stable regions are filled they are known as bunches. One may expect that as the particles are accelerated the RF frequency would need to be altered, and indeed this is the general principle of a synchrotron. However, at these energies the speed of the particles

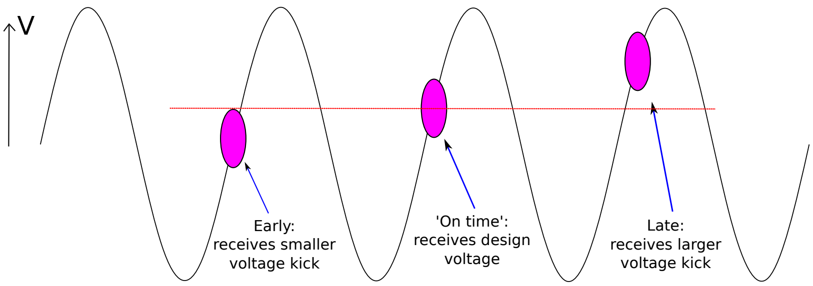

Figure 2.1.4: Principle of RF acceleration

changes very little as the energy is ramped and the frequency needs only be modified by about 1 kHz[226]. Of the 35640 possible bunch positions only every 10th is treated as a bunch slot to give a minimum bunch spacing of 24.95ns. This spacing allows for the rise time of the injection kicker magnets and the rise time of the beam dump kicker. This results in 3564 available buckets only 2808 of which are filled at design energies. The exact prescription for filling this bunches changes from run to run is known as the bunch filling scheme.

2.2 The ALICE detector

The ALICE detector (A Large Ion Collider Experiment) is a heavy-ion detector located in IP2 at the LHC and was designed specifically to study the properties of the quark-gluon plasma. At the time of design, in the early 1990's, experimental relativistic heavy-ion physics was only in it's infancy. Making predictions about what should be observed at center of mass energies hundreds of times greater than had already been achieved was extremely difficult. The construction of a flexible 'general-purpose' detector that could detect a wide variety of possible signals, both expected and not, was thus required. This flexibility is apparent in the various upgrades that have been implemented since the original design (the muon spectrometer approved in 1995, the transition-radiation detector in 1999 and the electromagnetic calorimeter in 2007, in addition to a host of upgrades planned for the 2017-2018 shutdown [237, 238]). That the ALICE detector has the capacity to detect a wide variety of signals is evident in the large number of detector sub-systems that utilize essentially all known detection mechanisms. It is comprised of 18 subsystems each with their own relative strengths and weaknesses that when combined provide the possibility of tracking up to 8000 particles in each event from momenta of 10 MeV/c to more than 100 GeV/c, performing identification of these particles over a wide energy range and reconstructing interesting decay vertices.

The detector sub-components can be divided according to the spatial region they occupy: the muon detectors at forward rapidity, the 'forward detectors' also at forward rapidity and used for triggering, and the central-barrel detectors at mid-rapidity; Figure 2.2.1 shows the pseudorapidity ranges for the various detector subsystems. The central-barrel detectors (except ACCORDE) are all located within a solenoid originally used by the L3 experiment (when the LHC tunnel was occupied by LEP) which provides a 0.5 T bending magnetic field within the central barrel. This is the largest non-superconducting solenoid ever constructed, and while it provides exactly the required characteristics at low cost (a weak solenoidal field as the best compromise between low momentum acceptance, tracking resolution and tracking efficiency), it does impose some constraints on the

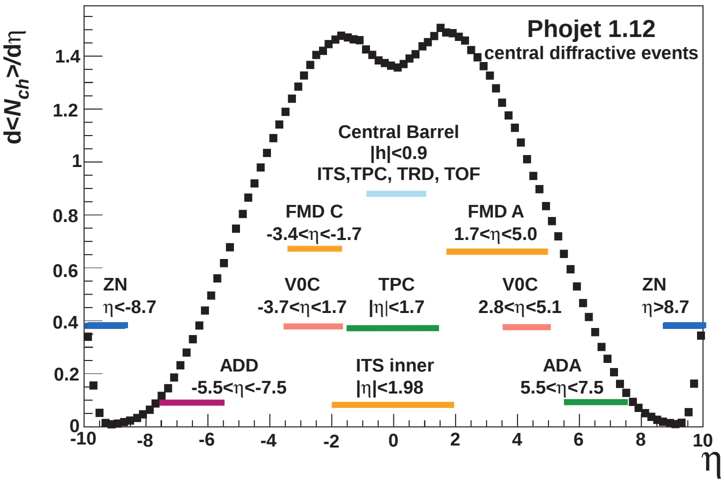

Figure 2.2.1: Simulation of the pseudorapidity distribution for central diffractive *pp* events in ALICE with the pseudorapidity acceptance of each detector subsystem overlayed.

overall detector design (for instance the depth of the EMCal is restricted by the existing structure). The total volume of the entire detector is 16m×16m×26m=6656m^3 and the approximate weight is 10,000 tonnes. Figure 2.2.2 shows the layout of the ALICE detector and the various subsystems. At the time the LHC began operation (2008) all detector subsystems were complete and installed except for the EMCal (ElectroMagnetic calorimeter), the TRD (transition radiation detector) and PHOS (photon spectrometer). In 2010, 4 of 10 supermodules of the EMCal were installed, 7 of 18 TRD modules were installed and 3 of 5 PHOS modules were installed. In 2011 (at the time of data taking for this analysis), the remaining EMCal modules were installed, and 3 more TRD modules were installed. Since then another 3 TRD modules have been installed and the rest will be installed during the 2013 shut-down. Funding issues mean the PHOS will not be completely installed. However a new calorimeter project, the ALICE DCal [239], is being undertaken with plans to install one more PHOS module and utilize unused space around PHOS to significantly increasing the η acceptance of calorimetry; this would bring the total calorimeter coverage to around 60% of the central barrel. Figure 2.2.3 shows the cross section of the ALICE detector between 2010-2012 at various stages of completion. The ALICE coordinate system is described in Appendix A

2.2.1 The Central Barrel

2.2.1.1 The Time Projection Chamber (TPC)

One of the most demanding constraints on the design of the ALICE detector is the large particle multiplicity that is expected in heavy-ion collisions. At the time of design, it was expected that

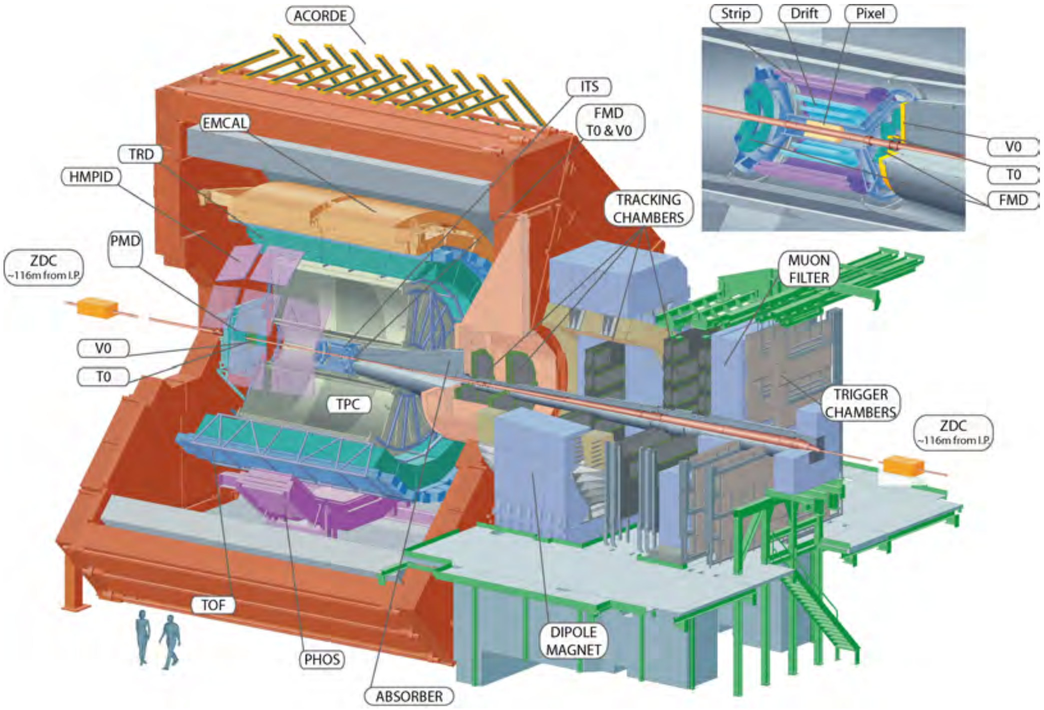

Figure 2.2.2: Schematic of the ALICE detector [31]

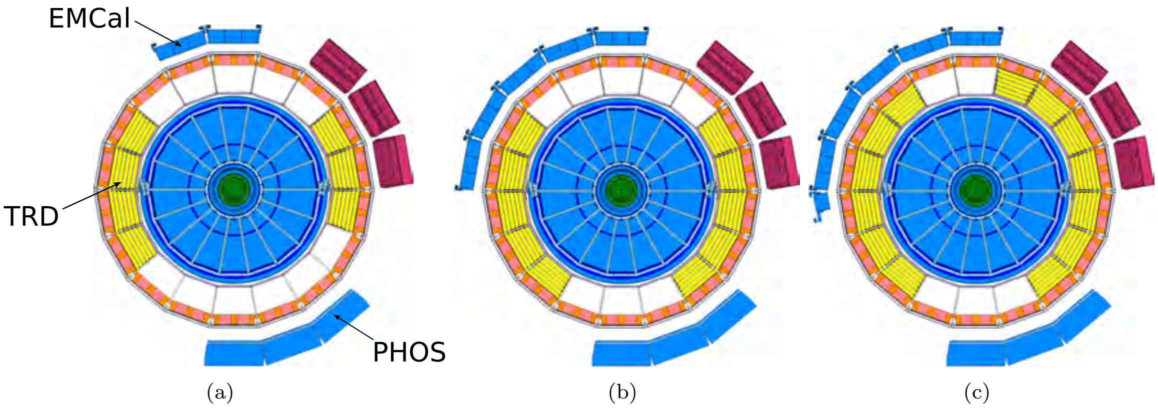

(a)

(b)

(c)

Figure 2.2.3: ALICE detector cross section during data taking in 2010 (a), 2011 (b), and 2012 (c). The data used for this analysis was recorded during March 2011 when the detector was in configuration (b) [31]

the charged-particle multiplicity, $\frac{dN_{ch}}{d\eta}$, may reach 8000. Subsequent extrapolations from RHIC data pointed to significantly lower values of 1500-4000 [35], and recent measurements at the LHC with ALICE conclude that $\frac{dN_{ch}}{d\eta} = 1584 \pm 4(\text{stat.}) \pm 76(\text{syst.})$ in Pb-Pb collisions at $\sqrt{s_{NN}} = 2.76$ TeV [240]. The desire for reliable performance at these large particle densities dictated the choice of a time-projection-chamber (TPC) as the main tracking detector in the ALICE experiment.

The operation principle of a TPC is illustrated in Figures 2.2.4 and 2.2.5. The TPC comprises a large field cage which functions to provide a uniform electric field across the enclosed volume which is occupied with a carefully chosen gas. As a particle traverses the gas it leaves an ionization trail (both electrons and positive ions). Usually a single electron/ion pair is produced per collision, but in a significant fraction (34% in Ar [241]) the primary electron may induce multiple ionizations. In most cases, the liberated electrons are of low energy and the electrons/ions tend to stay close together forming *clusters* which subsequently drift towards the end plates of the TPC as in Figure 2.2.4.

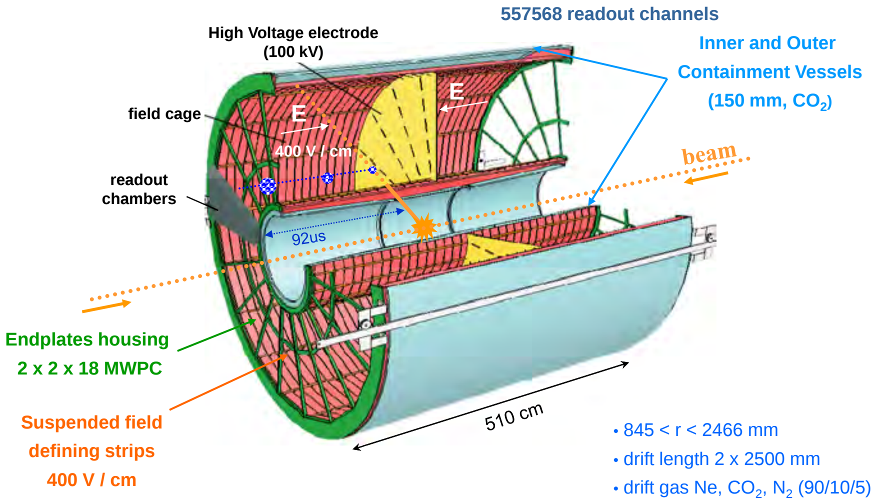

Figure 2.2.4: Diagram of the ALICE TPC indicating the major components. The drift principle is also illustrated: from a collision at the origin a track leaves an ionization trail (orange). At each point these *clusters* slowly drift towards the readout chamber (the dotted blue line indicates the drift trajectory of one such cluster) [32]

The detection mechanism at these end plates is provided by multi-wire-proportional chambers (MWPC). The typical formulation in a TPC comprises a grid of anode wires sandwiched between a grid of cathode wires and an array of cathode pads or strips separated by a few millimeters or less (see Figure 2.2.5). To prevent distortions of the drift field there is usually a gate which can be opened or closed to prevent the drift of ions back into the field cage. Due to the high voltage applied and the electric field around the anode wires that increases rapidly radially inwards, as the electrons approach the anode wires avalanches of electrons rapidly develop around the wire along

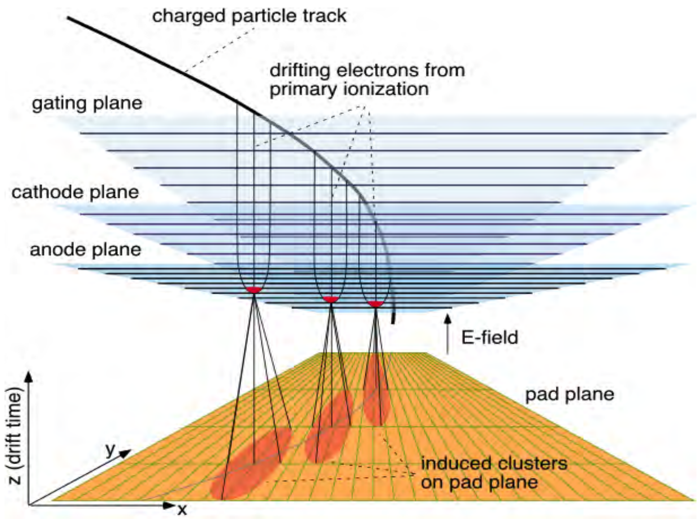

Figure 2.2.5: Illustration of a typical multi-wire-proportional-chamber (MWPC), that which provides readout in the ALICE TPC at the endcaps of the TPC. A charged particle within the drift volume ionizes the gas, and leaves a trail of *clusters*. These slowly drift towards the endcaps, whereupon they pass through a gating grid and cathode plane and subsequently form avalanches around the anode wires. The image of the ions produced in the avalanches constitutes the signal on the cathode read out pad [33]

with associated ions. The signal in the anode wire is dominated by the drift of these ions away from the anode wires, and the observed signal on the cathode pads is constituted by the image charge of these ions. Depending on the configuration of the anode wires and cathode pads or strips, coincidence of the observed signals in the anode wires and the cathode pads, or solely observation of the signals on the cathode pads (as in ALICE), allow for precise measurements of the azimuthal and radial coordinates (r, ϕ in a cylindrical coordinate system defined by the field cage) of the drift electron. Signal timing information and knowledge of the (constant) drift velocity enables extraction of the z coordinate. Pulse heights indicate the ionization energy loss which can be used later for particle identification.

The ALICE TPC is the largest TPC constructed to date, providing full azimuthal coverage and a pseudorapidity acceptance of $|\eta| < 0.9$ for full length tracks and $|\eta| < 1.5$ for partial length tracks (the pseudorapidity acceptance being a balance between cost and desired coverage). This coverage is provided by a cylindrical field cage of length 5m in the z-direction, an inner radius of 85cm and an outer radius of 250cm, with a total gas volume of nearly 90m^3 [242]. The inner radius is constrained by the maximum particle density that can be tolerated. Moreover, the inner silicon detectors at smaller radii provide better position resolution than the TPC alone, as is required for the reconstruction of heavy flavor decay vertices. The outer radius is large enough to reach the required $\frac{dE}{dx}$ resolution which scales with effective detector length [243, 244].

A $Ne/CO_2/N_2$ (85.7/9.5/4.8) gas mixture is used in the drift volume. Neon provides a very low radiation length and low multiple scattering, and the high ion drift mobility provides minimal field distortions and excellent position resolution. However, the choice of this drift gas imposes a large drift field (400 V/m) to provide a reasonable drift time (88μs). This requires a potential of 100kV between the 23μm thin Mylar foil central electrode ($z = 0$ m) and end plates ($z = \pm 2.5$ m). A layer of CO_2 gas surrounding the field cage (147mm from the outer field cage vessel to the outer containment vessel) provides the necessary electrical insulation from the rest of ALICE. The gas also exhibits a drift velocity with a strong temperature dependence and thus the gas has to be held to a temperature stability of <0.1K. An extensive set of cooling systems and thermal insulation provide the required thermal stability. A gas system circulates the drift gas ensuring that the ratio of the different gas components is held constant which is critical for drift velocity stability.

The end caps are divided into 18 sectors which support 2 MWPC's (one at smaller radii between 84.8 cm and 132 cm, and another at larger radii between 134.6 cm and 246.6 cm). This division of each sector into regions allows for smaller pad sizes (and hence greater resolution) at smaller radii where the track density is greatest; the inner pads are of $4 \times 7.5\text{mm}^2$ whereas the outer MWPC's has pads of sizes $6 \times 10\text{mm}^2$ and $6 \times 15\text{mm}^2$. In total 557,568 pads occupy an active area of 32.5m^2. The boundaries between the MWPC's are inactive ($\sim$ 27mm [245]) and in total 10% of the azimuthal acceptance is inactive for perfectly straight tracks [35]; of course, the bending field ensures that for the majority of tracks the active acceptance is larger than 90%. The readout is sampled at a rate of 10MHz resulting in digital time bins of 100ns (which corresponds to 0.265cm at a typical drift speed of 2.65 cm/μs [245]).

Between 2006 and 2008 the TPC was commissioned in several phases, initially at the surface and subsequently within the ALICE experimental area [245]. In this time period a number of distinct calibration methods were undertaken and tested for later data taking: Krypton calibration, laser system calibration and cosmic calibration. The laser calibration utilizes the TPC laser system. Within the end caps and within 6 of 18 axial support rods are a system of mirrors, lenses, prisms and beam splitters which are used to distribute and control two wide laser beams that enter the TPC at the bottom of each end cap. The resulting 336 narrow laser beams that enter the gas volume enable careful monitoring of the TPC drift field and keep field uniformity with a relative error of 5×10^{-4}. The laser tracks are also used for online drift velocity calibration and alignment; laser runs are taken at the beginning of each run and every hour subsequent. The gain calibration of the cathode pad readouts is achieved using Krypton calibration which is undertaken once a year [245]. Radioactive krypton ($^{83}_{36}$Kr, whose decay spectrum is well known, is released into the TPC gas. The measurement of the spectrum, and in particular a Gaussian fit of the main peak $E_{Kr} + 41.6$ keV), provides a suitable reference for gain calibration. There are also time-dependent gain calibrations due to variations in pressure, temperature and gas composition which are taken every 5-15 minutes during a run [246]; these are implemented in the calibration database (the OCDB, see 5.1). During 2008/9 some 8.3 million cosmic ray events were recorded by the TPC and this forms the basis of the cosmic ray calibration. The measurement of cosmic rays also allowed for the first measurements of the momentum resolution and the $\frac{dE}{dx}$ resolution. During cosmic runs the tracks were reconstructed in two segments (segmented by the center of the TPC) and by comparing the measured momentum and energy loss values for each half an estimate of the resolution is obtained. The $\frac{dE}{dx}$ resolution meets the design objectives, reaching $\sim 5\%$ for tracks with the maximal number of clusters. The momentum resolution (which is TPC stand-alone resolution) is 8% at 10 GeV/c, which is somewhat higher than the expected 4% [35]. In the initial data taking, a momentum resolution (combined ITS+TPC) of $\sim$ 10% at 50 GeV/c was observed which is also significantly higher than the 3% design resolution. Improvements in the ITS-TPC alignment have been made since that time and the momentum resolution for the data used in this analysis is shown in Figure 2.2.6, which indicates that the p_T resolution was 5% at 50 GeV/c for this analysis. In this case the momentum resolution is determined using the covariance matrix that is obtained during track reconstruction. The tracking algorithm follows a Kalman fitting approach [35] and is briefly described in Chapter 4.1.

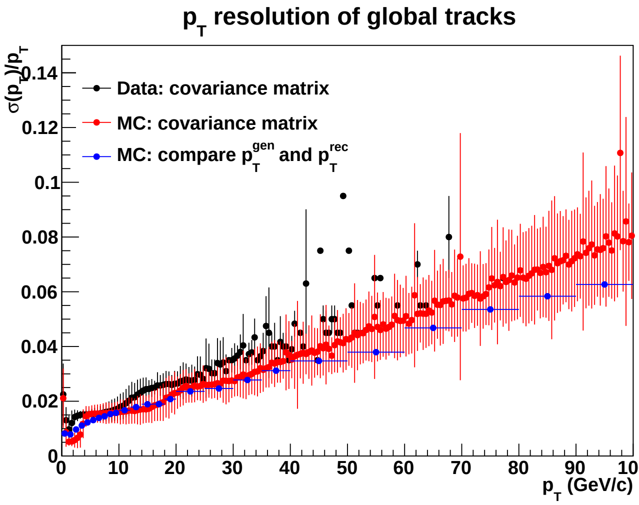

Figure 2.2.6: p_T resolution of the tracking system in the data set used for this analysis [34]

The experimental counterpart of the physical clusters of charges is the TPC cluster. If the measured charge in a 5x5 window (5 pads in MWPC, and 5 time bins) exceeds a certain threshold it is called a *cluster*. Given the number of pad rows of 159, the maximum number of TPC clusters

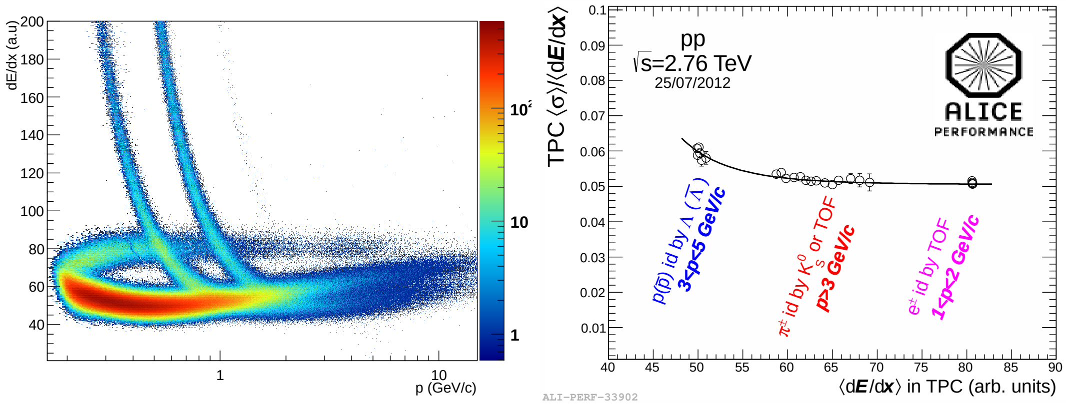

(a) (b)

Figure 2.2.7: Figure (a) shows the dE/dx distribution for all tracks and (b) shows the dE/dx resolution for pions, electrons and protons in the data used for this analysis. For the resolution plot, pions and electrons are identified using the TOF detector and protons are identified from lambda decays [31]

per track is 159. The underlying energy loss mechanism is such that the probability distribution (and thus charge distribution observed on the pads) is not Gaussian but landau distributed - the so-called straggling function [48] - and hence the average loss is not a good estimator of the energy loss. To circumvent this problem the *truncated mean* method is used whereby a certain fraction of the highest charge (energy) clusters are excluded; the resulting energy loss curves are Gaussian distributed. The resolution, $\sigma_{dE/dx}$, is given by the width of this Gaussian distribution. Figure 2.2.7 shows the $\frac{dE}{dx}$ distribution for all tracks and resolution for protons, pions and electrons for my data set. Consistent with the cosmic beam data, the resolution lies between 5% and 7% meeting the design specifications, and allows for particle identification over a wide momentum range.

2.2.1.2 The Inner Tracking System (ITS)

Within the TPC, and closest to the beam pipe, lies the inner tracking system (ITS). The ITS is critical for many analyses, and performs many vital functions. It is designed to reconstruct the primary vertex within 100μm, to identify and reconstruct secondary vertices from the decays of hyperons and D/B mesons with a resolution of better than 100μm in the radial direction, to improve the momentum resolution of tracks (as compared to using the TPC alone), to aid in the reconstruction of tracks that may pass through dead zones of the TPC, and to provide tracking and $\frac{dE}{dx}$ measurements of particles that do not reach the TPC (p$_T$ $\lesssim$200 GeV/c). The primary design constraints of dealing with large track multiplicities (as for the TPC but with a large increase in track density) and the ability to provide trigger decisions in the order of μs led to the choice of

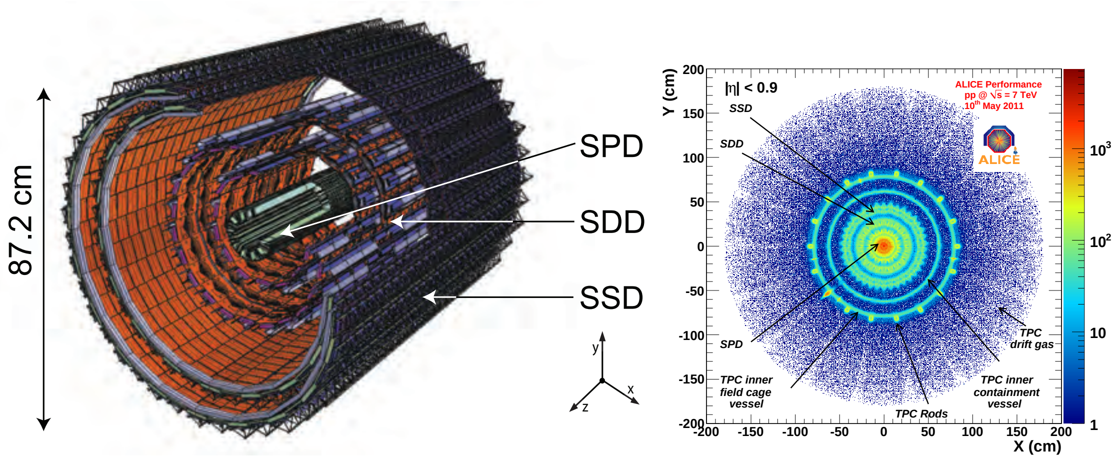

(a)

(b)

Figure 2.2.8: Layout of the ALICE ITS detector: (a) Schematic of the detector where geometrical position of the 6 layers can be seen with respect to the ALICE coordinate system (see Appendix A) [35] (b) Cross-section of the ALICE detector as defined by the (x,y) distributions of gamma conversion points in 7 TeV *pp* collisions [31]

Table 2.2.1: Characteristics of the ITS detector subsystems [47]

Layer	**Detector Type**	$r_{inner}-r_{outer}$ (cm)	$\pm z$ (cm)	**Number of Modules**	**Active Area Per Module** $r\phi \times z$ (mm^2)	**Resolution** $r\phi \times z$ (μm^2)
1-2	SPD	3.9-7.6	-14.1, 14.1	80-160	12.8×70.7	12×100
3-4	SDD	15.0-23.9	-22.2, 29.7	84-176	70.17×75.26	35×25
5-6	SSD	38.0-43.0	-43.1, 48.9	748-960	73×40	20×830

solid-state detectors for the ITS. The momentum and impact resolution is dominated by multiple scattering [35] and thus the material budget was also a concern. Although the material budget of such detectors is often a drawback, careful design and manufacturing resulted in a total radiation length of $X/X_0 < 8\%$.

The ITS comprises 6 layers using three different technologies (and comprising three detector subsystems), the resolution of which decreases radially as a balance between performance and cost. Figure 2.2.8 illustrates the layout of the ITS: the two innermost layers utilize silicon pixel detectors (SPD) which provide the highest position resolution, silicon drift detectors (SDD) occupy the two intermediate layers and the outer layers are comprised of silicon strip detectors (SDD). The entire ITS system measures 97.6 cm in the z direction and 43.6 cm radially, though the individual subsystems have varying dimensions and coverage; Table 2.2.1 lists the dimensions and some of the detector parameters for each subsystem. Note that the inner two layers (SPD) have a pseudorapidity coverage of $|\eta| < 1.98$ which ensures, in combination with the FMD, continuous coverage in $|\eta|$ necessary for charged multiplicity measurements.

In ALICE the two innermost ITS layers comprise SPD's which provide the necessary resolution in a region where there may be 50 particles/cm^2. The basic unit of assembly is a *ladder* consisting of 256×160 pixel cells bump-bonded to 16 readout chips with a total thickness of 350μm. 4 of these ladders comprise a *stave* which are mounted onto the sectors (6 per sector, 10 sectors in the entire barrel) of the support structure. In total, 60 layers form the inner layer and 160 form the outer layer resulting in some 9.8 million SPD channels in total. This large number of channels are easier to deal with binary readout and thus the SPD provides no $\frac{dE}{dx}$ information. Although the SPD's are not extremely temperature sensitive, the outer layers (SDD in particular) are more so and a cooling system is utilized to extract the 15-20W of heat that is expected to be produced per stave. In addition a heat shield is placed on the outer of the 2 SPD layers to further insulate the outer layers which have their own cooling systems to provide the required temperature stability.

SDD's occupy the middle two layers and provide sufficient position resolution (the track density drops to $\sim 7\text{cm}^{-2}$ at these distances from the beam pipe), though at a lower cost than the SPD. In the ALICE SPD's the detection region is partitioned into 2 by a central cathode (much like a TPC) and the liberated electrons drift away from this central electrode towards n-doped anode terminals. As for the SPD, the detector elements are assembled in *ladders*, the inner layer comprising 14 ladders and 84 detector elements and the outer layer containing 22 ladders and 176 detector elements. The SSD's are mounted on identical support structures but with 24 layers and 748 strip modules in layer 5 and 38 layers and 950 modules in layer 6. The readout is analogue in both the SDD's and the SPD's and thus can provide $\frac{dE}{dx}$ measurements. To utilize the truncated mean method of $\frac{dE}{dx}$ measurement (see Chapter 2.2.1.1) a minimum of 4 ITS layers are required; the SDD's and SSD's provide this requirement.

The primary aims of the initial calibration, commissioning, and data taking phases of the ITS are verification of the alignment between the detector subsystems and individual layers, measurement of the resolution and possible tuning of the vertex finding algorithm, measurement of the secondary vertex resolution and a determination of the particle identification capabilities via $\frac{dE}{dx}$ measurements. The initial survey (measurement of the placement detectors in the chamber using lasers) provides a baseline for the alignment. Both cosmic ray data collected in 2008-10 and the first proton collisions in 2010 with and without magnetic field were used for the alignment procedure. An iterative algorithm (Millipede [247]) minimizes the track-point residuals to identify the most probable position for the modules. The residual misalignment is estimated by examining the residuals of 'overlapping' clusters: to ensure full coverage the individual ladders have regions of overlap, and if a track traverses this overlap region a hit can be recorded in each detector element. At the time of data taking for this analysis, the estimated residual misalignment was $\sim$8μm for the SPD, $\sim$35μm for the SDD and $\sim$20μm for the SSD [47, 247, 248].

A measure of the vertex resolution is given by the σ of a Gaussian fit to the x and y vertex position distributions. To resolve secondary vertices a primary vertex resolution of the order of 50μm in the bending plane is required [249]. The final vertex resolution actually depends on the value of β^* which is controlled to manipulate the luminosity and thus control the interaction rate. Figure 2.2.9 shows the width of the x, y vertex position distributions in $\sqrt{s} = 7$ TeV pp collisions with $\beta^* = 10$ m; the width of the distribution is $51 \pm 3\mu$m in the x direction and $74 \pm 3\mu$m in the y direction and agrees well with simulations. At $\beta^* = 2$ m the resolution is $34{\pm}2\mu$m in the x direction and $33{\pm}3\mu$m in the y direction which is more than enough to satisfy the design requirements. Indeed measurements of D^0 yields via displaced vertex measurements have already been undertaken [250]. In Pb-Pb collisions the track multiplicity is high enough to employ the 'half-event' method where the tracks are randomly split into two samples and a primary vertex is reconstructed for each. A comparison of the two vertex positions gives an estimate of the vertex resolution. For the case of Pb-Pb collisions this was measured to be $\lesssim$ 10 cm in x, y and z directions. This improvement is both due to the large multiplicity and the lower value of β^* (0.2m) used for Pb-Pb beams.

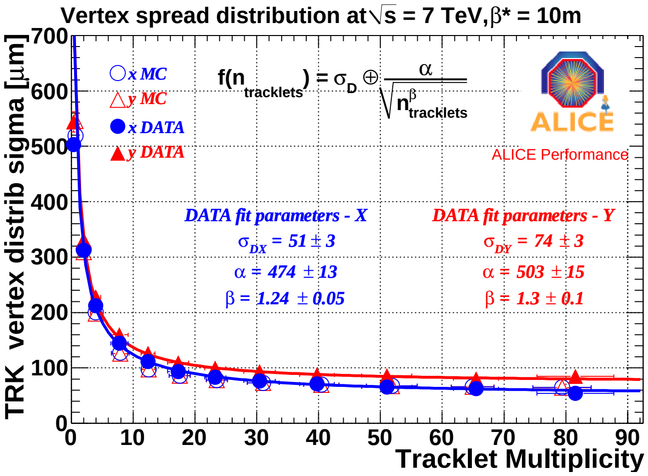

Figure 2.2.9: Vertex resolution in 7 TeV pp collisions as measured by the width of the vertex position distributions

The impact parameter resolution is estimated as the width of the distance of closest approach (DCA) distribution (that is the shortest distance between the track and the calculated primary vertex position). The result for 7 TeV pp collisions is shown in Figure 2.2.10(a), it agrees with simulations to within 10%. The impact parameter resolution, like the vertex position resolution, is critical for measurement of displaced vertices and currently comes close to design specifications.

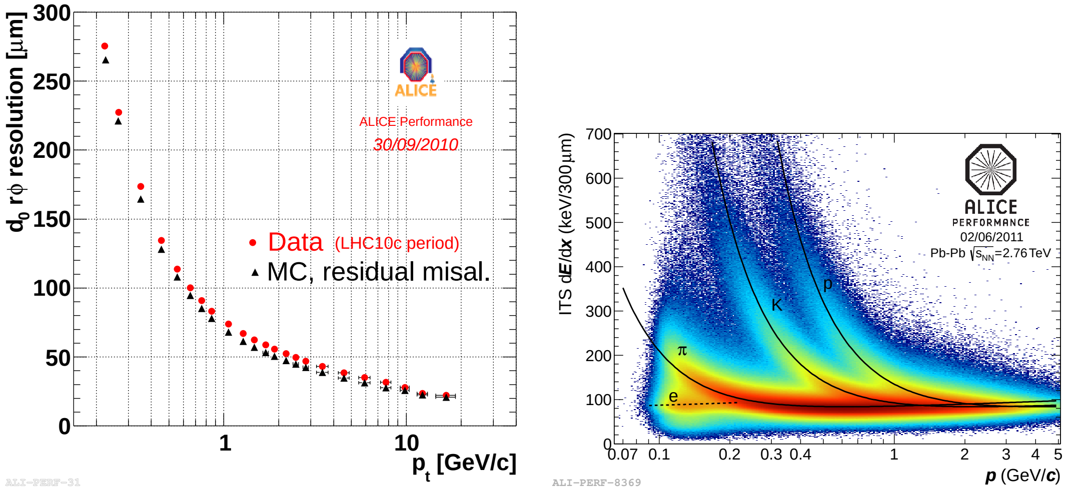

(a)

(b)

Figure 2.2.10: ITS performance: (a) is the impact parameter resolution as estimated from the width of DCA distributions in 7 TeV *pp* collisions [31] (b) is the dE/dx distribution of all tracks in 2.76 TeV Pb-Pb collisions using the ITS as a standalone detector [31]

Finally, the ITS has shown to have excellent PID capabilities using ionization energy loss. Figure 2.2.7 which show the $\frac{dE}{dx}$ distributions for complete tracks (TPC+ITS) utilizes solely the ITS information below 1GeV/c. Moreover, the ITS as a standalone detector has good particle identification capabilities at low momenta and Figure 2.2.10(b) shows the $\frac{dE}{dx}$ distributions in 2.76 TeV Pb-Pb collisions using the ITS as a standalone detector; the resolution is of the order of $\sim$ 6%.

Despite the success of the ITS in the ALICE physics program thus far, there is some interesting physics which cannot be accessed with the present ITS. For instance, better impact parameter resolution is required to separate the beauty and charm contribution via secondary vertex identification, which is necessary to investigate the mass dependence of in-medium energy loss. Moreover, to reconstruct D mesons at $p_T \sim 200$ MeV/c requires better tracking capabilities at low momenta than are currently attainable. To address these limitations an upgrade to the ITS tracking system has been proposed and recently approved which would increase the number of layers to 7 and significantly increase the position resolution [237]. The will be installed in the 2017-2018 shutdown.

2.2.2 The Transition Radiation Detector (TRD)

A particle traveling uniformly does not emit radiation unless it travels faster than the the phase velocity of light in the medium traversed (Cerenkov radiation). However, when a particle crosses a boundary between materials of differing dielectric constants there is a change in configuration of the fields as the particle traverses the boundary and radiation, *transition radiation*, is emitted. In the case of a vacuum to perfect conductor transition this can be seen as the 'annihilation' of a particle and it's image charge at the boundary [251], and more generally as the emission of radiation due to a time-dependent induced polarization in the distant medium that adds coherently only as the particle traverses the boundary [252]. The intensity of transition radiation emitted increases with an increasing relativistic γ-factor, and thus electrons emit greater intensity transition radiation than other species. This transition radiation is exploited in in transition radiation detectors to perform particle identification, in particular electron identification.

The ALICE transition radiation detector (TRD) provides full azimuthal coverage within the central barrel, has a pseudorapidity acceptance of $|\eta| < 0.9$ and is located between 2.9m and 3.7m from the beam pipe. It's main objective is particle identification, in particular electron and pion separation above 1 GeV/c (where the $\frac{dE}{dx}$ information is not enough for the requisite particle separation as the bands begin to overlap). The excellent electron PID capabilities also allow it to provide a L1 trigger (see Chapter 2.2.10). In addition, it provides tracking capabilities and as such provides a modest improvement in the total track momentum resolution (in combination with TPC and ITS). The commissioning, calibration and initial data taking has been successful, with performance largely consistent with simulation and coming close to design specifications [253, 254]. The PID capabilities of the TRD have already been demonstrated in several physics results, notably (with relevance to this thesis) in the measurement of semi-leptonic decays of heavy-flavor hadrons in $\sqrt{s} = 7$ TeV pp collisions [23].

2.2.3 Time of flight detector (TOF)

In general, time of flight detectors (TOF's) seek to identify particles through a careful measurement of the velocity via a measurement of the time to traverse a known length. With a measurement of the momentum (from the TPC, which entails a track matching procedure between the TPC and TOF), the particle's mass is determined as:

$$m^2 = \frac{p^2}{c^2}\left(\frac{c^2 t^2}{L^2} - 1\right) \tag{2.8}$$

where m is the particles mass, p is the particles momentum, t is the time taken to traverse the known distance L. Hence by measuring the mass, particle separation can be achieved. Alternatively one can distinguish particles based solely on their velocity:

$$\beta = \frac{p}{\sqrt{mc^2 + p^2}} \tag{2.9}$$

In either case the resolving power depends critically on the time resolution of the detector - to achieve the design requirements (3σ separation of π/K up to $\sim$ 2.5 GeV and 3σ separation of p/K to $\sim$ 4 GeV) a resolution of better than 100ns is required.

The ALICE time of flight detector (TOF) lies between the TPC and the TRD at 2-9-3.7m from the beam pipe and spans the full azimuth. In order to study the shape of p_T distributions of pions, kaons and protons, the thermodynamically significant ratios π/K/p, and to identify open charm decays like $D^0 \rightarrow K^+\pi^-$, good particle separation between these species is necessary. The TPC can provide such PID capabilities up to about $\sim$ 0.5 GeV/c. Whereas the TRD focuses mainly on separation of electrons and hadrons, the goal of the TOF detector is to extend the K, π and p identification and separation capabilities out to around 2.5 GeV/c. The particle identification capabilities can be inferred from Figure 2.2.11 which shows the measured β values in $\sqrt{s}$ = 2.76 TeV Pb-Pb collisions where the clear separation between hadron bands can be seen. The time resolution is determined as the width of the measured time of arrival of pions, and presently stands at around 86ns which meets the requirements for the desired particle species resolving power. The efficiency is estimated by examining the matching efficiency of tracks between the TPC and TOF in both Monte-Carlo simulations and data, and is estimated to be $\sim$ 98%.

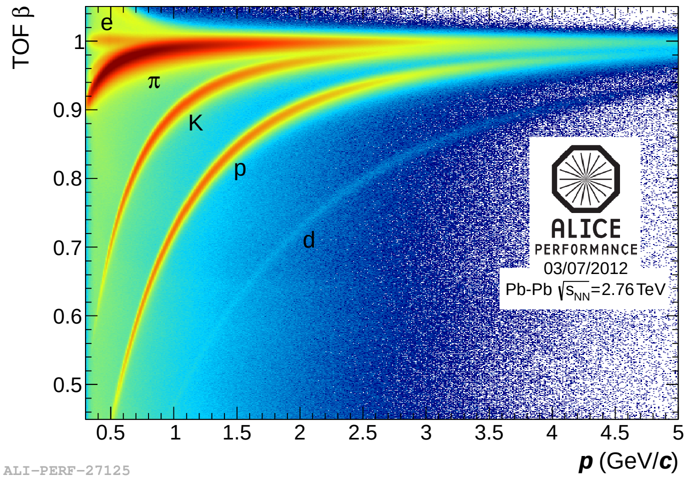

Figure 2.2.11: β for different particle species as measured by TOF in $\sqrt{s}$ = 2.76 TeV Pb-Pb collisions [31]

2.2.4 High momentum particle identification detector (HMPID)

Like the TRD, the high momentum particle identification detector (HMPID) exploits radiation that is emitted when a uniformly charged particle moves through a medium. For the TRD this radiation is transition radiation; for the HMPID this radiation is Cerenkov radiation, radiation that is emitted when a particle travels faster the phase velocity of light in a dielectric medium and is analogous to sonic booms that are created when traveling faster than sound through air. In the case of Cerenkov radiation, it can be seen as the effect of induced polarizations along the path of a charged particle. At velocities below the speed of light in the medium, the polarized molecules are symmetric with respect to the particles path and no net emission from the dipoles is evident. However, if the charged particle exceeds light speed then the distribution of polarized molecules is no longer symmetric and a net field disturbance is produced from the net effect of the dipoles. The resulting radiation is emitted conically about the particle trajectory with an emission angle:

$$\cos\theta_c = \frac{1}{n\beta} \tag{2.10}$$

where θ_c is the conical emission angle, n is the index of refraction of the medium and $\beta = v/c$ is the relativistic β-factor. Since the β values differ between particles due to mass differences as was described for the TOF detector, a measurement of the Cerenkov angle provides a distinguishing characteristic for particle identification.

The ALICE HMPID aims to further extend the transverse momentum range of PID in ALICE through the identification of protons between $\sim 1.5-5$ GeV/c, and charged pions and Kaons between $\sim 1-3$ GeV/c. These capabilities allow measurements of particle ratios (π/K, K/π, $\bar{p}/p$), resonances such as $\phi \rightarrow KK$ and the study of high p_T jet fragmentation. The detector covers approximately 5% of the detector phase space (occupying a total area of 10 m^2 with $\Delta\phi = 51.7°$ and $|\eta| < 0.48$). and lies at 4.7m from the interaction point where the particle density is reduced to $100\mathrm{m}^{-2}$. 7 modules are arranged within a 9×9 'grid' as can seen in Figure 2.2.2, and thus the acceptance in ϕ is not continuous across the η range (and vice versa).

2.2.5 Photon Spectrometer (PHOS)

The photon spectrometer (PHOS) is an electromagnetic calorimeter whose goal is the study of the initial thermodynamics of the quark gluon plasma through the measurement of direct photons and direct di-photons, an examination of jet quenching through the measurement of jets (both charged and neutral components), and measurements of π_0 and η spectra that are useful in a variety of contexts [255, 256] in addition to be interesting in their own right.

The essence of a calorimeter is the determination of a particles energy through destructive interaction. Destructive in that the particle interacts strongly with the detector and is no longer available for further measurements after detection. The interaction of the particle with the material is measured through a variety of techniques, and ideally the entire energy of the particle is deposited in the detector material. The later requirement often leads to a distinction between *hadronic* calorimeters and *electromagnetic* calorimeters. Electromagnetic calorimeters tend to be less deep than their hadronic counterparts as they are designed to measure the energy of particles like electrons that interact primarily electromagnetically that tend to deposit their energy quite readily. The deeper hadronic calorimeters allow for full energy deposition of neutral particles that interact primarily via the strong force. In ALICE there are no hadronic calorimeters, and spatial constraints limit the depth of the electromagnetic calorimeters. Hence although the detectors can measure the total energy of a variety of particles over a wide energy range, there is still considerable 'leakage' that introduces detector non-linearity at high momenta that must be accounted for.

The method of energy measurement defines two categories of calorimeter: *sampling* calorimeters and *homogeneous* calorimeters. Sampling calorimeters comprise layers of passive absorber (dense materials like lead provide large interaction cross sections) interlaced with layers of active detector medium like silicon. Homogeneous calorimeters have a single medium that provides both absorption and detection. Sampling calorimeters allow for better control of the detection and absorption properties as differing materials are used for each. This is typically necessary in hadronic calorimeters where the showers can be very deep and depend critically on the nuclear interaction length, a parameter that scales with the atomic number of the material. By careful choice of the absorbing medium the depth of hadronic showers can be limited. On the other hand, the energy resolution of homogeneous calorimeters is significantly better due to larger sampling fluctuations in sampling calorimeters. In homogeneous calorimeters the detection of the particles energy relies on the production of scintillation light, ionization or Cerenkov light which is subsequently detected. The PHOS calorimeter is a homogeneous detectors based on scintillation. In the inorganic substances used for scintillation, the conduction and energy bands are well separated and the material functions as an insulator. When a particle interacts with the medium it can induce the excitation of electrons from the valence band to the conduction band. This electron can subsequently recombine with the hole, or it can form a bound state with a hole (called an exciton) which is eventually de-excited through recombination or collision with a phonon (quanta of lattice excitations). In either case the result is the emission of a scintillation photon. This scintillation light is a measure of the energy deposition and is typically detected at the end of the active volume. The correlation between the measured scintillation light and the incident particle energy necessarily involves some form of calibration.

The PHOS calorimeter is located at a radius of 4.7m from the beam pipe, extends over the pseudorapidity range $|\eta| < 0.13$ and currently covers 66° in azimuth. Although the original proposal called for $\Delta\phi = 100°$, not all the PHOS modules have been installed. In coordination with a new calorimeter project, the DCal, one more PHOS module is planning to be installed along with the installation of more electromagnetic calorimeters on either side of PHOS to increase the total $|\eta|$ acceptance of calorimetry. Each PHOS module consists of a charged particle veto detector (CPV), some 64×56 $PbWO_4$ crystals which provide the scintillation volume, and an avalanche photo-diode (APD) which detects the scintillation photons. PHOS has contributed to a number of analyses since commissioning. For instance, the η and π_0 spectra have been measured in 7 TeV, 900 GeV, and 2.76 TeV (the latter yet to be published) *pp* collisions [257]. In addition to be interesting measurements of their own merit, the PHOS measurements are critical in the analysis undertaken for this thesis as necessary input for the cocktail subtraction (see Chapter 7). The measurement of π/η spectra, has already been critical for similar results in 7 TeV *pp* collisions [23].

2.2.6 Electromagnetic Calorimeter (EMCal)

The largest US contribution to the ALICE project comes in the form of the electromagnetic calorimeter (EMCal). With construction at Wayne State, cosmic ray calibration at Yale and funding provided by the US department of energy (DOE), US institutions have been heavily involved in every stage of construction and calibration. Like PHOS, the electromagnetic calorimeter (EMCal) is a calorimeter used to measure energy of particles via destructive energy deposition. However, the EMCal is focused more towards high p_T measurements, in particular the measurement of jets and high p_T electrons and photons. Indeed, the electron identification capabilities of the EMCal beyond 10 GeV/c are unique within ALICE; this complements the capabilities of the ITS, TPC, TOF, and TRD which can perform electron identification up to around 10 GeV/c [36]. Moreover, the capability to measure high p_T jets provided by the EMCal allows ALICE to pursue precise measurements of jet cross-sections and jet quenching [36] that extend the interesting observations already made at RHIC [258, 259, 260]. The fast electronics also allow for an event trigger with the EMCal that significantly extends the kinematic reach of many potential physics results (see Chapter 6 and [261]) As part of my collaboration duties I was involved in the calibration using cosmic rays and the analysis of test beam data for the ALICE EMCal. In addition, the analysis undertaken for this thesis utilizes the ITS, TPC and EMCal to identify electrons and uses data collected with the EMCal trigger.

The focus on high p_T physics, in addition to balancing cost with performance, led to the choice of a sampling calorimeter based on Shashlik technology (a design already in operation in the PHENIX experiment [262]). Although the resulting energy resolution is worse than the homogeneous PHOS calorimeter, which is also targeting low momenta thermal properties of the medium, the resolution is sufficient for the identification of electrons at high p_T and provides sufficient resolutions for jet energy measurements [263]. The basic detection element of the calorimeter is a *tower* comprising 77 alternating layers of 1.44m thick Pb absorber (1% Sb) , and 1.76mm thick injection molded polystyrene active medium. The scintillation photons are collected via 36 wavelength shifting (WLS) fibers running longitudinally through the detector volume (see Figure 2.2.12 for an illustration). These fibers absorb the scintillation light and emit light at a longer wavelength. These enables the light to be directed towards the rear-end of the detector element. As opposed to the older configurations where each active layer is read out individually, this allows for the hermetic coverage required by particle physics experiments. At the front face of the calorimeter the fiber bundles meet at a mirror, and at the back face they meet at an avalanche photo-diode (APD) and preamplifier for detection of the scintillation light. These are essentially p-n junctions with large depleted regions that are held under a high voltage. Incident photons induce the production of electron-hole pairs in the depleted region that quickly, due to the large bias voltage, gain enough energy to stimulate the production of more electron-hole pairs and an avalanche thus forms generating a measurable current pulse.

Figure 2.2.12: Photograph of an individual EMCal module comprising four towers. The Shashlik WLS fibers that penetrate the module longitudinally are visible [36]

The towers are assembled into 2×2 modules, the dimensions of which are indicated in Figure 2.2.13. The towers are in turn arranged into a 12×1 (or 24×2 tower) *strip module* as in Figure

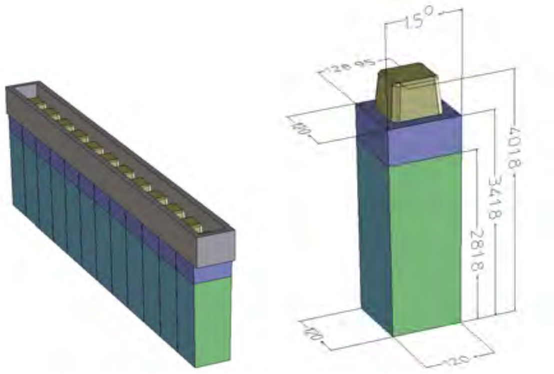

Figure 2.2.13: Illustration and dimensions of a single module (right) and depiction of strip module assembly from 12 modules (left) [37]

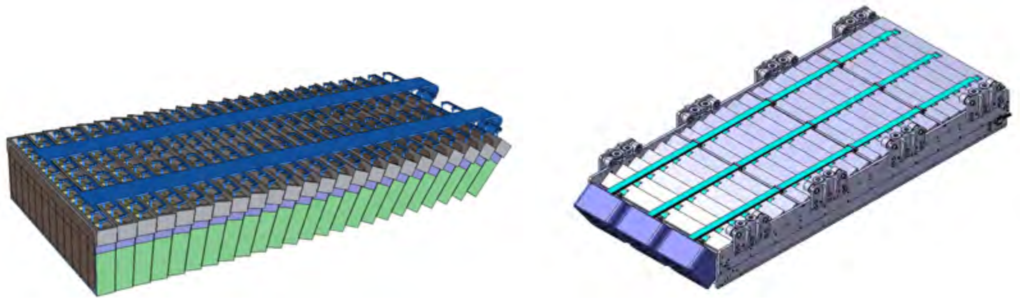

(a) (b)

Figure 2.2.14: Illustration of the construction of a supermodule from the individual strip modules [37]

2.2.13. These form the basis of a *supermodule* and 24 modules are installed projectively to form a full supermodule as in Figure 2.2.14. Within the EMCal, there are 10 full-size supermodules and a two half-sized supermodules, the later comprising 24 half-size strip modules (6×1 modules as opposed to 12×1). The configuration is illustrated in Figure 2.2.15, and positioning with respect to the rest of ALICE can be seen in Figures 2.2.2 and 2.2.3. In total 12,672 towers span a total region occupying $|\eta| < 0.7$ and $\Delta\phi = 100°$ in phase space. The sampling fraction (which is typically the dominant source of error in the measured energy resolution) was carefully chosen to minimize the resultant energy resolution with the use of simulations. The space available limited the radiation depth to $\sim 20\text{X}_0$, but the resultant non-linearity is still less than 5% for electrons up to 100 GeV.

Initial calibration of the APD gains was undertaken using cosmic data. To achieve the desired energy resolution a tower-by-tower relative energy calibration of the level of 1% is required and thus in addition to this basic level of calibration the EMCal has a built in LED calibration system. A ultra-bright light pulse from a calibrated LED mounted outside of the EMCal module for electrical

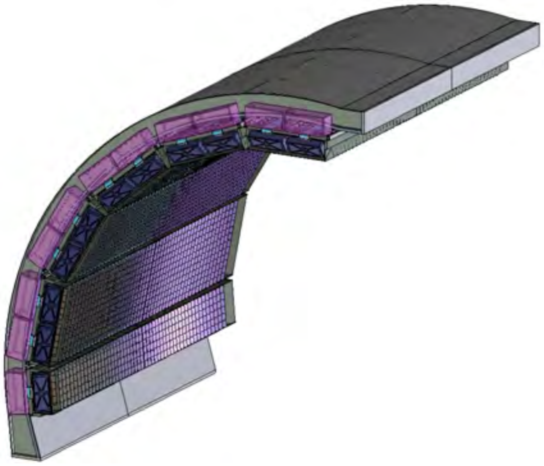

Figure 2.2.15: Diagram of the ALICE EMCal as it is installed in ALICE. Note the structure of the 10 full and two half supermodules [36]

isolation is fed into the EMCal modules via light fibers. These LED pulses enable careful monitoring of the time-dependent APD gain voltages. In addition, with large enough statistics, it is possible to perform calibration using π_0 signals. By computing the π_0 invariant mass peak and minimizing the width as a function of the gain voltages the requisite energy calibration can be achieved [36].

For a small segment of the EMCal the gain voltages were calibrated with test beams of electrons and pions of specified energies. Primarily the test beam was utilized to assess the performance, in particular, the energy resolution of the ALICE EMCal. For jet energy reconstruction simulations indicate the energy resolution required to be $15\%/\sqrt{E} \oplus 2\%$. The measured energy resolution is consistent with design requirements and electron hadron separation with rejection factors of ~ 100 can be attained up to ~ 100 GeV/c via E/p measurements.

Not including the analysis presented in this thesis, where the EMCal trigger was critical for providing the necessary kinematic reach with limited statistics, the EMCal has been an integral part of other analyses. The measurement of electrons from semi-leptonic heavy-flavor decays in $\sqrt{s} = 7$ TeV *pp* collisions utilized TPC and EMCal electron identification in concert [23]. The first jet cross-sections have already been published [261] in $\sqrt{s} = 2.76$ TeV *pp* collisions and similar measurements have recently been made in $\sqrt{s}$ =2.76 TeV Pb-Pb collisions that enable preliminary jet R_{AA} measurements.

2.2.7 The Muon Spectrometer

The muon spectrometer is dedicated to the measurements of heavy-quark vector meson resonances ($J/\psi, \psi', \Upsilon, \Upsilon', \Upsilon''$) via the $\mu^+\mu^-$ decay channels, and the measurement of open heavy-flavor decays (open charm/beauty hadrons being those with non-zero net total charm/beauty) via semi-leptonic decays primarily through $\mu^+\mu^-$ but also through the μ, e decay channel in combination with the central barrel detectors. The measurement of direct J/ψ requires acceptance of low p_T tracks, as high p_T production has a large fraction of J/ψ from b decays [264]. The flux of hadrons is so great at LHC energies that statistically significant measurements of muons can only be made at momenta greater than 4 GeV/c due to the large amount of material required for filtering. Hence the measurement of low p_T charm production must take place at small angles to the beam pipe. Thus the muon spectrometer is built outside the central barrel at large rapidities covering the range $-4 \leq \eta \leq -2.5$. The total coverage is completed with $\phi = 2 - 9^\circ$ which is as large as possible (to maximize the precision of statistically limited measurements of the Υ family resonances) within budget constraints. The detector consists of a 4.13 m front absorber for the absorption of hadrons and photons from the interaction vertex, a small angle absorber that surrounds the beam pipe to reduce background, a pair of trigger chambers located behind a 1.2 m lead wall which provides information for triggering on the presence of muons, an array of 10 tracking chambers and a large 0.7 T dipole magnet. A 100μm position resolution is required to achieve the required invariant mass resolution to resolve the $J/\psi, \psi', \Upsilon, \Upsilon'$ and Υ'' peaks. This defines the dipole magnet strength and places constraints on the tracking system and the tolerable scattering. The tracking chambers comprise MWPC chambers with segmented cathode planes, and in addition to this position resolution requirement have to be able to cope with large track densities of the order of 5×10^{-2} cm^{-2}. The tracking system has been shown to exceed the required position resolution in the 0.7 T field, and has a momentum resolution of $\sim 3\%$ at 50 GeV/c.

2.2.8 ACORDE

The ALICE cosmic ray detector (ACORDE) lies outside of the L3 magnet and serves two purposes. The first is to act as a trigger for cosmic ray events which were recorded during 2008-2009. The cosmic ray data taking served an important part of calibration and commissioning for many detector subsystems. Moreover, following the example of the L3 experiment and DELPHI, ALICE has embarked on a cosmic ray physics program. The underground location of ALICE and other high-energy particle/nuclear physics experiments allows the measurement of the energy spectrum and mass composition of cosmic rays well beyond that which is possible at the surface. The ALICE detector can measure the energies of cosmic ray muons in the energy range 10^{15} eV-10^{17} eV, right around the region of the *knee*. The cosmic ray energy spectrum exhibits a power law dependence on energy, and at around 10^{16} eV the spectrum steepens which is known as the knee. The origin of this abrupt change in behavior is not yet understood [48], and thus measurements of cosmic rays in this region may provide insight. During down-time in 2011 and 2012 more cosmic ray data was collected to this end. Moreover, a specific cosmic ray trigger has been developed to enable cosmic ray data taking during proton-proton runs. The detector design is based on a similar design by the DELPHI experiment and consists of some 60 paddle scintillator pairs arranged at the top of detector ($r = 8.5$m) covering $-60° < \phi < 60°$ and $-1.3 < \eta < 1.3$ ($\sim$10% of the detector surface). Each scintillator module has a 190×19.5 cm^2 active area and consists of two scintillator counters back to back. Scintillation light is collected and amplified with photomultiplier tubes. A coincidence signal within a 40 ns window then provides a trigger signal for that module. The cosmic ray trigger to be implemented during proton-proton collisions requires a coincident trigger in at least 4 ACORDE modules. During down-time in 2011/2012 cosmic data was collected, and the atmospheric muon energy and angular distributions were measured. Similar measurements were taken in 2009 and the ratio of μ^+/μ^- formed the basis of a 2009 ALICE thesis.

2.2.9 Forward and Trigger Detectors

2.2.9.1 Zero Degree Calorimeter (ZDC)

In Pb-Pb collisions many measurements exhibit a dependence on the collision geometry, as quantified by the centrality, knowledge of which is crucial. The zero degree calorimeters (ZDC) offer the possibility of measuring the centrality via a measurement of the energy carried in the forward direction by non-interacting spectator nucleons. When the incident Lorentz contracted nuclei collide, the number of interactions will obviously scale with the size of the ‘overlap’ region (or equivalently the impact parameter) of the two nuclei. Those that do not interact will continue approximately in the forward direction. The LHC bending magnets will cause spectator protons to be bent away from the beam pipe, whereas spectator neutrons will continue without such deflection. This necessitated the use of separate neutron calorimeters (ZN) and proton calorimeters (ZP). ZN/ZP are located at 116m from the center of the detector; at this point the 8cm separation between the beam pipes at this point allows for the installation of the ZN between the beam pipes. The ZP is placed outside the beam pipe to allow for the magnetic deflection. Even at this separation the spatial constraints are still severe, and necessitate the use of a very dense material for the neutron calorimeter. The choice was a dense W-alloy ‘spaghetti’ type calorimeter. Such calorimeters utilize Cerenkov light emitted via interactions with the passive absorber. A similar design was utilized for the ZP, however the transverse and longitudinal size of the spectator protons is larger than that of the spectator neutrons primarily due to the defocussing effects of the LHC quadrupoles. Moreover, the spatial constraints are much less severe, and hence the proton calorimeter is significantly larger and constructed from a less dense brass.

With solely the ZN/ZP configuration there is still some ambiguity in determining the centrality. For very peripheral collisions, the spectator remnants may not be neutrons and protons, but nuclei with atomic numbers very close to that of lead. In this case, the mass to charge ratio is such that the remnants will not leave the beam pipe. Hence, as in the case of very central collisions, the observed energy in the calorimeters will be very low. To distinguish these cases, the ZDC system is completed with electromagnetic calorimeters (ZEM) at 45° to the beam-line (the Cerenkov radiation production is maximal at 45°). These calorimeters measure the energy of particles emitted at forward rapidity (primarily photons from π^0 decays), a quantity that increases monotonically with collision centrality and thus enables the two cases to be distinguished.

2.2.9.2 Photon Multiplicity Detector (PMD)

The photon multiplicity detector (PMD) is a pre-shower detector located at $z = -3.64$ m designed to measure the photon multiplicity and spatial distribution in the pseudorapidity range $2.3 \leq \eta \leq 3.7$ over the full azimuth. The PMD also aims to provide determination of the reaction plane for measurements of flow and azimuthal anisotropy. In combination with other detectors, the additional pseudorapidity coverage is useful for measurements of global variables and fluctuations in those global variables. Finally, measurements of the ratio N_γ/N_{ch} in combination with the V0 detector (which provides charged particle measurements over a similar phase space) enable a study of chiral-symmetry restoration.

2.2.9.3 Forward Multiplicity Detector (FMD)

The forward multiplicity detector consists of 5 detector rings (FMD1,FMD2i,FMD2o,FMD3i,FMD3o) at $z = -62.8$ cm, -75.2 cm, 75.2 cm, 83.4 cm and 320 cm. The inner rings (FMD2i, FMD3i, FMD1) lie between $r = 4.2 - 17.2$cm and the outer rings (FMD2o, FMD3o) lie between $r = 15.4 - 28.4$cm, all covering full azimuth. Each ring is segmented azimuthally into 10 (20) segments for the inner (outer) rings, and annularly into 512 (256) strips for the inner (outer) rings. The individual detector elements (some 51,200) are silicon strip detectors of two types (for inner and outer rings) and segmentation was designed such that the expected multiplicity is $\sim 2 - 3$ particle per strip. In total, the FMD provides complete azimuthal coverage and pseudorapidity coverage in the range

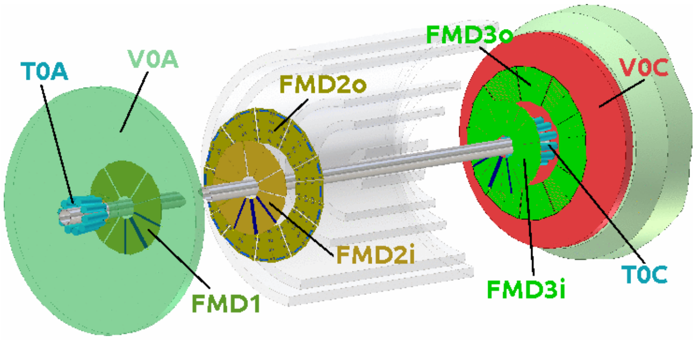

Figure 2.2.16: Illustration of positioning of the V0, T0 and FMD detectors in ALICE [38]

$-3.4 < \eta < -1.7$ and $1.7 < \eta < 5.0$. The arrangement and relative positioning of the forward detectors (except PMD, ZMC) including the 5 FMD rings is shown in Figure 2.2.16.

The primary aim of the FMD is to provide enhanced pseudorapidity coverage for multiplicity measurements to study event-by-event fluctuations in global variables. The overlapping coverage with the SPD and V0 detector provide cross checks for these measurements. Furthermore, it can provide an independent measure of the event plane and v_2. The slow response time ($< 1.2\mu$s) does not allow for online triggering which is provided by the T0 and V0 detectors.

2.2.9.4 V0 detector

Like the FMD, the V0 detector comprises two rings of scintillators on either side of the interaction point, labeled V0A and V0C according to which side of the detector they lie. V0A lies at $z = +340$ cm and V0C is located at $z = -90$ cm in front of the muon spectrometer. As with all the forward detectors, azimuthally there is complete coverage. In pseudorapidity, V0A covers $2.8 < \eta < 5.1$ and V0C covers $-3.7 < \eta < -1.7$. Each detector consists of 4 annular rings divided azimuthally into 8 sectors for the inner two rings and 16 sectors for the outer two rings. In total 48 scintillator counters cover the 100 cm (88 cm) V0A (V0C) detector rings. Each channel provides a large dynamic range to deal with the potential occupancies from 1 to ~ 1000 particles. The 1 ns timing resolution also allows for efficiency rejection of beam-gas events by correlating hits on either side of the detector. It is expected that due to high radiation doses some of the inner detector elements may need to be replaced.

The V0 detector provides the primary minimum bias trigger and is thus critical for almost all analyses. The minimum bias data set collected for this analysis utilizes an OR signal in either of the V0 detectors or the SPD. By measuring the V0 trigger rate as a function of beam separation (Van de Meer scan), a normalization cross-section has been measured which allows a conversion from yields to cross-sections in many analyses [265]. Such measurements are also important for the online monitoring of the luminosity. The capability to trigger on either or both of the V0 detectors is also useful to reject beam-gas background, in addition to the analysis of diffractive cross-sections [266]. In addition, the signal recorded by the V0 detector provides an indication of centrality and thus it also provides three classes of triggers based on centrality. Although not the primary aim of the detector, V0 can provide a measurement of the charged particle multiplicity in the forward direction, providing redundancy and cross-checks for measurements made the FMD.

2.2.9.5 T0 detector

Like the V0 and the FMD, the T0 consists of two detectors located on either side of the interaction point; T0A at $z = 375$ cm and T0C $z = -72.7$ cm. 12 Cerenkov counters constitute these detectors arranged in a ring alongside the V0 detectors. Although they do provide full azimuthal coverage, the pseudorapidity coverage is reduced with respect to the other forward detectors. Specifically, the T0A detector provides measurements in the range $4.61 < \eta < 4.92$ and the T0C provides measurements in the range $-3.28 < \eta < -2.97$. Each detector element is constructed from a 3 cm long quartz radiator designed to induce the production of Cerenkov radiation as incident particles exceed the phase velocity of light. The Cerenkov radiation is collected with photomultiplier tubes. The high intrinsic speed of the Cerenkov detection mechanism, in combination with the high photon yield quartz crystal, combine to provide the necessary 50 ns timing resolution. Indeed, the T0 functions primarily to provide timing signals. Prior to the L0 trigger it provides a wake-up signal to the TRD. It provides a starting time, with respect to the LHC clock, of high resolution for the TOF detector. Although not the primary trigger detector (the V0 fulfills MB trigger requirements), the T0 provides redundancy for the V0 detector in its triggering capabilities. Not only can it provide a minimum bias trigger, but it can also perform crude indications of the multiplicity (in 3 classes) to provide multiplicity triggers much like the V0 detector. Unlike the V0 however, the T0 can provide an approximate vertex position (the *T0 vertex* with a precision of ± 1.5cm) which allows for rejection of beam-gas events in triggering.

2.2.10 The ALICE Trigger

The trigger is an essential element of any modern nuclear or particle physics experiment. Collision rates can be so high that latency of the detectors means that in any event only a subset of the collisions can possibly be recorded. Moreover, even in the ideal case where all events could theoretically be recorded, the data rate is often too high for current technologies to deal with. In ALICE, these constraints are more severe than the other experiments at the LHC. The choice of a TPC as the primary tracking detector means that in the high multiplicity environment of Pb-Pb collisions the TPC alone could provide 75 MB of data per event, and the total output rate can be as high as 25 GBs^{-1}. These considerations lead to the introduction of a trigger to reduce the output data rate, and to select from the multitude of uninteresting events those that show signs of having promising signatures. Typically the trigger rejects $\sim 10^4 - 10^5$ events for each accepted event in modern particle physics experiments. In general purpose experiments with a gamut of different detectors, the variable latencies between detector subsystems often necessitate the implementation of a multi-tier trigger system with each level typically labeled L0,L1,...,LN (there is some ambiguity in whether the triggering starts from L0 or L1). L0 will provide the fastest trigger information and will usually involve simple triggers (such as a boolean indicating hit or no hit in a detector), and LN will provide the slowest trigger but may allow for more complex conditions (such as the existence of displaced vertices).

The ALICE triggering system can be divided into two distinct components: a hardware component headed by the central trigger processor (CTP), and a software component called the high level trigger (HLT) system. The CTP, given a definable configuration, determines what detectors constitute a trigger and what detectors should be read out. The HLT operates at the point where a trigger has been fired, has passed all vetoes (for instance pile-up), and the CTP has determined the data should be processed. The HLT functions to reduce the readout rate by selecting the most interesting subset of data using sophisticated triggers. Raw data are provided to the $\sim$ 1000 processors in the HLT processor farm where the data are *reconstructed*. Reconstruction involves the assembly of raw signals into entities closely related to particle and event properties: TPC tracks, event vertices and calorimeter clusters for example. HLT then reduces the output rate in 3 ways: (i) selecting interesting events with a rejection factor of $\sim$ 10 (ii) filtering events by for instance rejecting low momentum tracks, and removing tracks from pile-up events (iii) compression of the selected data.

The ALICE CTP utilizes a three tier trigger system (L0, L1, L2) defined by timing capabilities of each sub-detector. To reduce dead-time (time where a detector is unable to record new information, for instance when processing the current event), particle detectors often utilize *pipelining*. In a pipelined readout, data are continually read for some multiple of the ‘fundamental cycle’ (in the case of a collider the bunch crossing is an appropriate cycle) and this finite sized buffer is continually refreshed. When the detector receives a trigger signal, the buffered data are then recorded or passed

Table 2.2.2: The minimum bias trigger class definitions

Trigger Class	Trigger Condition
`MB1`	`V0_OR` or `SPD_OR` and not `V0_BG`
`MB2`	`V0_OR` and `SPD_OR` and not `V0_BG`
`MB3`	`V0_AND` and `SPD_OR` and not `V0_BG`

to higher level buffers for further triggering. In ALICE, many of the detectors use 'stack and hold' readouts which are not pipelined and require a *strobe* signal to initiate processing. This strobe is provided by the L0 trigger at 1.2 μs. However, not all detectors are able to provide triggering within this stringent time interval and thus a L1 trigger at 6.5 μs provides a further trigger for other detectors. Finally a third trigger, L3, is provided at the end of the TPC drift time (88 μs) and primarily functions to allow for the necessary 'past-future pile-up protection'. At nominal luminosity in *pp* collisions as many as 40 events could occur during the drift time of the TPC, and even at the lower running luminosities of Pb-Pb collisions pileup is inevitable. The past-future pile-up detection deals with this possibility, and dedicated electronics decide whether or not to veto the event. The exact conditions for rejecting an event based on undesirable pile-up depends on the detector in question and the collision mode. In Pb-Pb collisions two central collisions are not reconstructible in the TPC due to the large track multiplicities. In this case, if more than one event is recored within a window of $\pm 88\mu$s of the current event the event is rejected. However, in the lower density environment of *pp* collisions, more pile-up is tolerable and looser constraints are placed. As mentioned previously, there is also a very fast ($\leq$ 200 ns) 'pretrigger' provided by the T0 and V0 detectors which serves to 'wake-up' the TRD electronics and provide a starting time (T0) for the TOF detector.

The division of the trigger into multiple levels allows the accommodation of the vastly different latencies exhibited by each detector subsystem. Another aspect of the trigger system that provides the flexibility to deal with these differing latencies is the dynamic definition of triggering signals and readout detectors. The CTP receives in total 24 trigger inputs (inputs are well defined pulses that are synchronized with the LHC clock) from different triggering detectors. These are logically combined in different trigger *classes*. The set of detectors that are utilized for readout defines a trigger *cluster*. Multiple clusters can be defined simultaneously and they may be non-overlapping, in general they will have common components. This allows for the prioritization of certain rare trigger signals and allows for the exclusion of a single detector to maximize statistics. For instance, in cases where all of the muon detectors successfully record data with no pile-up but the TPC signals excessive pileup, the cluster corresponding to the muon detector can be read out without using the TPC. In total 50 programmable trigger input classes have been defined. For my data set the relevant trigger classes are the minimum-bias classes and the EMCal high trigger classes. There are 3 minimum bias classes that utilize the SPD and V0 as triggering detectors that represent all logical combinations of trigger inputs. Table 2.2.2 lists the minimum bias trigger classes and conditions.

`V0_OR` indicates a signal in either V0A or V0B, `V0_AND` indicates a signal in both V0A and V0B, `V0_BG` indicates the V0 has triggered as a beam gas event and `SPD_OR` indicates a hit in at least one pixel in the SPD. Beam gas events are triggered based on an asymmetric timed signals (with respect to the LHC clock) in the V0A/V0B detectors.

3

Data Set and Event Selection

3.1 Description of Data and Run Conditions

In 2011 the LHC operated from February 21^{st} to December 7^{th}, during which time some 5.63 fb^{-1} of $\sqrt{s} = 7$ TeV pp integrated luminosity were delivered to ATLAS and CMS, and 4.88 pb^{-1} were delivered to ALICE (see Figure 3.1.1). In addition to the main $\sqrt{s} = 7$ TeV pp program, various other running conditions were employed including a heavy-ion ($\sqrt{s_{NN}} = 2.76$ TeV Pb-Pb) run at the end of the year and an intermediate energy pp run ($\sqrt{s} = 2.76$ TeV) at the beginning of the year. The

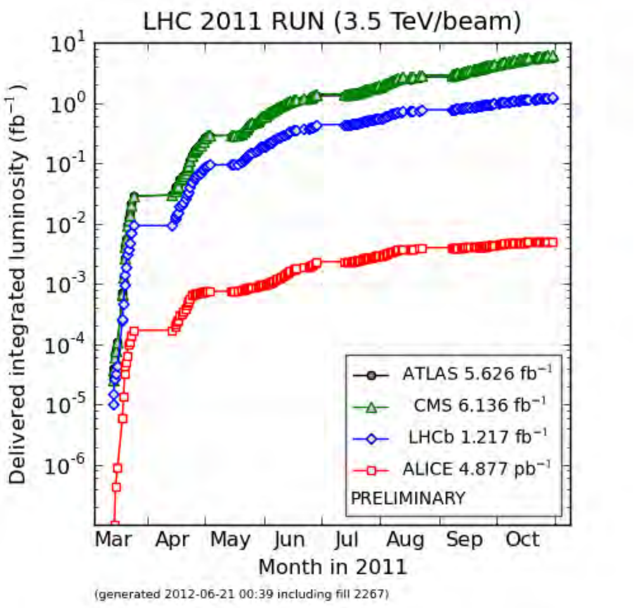

(generated 2012-06-21 00:39 including fill 2267)

Figure 3.1.1: LHC delivered luminosity at the four interaction points during 2011

latter formed the basis of the analysis undertaken for this thesis. The *pp* run ($\sqrt{s} = 2.76$ TeV) was specifically requested by ALICE as it forms a crucial reference for comparison to $\sqrt{s_{NN}} = 2.76$ TeV Pb-Pb collisions. The data were recorded over three days ($\approx$ 90 h) just before the first technical stop of 2011 (data being recorded between 03/25/2011-03/27/2011). The beam angle at all interaction points was zero with $\beta^* = 10$ m and filling schemes employing (72/80) bunches with 525 ns spacing were utilized. Two of the fills at this energy were used to undertake a Van-de-Meer scan [265] (the results from the Van-de-Meer scan were used in this thesis to convert the yield to a cross-section), while fills 1650 and 1651 provided the collisions used in this analysis. During each fill any of the experiments may or may not be recording data. Lapses in data taking may be due to problems with individual detectors or simply to allow data taking to take place with different trigger classes or different trigger clusters. In ALICE, each continuous period of recording data is called a *run*, and although detector configurations may change slightly within a run, large alterations typically only take place between runs. The state of the individual detectors (gain, calibration constants etc) are thus mostly fixed within a given run and define a *run configuration*. The run configuration, along with a variety of other relevant information, is saved into a database known as the OCDB (off-line condition database). The data recorded by ALICE during fills 1650 and 1651 correspond to the following run numbers: 146860, 146858, 146856, 146824, 146817, 146807, 146806, 146805, 146804, 146803, 146802, 146801, 146748, 146747 and 146746. Each run number obviously comprises a varying number of events. For each triggered event, raw data is recorded at differing levels of abstraction. For example, a detector may store a raw analogue signal corresponding to energy deposition, or it may just record a single bit indicating a hit. The process of converting raw signals from the various sub-detectors to more physically relevant quantities (energy, momenta, positions etc) occurs during *event reconstruction*. In addition to detector level reconstruction, other important event characteristics are determined at this stage such as the position of the interaction point (or *primary vertex*). Although some on-line adjustment of the detector configuration does take place (adjusting gains in the TPC for instance), often off-line analysis allows for improved calibration and adjustment. As the calibration of the detectors is improved, multiple reconstructions on the same data set are undertaken; it may take a few iterations before the data passes all quality assurance. The data set used in this analysis (corresponding to the runs above) is 'lhc11a/pass2', the 'pass2' indicating that it was the second reconstruction of raw data.

The data set comprised of two trigger classes: a minimum bias (MB) trigger and an EMCal trigger. The 'MB trigger' corresponded to the trigger class `MB1`, having the requirement of a signal in either of the V0 detectors (V0A or V0C) or a signal in the SPD in coincidence with the presence of a bunch crossing. A peculiarity of this data set was that approximately half of the MB data set was recorded without the presence of the SDD. Due to the short time-span available for this data set, it was decided that to increase statistics the SDD would be excluded for recording some of the data. Although the TPC has a very large drift time, distinct events can be well separated in *pp* collisions at these energies by looking at the position of the reconstructed primary vertex, and thus the SDD provides the bottle-neck in recording rates. Since the analysis focused on the EMCal triggered data set, and since the SDD was included in that sample, half of the MB data set was rejected for consistency. The unique aspect of this analysis is the application of the EMCal triggered data set. The EMCal trigger requires the presence of a 4×4 trigger patch with an energy deposition greater than a 3 GeV trigger threshold in coincidence with the same MB trigger used for the MB data set (see Chapter 6 for more details about the EMCal trigger). After event selection, the MB data set corresponded to an integrated luminosity of 0.5 nb^{-1}and the EMCal trigger data set corresponded to 13.1 nb^{-1}.

In addition to the MB and EMCal trigger data collected in *pp* collisions, simulations were used to obtain the tracking efficiency and p_T unfolding corrections in addition to providing a cross-check of the data derived EMCal trigger correction. In ALICE, simulations are generated with the event generator PYTHIA [165]; the detector response and particle transport are simulated in GEANT 3 [267], GEANT 4 [268] and PHOJET [269]; in particular, the simulations generated in this analysis utilized GEANT 3 v1-11-23 and PYTHIA 6.4.21. To enhance the population of electrons in the simulation, the events generated did not correspond to minimum bias collisions, but were heavy-flavor 'enhanced'. Specifically, the events were constrained such that in 20% of the events a $c\bar{c}$ pair (one within $|\eta| < 1.5$) is produced with D mesons decaying hadronically, in 20% of the events a $b\bar{b}$ pair (one within $|\eta| < 1.5$) is produced with B mesons decaying hadronically, in 20% of the events a $c\bar{c}$ pair is produced without forced decays but with at least one electron within $|\eta| < 1.2$, in 20% of the events a $b\bar{b}$ pair is produced without forced decays but with at least one electron within $|\eta| < 1.2$, in 10% of the events a J/ψ is produced within $|\eta| < 1.0$ subsequently decaying via the channel J/$\psi \rightarrow e^+e^-$, and in 10% of the events a B hadron is produced within $|\eta| < 2.0$ decaying via the decay chain B$\rightarrow$J/$\psi \rightarrow e^+e^-$. In addition, pions with a flat momentum spectrum are superimposed onto these underlying hard scattering events. The configuration of all detector elements was identical to that during recording of the lhc11a/pass2 data set (being loaded from the OCDB); thus the simulation is said to be an *anchor run* for the lhc11a/pass2 data set.

Summary of data sets used, and terminology used hence for identification:

- ‘MB data set’: lhc11a/pass2 (with SDD), MB trigger (analysis utilizing AliROOT trunk rev. 60321 and ROOT v5-34-02). 33,269,288 events before event selection.
- ‘EMCal trigger data set’: lhc11a/pass2 (with SDD), with EMCal trigger (analysis utilizing AliROOT trunk rev. 60321 and ROOT v5-34-02). 699,084 events before event selection.
- ‘Simulation’: lhc11b10b, heavy-flavor enhanced $\sqrt{s} = 2.76$ TeV pp collisions anchor-run for lhc11a/pass2, generated with GEANT 4 v1-11-23 and PYTHIA 6.4.21 (analysis utilizing AliROOT trunk rev. 60321 and ROOT v5-34-02). 1,844,783 events before event selection.
- lhc11b10a: a MB $\sqrt{s} = 2.76$ TeV pp collisions anchor-run for lhc11a/pass2, generated with GEANT 4 v1-11-23 and PYTHIA 6.4.21 (analysis utilizing AliROOT trunk rev. 60321 and ROOT v5-34-02). 2,110,437 events before event selection.

3.2 Event Selection

Not all events are used for event selection; various event selection criteria are implemented to improve data quality. In this analysis, event selection criteria fell broadly into 4 categories: physics selection, vertex quality criteria, pile-up rejection, and EMCal trigger bit validation.

The standardized *physics selection* classes serve to reject trivially uninteresting events such as LED events used by the EMCal for calibration purposes. They further serve to reject beam-gas interactions in one of two ways: (i) using timing information from the V0 and (ii) comparing the number of reconstructed tracklets to the number of hits in the SPD (see Figure 3.2.3 and following discussion for a description of tracklets). Both techniques exploit some characteristic of beam-gas events. The former utilizes the fact that beam-gas events are typically asymmetric due to momentum conservation. Such events will therefore only trigger the V0A/V0C on both sides of the detector if the beam-gas interaction occurs before the beam reaches either V0A or V0C. Hence, beam-gas events can be rejected by requiring that the signals observed in V0A/V0C occur after the collision time (see Figure 3.2.1). The latter criteria is based on the fact that in beam gas events it is possible to observe a large number of ITS clusters which nevertheless result in a small number of valid tracklets. In real events one expects a large number of ITS clusters to correspond to a large number of valid tracklets. Examining the correlation between clusters and tracklets enables the rejection of beam gas events on this basis. In this analysis, beam-gas events were not rejected using this method. However, as can be seen in Figure 3.2.2, the rejection of beam gas based on V0 alone removes the majority of events with anomalous tracklet-cluster distributions.

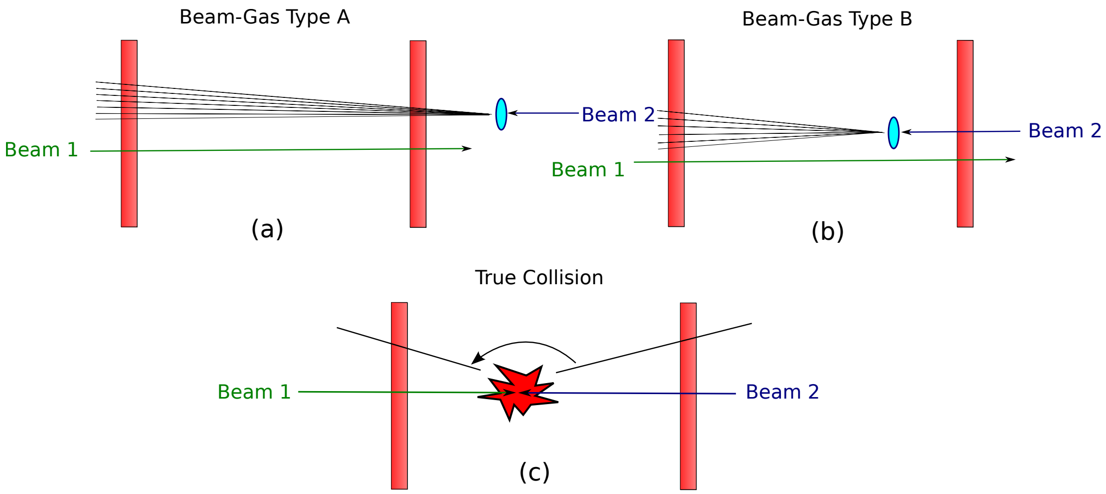

Figure 3.2.1: Illustration of the rejection of beam gas using V0 timing information. In case (b) a beam gas event occurs within the detector which results in a signal in only one of the V0 detectors; these are rejected by requiring a signal in both V0 detectors. In beam-beam collisions, and in beam-gas events similar in nature to case (a), a signal is seen in both V0 detectors. Timing information can be used to reject beam-gas events like those in case (a) by demanding that the collision time occurs before signals are recorded in the V0 detectors.

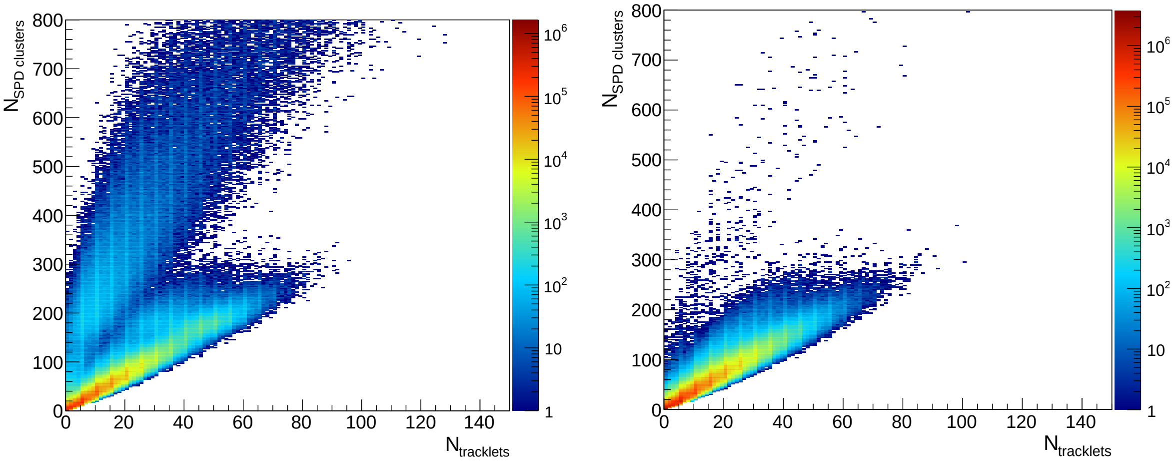

Figure 3.2.2: Correlation of the number of SPD clusters and the number of generated tracklets without (left) and with (right) physics selection. Only V0 timing information is used to remove beam-gas background

Three of the event selection criteria are based upon the nature and quality of the reconstructed primary vertex. Vertex reconstruction in ALICE can be performed using the SPD alone, the TPC alone, or using the ITS and TPC. A priori one would expect that the resolution would be greatest using the latter method, and indeed that is the case. However, the reconstruction of a vertex is a step-by-step procedure where in calculating the vertex position using the ITS and TPC one first reconstructs a vertex using the SPD standalone and hence reconstructed vertices using both methods are always potentially available. Moreover, in some cases vertex reconstruction may fail using both detectors and succeed with only a single detector and in that case the vertex position is derived from the lone detector.

In condensed form, the procedure for reconstruction is as follows (see [35, 270] for more details):

1. First, candidate *tracklets* are formed by assuming a vertex position of (0,0,0) in the ALICE coordinate system, and requiring the extrapolation of hits in the inner SPD layer to the outer SPD layer to be within some small azimuthal window of a hit in the outer SPD layer (see Figure 3.2.3). Correlations between all tracklets are used to identify a preliminary vertex position (the *SPD-only vertex*).

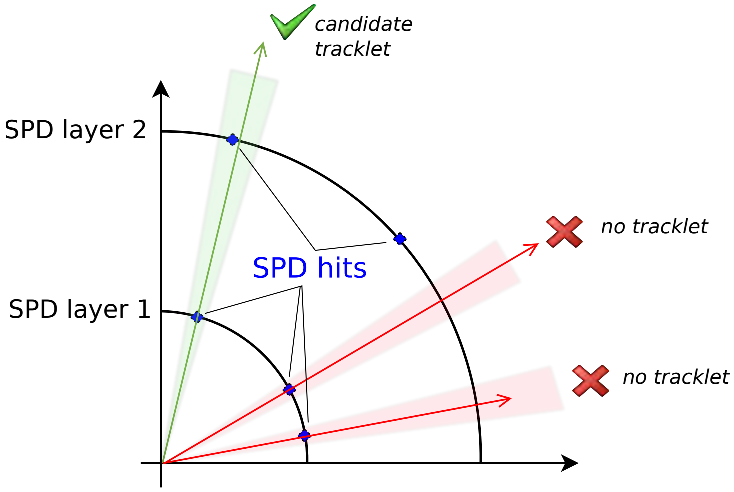

Figure 3.2.3: Illustration of the construction of tracklets in the SPD

2. Tracks are reconstructed in the TPC inward with a Kalman filtering algorithm [35, 39] towards the primary vertex reconstructed in step 1 (so called *TPC-only tracks*). Correlations among these tracks form the basis of the TPC only vertex identification.

3. The TPC-only tracks are combined with ITS data to provide fully reconstructed tracks in two passes. In the first pass the TPC-only tracks are extrapolated inwards towards the ITS and

through to the interaction vertex reconstructed in step 1. This ensures maximal identification efficiency for tracks that originate from the primary vertex. In the second pass the TPC tracks are extrapolated through the ITS without the final constraint of the SPD-only vertex. The latter pass allows for the reconstruction of tracks from displaced vertices.

4. The tracking is improved by back-extrapolating the tracks from the SPD-only vertex to the ITS, TPC and to the TRD that provides further tracking information. Tracks can also be further extrapolated to other detectors for particle identification (for example to the EMCal). A final inward extrapolation from the TRD through the TPC and ITS to the SPD-only primary vertex is also performed.

5. At this stage, correlations between the full set of reconstructed tracks are used to generate the primary vertex position with the highest possible resolution.

In some instances more than one collision can take place within an event; these are known as *pileup* events. To reject pileup events, events where two interaction vertices are reconstructed with at least three tracklets as well as being greater than 8 mm apart are rejected. In the minimum bias data around 0.8% of the events are rejected as pile-up, whereas in the EMCal trigger data around 2.5% are rejected as pile-up (see Figure 3.2.4) The first vertex reconstruction quality cut is

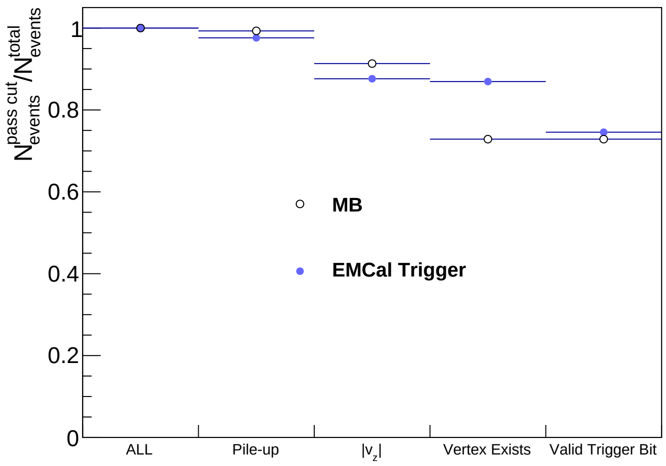

Figure 3.2.4: Cut efficiency after physics selection for various event quality criteria for MB and EMCal trigger data

to trivially demand that the number of contributors (tracklets,tracks) used in the determination of the primary vertex position is greater than 0. This has the effect of rejecting events where a vertex is only reconstructed with TPC-only tracks, thus ensuring only events with the highest possible quality of vertices are utilized.

Events are also rejected when the primary vertex position along the z-direction lies outside the window ($|z| < 10$ cm). This was so as to reduce edge effects at the limit of the central barrel acceptance. Figure 3.2.5 shows the appropriately normalized vertex position along the z-axis for the MB data set, the EMCal triggered data set and the simulation used in this analysis. As the EMCal trigger requires a hit in the EMCal, which lies within $|\eta| < 0.7$, one sees a very slight narrowing of the distribution with respect to the MB data. Despite having a vertex distribution constrained such that the width corresponds to what is observed in data (being an anchor run), the distribution is somewhat narrower in the simulation. The simulation is used only for the tracking efficiency and the trigger efficiency of electrons, and it is not expected that this small difference in the v_z distribution would affect these quantities. Figures 3.2.6 and 3.2.7 show the vertex position in (x, y) coordinates for the MB and the EMCal triggered data respectively. Superficially, the EMCal trigger data looks significantly narrower in these coordinates. However, this is due to the vast difference in the number of events, and when appropriately normalized the similarity between the MB and EMCal triggered distributions is much like that for v_z.

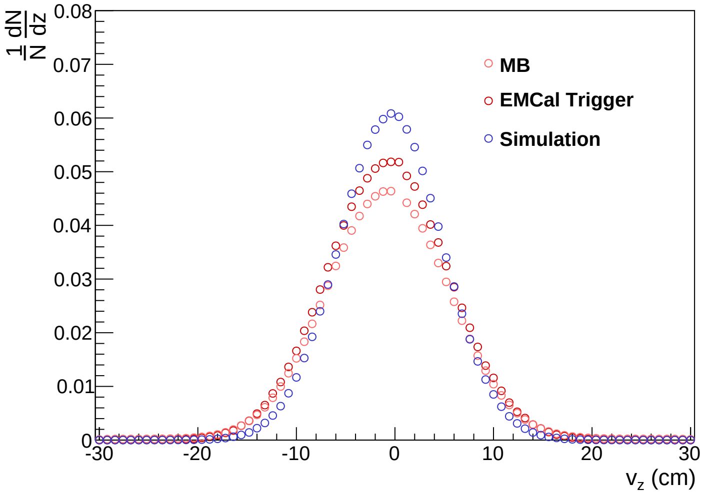

Figure 3.2.5: z coordinate of the reconstructed vertex for EMCal Trigger data, MB data and simulation (lhc11b10b)

In addition to the primary vertex quality criteria, event level cuts are also placed based on information from the EMCal. Although the physics selection task explicitly rejects LED events used for gain calibration, in some instances the LED's can fire unintentionally during physics runs. These events are rejected by placing a cut on the number of the active towers with an energy above 100 MeV in a given super-module ($N^{\mathrm{SM}\ i}_{active}$). Specifically:

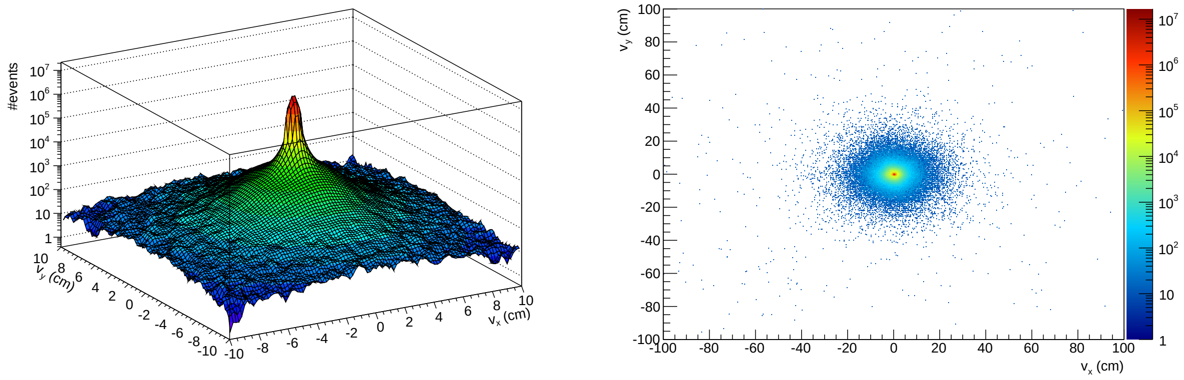

Figure 3.2.6: (x, y) coordinates of the reconstructed vertex for the MB data

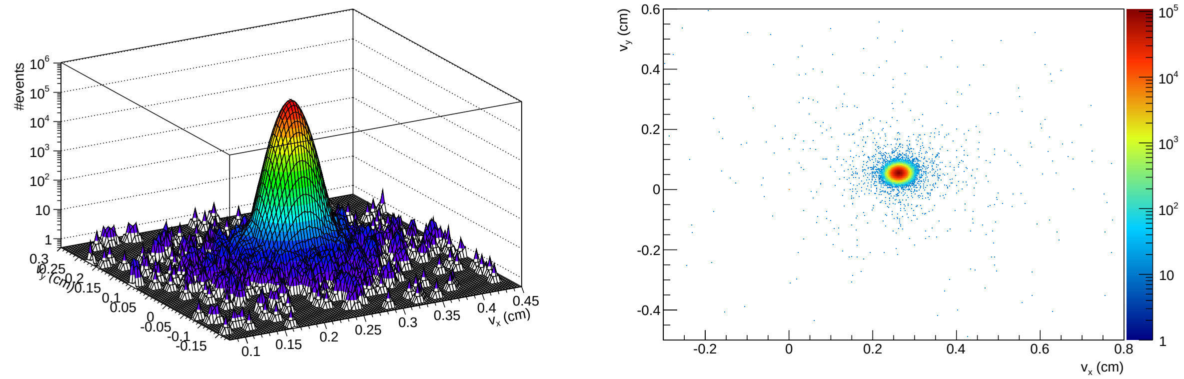

Figure 3.2.7: (x, y) coordinates of the reconstructed vertex for the EMCal trigger data

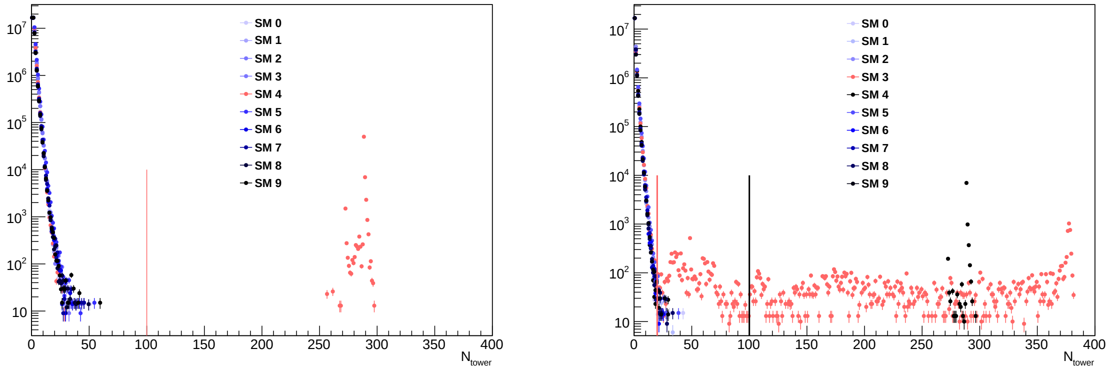

Figure 3.2.8: Number of towers with an energy above 100 MeV in each super module for the first 13 runs (left) and the last 3 runs (right) in MB data. The lines indicate the LED event rejection criteria.

- For the first 13 runs only SM4 is affected by faulty LED's and events are rejected where $N^{\mathrm{SM}\ 4}_{active} \geq 100$.
- For the last 3 runs both SM4 and SM3 are affected by faulty LED's and events are rejected where $N^{\mathrm{SM}\ 4}_{active} \geq 20$ or $N^{\mathrm{SM}\ 3}_{active} \geq 34$.

The basis for these cut choices is the distribution of towers with an energy greater than 100 MeV in each of the run classes (see Figure 3.2.8).

For the EMCal triggered data set events are also rejected where a cluster is not present that possesses a valid trigger bit. As described in Chapter 6, the EMCal trigger is based upon a trigger patch energy threshold of 3 GeV. If such a patch is found then all cells within the patch are assigned a positive trigger bit. Since the trigger patches do not necessarily have a one to one correspondence with the reconstructed clusters, it is possible that a triggered event will possess zero clusters with a valid trigger bit. Much more salient than this small effect is the impact of the *trigger mask*. Due to *hot towers* which fire triggers at rates far greater than other towers, a trigger mask is employed to prevent certain regions of the EMCal instigating a trigger. A trigger bit is deemed valid only if it does not lie within this trigger mask. The trigger mask employed for the EMCal triggered data set is shown in Figure 3.2.9.

The efficiency of each of the employed event cuts is illustrated in Figure 3.2.4 for MB and EMCal triggered data, and Table 3.2.1 presents the results numerically.

The basic event level characteristics of track multiplicity and EMCal cluster multiplicity are compared in Figures 3.10(b) and 3.10(a) for the two trigger classes. As one would expect, the EMCal trigger data sample is biased towards events with higher cluster multiplicity, and to a lesser

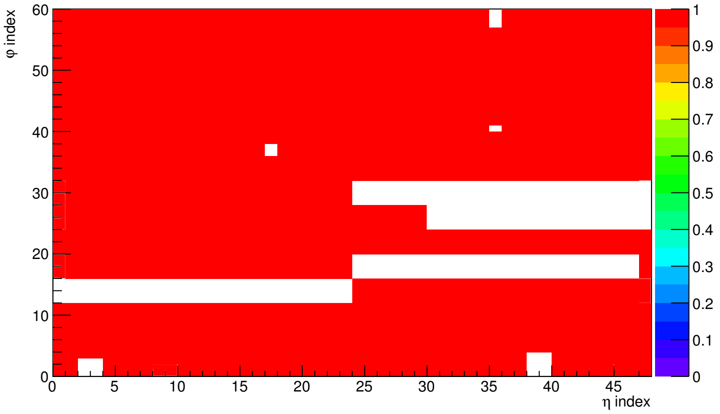

Figure 3.2.9: Trigger Mask employed during data taking for lhc11a/pass2 EMCal triggered events. The white regions are not triggered on, while the red regions are allowed to be triggered on

Event Cut	MB Efficiency (Total)	EMCal Triggered Efficiency (Total)
Pile Up Rejection	99.3% (99.3%)	97.6% (97.6%)
$\lvert v_z \rvert$ <10 cm	92.0% (91.3%)	89.8% (87.6%)
Vertex Existence	79.8% (72.8%)	99.2% (86.9%)
Valid Trigger Bit	100% (72.7%)	85.8% (74.5%)

Table 3.2.1: Event selection efficiency for various event cuts placed after physics selection

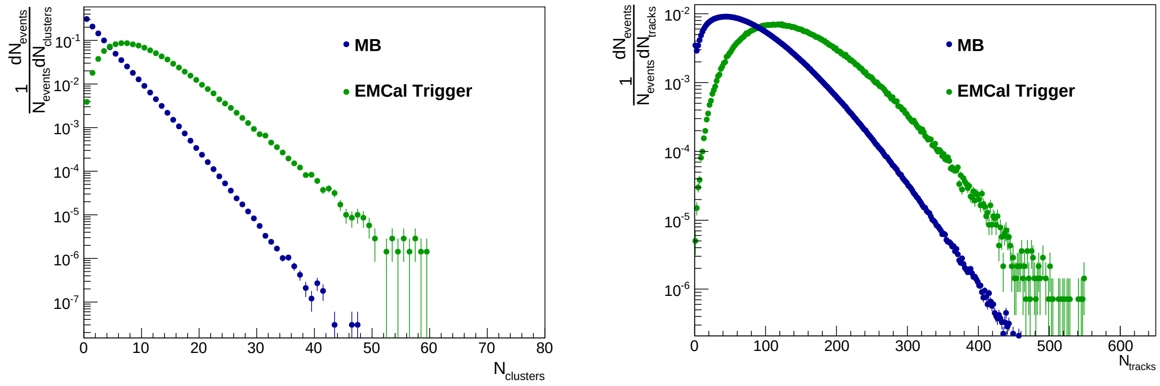

Figure 3.2.10: Cluster multiplicity (left) and track multiplicity (right) for MB and EMCal trigger data sets

extent higher track multiplicity.

3.3 Data Quality Assurance

In addition to event level cuts, other quality assurance cuts are placed to ensure a high quality data sample. In this analysis essentially two abstract objects are utilized: tracks and clusters. Details of the track cuts employed are to be found in Chapter 4. In this section the quality assurance criteria imposed on EMCal clusters is delineated.

The energy deposition of a typical particle spans a region greater than that occupied by a single tower, and thus the energy is deposited in several adjacent towers. Thus to make an estimate of the energy deposition of a single particle, some form of clusterization has to be employed to group adjacent active towers into clusters that likely correspond to a single incident particle's interaction. For the test beam data only two clusterizers were available: the 3×3 clusterizer and the 'v1' clusterizer. However, by the time data was taken in 2011 another clusterizer had been developed, the v2 clusterizer. The v2 clusterizer employs the same methodology as the v1 clusterizer: the highest energy tower is taken as a seed, any of the 4 nearest towers that are active are added to cluster, and the process is repeated for all clusters until no further towers can be added. However, to limit the size of the generated clusters and to cope with overlapping clusters, clusters are constrained to include only a single local energy maxima. In essence, the v2 clusterizer implements an 'unfolding' procedure to separate large clusters (presumably from overlapping energy deposition of multiple particles) into constituent clusters based on the energy distribution.

The v2 clusterization is performed off-line using the *EMCal tender* (r55343). The tender also performs a host of other EMCal calibration functions:

- Rejection of problematic towers: 97 *hot towers* were rejected on-line. In addition, off-line quality assurance identified a further 24 towers to be rejected (after these cuts are placed $\approx 99.79\%$ of towers are still left active). The rejection is based upon counting the number of times a particular tower records an energy above 0.1 GeV; the distribution is seen in Figure 3.3.1 and the rejection cut is indicated (those above 5σ are rejected)

- Perform the v2 clusterization, with a *zero suppression* cut: towers with $E < 0.05 GeV$ are not incorporated into the clusterization

- Based on in-situ survey measurements, the position of the EMCal super modules is updated, which updates the cluster position

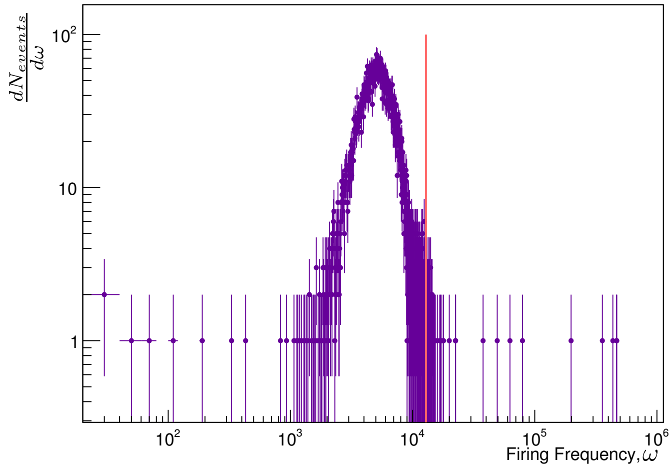

Figure 3.3.1: Firing frequency of the ≈12000 towers in the EMCal. The distribution is fitted with a Gaussian and those towers 5 standard deviations above the mean are deemed as hot towers and are removed from the analysis

- The cluster energy is recalibrated in two ways: (i) the non-linearity is corrected based on the test-beam measurements (ii) the energy is calibrated according to π^0 mass measurements

- A time recalibration is performed

- In order to associate a track with a cluster, all tracks are extrapolated (see Chapter 4) from the end of the TPC to the face of the EMCal. If the track lies within some window in (η, ϕ) space of a certain cluster, then the track-cluster pair are associated with one another and are said to be *matched*. During reconstruction a very loose condition $(|\Delta\phi| < 0.05, |\Delta\eta| < 0.025)$ is imposed. The EMCal tender tightens this track-matching window to $(|\Delta\phi| < 0.03, |\Delta\eta| < 0.015)$. The $\Delta\phi$ and $\Delta\eta$ distributions are illustrated in Figure 3.3.2.

The distribution of accepted EMCal clusters is shown in Figure 3.3.3 for the MB and EMCal data sets. In the MB and EMCal triggered data sets SM0 and SM5 had dead regions at $(\eta \approx 0.45, \phi \approx 1.65)$ and $(\eta \approx -0.6, \phi \approx 2.35)$ respectively. In addition, the region $(\eta > 0, 107° < \phi < 114°)$ in SM4 was excluded off-line as it was reading signals from wrong events. Also note the visible gaps between the super modules. For the EMCal triggered data set further regions were excluded corresponding to the trigger mask in Figure 3.2.9.

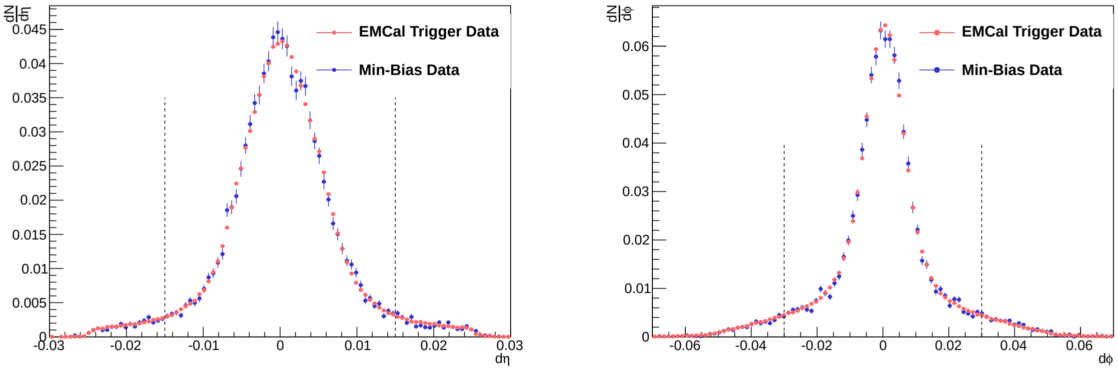

Figure 3.3.2: $d\eta$ (left) and $d\phi$ (right) distributions of matched track-cluster pairs in MB and EMCal trigger data. The dased lines represent the matching cuts placed in this data analysis

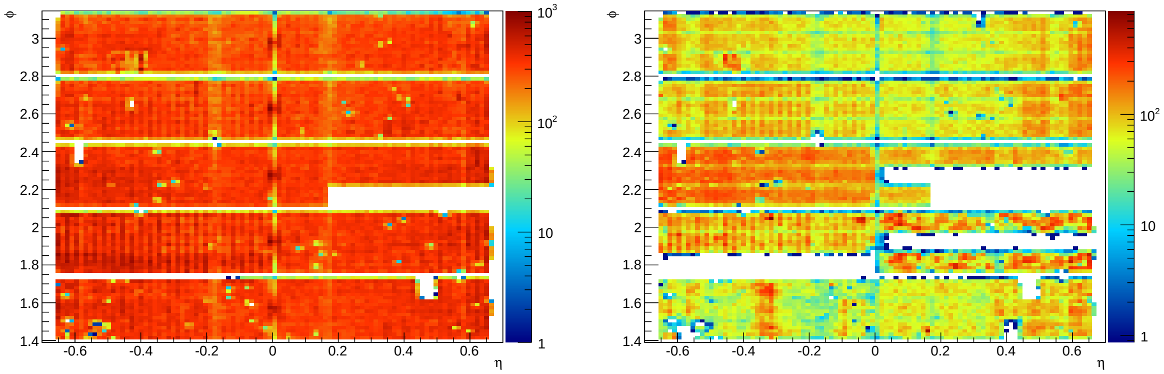

Figure 3.3.3: Cluster positions in MB (left) and EMCal trigger (right) data sets for clusters with an energy above 1 GeV.

3.4 Brief Overview of the Analysis Methodology

This thesis presents the cross section of heavy-flavor electrons in $\sqrt{s} = 2.76$TeV pp collisions. The analysis involves a number of steps an overview of which is given here to provide context for the following chapters (where further information about each step is provided). In order of presentation:

- Tracking Efficiency determination and correction: The TPC has a finite probability of reconstructing a track corresponding to a particle's path (at the very least is a geometric inefficiency along chamber boundaries), and a finite momentum resolution. Both of these effects need to be quantified and corrected for. Details are provided in Chapter 4

- Electron identification: Using the PID capabilities of the ITS, TPC and EMCal, electrons are identified from the sample of tracks and clusters using dE/dx and E/p measurements. Details appear in Chapter 5. The resulting raw electron spectrum provides the basis of the rest analysis

- Electron identification purity and efficiency: not all electrons will be identified using a given PID strategy, and some hadrons may be misidentified. The method for correcting for the efficiency and purity are detailed in Chapter 5

- EMCal trigger bias correction: Although the EMCal trigger significantly extends the kinematic reach of the measurement, it also introduces a bias that needs to be accounted for. The correction procedure is described in Chapter 6

- Non-heavy-flavor cocktail: The tracking, p_T resolution, electron PID efficiency, electron PID purity, and EMCal trigger bias corrections allow for the measurement of the inclusive electron cross-section. To proceed to measure the heavy-flavor electron cross-section, the non-heavy flavor component has to be subtracted. A cocktail is generated for that purpose using simulations appropriately weighted with real measurements. Chapter 7 provides a description of the method used

- Heavy-flavor electron cross-section: In Chapter 8, the heavy-flavor electron cross-section is obtained by subtracting the cocktail of Chapter 7

- The systematic error associated with each correction is also estimated, and the methodology for doing so is discussed in the context of the corresponding correction methodology

4

Tracking

4.1 Tracking in ALICE

The reconstruction of tracks in ALICE is inseparable from the determination of the primary vertex described in section 3.2, and as such has already been alluded to when describing vertex reconstruction. The only aspect not yet described is the algorithm for generating tracks from the information recorded by the TPC, ITS and TRD. The chosen methodology is widely known, and is an application of the Kalman Filter [271, 272, 273]. A *filter* is a method for taking a sequence of noisy data and making an estimate of some underlying unknown variable. The estimate should be an improvement on that which could have been obtained with any individual datum. The Kalman Filter is one example of a filter, and is in fact the optimal filter, in the sense of minimizing the mean square estimation error, when the random disturbances to the underlying variable and the measurement noise are both Gaussian distributed [273].

In the case of tracking in a TPC, the individual data elements comprise the position of, and the charge deposition in, the TPC clusters described in section 2.2.1.1. The first step in the tracking is thus the cluster finding, where adjacent active pads are combined to form clusters. If the cluster is too large (the r.m.s of the charge distribution is above some threshold) then a form of cluster unfolding is implemented to try to separate potentially overlapping physical clusters. The position of the clusters is characterized by 'the center of gravity' (with respect to charge) of the cluster. These clusters then form the input to a Kalman Filtering algorithm whose purpose is to reconstruct the trajectory of the particle that generated the clusters. The trajectory of the particle is assumed to be a helix of the form [39]:

$$
\begin{aligned}
y(x) &= y_0 - \frac{1}{C}\sqrt{1-(Cx-\eta)^2} \qquad (4.1)\\
z(x) &= z_0 - \frac{\tan\lambda}{C}\sin^{-1}(Cx-\eta) \qquad (4.2)
\end{aligned}
$$

where λ is the dip angle, C is the curvature, x, y and z define the local track position, and $\eta = Cx_0$ where x_0 is the local position of center of the helix. The parameters (y, z, C, λ, η) fully define the helix.

The Kalman Filtering algorithm requires some reasonable *seed* values of the helix parameters in order to begin the iterative track reconstruction. In the first pass, the *combinatorial* seeding approach is employed. All possible pairs of clusters, comprising one cluster from the outermost pad row and one from the paw row 20 rows closer to the origin, are first formed. For each pair, a helix is attempted to be constructed that passes through this pair of clusters and extrapolates to the vertex calculated by the SPD within some distance (Figure 4.1.1 illustrates the idea). Pairs that satisfy a maximum curvature constraint generate seed parameters for the helix. The Kalman filtering algorithm operates with this seed helix and extrapolates between the two clusters that defined the seed. If at least half of the possible clusters between the two clusters are successfully added (acceptance based on deviation of cluster position from the seed helix) to the track then the seed is saved. The initial covariance matrix utilizes the point errors from the cluster finder and the uncertainty in the vertex position. The *track following* seeding algorithm is used after the first pass, and has the benefit of a higher efficiency of track identification from displaced secondary vertices (there being no constraint to the SPD). In this procedure, the outermost padrow and a padrow 20 rows inwards again are used. The starting point is taken as the padrow directly between these two

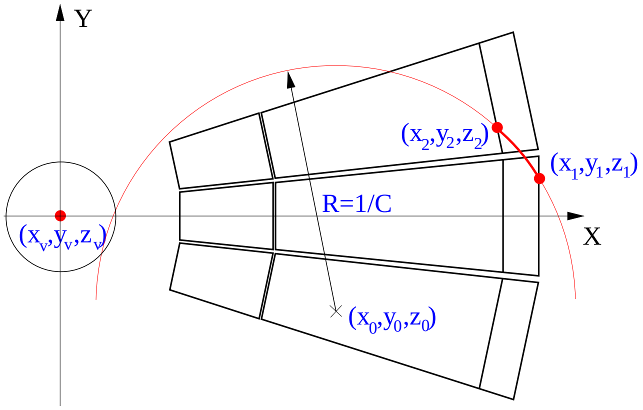

Figure 4.1.1: Illustration of the combinatorial seed generation procedure (from [39])

padrows (i.e the padrow 10 rows closer to the origin that the outermost padrow). For each cluster in this middle row, adjacent pad rows are searched for adjacent clusters. If nearby clusters are found, then a linear extrapolation is employed between these three points. The algorithm continues recursively in this way towards the outer two pad rows, but after 7 clusters have been added a polynomial is used to perform the fit as opposed to a linear extrapolation. If more than half of the potential clusters are successfully added, then the clusters are used to generate a seed helix without the primary vertex as a constraint.

For each seed, the Kalman filtering algorithm starts at the outermost pad row. The current track is extrapolated to the next pad row and the cluster nearest to the extrapolation is found. The covariance matrix predicts the expected error in the x, y positions of the track and if the nearest cluster lies within 4σ then the cluster is added to the track and the covariance matrix is updated. This procedure is repeated until the track has been extrapolated to the innermost pad row. At this stage the procedure continues as described in section 3.2 with extrapolation first through the ITS to the primary vertex, followed by extrapolation from the primary vertex outwards through the ITS, TPC and TRD. Finally the tracks are extrapolated backwards from the TRD to the primary vertex.

The procedure obviously has some finite efficiency for reconstructing tracks. Excluding the effects of acceptance, the tracking efficiency is close to 100% [35]. Incorporating the acceptance effects (dominated by the gaps between TPC chambers) the tracking efficiency reaches 90%. However, in any particular analysis various track quality cuts are employed. Even with a near 100% tracking efficiency, some of the reconstructed tracks may be of low quality. For instance, short tracks which do not span the entire TPC have fewer clusters and accordingly have a higher uncertainty associated with position and momenta. Moreover, particular analyses may demand particularly stringent quality controls to perform certain measurements (for example requiring a certain momentum resolution in order to achieve a desired resolution in the final result). Hence, for each analysis a set of quality cuts are defined, and the corresponding tracking efficiency has to be determined to correct the final result. The next two sections describe the track quality cuts employed, the determined tracking efficiency, and the methodology for estimating the tracking efficiency.

4.2 Track Selection and Quality Assurance

The lhc11a/pass2 data is for the most part of good quality, and all but one of the detectors utilized were operating at or near design expectations. The major exception to this was the ITS, the operation of which exhibited two abnormalities. The first, unique to this data set, is that in half of the data sample the SDD was not utilized to improve statistics. This had a major impact on the final tracking efficiency. In typical circumstances there are a maximum of 6 possible ITS clusters, and with the designed redundancy 4 ITS clusters are usually enough to guarantee track quality. However, to guarantee the same kind of track quality one would require 4/4 ITS layers to have a hit which greatly reduces the tracking efficiency. In fact, to improve statistics only 3 ITS hits were required as opposed to 4, but the tracking efficiency is still reduced to $\approx 50\%$. The second issue was omnipresent during the first periods of data taking. The cooling elements of the SPD have reduced efficiency, and hence some of the staves cannot be turned on without exceeding safe temperature limits. This is thought to be due to impurities clogging cooling filters [274]. The end result is that only $\approx 83\%$ of the SPD is active in the data (the regional activity can be seen in Figure 4.2.1).

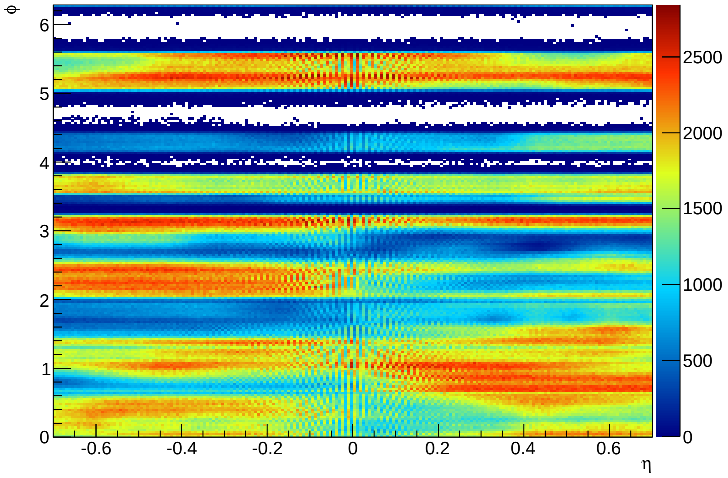

Figure 4.2.1: (η, ϕ) position of tracks with 4 ITS hits in lhc11a/pass2. Since the SDD layers are not active, this can only occur when both SPD layers have hits. The gaps in acceptance due to the faulty cooling system are clearly observed

To ensure track quality, various track cuts are employed. In general, utilized track cuts may be one of three classes: (i) 'standard' track cuts common to many analyses which are well known to improve track quality in understood ways (ii) analysis specific track cuts (iii) data specific track cuts. The latter case pertains to situations where the data set being analyzed may have had some detector problems that necessitate further track quality cuts to reject poorly reconstructed tracks. Basic quality assurance is undertaken to identify such issues, part of which involves examining the distributions of various track parameters to see if they exhibit the features one would expect. To give motivation for the imposed track cuts some of these distributions are presented in this section.

The η distribution of tracks in the MB data set is uniform over the region the TPC is fully

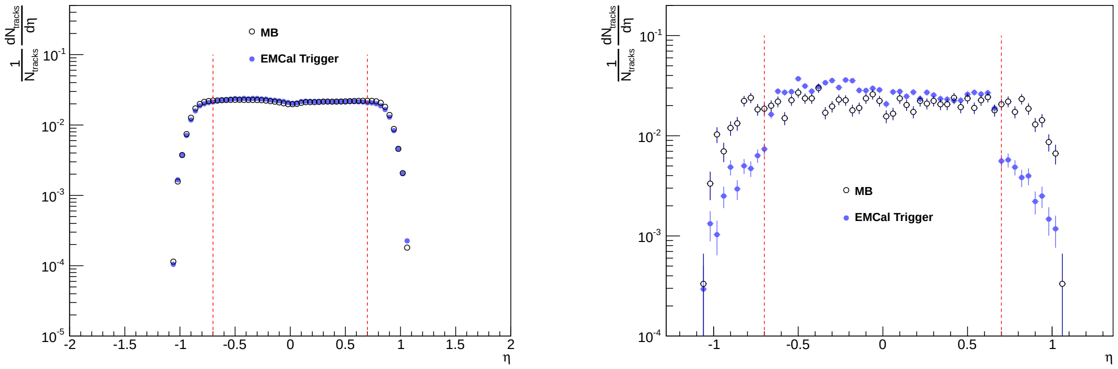

Figure 4.2.2: η distribution of accepted tracks for all tracks (left) and high p_T tracks (right). In both sets the distribution is approximately uniform at low p_T but a characteristic enhancement is observed for high p_T tracks in the EMCal triggered data set. The red lines indicate the imposed track cut

efficient ($|\eta| < 0.9$), whereas the EMCal exhibits an enhancement in the η range occupied by the EMCal at high p_T as one would expect (see Figure 4.2.2). The slight non-uniformity at $\eta = 0$ is due to the TPC central membrane. Since the EMCal occupies the region $|\eta| < 0.7$, a cut requiring that tracks lie within this range is one of the track cuts imposed. This ensures an exact region of phase space is being explored (otherwise some tracks are accepted which lie outside of the acceptance initially and curve within the acceptance). Moreover, imposing a cut on η to restrict accepted tracks to those within the plateau in Figure 4.2.2 is a common method to avoid having to deal with edge effects of the TPC (where the TPC is no longer fully efficient).

Due to the non-uniformity of the SPD response, the distribution of accepted tracks is not uniform in either data set (see left side of Figure 4.2.3). However, one of the track cuts employed is to demand three *ITS hits* (a signal in at least 3 layers of the ITS), and removing that condition (and thus the dependence on the SPD) results in a uniform distribution of tracks in the MB data set (see right side of Figure 4.2.3). The EMCal data set is enhanced in the region occupied by the EMCal, and it is also enhanced in opposing azimuth due to the production of di-jets.

The track p_T distribution for MB and EMCal triggered data sets are shown in Figure 4.2.4; the distribution is clearly biased towards higher p_T for the EMCal trigger data set as one would expect.

Verifying the spatial homogeneity of the track distributions and probing other fundamental distributions like track p_T for anomalies forms one aspect of the quality assurance, which may in turn lead to the implementation of certain track quality criteria. Beyond this basic quality assurance other track quality criteria are employed, not solely to remove tracks which are irregular or result from detector performance issues, but to ensure tracks of high quality. The complete list of track

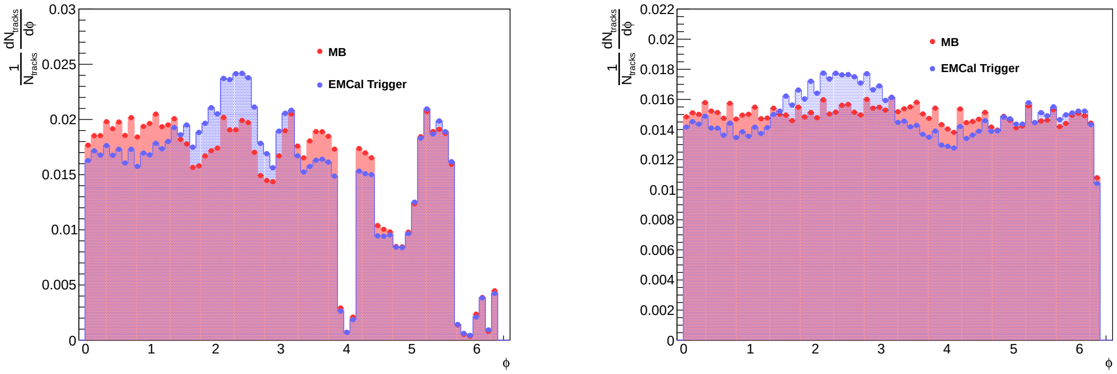

Figure 4.2.3: ϕ distribution of tracks passing all track quality cuts with (left) and without (right) requiring 3 ITS hits. The distribution of tracks is approximately uniform for the MB data set as one would expect, however requiring 3 ITS hits introduces inhomogeneity due to the non-uniform response of the SPD

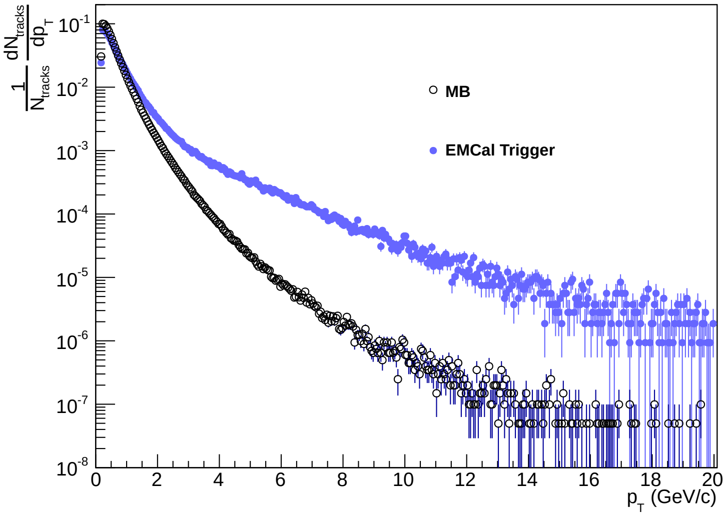

Figure 4.2.4: Track p_T distribution for the MB and EMCal triggered data sets

Track Cut	MB Efficiency (Seq./Cum./Final/Sole)	EMCal trigger Efficiency (Seq./Cum./Final/Sole))
$\lvert\mathrm{DCA}_{xy}\rvert \leq 1\mathrm{cm}$	36.4% — 36.4% — 98.2% — 36.4%	40.6% — 40.6% — 98.0% — 40.7%
$\lvert\mathrm{DCA}_{z}\rvert \leq 2\mathrm{cm}$	56.8% — 20.7% — 97.1% — 23.8%	67.1% — 27.3% — 97.1% — 31.1%
$N^{TPC}_{clusters} \geq 110$	41.0% — 8.5% — 85.6% — 34.6%	43.1% — 11.8% — 85.8% — 37.2%
$N^{ITS}_{clusters} \geq 3$	70.5% — 6.0% — 92.6% — 15.2%	70.4% — 8.3% — 92.1% — 21.1%
$\frac{N^{TPC}_{clusters}}{N^{TPC}_{findable\ clusters}} \geq 0.6$	100% — 6.0% — 100% — 82.8%	100% — 8.3% — 100% — 86.6%
$\chi^2 \leq 4$	99.9% — 6.0% — 99.9% — 96.0%	99.9% — 8.3% — 99.8% — 96.4%
$N^{SPD}_{hits} > 0$	100% — 6.0% — 100% — 16.7%	100% — 8.3% — 100% — 23.1%
$\lvert\eta\rvert \leq 0.7$	75.9% — 4.5% — 78.1% — 64.3%	77.5% — 6.4% — 100% — 66.7%
ITS/TPC Refit	99.9% — 4.5% — 100% — 10.6%	99.9% — 6.4% — 100% — 14.6%
Kink Rejection	99.1% — 4.5% — 99.1% — 97.4%	98.6% — 6.3% — 98.5% — 97.2%

Table 4.2.1: Track quality cut efficiencies for MB and EMCal trigger data. Four efficiencies are listed: 'final' refers to the efficiency of the cut once all other cuts have been applied; 'sequential' (Seq.) refers to the efficiency of the cut when applied in the order the cuts are listed in the table; 'cumulative' (Cum.) refers to the total track efficiency of all tracks cuts applied sequentially in the order the cuts are listed in the table; and 'sole' refers to the efficiency of the cut when no other cuts have been applied. It is the cumulative efficiency that is visually represented in Figure 4.2.5

cuts implemented in this analysis along with the corresponding track cut efficiencies can be seen in Table 4.2.1; Figure 4.2.5 illustrates the cumulative track cut efficiency as a function of the cut placement.

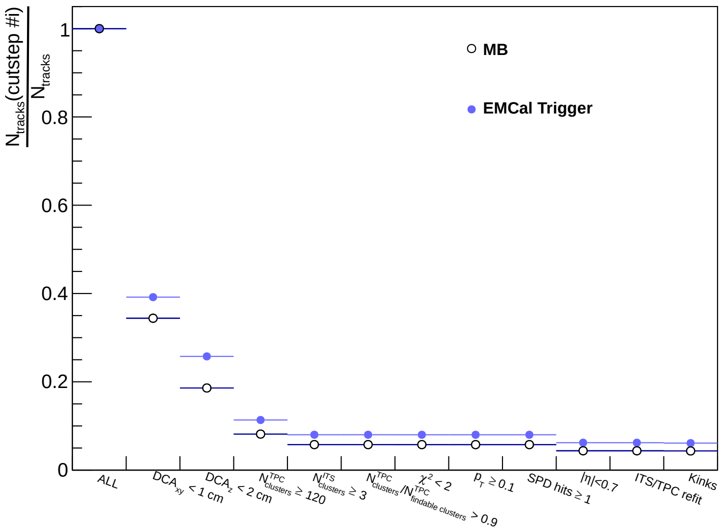

Figure 4.2.5: Cumulative track cut efficiency as a function of the track cut being applied for the MB and EMCal trigger data

Tracks are rejected based on the distance of closest approach to the vertex in both the $x-y$ plane (DCA_{xy}) and in the z-direction (DCA_z). Both DCA_{xy} and DCA_z are sensitive to track quality at high p_T. Most high p_T tracks are expected to originate from the primary vertex and have little change in direction from (even multiple) scattering. Moreover, those tracks considered for electron

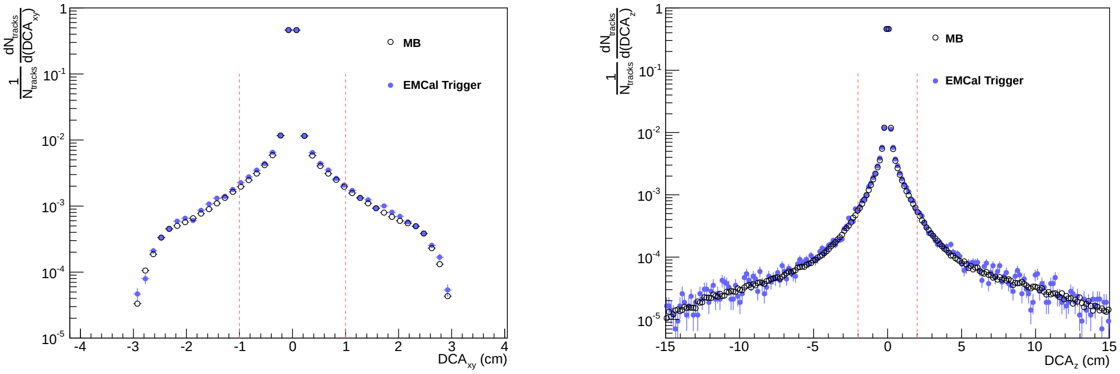

Figure 4.2.6: DCA$_{xy}$ (left) and DCA$_z$ (right) distributions of all tracks that *pass all other cuts* except the DCA$_{xy}$ (left) and DCA$_z$ (right) cuts in MB and EMCal trigger data. The red lines indicate the cut placement

identification have to reach the EMCal and as such are guaranteed to have $p_T \gtrsim 1$ GeV. Hence, to ensure high quality for tracks of interest, cuts on DCA$_{xy}$ and DCA$_z$ were imposed as indicated in Figure 4.2.6.

The greater the number of inputs to a Kalman filter, the better the estimation of the true underlying variable; for tracking in a TPC both the spatial and momentum resolution increase with increasing number of TPC/ITS clusters as $\sigma \sim 1/\sqrt{N_{clusters}}$ [35]. Hence, cuts are placed on the number of TPC and ITS clusters that constitutes a track. The constraint on the number of TPC clusters also ensures that tracks where large portions of the trajectory lie between sector boundaries, and tracks that leave the TPC early on in their trajectories, are rejected. The ITS cluster cut in addition has the effect of constraining tracks to lie at least as close as the ITS to the origin, and thus serves as a loose DCA cut. In the context of analyses involving electrons, this constraint is important to minimize the effects of conversion electrons. A large number of these conversion electrons originate within the ITS itself, so in addition to 3 ITS hits, at least 1 SPD hit is required to further constrain the production vertex and reject as many of these conversion electrons as possible.

Relating to the quality of the Kalman filter generated helix are a cut on χ^2 and a cut demanding 'ITS/TPC refit'. The latter is in reference to the tracking procedure: if the track reconstruction that takes place in the third pass (from the TRD back to the ITS) is not successful then the track is labeled as such. This cut ensures we only examine tracks where all three passes of the track reconstruction are successful. The former refers to the global χ^2 value of the reconstructed track (a standard measure of the statistical quality of a fit). The χ^2 distribution for tracks passing all other track quality selection criteria is shown in Figure 4.2.8

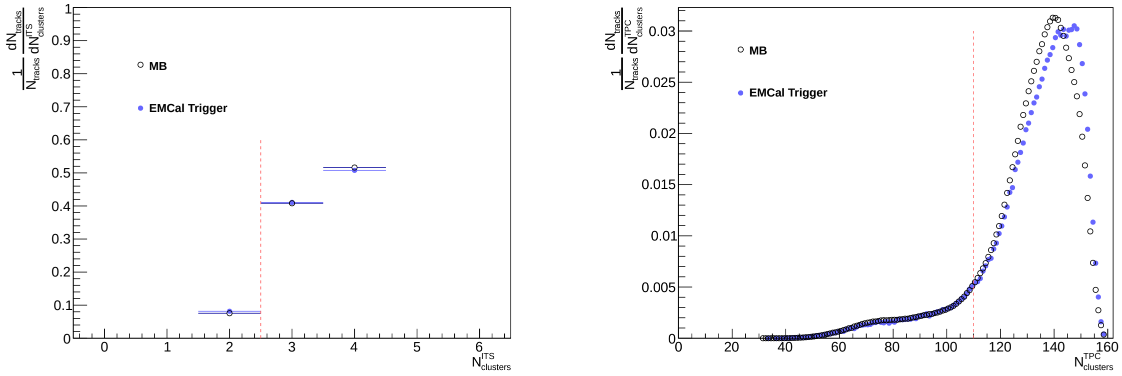

Figure 4.2.7: Number of ITS (left) and TPC (right) clusters possessed by tracks that *pass all other cuts* except the ITS (left)/TPC (right) cluster cuts. The red line indicates the cut placement

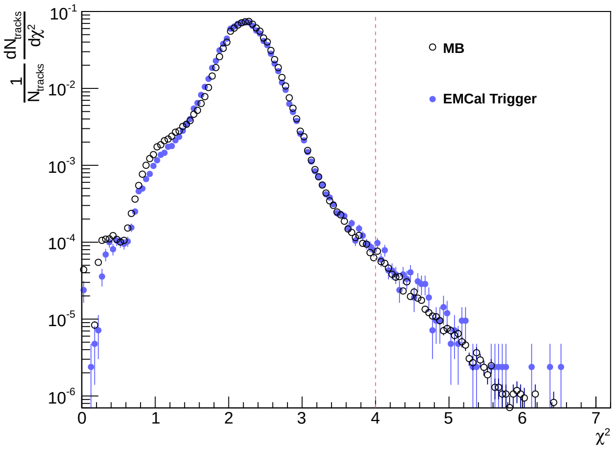

Figure 4.2.8: χ^2 distribution of tracks that *pass all other cuts* except the χ^2 cut in MB and EMCal trigger data. The red line indicates the cut criteria

Note that Table 4.2.1 indicates that the most stringent track cuts are the ITS/TPC cluster requirements. These cuts alone would result in an efficiency of $\approx 6.5\%$ for the MB data, highlighting the highly correlated nature of the imposed track cuts. The ITS hit requirement already requires some maximum distance of closest of approach, and the TPC cluster cut imposes geometrical and track quality constraints that overlap with some of the other cuts. The low cut efficiency for ITS clusters ($\approx 15\%$) is partially due to the inactive layers, but also indicates that a large fraction of the rejected tracks originate from conversions or decays.

4.3 Tracking Efficiency

Not all particles present in the TPC will be detected, both because of intrinsic limitations of the detector (such as acceptance effects where a high p_T particle may traverse the TPC between the chambers), and due to additional track quality cuts that may be applied (to select tracks with higher p_T resolution for instance). The desired track quality cuts may vary between analyses depending on the desired observable. Thus the determination of the efficiency with which particles are reconstructed in the TPC, the *tracking efficiency*, is necessary to measure physical observables derived from the reconstruction of tracks in the TPC. Since those particles which do not produce reconstructed tracks are by definition unobservable, the determination of the tracking efficiency using measured variables is difficult. One method is to employ some type of 'tag and probe' approach, where one observable (that is tagged) is associated with the production of a known number of other particles (and hence tracks), and compare the number of tracks observed to that implied by the tag. For instance, the tracking efficiency of muons can de determined by studying the dimuon resonance J/ψ and decay $J/\psi \rightarrow \mu^+\mu^-$ (this is one approach taken by CMS [275]). Due to the limited statistics, especially at high p_T, a data driven approach is not feasible in this analysis. Thus simulations are employed to determine the tracking efficiency.

The degree of reliance on the simulations depends on the exact method used. A robust method that is utilized by STAR[276] and CMS [275] is to use *embedding*. Here a simulated particle is superimposed upon an event that was actually recorded (this ensures we replicate the exact event conditions such as track multiplicity), and the particle is reconstructed within the simulation. Repeating this procedure over a large number of events enables the estimation of the tracking efficiency (and many other kind of efficiencies such as the particle identification efficiency). At the time this analysis was undertaken, there was no unified framework for performing embedding within the ALICE collaboration and hence the tracking efficiency was estimated solely using simulations.

For this purpose, the simulated data sample described in Chapter 3 was utilized: lhc11b10b, a heavy-flavor enhanced data sample. The heavy-flavor enhanced sample was used for this step of the analysis as it has a greater population of electrons at higher p_T and in this sense is more practicable for the calculation of tracking efficiency for electrons in this region. A priori one can foresee that there may be problems with using a heavy-flavor enhanced sample to compute the tracking efficiency, and a MB anchor run may be more suitable. For instance, it is observed that the tracking efficiency has a slight species dependence, so the ratio of species present in the sample will be a factor in estimating the total tracking efficiency and the heavy-flavor enhanced sample clearly has a biased distribution of particle species. This potential difficulty is easily overcome by determining tracking efficiency for each species separately. However, there may be other discrepancies and thus a MB simulation sample was used (lhc12e6) to verify that the tracking efficiency is (in the region where the MB sample is not statistics limited) consistent in the heavy-flavor enhanced and MB simulations.

Beyond this issue is the more systemic question of the reliability of the simulation regardless of sample choice. Ultimately it is the determination of the systematic uncertainty by varying the track cuts that provides the best evidence of the validity of the approach. If the simulation had systematic problems, then by varying the track selection cuts and recalculating the tracking efficiency and reconstructing the final spectrum one would see large deviations between the reconstructed spectra. Thus one proceeds with a determination of the tracking efficiency under different track quality cuts. Given that the simulation incorporates particle propagation and interaction with the detector one needs to be careful in defining the tracking efficiency solely from simulations (e.g. interaction in the ITS may produce a plethora of different low momenta particles which we do not desire to reconstruct as originating from the collision). In this analysis the following definition is adopted:

$$\varepsilon^{e^{+/-}}_{efficiency}(p_T^{MC}) = \frac{\frac{dN_{tracks}}{dp_T}\left(|\mathrm{PDG}| = 11 \;\&\&\; |\eta_{MC}| < 0.7 \;\&\&\; R_{MC} < 7 \;\&\&\; |v_z^{MC}| < 10\right)}{\frac{dN_{particles}}{dp_T^{MC}}\left(|\mathrm{PDG}| = 11 \;\&\&\; |\eta_{MC}| < 0.7 \;\&\&\; R_{MC} < 7 \;\&\&\; |v_z^{MC}| < 10\right)} \qquad (4.3)$$

where $\frac{dN_{particles}}{dp_T^{MC}}$ (*condition*) is the number of *particles* that are present in the simulation that satisfy the condition in parenthesis in a given *true* p_T bin, $\frac{dN_{tracks}}{dp_T^{MC}}$ (*condition*) is the number of *reconstructed tracks* that are present in the simulation that satisfy the condition in parenthesis in a given *true* (not reconstructed) p_T bin, PDG indicates the particle data group [48] code assigned to the particle species, η_{MC} is the true η coordinate of the particle in simulation, R_{MC} is the true radius of production of the particle in simulation, v_z^{MC} is the true z position of the vertex in simulation. In essence, this stipulates that the particles we want to reconstruct are electrons that 'truly' (ignoring effects of detector resolution) lie within $|\eta| < 0.7$, originate from events where the event vertex is 'truly' within 10cm of the origin, and are 'truly' within 7cm of the origin of the detector/coordinate system. The former three conditions replicate the event and geometric cuts that are imposed on the measured tracks at the level of simulated particles. Since the second layer of the ITS lies at a radius of 7cm and the track quality cuts demand at least 3 ITS hits, any particles produced further from the origin than 7cm would not produce tracks, and this condition ensures those particles are excluded. With this definition of tracking efficiency, the obtained tracking efficiency for pions and electrons is shown in Figure 4.3.1. Due to the absence of 2 ITS layers, the tracking efficiency is considerably lower than design specifications at around 60%. Due to differing detector responses, and different material interactions (electrons produce copious conversion electrons in electromagnetic showers), there is a slight difference in the tracking efficiency of electrons and pions (especially at $p_T \lesssim 2$ GeV/c).

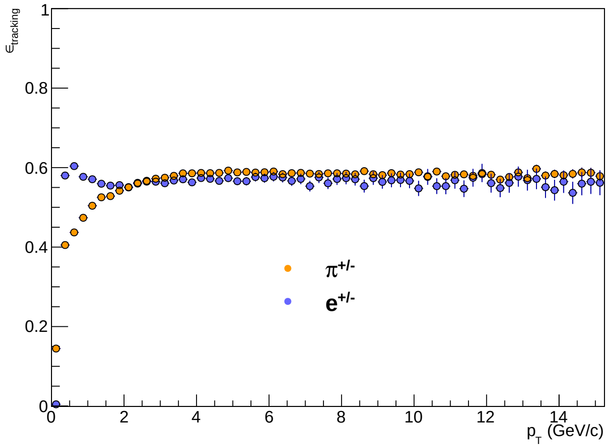

Figure 4.3.1: Tracking efficiency of pions and electrons in simulation (lhc11b10b)

4.4 Momentum Resolution and Bremsstrahlung Unfolding

In addition to the possible failure of reconstruction, another issue arises from the imperfection of the TPC: like all detectors, it has some finite measurement resolution. Particularly relevant for the cross-section as a function of p_T, is the finite momentum resolution. In the data set used in this analysis, Figure 2.2.6 illustrates the momentum resolution as determined from the Kalman Filter covariance matrix, and as determined from simulations. Over the p_T range of the cross-section measurement performed in this analysis (2-12 GeV/c) the momentum resolution is less than ≈2%. The effect of

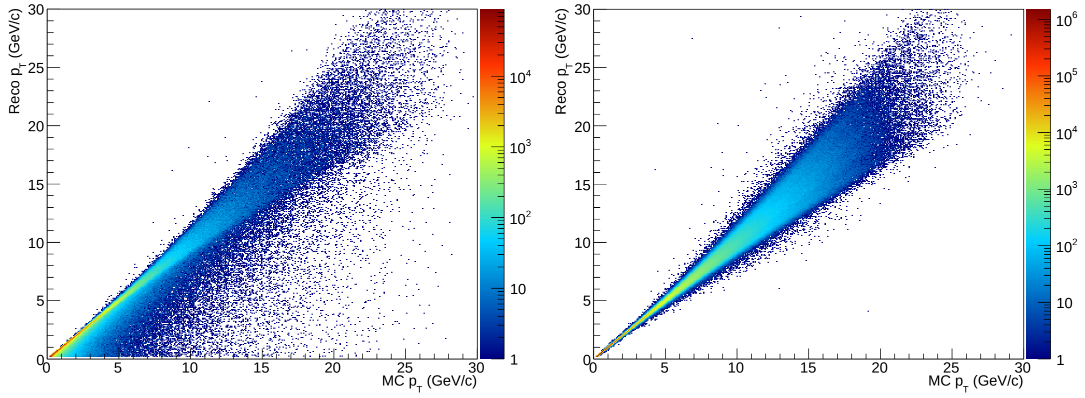

(a) (b)

Figure 4.4.1: Apparent momentum resolution for electrons (left) and pions (right) in simulations

finite momentum resolution is to induce some *bin shifting* effects: the true number of particles in each p_T bin will be slightly different than what is measured due to an imprecise measurement of the transverse momentum. Given the small momentum resolution, one would expect the necessary correction to be quite small. This effect should always be corrected for, but it is especially critical for electrons. In the case of electrons, in addition to bin shifting as a result of the finite momentum resolution, one observes bin shifting due to Bremsstrahlung effects. As the electron traverses the TPC it can emit Bremsstrahlung radiation reducing its energy and momentum during it's motion. This causes significant broadening of the apparent momentum resolution. This effect can be observed from simulation in Figure 4.4.1 where the reconstructed momentum is plotted as a function of the true momentum for electrons and pions respectively. Thus one has to convert the measured spectrum into the underlying true spectrum to resolve these bin shifting effects; this general process is known as *unfolding*, *unsmearing* or *deconvolution* (in particle physics *unfolding* is the most common term) [277].

The general problem addressed by unfolding is the following. A measurement is made of some quantity F as a function of some other quantity X in order to obtain the distribution $F(X)$. The true value of X is denoted x and the measured value is denoted y; the measured distribution is thus denoted $g(y)$ and the true distribution is denoted $f(x)$. A number of effects can lead to the distinction between $f(x)$ and $g(y)$: the finite resolution of the measurement, limited detector acceptance, non-linear response of the detector and radiative corrections can all play a role. Intuitively one has to parameterize the detector response and perform some inversion on the measured spectrum.

Mathematically one needs to solve the following for $f(x)$:

$$g(y) = \int A(y,x) f(x) dx \tag{4.4}$$

The response of the detector is parameterized by the kernel $A(y,x)$. This can often be determined via simulations or by performing tests on the detector to characterize its response. Typically the measured distributions are discrete and the problem becomes the solution of a matrix equation:

$$g_i = \sum_j A_{ij} f_j \tag{4.5}$$

The simplest solution would be to calculate the correction factors, c_i, in each bin from simulation and apply those to the measured distributions. However this approach, the *bin-by-bin* approach will only work where the resolution effects are extremely well described by simulation; any smearing not incorporated directly in the simulation will cause this method to fail. In theory one would just find the inverse matrix $\mathbf{A}^{-1}$ and solve for $\mathbf{f}$. Unfortunately the inversion of this equation is typically *ill-posed* in that it exhibits high sensitivity to the initial conditions [278]. The effect of statistical fluctuations and finite statistics exacerbate this problem. Intuitively this can be best seen with a simple example. Suppose we have some distribution that has some very fine structure, for instance:

$$f_i = \begin{cases} i^2 & \text{if } i \in \{2k; \forall k \in \mathbb{Z}\} \\ 0 & \text{if } i \in \{2k+1; \forall k \in \mathbb{Z}\} \end{cases} \tag{4.6}$$

In this case the function alternates between i^2 and 0 every other bin. If this distribution were to be measured, a finite measurement resolution would necessarily smooth out this distribution considerably, in some cases completely removing any sign of the original oscillations. Therein lies the problem: the inversion process cannot distinguish between cases with genuine fine structure like this and pure statistical fluctuation (which is omnipresent in particle physics as we try to reach ever higher momenta and energies). Hence given a smooth input distribution the inversion can introduce large statistical fluctuations between neighboring bins. Physically then we want to solve the system subject to the additional constraint that the solution should be reasonably smooth: mathematically this is achieved with some form of *regularization* [277, 278, 279]. The regularization parameter has to be chosen carefully so as not to over-smooth the distribution and remove possibly significant structures.

There are several approaches to achieve this necessary regularization, the two broad classes being matrix inversion methods and Bayesian methods. In the former, the matrix inversion is explicitly undertaken with some additional regularization technique employed [280]. The Bayesian approach starts from Bayes theorem and avoids the explicit inversion of the equation [281]. The Bayesian approach provides an iterative solution and again the iteration parameter must be carefully chosen; for large iterations the procedure becomes identical to pure matrix inversion and suffers the same problem of correlations between neighboring bins. This analysis employs the RooUnfold package to perform unfolding [282]. The package is integrated within ROOT, and codes a number of different approaches to the problem: the bin-by-bin method, the ‘SVD method’ (a matrix inversion approach) and the ‘Bayes method’ (employing an implementation of D’Agostini’s Bayesian algorithm [281]). All three methods were compared in order to ascertain the systematic uncertainty associated with the unfolding.

The general procedure relies on some simulation of the detector response that enables a parameterization of the matrix A. The simulation is known as a *training sample* and in this analysis was provided by lhc11b10b, described in Chapter 3. For each particle the true momentum and the reconstructed momentum are recorded in the *response matrix*. The response matrix encodes the information visually represented in Figures 5.4.1(a) and 5.4.1(b). The RooUnfold package takes the response matrix thus generated along with the measured data, and employing one of the various algorithms, produces an unfolded spectrum. The only other input required is an appropriate regularization parameter. For the SVD algorithm, the regularization parameter is selected as described in the paper by Hoecker and Kartvelishvili [280]. In essence this procedure minimizes:

$$-\ln(L) + \alpha S \tag{4.7}$$

where L is a likelihood (often $\ln(L)$ is replaced by χ^2) which expresses the disagreement between the prediction $\mathbf{Af}$ and the data $\mathbf{g}$, S expresses the spikiness of the distribution, and α is the regularization term. The optimal regularization parameter was determined to be 7 for the MB data set and 14 for the EMCal trigger data set. In the case of the Bayesian algorithm, the regularization optimization involves the selection of an iteration parameter. There is no definitive selection criteria for the number of iterations; in principle the method is quite insensitive to choice of the iteration parameter. The primary constraint is that it should be as small as possible to prevent introducing statistical fluctuations (the first few iterations represent real improvement and convergence to a solution, higher iterations represent the introduction of statistical fluctuations). To determine an appropriate choice, the training sample was split into two samples. One half was used to generate a response matrix

Algorithm, Data Set	Selected Regularization/Iteration Parameter
Bayesian, MB	5
Bayesian, HT	5
SVD, MB	7
SVD, HT	14

Table 4.4.1: Selected iteration parameters for the different unfolding algorithms and data sets

and the unfolding procedure was applied to the other half. As one would a priori expect, the result doesn't depend too severely on the iteration parameter, and for both the MB and EMCal triggered data sets an iteration parameter of 5 was used. Table 4.4.1 summarizes the choices. The results provided by the different algorithms are very similar and thus there was no strong preference for choosing one algorithm over the other in the final result. To conform with ALICE convention, the final spectrum utilized the Bayesian unfolding algorithm.

4.5 Systematic Uncertainties

4.5.1 Systematic Uncertainty Associated with the Tracking Efficiency

In the final spectrum, only a systematic uncertainty that combines the uncertainty in the response matrix (Section 4.5.2) and the tracking efficiency is included. This is because it is impossible to disentangle these contributions completely. That this is the case derives from the methodology used for determining the systematic uncertainty: the tracking cuts are varied, and in each case the tracking efficiency and response matrix are determined and used to correct the spectrum. When performing this procedure the spectra are only comparable when both the tracking efficiency and unfolding corrections are implemented, so one cannot apply just the tracking efficiency or just the unfolding alone. However, an estimation of the systematic uncertainty associated with the tracking efficiency alone can be determined by utilizing a *smeared* tracking efficiency: in equation 4.3 one counts tracks in the reconstructed track p_T bins in the numerator instead of the underlying true p_T bins. This is equivalent to correcting for the unfolding using a bin-by-bin method (see section 4.4). Although the result may not properly account for any smearing not modeled by the simulations, it enables an estimation of the systematic uncertainty associated with solely the tracking efficiency. It is apparent that if the simulated tracking efficiency provided a poor estimation of the true tracking efficiency, then when the track quality cuts are varied (obtaining differing tracking efficiencies) and the spectrum corrected in each case, the resulting spectra would differ significantly.

To ascertain the systematic uncertainty associated with the tracking efficiency the track cuts

Track Property	loose cut	normal cut	hard cut
No. of TPC Clusters	≥ 80	≥ 110	≥ 120
No. of TPC Clusters used for PID	≥ 60	≥ 60	≥ 60
DCA to the primary vertex in (x, y)	≥ 60	≥ 60	≥ 60
DCA to the primary vertex in z	≥ 60	≥ 60	≥ 60
ITS hits	≥ 2	≥ 3	≥ 4

Table 4.5.1: The three set of track cuts used for determining the systematic uncertainty in the estimation of the tracking efficiency and response matrix.

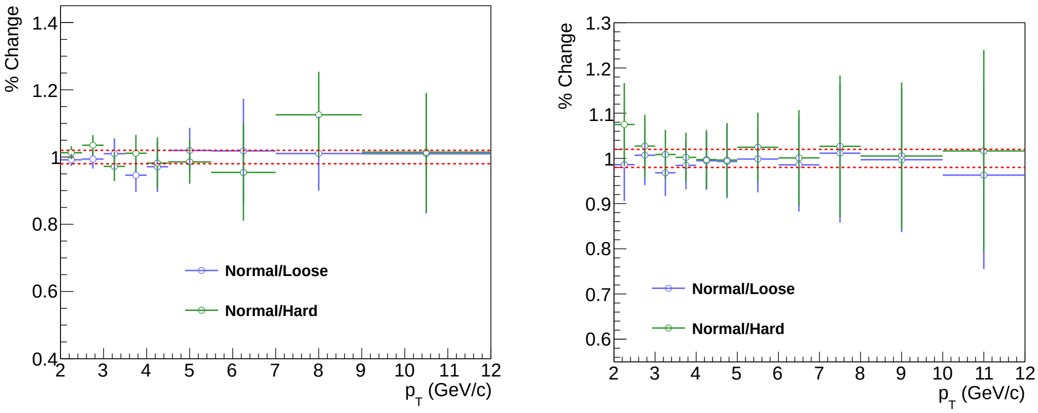

(a) (b)

Figure 4.5.1: Ratio of reconstructed spectrum with normal tracking cuts to the reconstructed spectra with loose and hard tracking cuts in MB (left) and EMCal trigger data (right). The red line indicates the assigned systematic uncertainty

were varied within reasonable bounds. The three sets of track cuts examined were labeled as *loose*, *normal* and *hard*, the cut criteria for each are listed in Table 4.5.1. Any track quality cuts not listed in the table were not varied and are identical to those listed in Section 4.2. For each set of track cuts the smeared tracking efficiency was determined and the spectra were corrected. Figure 4.5.1 shows the ratio of the reconstructed spectrum for the normal track cuts to the spectra for the hard and loose cuts in the MB and EMCal trigger data. Based on the figure, the systematic uncertainty was estimated to be 2% for both MB and EMCal trigger data.

4.5.2 Systematic Uncertainty Associated with Unfolding

There are two possible sources of systematic uncertainty associated with the unfolding procedure: uncertainty in the input response matrix and an uncertainty associated with the algorithm itself. The uncertainty in the response matrix was determined, as for the pure tracking efficiency, by varying the tracking cuts. For each set of track cuts, a tracking efficiency and response matrix

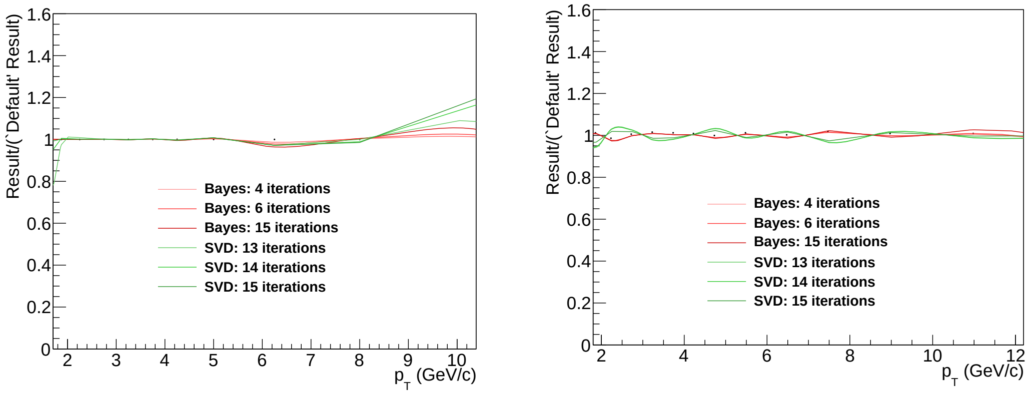

(a)

(b)

Figure 4.5.2: Ratio of the reconstructed spectrum for various unfolding algorithms and iterations to the reconstructed spectrum for the 'default algorithm' (Bayesian) with the optimal iteration parameter (5)

were generated, and the spectrum was reconstructed correcting for the tracking efficiency and p_T smearing. Since altering the cuts also changes the tracking inefficiency, it is impossible to disentangle the systematic uncertainty in the tracking efficiency and the uncertainty in the response matrix. However, a sense of the relative size of the contributions can be taken from a comparison of the systematic uncertainty associated with the tracking efficiency and uncertainty in response matrix to the uncertainty associated with the tracking alone. Henceforth the *tracking systematic* refers to the systematic uncertainty due to the tracking efficiency and the systematic uncertainty due to uncertainty in the response matrix combined. The ratios of the reconstructed spectra employing normal track cuts to those employing loose and hard track cuts indicated a systematic uncertainty of $\approx 3\%$.

The systematic uncertainty associated with the algorithm itself was determined by utilizing two different algorithms (the Bayesian and the SVD), and by slightly varying the iteration parameters from those determined to be optimal. Figure 4.5.2 shows the ratio of the different results obtained with the different algorithms and iteration parameters to the result obtained with the Bayesian unfolding algorithm with iteration parameter 5 for the MB and the EMCal trigger data. The results are consistent within 1% for the MB data and a corresponding systematic uncertainty of 1% could be assigned in this case. The statistical fluctuations only become apparent in the statistically limited region. In the EMCal triggered data set however, the bin-by-bin fluctuations characteristic of unfolding methods is more apparent. It is hypothesized that this is due to the difference in the shape of the training sample and the data sample, the latter having a pronounced hump around the trigger threshold. One could overcome this in two ways: (i) combining the spectra before unfolding and applying the unfolding algorithm to the merged spectrum or (ii) generate a simulated trigger sample and use this to generate a new response matrix. In this analysis the former approach was taken, and in the final result the spectra are merged before applying the unfolding and tracking efficiency corrections. It is assumed that the tracking efficiency is similar in both data sets; the fact that the systematic uncertainty is similar in both cases supports this assumption.

Figure 4.5.3 shows the result of applying different unfolding algorithms and varying the iteration parameter to the merged spectrum; the lower panel shows the ratio to the standard unfolding algorithm in a similar vein to Figure 4.5.2. In this case the optimum iteration parameter for the SVD algorithm was determined to be 18 (again employing the methodology in [280]). The bin-by-bin fluctuations that appear when applying the unfolding to the EMCal spectrum alone are significantly reduced, and a generous 2% systematic uncertainty was assigned. Table 4.5.2 summarizes the ascertained systematic uncertainties associated with the tracking efficiency and unfolding corrections.

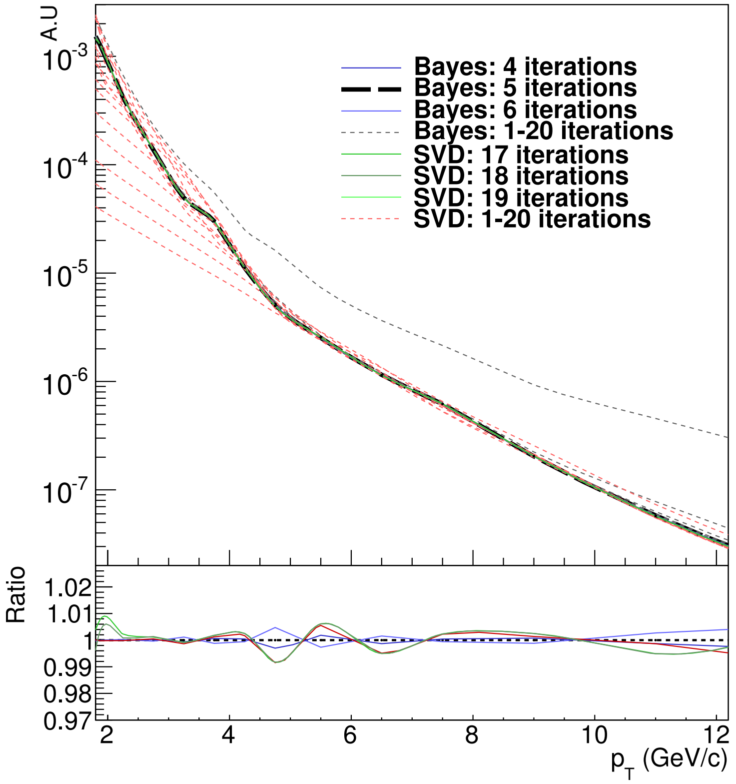

Figure 4.5.3: Comparison of the result of various unfolding algorithms when the MB and EMCal trigger spectra are first combined before unfolding. The lower panel shows the ratio of the spectrum obtained from some of the unfolding algorithms (those used for estimating the systematic uncertainty) to that obtained with the default algorithm (Bayesian with iteration parameter 5)

Correction	Estimated Systematic Uncertainty
'Pure' Tracking Efficiency	2%
Tracking Efficiency + Response Matrix	3%
Unfolding Algorithm	2%

Table 4.5.2: Summary of the estimated systematic uncertainties associated with the tracking efficiency and unfolding corrections. In the final cross-section the 'Tracking Efficiency + Response Matrix' uncertainty is combined in quadrature with the 'Unfolding Algorithm' uncertainty

5

Electron Identification

The ALICE detector employs a wide variety of particle identification techniques utilizing an array of detectors. At mid-rapidity, the TPC, TOF, TRD and EMCal detectors are particularly well suited to electron identification in complementary momentum ranges. Any combination of these detectors may be used for electron identification; indeed, in a recent ALICE publication the heavy-flavor electron spectrum in $\sqrt{s}$ =7 TeV pp collisions was obtained using 3 different detector combinations for particle identification (TPC+TOF+TRD, TPC+TOF and EMCal+TPC) [23]. Moreover, the analysis in this thesis is soon to be published in a paper where the measured heavy-flavor electron cross-section combines results from 3 analyses using the TPC+TOF, TPC stand-alone and TPC+EMCal for electron identification [283]. Electron identification in this analysis was performed with a combination of the EMCal and the TPC. These detectors are nicely complementary in that the PID capabilities of the TPC decline with p_T (the p_T resolution decreases and the $\frac{dE}{dx}$ bands begin to cross making identification based on $\frac{dE}{dx}$ difficult), whereas the energy resolution of any calorimeter improves with increasing energy and particle identification capabilities should not deteriorate with p_T. Combining measurements from the TOF and/or TRD may increase the efficiency and/or purity in the intermediate p_T region. However, an analysis using solely the TPC and EMCal highlights the capabilities of the EMCal detector. Moreover, Yale was heavily involved with the EMCal project and I was more aware of the technical details of the EMCal detector operation. Hence in this analysis particle identification was performed solely with the EMCal and TPC. In this chapter the PID strategy is delineated, the method of estimating the PID efficiency and purity is described, and finally the estimation of the systematic uncertainties in this part of the reconstruction is presented.

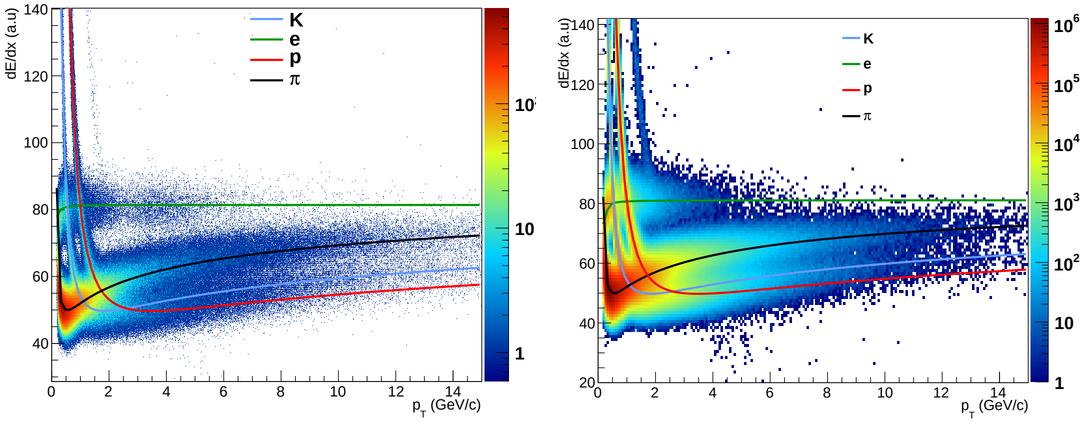

(a) (b)

Figure 5.1.1: $\frac{dE}{dx}$ as a function of momentum, p, for 2.76 TeV pp EMCal triggered (left) and MB (right) events. The solid lines are tuned Bethe-Bloch parameterization curves for different species

5.1 Electron PID Optimization and Strategy

The total energy loss of particles as they traverse the TPC is highly species dependent; the characteristic Bethe-Bloch bands for different particle species illustrate this. These differing responses are the basis of particle identification using the TPC. Figure 5.1.1 shows the $\frac{dE}{dx}$ signal of all tracks that pass the track quality cuts for EMCal triggered and MB data along with tuned Bethe-Bloch parameterizations for each species. The possibility of using the TPC to perform particle identification is apparent from the differing particle responses. In practice, the exact form depends upon features of the TPC design, such as the drift gas composition, and upon time-dependent factors such as the temperature and pressure of the drift gas [284]. Hence a parameterization of the Bethe-Bloch curve is often employed, and ALICE follows the ALEPH collaboration in using the following parameterization [285]:

$$f(\beta\gamma) = \frac{P_1}{\beta^{P_4}}\left(P_2 - \beta^{P_4} - \ln\left(P_3 + \frac{1}{(\beta\gamma)^{P_5}}\right)\right) \tag{5.1}$$

Since the ALICE TPC utilizes a truncated mean method, the signal depends somewhat on the detector configuration (in particular the gains). For each data production period the parameters of the Bethe-Bloch response are extracted and saved to the offline conditions database (OCDB) as *TSplines*; corrections for the time-dependent factors within a period are updated every 5-15 minutes. The determination of these parameters is based on pions, protons, kaons and electrons in regions of clear separation (at lower momenta). Where there is ambiguity (primarily at higher momenta where the bands begin to cross) TOF identification is also employed to provide a cleaner sample. The curves in Figure 5.1.1 are examples of these TSplines for the data used in this analysis.

These distributions indicate that (with an efficacy depending upon the p_T range in question) that particle separation may be achieved by placing cuts on the $\frac{dE}{dx}$ value, or more robustly (allowing for a Bayesian analysis), by placing cuts on the number of sigmas from a particular parameterization (the width of the $\frac{dE}{dx}$ distribution also being parameterized in the TSplines). In this analysis a cut on the $n\sigma_e$ value (the number of sigmas from the electron band) is used to identify electrons with the TPC.

The second element of the PID already alluded to is an examination of the $\frac{E}{p}$ distributions using the energy deposition in the EMCal. In the EMCal testbeam analysis, the rejection factor was examined for various EMCal particle identification parameters. It was shown that by far the most effective parameter was $\frac{E}{p}$. Figure 5.1.2 shows the $\frac{E}{p}$ distributions for electrons and hadrons as measured during the testbeam data taking. There is a clear separation of hadrons from electrons in $\frac{E}{p}$ space, and it was expected that an appropriately chosen cut on $\frac{E}{p}$ could be used to identify electrons. Combining other parameters in some multi-variate analysis was seen as a promising possibility but time did not allow for an exploration of this option. In this analysis good purity and efficiency was obtained using $\frac{E}{p}$ alone (in addition to the TPC). Hence, consideration of various shower shape parameters was not undertaken, although in other analyses (for instance heavy ion collisions where the density of clusters will be greater) it may be useful.

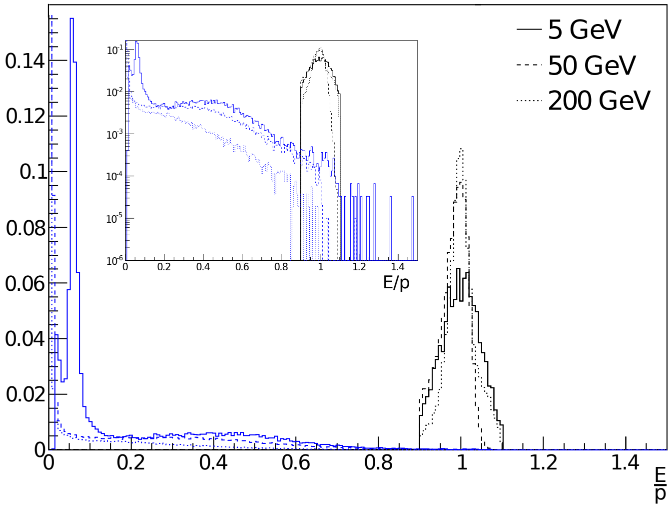

Figure 5.1.2: E/p distributions of electrons (black) and hadrons (blue). The inlay is the same plot with a logarithmic y-axis

To take advantage of possible correlations between PID selection criteria, electron identification was performed with a cut placed in 2D ($n\sigma_e$, $\frac{E}{p}$) space. Figure 5.1.3 shows the $n\sigma_e$ vs $\frac{E}{p}$ distribution

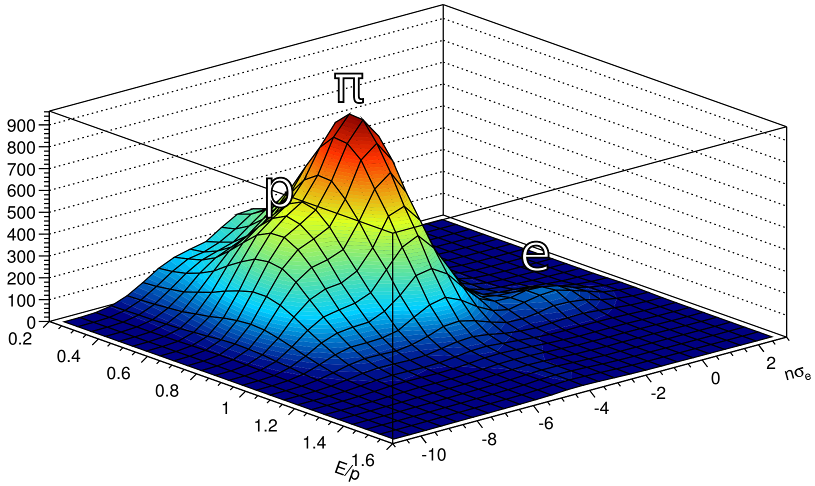

Figure 5.1.3: $n\sigma_e$ vs $\frac{E}{p}$ for the EMCal triggered data integrated over all $p_T > 4$ GeV/c

for the EMCal triggered data integrated over all $p_T > 4$ GeV/c. Although this plot does not show the explicit p_T dependence (Appendix C.1 shows the same distribution for different p_T slices), the visibility of the electrons as an ellipse around (1,0) makes it clear it is clear that the strong correlation between the two parameters should enable good electron identification. Given the apparent shape of the electron distribution in ($n\sigma_e$, $\frac{E}{p}$) space, two different cut selection profiles were studied; a rectangular cut selection and an ellipsoidal cut selection in ($n\sigma_e$, $\frac{E}{p}$) space. The rectangular cut selection should be adequate when no correlations are present and it is often the first cut selection choice employed when selecting on several variables. An ellipsoidal cut seemed visually to be an ideal shape to exploit the correlations between the variables. Hence, the selection of electrons based on both rectangular and ellipsoidal cut criteria was investigated.

The PID cut selection was optimized using the effective signal parameter discussed in Appendix B and utilized in the context of testbeam data. To cope with any possible p_T dependence, the $n\sigma_e$ vs $\frac{E}{p}$ distributions were plotted in various p_T slices. For each p_T bin a simple optimization algorithm was implemented: the idea was to draw ellipses of varying centers and axes, and determine the purity and efficiency of selecting electrons based on each such constructed ellipse. Some reasonable constraints were first placed on the center, the major axis and minor axis of the ellipse. The parameters were then varied between these constraints, generating an ellipse for each set of parameters and the purity and efficiency was calculated. To determine the efficiency and purity, some region of $n\sigma_e - \frac{E}{p}$ space has to be characterized as a pure electron sample. A standard methodology, which was also employed in this optimization procedure, is to classify particles with $n\sigma_e$ greater than 0 (or more precisely the position of the electron peak maximum, e_0) as an electron. At higher p_T this assumption begins to fail as the $\frac{dE}{dx}$ bands start to merge, and this is taken into account in the determination of the PID efficiency and purity, but it is not taken into account in this optimization algorithm. The signal (S) enclosed within the ellipse is then taken to be the sum of the number of tracks inside the ellipse and greater than e_0, plus the number of tracks enclosed within a 'mirror ellipse' (an ellipse reflected about the line $y = e_0$) and greater than e_0. The latter step assumes that the electron distribution is symmetrical around the peak position of the electron. The background (B) is taken to be the number of tracks enclosed within the ellipse below the electron peak position minus the number of tracks enclosed within a 'mirror ellipse' and greater than e_0. The procedure is illustrated in Figure 5.1.4. A similar procedure was followed to select an optimum rectangular cut criteria.

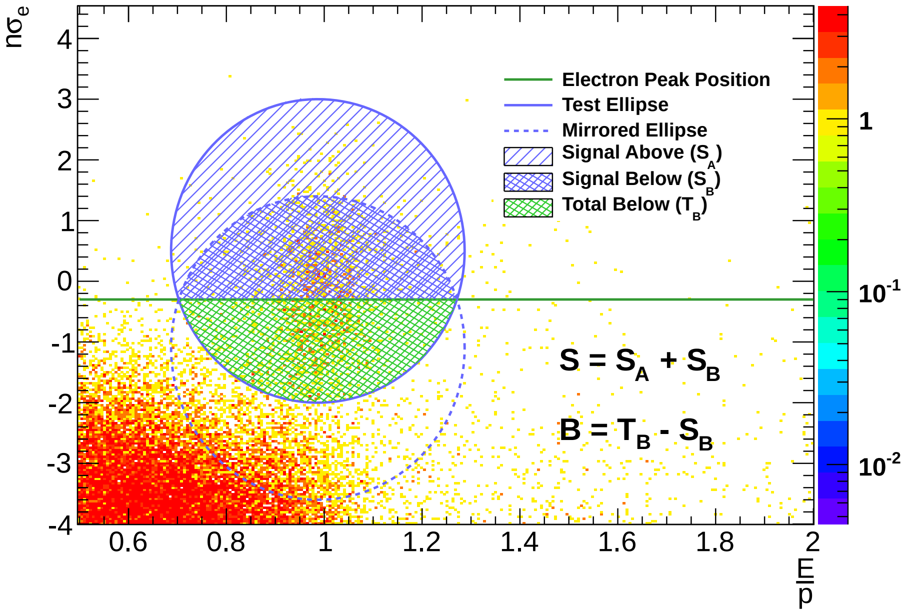

Figure 5.1.4: $n\sigma_e$ vs $\frac{E}{p}$ for the EMCal triggered data integrated over all p_T illustrating the PID optimization method. A test ellipse is drawn followed by a mirror of this ellipse about the peak position of the electron distribution in $n\sigma_e$ space. The highlighted regions are used to calculate the signal (S) and background (B) as described in the text

Following this procedure, an optimum ellipse and an optimum rectangular cut criteria for each p_T bin were obtained. The optimization procedure was also applied to a rectangular and ellipsoidal selection criteria *integrated over* p_T for reasons to be discussed (i.e $n\sigma_e$ vs $\frac{E}{p}$ was plotted for all p_T and optimized, rather than being plotted in p_T slices and optimized for each p_T bin). The effective signal was also calculated for an ellipse that was constructed so as to visually take into account the correlations. Hence, an effective signal was obtained for 2 optimized rectangles, 2 optimized ellipses, and one ellipse constructed ad-hoc. Figure 5.1.5 shows the effective signal for MB and EMCal trigger data as a function of p_T for these various cut choices. As one may expect, the p_T dependent optimized ellipse exhibited the greatest effective signal at most values of p_T.

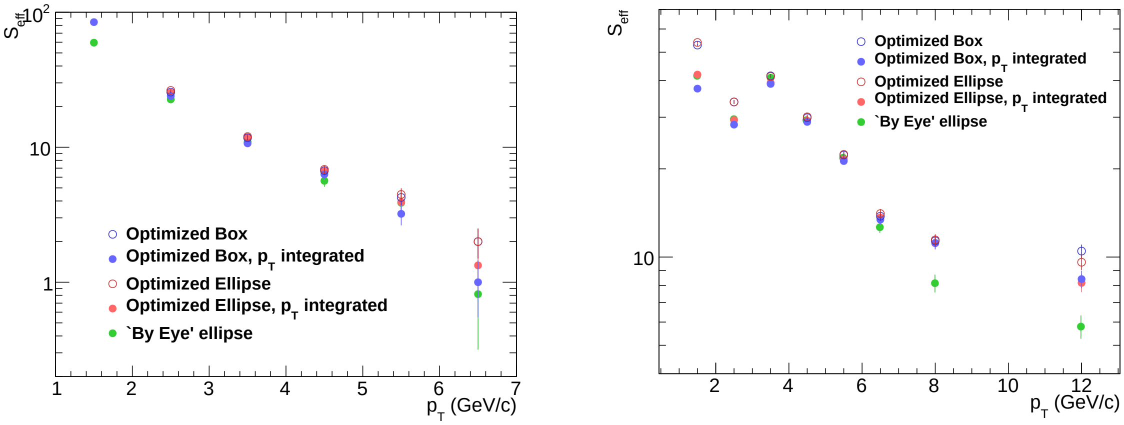

Figure 5.1.5: Effective Signal of various PID selection criteria in MB (left) and EMCal triggered data (right)

Although the p_T dependent optimized ellipse exhibited the greatest effective signal, there were problems with implementing a p_T dependent cut for this data set. Unfortunately, limited statistics impose quite a severe restriction on the number of p_T bins that could be used for the determination of the purity and efficiency corrections (see Figure 5.2.8 to see the size of the bins selected). This necessitates large extrapolations between widely separated p_T bins. When a p_T independent cut is placed this does not pose too much of a problem: the shape of the purity and efficiency as a function of p_T are expected to be smooth, and the general shape is expected to be similar to that in simulation. However with a p_T dependent cut, the purity and efficiency may have some seemingly discontinuous jumps as a function of p_T. This limits the ability to perform reasonable extrapolations between p_T bins. Moreover, although the p_T dependent optimized ellipse does generate the greatest effective signal at most points, the differences in the effective signal between cut criteria is small, and mostly within statistical uncertainty. These factors led to the selection of a p_T independent PID cut to improve the PID efficiency and purity estimation. Since the difference between the various methodologies was small, and the implementation of rectangular cut was simpler, a p_T independent rectangular PID cut was employed. Figure 5.1.6 shows the optimized p_T independent ellipsoidal and rectangular cut choices along with the visually constructed ellipse in MB and EMCal triggered data. The relatively wide rectangles are a consequence of the defining characteristic of electrons

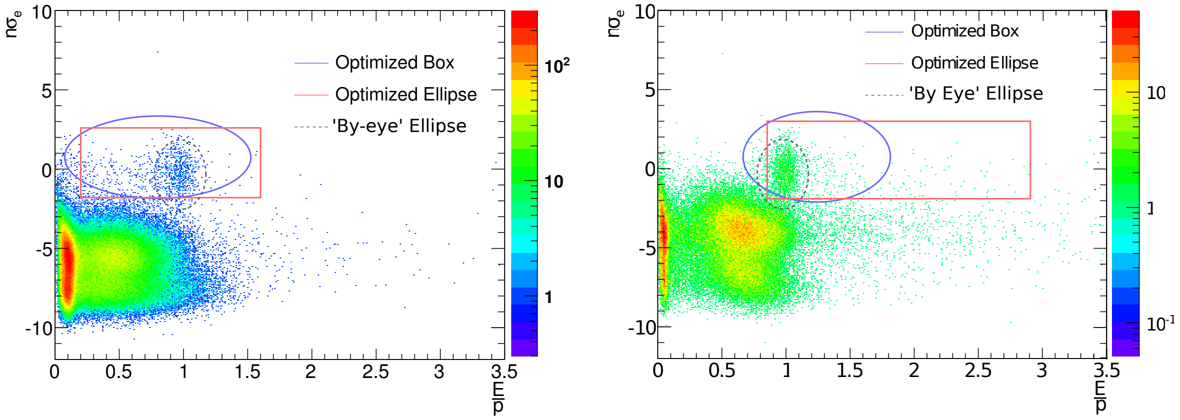

Figure 5.1.6: p_T independent optimized cut choices in MB (left) and EMCal triggered data (right)

PID Cut Parameter	Data Set	Selection Criteria
$\frac{E}{p}$	MB	$0.2 \leq \frac{E}{p} \leq 1.6$
$n\sigma_e$	MB	$-1.8 \leq n\sigma_e \leq 2.6$
$\frac{E}{p}$	EMCal Triggered	$0.85 \leq \frac{E}{p} \leq 2.9$
$n\sigma_e$	EMCal Triggered	$-1.9 \leq n\sigma_e \leq 3$

Table 5.1.1: Electron PID cuts used in this analysis

which is taken to be $n\sigma_e > e_0$, and thus increasing the size in $\frac{E}{p}$ space allows more electrons to be included at high and low $\frac{E}{p}$. Another consequence of this characterization of electrons is that in the MB data, where the average p_T is lower and hence the $\frac{dE}{dx}$ bands have greater separation, the optimized ellipse and box are able to extend to lower values of $\frac{E}{p}$. Table 5.1.1 summarizes the PID strategy employed in this analysis. In the final analysis, the exact cut criteria selected should not have a noticeable impact on the final result as the PID efficiency and purity are to be corrected for. However, the optimization procedure verified that the optimization space was reasonably smooth, and no particular selection criteria would obviously allow for large increases in the effective signal.

5.2 Determination of the PID Efficiency and Purity

Having selected and employed a PID strategy, the resulting yield of identified electrons has to be corrected for both the PID efficiency (which results in some electrons not being correctly identified) and the PID purity (which results in contamination of the sample of identified electrons). In this analysis, the efficiency and purity are determined from data driven methods to circumvent any discrepancies between simulation and data. Two methods of estimating the purity were utilized (one was used solely as a cross-check, see further discussion), and one method for estimating the efficiency was implemented. The first method for estimating the purity utilizes the $n\sigma_e$ distributions ('TPC method'), and the second method for estimating the purity uses the $\frac{E}{p}$ distributions ('EMCal method'). In theory, the second method should be superior at higher energies (where the $\frac{dE}{dx}$ bands start to merge), however other difficulties limited it's efficacy. The only method for estimating the efficiency was based on the $n\sigma_e$ distributions.

5.2.1 TPC Method of Purity and Efficiency Estimation

The TPC method of PID efficiency and purity estimation relies on characteristics of the $n\sigma_e$ distribution. Figure 5.2.1 shows the $n\sigma_e$ distribution in EMCal triggered data for $5 < p_T < 6$ GeV/c and illustrates the method of PID purity estimation. Three peaks in the $n\sigma_e$ distribution are clearly visible: the rightmost peak consistent with the response of electrons, the middle peak corresponding to pions, and the leftmost peak being the sum of the kaon and proton responses which are clearly not distinguishable at this p_T. This indistinguishability of the kaon and proton bands is not pertinent for the estimation of the electron identification purity as the only component of the background which extends to within the PID cut criteria is the pion gaussian. The PID criteria employed involves both a cut in $\frac{E}{p}$ space and in $n\sigma_e$ space, so in this figure only tracks which also pass the $\frac{E}{p}$ cut are plotted to enable identification of those tracks which pass all of the PID cuts. The sample of tracks

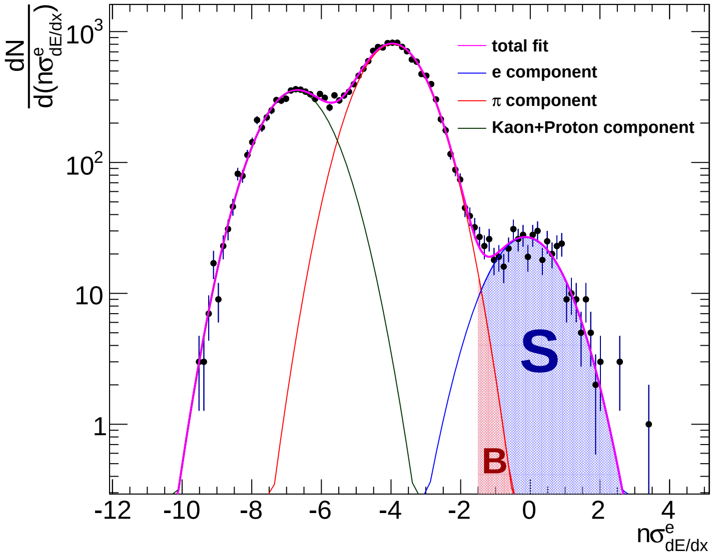

Figure 5.2.1: $n\sigma_e$ distribution of all tracks which pass the $\frac{E}{p}$ cut and have $5 < p_T < 6$ GeV/c in EMCal triggered data

identified as electrons thus corresponds exactly to the area under the $n\sigma_e$ distribution that also passes the $n\sigma_e$ selection cut (this is the blue region in the figure, which includes the red region as a subset). Evidently there is some contamination of the sample due to pions that extend beyond the lower PID cut. The contamination is estimated by fitting a sum of three gaussians to the total $n\sigma_e$ distribution. The pink curve represents this 3-gauss fit to the total $n\sigma_e$ distribution, and the blue, red and black curves represent the individual components of the fit (that correspond to electrons, pions and kaons/protons respectively). In some p_T bins, where the fitting procedure failed when unconstrained, visually appropriate constraints were placed on the fits. By taking the ratio of the area under the electron gaussian that passes the $n\sigma_e$ cut to the area under the total fit that passes the $n\sigma_e$ cut, an estimation of the purity was obtained. With reference to the diagram:

$$p_{PID} = \frac{S}{S+B} \tag{5.2}$$

The estimation of the PID efficiency requires an estimate of the total number of electrons in the sample. At low p_T it is clear that the electron band is well separated from the pion, kaon and proton bands (see Figure 5.1.1). Moreover, throughout almost the entire momentum range considered in this analysis, the electron response is clearly distinguishable from that of other species. In particular, all tracks with $n\sigma_e > e_0$ can safely be assumed to be electrons. Hence the total number of electrons in the sample can be estimated to be $N_e = 2\int_{e_0}^{\infty} f(n\sigma_e)d(n\sigma_e)$ where $f(n\sigma_e)$ is the sum of three gaussian fit to the $n\sigma_e$ distribution *without* the $\frac{E}{p}$ cut applied. To estimate the number of electrons using this method thus requires the $n\sigma_e$ distribution to be plotted both with and without the $\frac{E}{p}$ cut applied. Figure 5.2.2 illustrates the method for estimating the efficiency. The $n\sigma_e$ distribution is plotted both with and without the $\frac{E}{p}$ cut applied, and a sum of three gaussians is fitted to these distributions exactly as for the purity estimation. In Figure 5.2.2 the effect of applying the $\frac{E}{p}$ cut is apparent: the number of electrons changes very little, but a significant fraction of the pions, protons and kaons are rejected. A subset of the tracks are defined as pure electrons with a cut on $n\sigma_e$ which may or may not the same as the PID cut (this cut is denoted the *purity cut* as indicated in the figure), The fraction of electrons (as defined by the fitted electron gaussian) which pass the purity cut is denoted f_{pure} and the number which pass the purity cut is denoted N_{pure}. In the methodology hitherto described, the purity cut is defined as the electron mean position and $f_{pure} = 1/2$. The number of estimated electrons in the sample is then given by $N_e = N_{pure}/f_{pure} = 2N_{pure}$ exactly as previously noted. The number of identified electrons is determined using the $n\sigma_e$ distribution with the $\frac{E}{p}$ cut applied. One could utilize the estimated purity to determine the number of identified

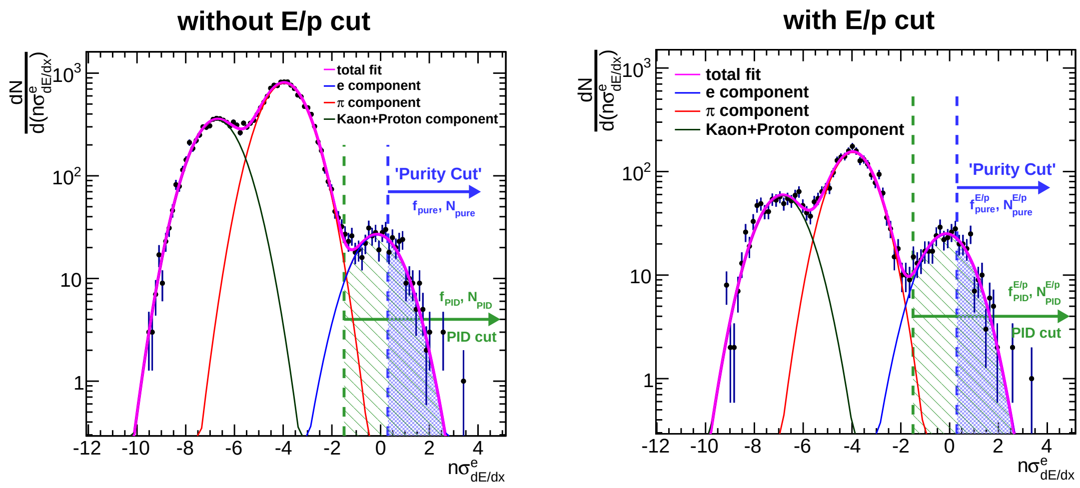

without E/p cut

with E/p cut

Figure 5.2.2: $n\sigma_e$ distribution of all tracks with $5 < p_T < 6$ GeV/c (left), and all tracks that pass the $\frac{E}{p}$ cut (right) in EMCal triggered data

electrons, but in this analysis the number of electrons in the sample is taken to be $\frac{N_{pure}^{\frac{E}{p}}}{f_{pure}^{\frac{E}{p}}}$, and hence (with reference to the right hand side of the figure):

$$\epsilon_{PID} = \frac{N_{pure}^{\frac{E}{p}}}{f_{pure}^{\frac{E}{p}}} f_{PID}^{\frac{E}{p}} = 2N_{pure}^{\frac{E}{p}} f_{PID}^{\frac{E}{p}} \tag{5.3}$$

where $N_{pure}^{\frac{E}{p}}$ is the number of tracks that pass the $\frac{E}{p}$ PID cut that also pass the 'purity cut', $f_{pure}^{\frac{E}{p}}$ is the fraction of electrons that pass the 'purity cut', and $f_{PID}^{\frac{E}{p}}$ is the fraction of electrons that pass the PID cut. The second equality follows from assuming $f_{pure}^{PID} = f_{pure} = 1/2$.

To estimate the efficiency and purity as a function of p_T, this procedure is repeated for multiple p_T slices. The appropriate binning used in this process is determined by the limited statistics. An essential cross-check of the methodology is to ensure that the fitted gaussians have mean positions and widths that are consistent with expectations. Figure 5.2.3 illustrates this cross-check. The figure shows the $n\sigma_e$ distributions as a function of p_T in MB and EMCal triggered data, along with the TSplines discussed in section 5.1, and the mean positions of the fitted gaussians. The error bars associated with the mean peak positions represent the width of the fitted gaussians (1 σ). The peak positions mostly track the respective TSplines well, and there are no obviously rogue fits. It is apparent that the fit to the third peak (lowest $n\sigma_e$) combines the effect of the kaons and protons. Another noticeable characteristic is that the electron mean position is slightly lower than TSpline for all momenta. This is a consequence of a slight error in the TSpline fit that was later corrected, but not before the analysis was complete. However, the absolute position of the electron peak is not

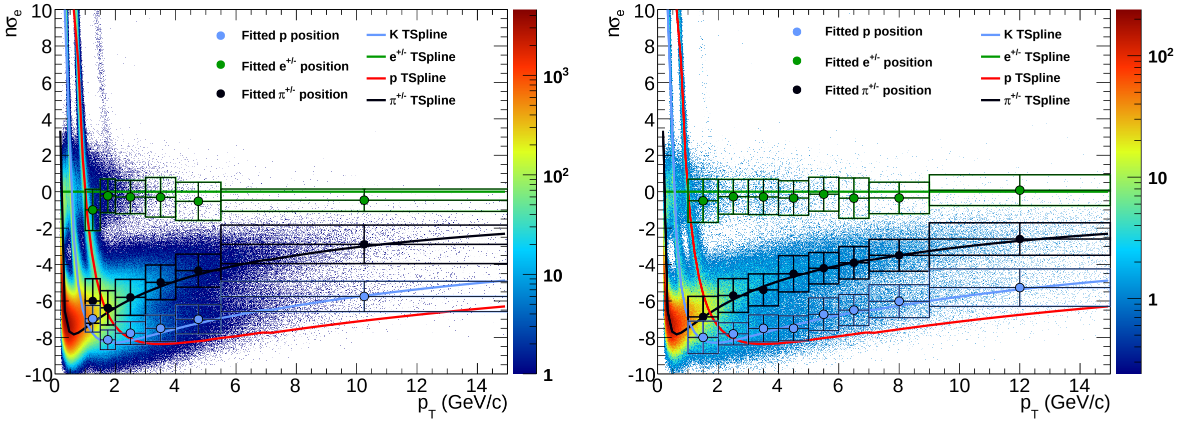

Figure 5.2.3: $n\sigma_e$ vs p_T with the Bethe-Bloch parameterizations (solid curves) for each particle species and the mean of the gaussian fitted to the $n\sigma_e$ distributions (circular points) for MB data (left) and EMCal triggered data (right). The error bars represent the sigma of the fitted gaussian

relevant as all calculations are performed *with respect* to this peak position.

One final correction was employed to determine the final PID efficiency and purity. Although the assumption that a pure electron sample is provided by all tracks with $n\sigma_e > e_0$ is reasonable for most of the momentum range covered in this analysis, at $p_T \gtrsim 10$ GeV/c the $\frac{dE}{dx}$ bands start to overlap and this assumption fails. This fact was observed in simulations, and it results in an estimated efficiency that is lower than the true efficiency. With reference to Figure 5.2.2, at high p_T the pion gaussian moves sufficiently far to the right that the pion tail begins to extend beyond the purity cut of e_0. To overcome this problem, the purity cut was moved further to the right, and the efficiency was calculated according to the first equality in equation 5.3. For example, one could take the top 1/3 of the electron gaussian to be a pure electron sample, and the total number of electrons in the sample would be 3 times the integral of this top 1/3 of electrons. To understand how the efficiency is expected to behave as the purity cut is varied, and to determine an appropriate choice of the purity cut, a simple toy model was employed. The model is described in Appendix C.2, but the main result is presented in Figure 5.2.4. The figure shows how the estimated efficiency changes as a function of the purity cut in 4 different background scenarios: 3 cases with pion gaussians of different mean positions that represent different levels of contamination, and one pion gaussian with a non-gaussian tail that extends into the sample of tracks defined as pure electrons. No evidence was observed of non-gaussian behavior of $n\sigma_e$, so only the three gaussians were relevant. The conclusion of the study was what one may expect: at low values of the purity cut the estimated PID efficiency is lower than the true value. Moreover, as the purity cut is increased, the efficiency plateaus at the

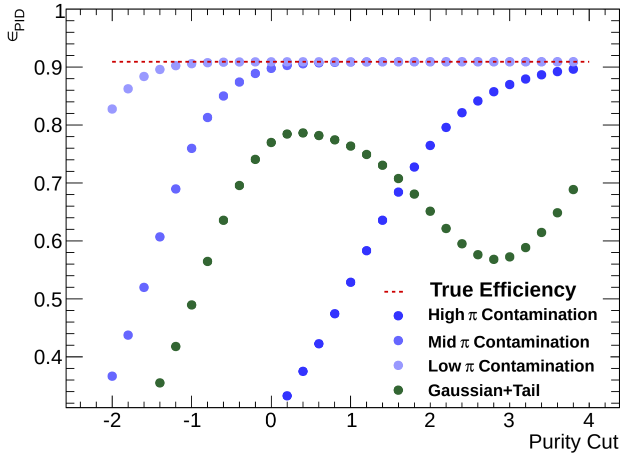

Figure 5.2.4: Estimated PID efficiency in the toy model for various background scenarios as a function of the purity cut

true value of the efficiency. This suggests a simple way to determine an appropriate choice of the purity cut: if the efficiency is calculated as a function of the purity cut, then where the efficiency reaches a plateau should provide an estimate of the true value.

Figure 5.2.5 shows the calculated efficiency for EMCal triggered data as a function of the purity cut for each p_T bin that the efficiency is calculated in. The behavior is as expected from the simple model: at low p_T the efficiency does not change as a function of the purity cut since there is low contamination; whereas in higher p_T bins the characteristic efficiency 'turn-on' is observed as the purity cut is varied, eventually reaching a plateau. The efficiency was thus redetermined by fitting a line to the plateau region in each p_T bin. This procedure reduced the statistical uncertainty in the estimated efficiency, and also prevented contamination from affecting the estimated efficiency. For all p_T bins except the last p_T bin, choosing a purity cut of e_0 produced results consistent with fitting a line to the efficiency plateau. Evidently, in the last p_T bin the assumption that all tracks with $n\sigma_e > e_0$ are electrons fails. In the final result the efficiency is calculated using these straight line fits and their associated uncertainties.

5.2.2 EMCal Method of Purity Estimation

In addition to PID purity estimation utilizing the TPC, the purity was also estimated using the EMCal alone. Hadrons typically deposit a fraction of their energy in the calorimeter while electrons typically deposit all of the their energy in the calorimeter due to the large difference in the radiation length and the nuclear interaction length. Thus the ratio of energy deposited in the EMCal to the

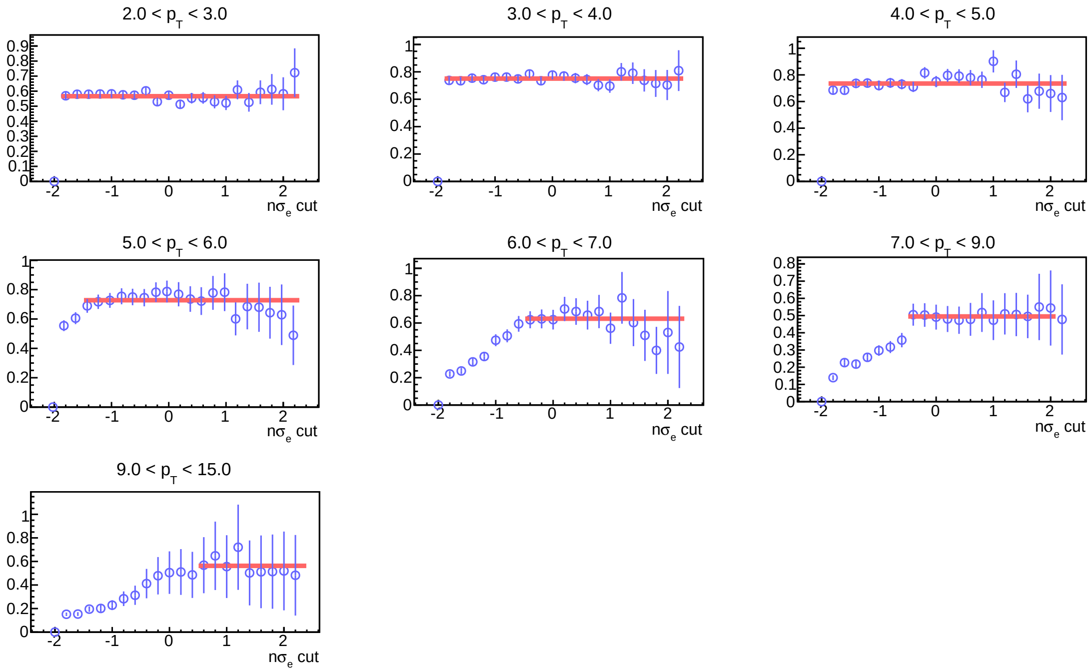

Figure 5.2.5: Estimated PID efficiency as a function of the purity cut in EMCal triggered data. Each histogram represents a different p_T bin in GeV/c

momentum of the matched track can provide discriminatory capabilities. Moreover, the characteristic responses enable an estimate of the PID purity to be made. Figure 5.2.6 shows the $\frac{E}{p}$ distribution in simulation (lhc11b10b) for tracks in the momentum range 4 GeV/c $< p_T <$ 5 GeV/c, and illustrates the PID purity estimation method. Like the TPC method of purity estimation, the cut parameter can be plotted with and without the other element of the PID applied; in this case $\frac{E}{p}$ can be plotted with and without the $n\sigma_e$ cut applied, and for the PID purity estimation it should be plotted with the $n\sigma_e$ cut applied. However, in the figure shown $\frac{E}{p}$ is plotted without the $n\sigma_e$ cut applied simply because the increased statistics provide a better illustration of the methodology. In the following discussion it is treated as if the $n\sigma_e$ cut has been applied.

In order to estimate the PID efficiency/purity using the $\frac{E}{p}$ signal, the characteristic responses of electrons and hadrons have to parameterized. The similar problem with the TPC method is relatively simple: it is well known that the $\frac{dE}{dx}$ signal for each species is a gaussian. The case of the $\frac{E}{p}$ distribution is less straight forward. The hadronic response is highly detector dependent, and there is no simple parameterization of its shape. In the region that is being considered ($\frac{E}{p} \approx 1$), an exponential tail is often a good approximation, and this is what is assumed in estimating the PID purity in this analysis. The electron response is expected to be a gaussian centered around $\frac{E}{p} \approx 1$. However there are tails at both low and high values of $\frac{E}{p}$. Low values of $\frac{E}{p}$ are due to energy

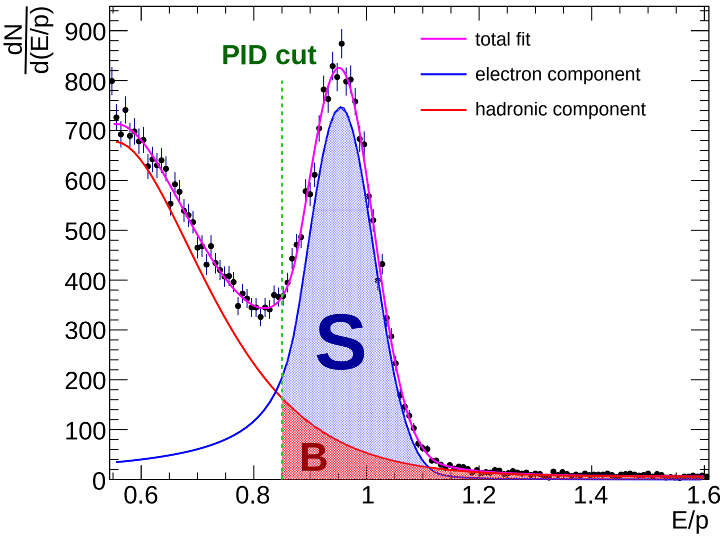

Figure 5.2.6: $\frac{E}{p}$ signal in simulation (lhc11b10b) for tracks with $4 < p_T < 5$. The curves are fits used to estimate the PID purity

losses of the electrons as they traverse the detector, in particular Bremsstrahlung energy losses. The characteristic shape of this energy loss is understood, and the total electron response including the Bremsstrahlung tail is well parameterized by a crystal ball function of the form[286]:

$$f(x;\alpha,n,\bar{x},\sigma) = N \cdot \begin{cases} \exp(-\frac{(x-\bar{x})^2}{2\sigma^2}), & \text{for } \frac{x-\bar{x}}{\sigma} > -\alpha \\ A \cdot (B - \frac{x-\bar{x}}{\sigma})^{-n}, & \text{for } \frac{x-\bar{x}}{\sigma} \leqslant -\alpha \end{cases}$$

where

$$A = \left(\frac{n}{|\alpha|}\right)^n \cdot \exp\left(-\frac{|\alpha|^2}{2}\right)$$

$$B = \frac{n}{|\alpha|} - |\alpha|$$

$$N = \frac{1}{\sigma(C+D)}$$

$$C = \frac{n}{|\alpha|} \cdot \frac{1}{n-1} \cdot \exp\left(-\frac{|\alpha|^2}{2}\right)$$

$$D = \sqrt{\frac{\pi}{2}}\left(1 + \mathrm{erf}\left(\frac{|\alpha|}{\sqrt{2}}\right)\right)$$

N is a normalization factor and α, n, $\bar{x}$ and σ are parameters which are fitted with the data. $\bar{x}$ and σ represent the mean and width of the electron gaussian, and ‘erf’ refers to the error function.

However, the high $\frac{E}{p}$ tail is not so well understood. Cases of high $\frac{E}{p}$ can occur when the track extrapolated to the EMCal is matched to the wrong cluster, when the momentum is underestimated in the TPC, and when the clusterization does not distinguish between two particles which strike the EMCal near the same point. Evidently, the nature of this tail depends greatly on the details of the specific detector, in particular upon the track-cluster matching algorithm and the clusterization algorithm. Moreover, even though the Bremsstrahlung tail can be well described by a known function, the magnitude of this tail (the size of the tail relative to the gaussian) is not fixed and is part of the parameterization. These effects, combined with the uncertainty in the shape of the hadronic response, make an estimation of the PID efficiency impossible. It is not possible, with reasonable uncertainty, to determine what fraction of the high $\frac{E}{p}$ and low $\frac{E}{p}$ tracks are electrons. However, a decent estimation of the purity can be made since the application of the $n\sigma_e$ cut cleans the sample of electrons considerably. The following procedure was used to determine the purity:

- All tracks with $n\sigma_e < -2$ are used to plot an $\frac{E}{p}$ distribution. This sample is taken as a pure sample of hadrons
- A fit is performed to this $\frac{E}{p}$ distribution with an exponentially decaying shape. This also provided a verification that the exponential shape reflected the hadronic response in data
- The $\frac{E}{p}$ distribution is plotted for all tracks that pass the $n\sigma_e$ cut
- The fit performed in the second step is scaled to match the total $\frac{E}{p}$ distribution at low values of $\frac{E}{p}$
- The total $\frac{E}{p}$ distribution is fitted with a sum of a *double* crystal ball function and the *fixed* hadronic response fitted in the previous step
- These fits are used to estimate the purity

What is referred to as a double crystal ball function assumes a form similar to the crystal ball function but with tails on both sides of the gaussian. This form is assumed to try to take into account the high $\frac{E}{p}$ tail in the electron response. Instead of the scaling procedure used for the hadronic response, it is also possible to just fit a sum of an exponential tail and the double crystal ball function with freely varying parameters. However, this introduces a large number of free parameters, and the fits are usually not very well constrained. The results are similar using both methods, but the uncertainty associated with the fit is smaller when the hadronic response is constrained as described.

The result of this procedure are three fits similar to those in Figure 5.2.6: one for the hadronic response, one for the electron response and one total fit. The purity is then estimated exactly as for the TPC method as (with reference to the figure):

$$p_{PID} = \frac{S}{S+B}$$

Although the results are consistent with the TPC method (see Figure 5.2.7), the lack of precise knowledge about the response of electrons and hadrons hinders the efficacy of this method. No estimation of the PID efficiency can be realistically made since the underlying response of electrons is not precisely known , and even the purity estimation involves a large number of free parameters and a large associated uncertainty. These factors, combined with the paucity of statistics, led to the selection of the TPC method to determine the PID efficiency and purity. However, the EMCal method provided a useful cross-check of the results.

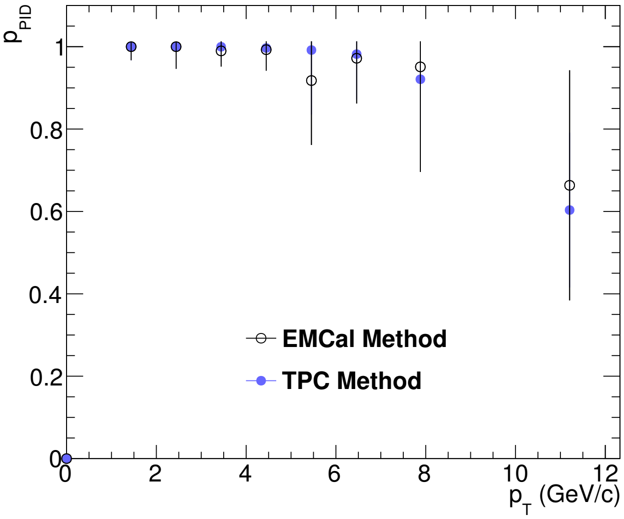

Figure 5.2.7: The estimated purity in EMCal data using the TPC method and the EMCal method. Within error bars, the results are consistent

5.2.3 Results

Figure 5.2.8 shows the estimated PID efficiency and purity in the MB data (left) and the EMCal triggered data (right). The black curve indicates the fit to the data points. Since the binning used for the determination of the PID purity and efficiency is different from the binning used for the spectrum, this fit is important as a method of interpolating between bins. Note that the efficiency and purity are placed not at the bin-center but at the appropriately weighted bin shifted position (this is relevant where the width of the bin is wide relative to the rate of change of the function

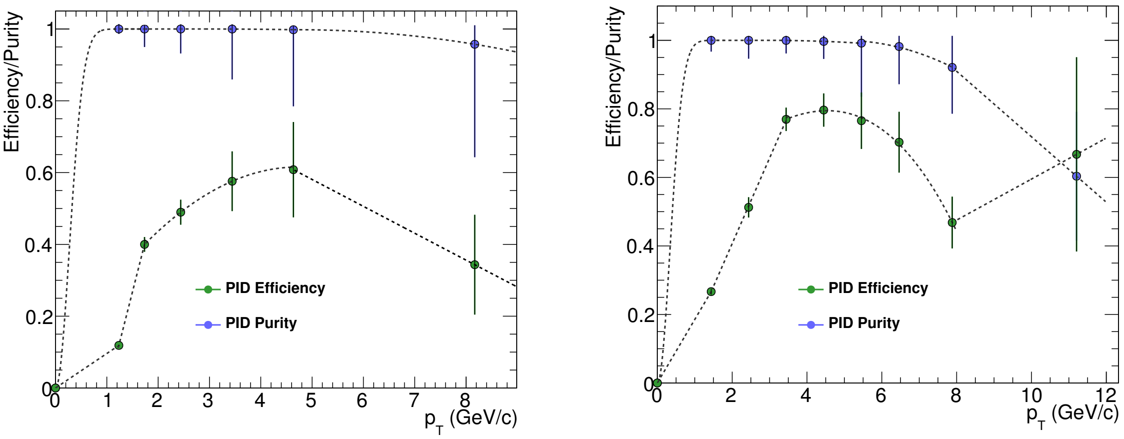

Figure 5.2.8: Estimated efficiency and purity in the MB data (left) and EMCal data (right)

across the bin, see section 8.1).

A comment should be made on the shape of the efficiency and purity. The $\frac{E}{p}$ cut provides a p_T independent purity as the central gaussian of the $\frac{E}{p}$ distribution does not change greatly as a function of p_T. On the other hand, the TPC provides a purity that declines at high p_T due to the crossing of the $\frac{dE}{dx}$ bands. The result of these two effects is as observed in Figure 5.2.8: the purity quickly reaches 100% and then gradually declines at high p_T.

The fixed $n\sigma_e$ cut results in a p_T independent efficiency (although the absolute position and width of the electron peak may change slightly with p_T, a fixed $n\sigma_e$ cut should select a constant fraction of the electrons). However, the $\frac{E}{p}$ cut exhibits a highly p_T dependent efficiency which is manifest in Figure 5.2.8. The general characteristics of the efficiency observed in data and simulations are most apparent in the EMCal triggered data: the efficiency gradually rises from zero to a maximum at $p_T \sim 4$ GeV/c, then slowly decreases before rising again at $p_T \sim 8$ GeV/c. There are a few competing effects which result in this shape. Any inefficiency is due to electrons with an $\frac{E}{p}$ ratio either much greater or much less than 1. The low $\frac{E}{p}$ is due to Bremsstrahlung energy losses which are the dominant mechanism of energy loss for electrons with $E \gtrsim 50$MeV. However, the amount of energy lost scales as $\log(E)$, and thus as p_T increases the fraction of energy lost via this process is reduced and thus the efficiency slowly increases. However, at $p_T \sim 5$ GeV/c the tail at high $\frac{E}{p}$ begins to *increase* and the efficiency decreases. At even higher p_T, the $\frac{E}{p}$ again begins to decrease with a resulting increase in the efficiency. The matching efficiency is approximately constant for $p_T > 2$ GeV/c, and thus the nature of the clusterization algorithm is solely responsible for this behavior at $p_T \gtrsim 4$ GeV/c.

PID cut	Data Set	loose cut	normal cut	hard cut
$\frac{E}{p}$	MB	$0 \leq \frac{E}{p} \leq 3$	$0.2 \leq \frac{E}{p} \leq 1.6$	$0.9 \leq \frac{E}{p} \leq 1.3$
$n\sigma_e$	MB	$-3 \leq n\sigma_e \leq 4$	$-1.8 \leq n\sigma_e \leq 2.6$	$-0.5 \leq n\sigma_e \leq 2$
$\frac{E}{p}$	EMCal Triggered	$0.6 \leq \frac{E}{p} \leq 3.5$	$0.85 \leq \frac{E}{p} \leq 2.9$	$0.9 \leq \frac{E}{p} \leq 1.3$
$n\sigma_e$	EMCal Triggered	$-3 \leq n\sigma_e \leq 4$	$-1.9 \leq n\sigma_e \leq 3$	$-0.5 \leq n\sigma_e \leq 2.5$

Table 5.3.1: The three set of track cuts used for determining the systematic uncertainty in the estimation of the PID efficiency and purity

Very few hadrons are expected to deposit a significant fraction of their energy at high p_T, and this fraction decreases with increasing energy. Thus perhaps at high p_T, the energy deposition of the electron is much greater than the energy deposition due to the copious hadrons present in the event. The clusterization algorithm can then quite easily unfold the contribution of the electron and generate an appropriately sized cluster. At intermediate p_T, the unfolding of the clusters may be less effective if the energy distribution is more uniform. Although a reasonable explanation, the exact reason for this shape was not ascertained. However, the fact it is observed in simulation and data suggests that it is a real effect associated with the clusterization algorithm.

Also note that the purity is similar in MB and EMCal trigger data, though the efficiency appears to be different. In fact, the efficiency is consistent for $p_T \lesssim 2$ GeV/c and also consistent for $p_T \gtrsim 8$ GeV/c. However, between these regions the EMCal trigger data exhibits a higher PID efficiency. This discrepancy is due to the effect of the trigger. In Chapter 6, it is shown that for most triggered events that have electrons with momenta greater than the trigger threshold, the event is triggered by this electron and not some other particle. Since the spectrum is exponentially falling as a function of p_T, by examining only triggered events we are selecting electrons that preferentially have $\frac{E}{p} \sim 1$, and hence the electron selection criteria is significantly more efficient near the turn-on.

5.3 Systematic Uncertainty

The systematic uncertainty associated with the PID efficiency and purity corrections was comprised of two components. Although it is not possible to completely separate these components, they roughly corresponded to the uncertainty associated with calculating efficiencies and purities with finite statistics, and the possible systematic uncertainty associated with the methodology itself. The latter is estimated by varying the PID cut selection between *normal*, *loose* and *hard* cut choices. Table 5.3.1 delineates the cut choices used to determine the PID efficiency and purity. Figure 5.3.1 shows the ratios of the reconstructed spectra using the various cut choices in the EMCal triggered

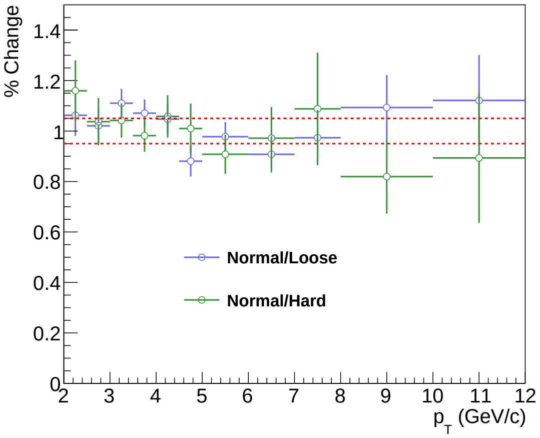

Figure 5.3.1: Ratio of reconstructed spectrum with normal PID cuts to the reconstructed spectra with loose and hard PID cuts in EMCal trigger data. The red line indicates the assigned systematic uncertainty

data set. The red band indicates the assigned systematic uncertainty; for both MB and EMCal triggered data the estimated systematic uncertainty was 5%.

The total PID efficiency and purity systematic uncertainty was dominated by the second contribution arising from the calculation of the efficiency and purity with limited statistics. The statistical uncertainty in the estimated efficiency and purity is quite significant at high p_T as Figure 5.2.8 makes clear. To incorporate this fact, three fits were made to the PID efficiency and purity: the fit indicated on Figure 5.2.8, in addition to a fit to the maximum and a fit to the minimum of the error bars associated with the calculated efficiency and purity. These fits were then applied to the raw yield to obtain three spectra which define the systematic uncertainty band associated with the PID efficiency and purity correction. Unlike for the first component of the systematic uncertainty where the systematic uncertainty is assigned a p_T independent figure, the second component is assigned a p_T dependent value since it is related to the available statistics. Figure 5.3.2 shows the reconstructed spectra for the three cases, where the maximum and minimum spectra are represented as error bands around the central spectrum. The systematic uncertainty associated with this component was determined to be $\sim$ 5% for $p_T \sim 2$ GeV/c, and grows to $\sim$ 30% in the last p_T bin. As a conservative estimate, these contributions are added in quadrature to obtain the final systematic uncertainty associated with the PID efficiency and purity corrections. Also see Chapter 8, where the different sources of systematic uncertainty are compared as a function of p_T.

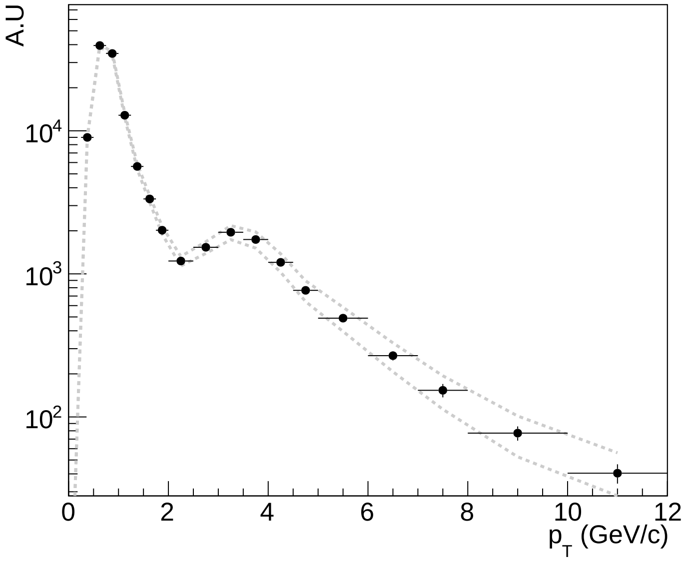

Figure 5.3.2: The reconstructed spectrum in the EMCal triggered data using the maximal, minimal and standard PID efficiency and purity. The gray lines indicate the spectra calculated with the maximum and minimum PID efficiency and purity corrections, and the deviation between the gray lines and the black points represents the second component of the associated systematic uncertainty in the PID efficiency and purity correction

6

The EMCal Trigger

With the LHC reaching event rates of $\sim 10^7$ Hz, all of the experiments implement extensive trigger systems for event selection and to reduce output to manageable levels. The data flow constraint is particularly stringent for ALICE; the focus on the high multiplicity environment of heavy-ion collisions, and the choice of a TPC as the main tracking detector results in a data rate of up to 25 GB/s. Calorimeters inevitably constitute an important element of any modern triggering system, and the ALICE EMCal is no exception. The information from calorimeters is typically available 50-500ns after a collision, and thus can function as important fast hardware level (L0) triggers [287]. The SPACAL collaboration demonstrated such efficacy in developing a 25ns electron trigger based on counting the number of the modules above a certain threshold [288]. Since other identification methods for electrons (such as Cherenkov radiation, transition radiation) can be computationally intensive, calorimeters can be particularly important in that context. One of the motivating factors for the proposal of the EMCal detector in ALICE was its ability to provide useful triggering capabilities. Although the LHC provides a large increase in the kinematic and statistical reach of high energy jets, photons and electrons, these events are still relatively rare. The EMCal allows ALICE to fully exploit the new energy regime attained at the LHC by providing triggering on high energy jets, photons and electrons. The overall trigger system was described in Chapter 2 and in this chapter the EMCal trigger, and how the trigger bias is corrected for, is described.

6.1 Description of the Trigger

The EMCal comprises 10 full super modules and 2 partial super modules. For the purposes of triggering, each of the full supermodules are subdivided into 3 regions (the smaller modules constitute a single region). The data from each region is fed into 12 FEE (front-end-electronic) cards which in turn provide 8 fast-OR signals to a *trigger region unit* (TRU). The arrangement is depicted in Figure 6.1.1. The fast-OR signals comprise analog sums over single modules (4×4 towers) which are digitized by the TRU's, which then provide triggering information. At the hardware level, 3 trigger algorithms can be employed: the L0 trigger algorithm, the L1 photon and the L1 jet patch trigger algorithms. In the L0 trigger algorithm the digitized TRU signals are continuously summed in patches of 2×2 modules and compared to the trigger threshold. This has the disadvantage of inefficiencies at the TRU region boundaries: since the sums are taken within each TRU, patches cannot lie across these boundaries. The L1 'photon' trigger algorithm overcomes this by utilizing a sliding patch over the entire detector. The L1 jet triggering algorithm aims to provide an unbiased jet trigger. The spatial extent of jets forces the introduction of a significantly larger patch size for the jet trigger. The jet patch comprises a sum over a 2×2 subregion window, where each subregion constitutes 4×4 modules (8×8 towers). The extent of each trigger patch is illustrated in Figure 6.1.2. Both L1 triggers are not pipelined and are initiated upon reception of an L0 trigger. In this analysis a MB data sample was used along with L0 EMCal triggered data sample. Although a multiplicity dependent threshold using information from the V0 detector can be employed, in the pp data sample used in this analysis a fixed threshold was used corresponding to 4 GeV.

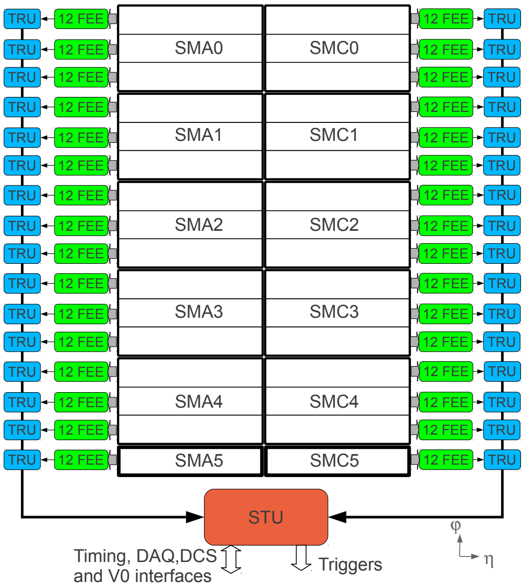

Figure 6.1.1: Schematic of the trigger electronics of the ALICE EMCal (from [40]). SMA/Ci refers to supermodule number i on the A/C side of the detector (see Appendix A for more information on the detector orientation and labelling). The Summary Trigger Unit (STU) collects and aggregates the information from the individual trigger units (TRUs) to generate the global L0 trigger decision

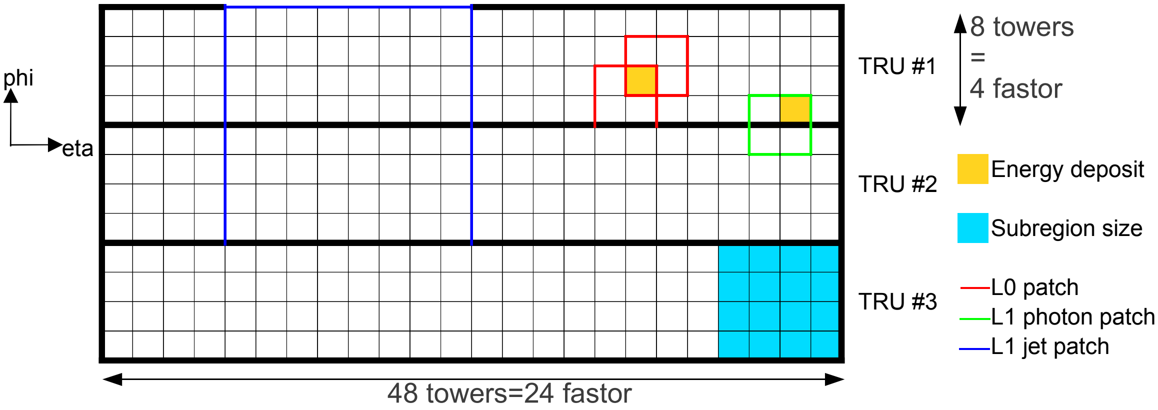

Figure 6.1.2: Depiction of the different trigger algorithm patch sizes over a single supermodule. From [40]

6.2 L0 Trigger Bias Correction

Although the EMCal L0 trigger successfully extends the kinematic reach of both jet [261] and electron[283] measurements, it also requires a correction for the trigger bias. The high event rates at the LHC mean that even the MB trigger can only select a small fraction of the total number of events. The L0 EMCal trigger also selects an even smaller fraction, however it will be a sample biased towards collisions where high energy jets are produced. These events would also fire a MB trigger, but the population of these events in a MB sample is much smaller than in a EMCal triggered sample. Figure 6.2.1 provides a schematic illustration of this trigger bias. In a given time period

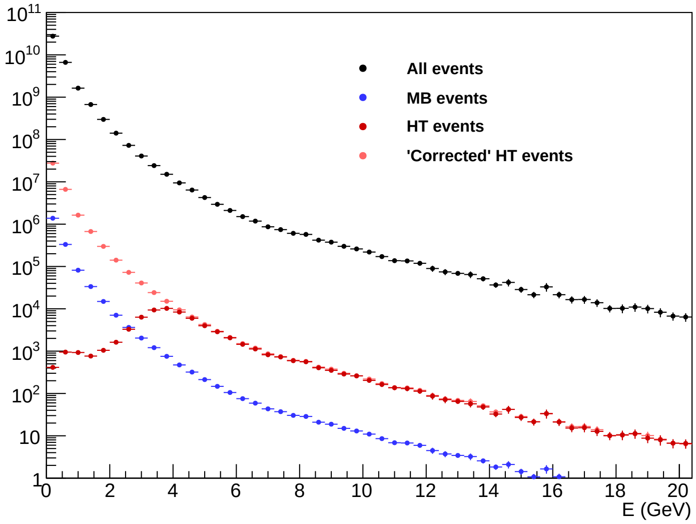

Figure 6.2.1: Schematic of a hypothetical cluster energy distribution obtained from a MB trigger and an L0 EMCal trigger

some total number of collisions occur, which produce the hypothetical (if all collisions could be recorded) spectrum in black. The blue curve represents the subset of these events which are selected by some MB trigger. This MB spectrum selects an essentially unbiased subset of the total, the curve being a fixed fraction of the total. The EMCal trigger selects a different subset of the total, which is biased due to the trigger turn on (the dark red points). The purpose of the trigger efficiency correction is to reconstruct the unbiased spectrum (light red points) that coincides with the EMCal spectrum at high energies where the EMCal trigger is essentially unbiased.

The necessary correction will entail two components: the *rejection factor* and the *trigger efficiency*. The rejection factor is essentially the scaling factor from the blue points to the red points at high p_T, and is indicative of the trigger selection rate: the EMCal trigger will trigger a different number of events per unit time than the MB trigger (the effective luminosity differs). The trigger efficiency quantifies the probability that the trigger will fire at a given energy. There are several possible sources of inefficiency. Since the trigger is based on a 4×4 tower patch, showers that greatly exceed this size may leave clusters in the MB signal but not leave enough energy in the patch to trigger events. The trigger may also have inefficiencies due to particles that hit the detector at the boundary of two trigger regions. Since the patches are constrained to each trigger region, the total energy may be shared among two L0 patches and hence not provide a trigger signal. In high density environments incorrect cluster unfolding (or ineffectiveness of the cluster algorithm in general) may lead to inefficiencies. These effects will become more prominent at low energies and lead to a smooth 'turn-on' around the trigger threshold (as opposed to a step function). However, at high energies these effects are expected to be negligible and the trigger is expected to be 100% efficient. The test beam data suggests that to be the case, and the validity of this assumption was verified with a simple cross-check (to be described). The total trigger bias correction then involves a scale factor which aligns the EMCal triggered data with the MB data and that takes account of the differing trigger rates (for a particular event subclass), and a trigger efficiency turn-on curve which corrects for inefficiencies in the trigger (where 'inefficiency' also includes clusters that have energies below threshold and do not trigger).

6.2.1 Electron Trigger Efficiency

The simplest way to correct for the trigger bias in the electron spectra is to simply divide the EMCal triggered electron spectrum by the MB electron spectrum to obtain the trigger efficiency correction (see Appendix D.1). This implicitly includes both the rejection factor and the trigger efficiency.

However, poor statistics in my MB data sample limit the efficacy of this approach. In principle, by dividing the spectrum of all triggered clusters (as opposed to electrons) in EMCal triggered data to all clusters in MB data the trigger efficiency correction could also be derived. Figure **??** shows the comparison of reconstructed electron ratios to all cluster ratios, and indeed within statistical errors they are consistent. However, there are two problems with using the ratio of all clusters: (i) the correction that I employ needs to be implemented based on p_T and not cluster energy, and the trigger turn-on in p_T space is certainly different for electrons than for all clusters (ii) one could imagine that the *energy* turn-on for all clusters may be different than for electron clusters; for instance, since electron showers are narrower, the inefficiencies of the L0 trigger at TRU region boundaries may be different.

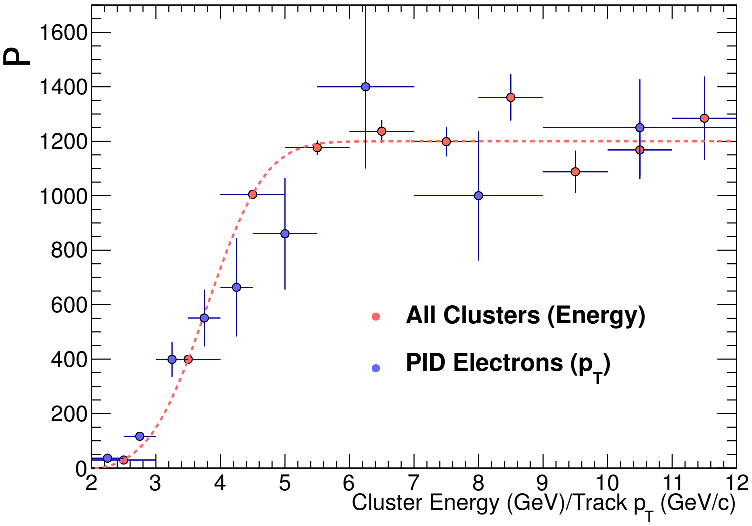

Figure 6.2.2: Comparison of the ratio of PID electron track p_T in EMCal triggered to PID electron track p_T in MB data to the ratio of inclusive cluster energy in EMCal triggered to inclusive cluster energy in MB data

Since the EMCal trigger applies to all clusters, whether the latter effect is significant depends on whether the events used in generating the electron p_T spectrum are triggering preferentially with electron clusters. A priori, one may expect that the preponderance of pions over electrons would indicate that the event trigger should behave exactly as for all clusters and possible differences between electron and pion turn-on curves will not have an affect. In fact, in the EMCal trigger data set $\approx 99\%$ of events with electrons (as determined by the PID of Chapter 5) are triggered *only* by electron clusters; in most cases the event would not be triggered by pions that are also in the event (the preponderance of high energy pions evidently not great enough to dominate their small energy deposition). However, the difference in the energy turn-on curve is expected to be very small and simulations confirm this. Hence this effect was assumed to be negligible.

Since the EMCal trigger applies to all clusters and not just electrons, the plateau obtained from all clusters can be used to provide the scaling factor. Dealing with the trigger efficiency however, especially in the turn-on region, requires an electron sample. Hence a simulation was utilized to generate an electron turn-on curve in p_T space with greater statistics than provided by data alone.

6.2.2 EMCal Trigger Simulation

Short of a simulation of the EMCal electronics, only two elements need to be incorporated into the trigger simulation (at the time of writing a simulation incorporating elements of the EMCal electronics is being developed). To avoid the effects of hot towers and otherwise misbehaving detector elements, a trigger mask is employed to ensure events do not trigger on faulty towers or regions of the detector which are excluded during data taking; the trigger mask is saved into the OCDB and needs to be taken into account in the simulation (Figure 3.2.9 shows the trigger mask utilized in this data set). The second element is an account of the (possibly) local variation in the trigger efficiency and a data-driven modeling of the detector response. For each super module, the ratio of the triggering clusters in triggered data, to all clusters in MB data was plotted. Figure 6.2.3 shows these ratios for each supermodule along with straight-line fits above 4-5 GeV where we assume the trigger is

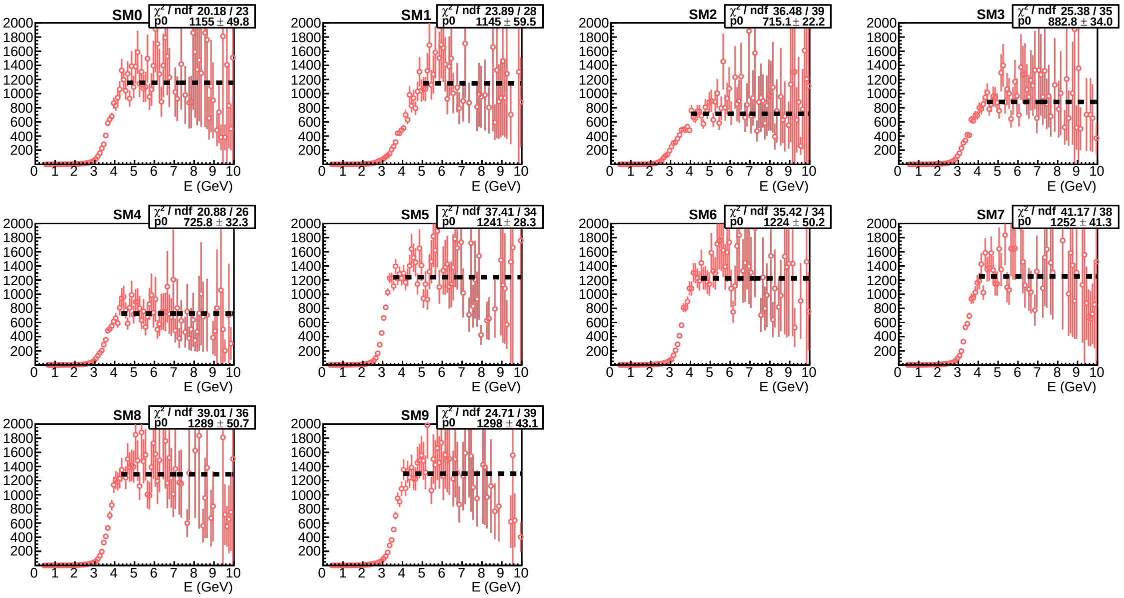

Figure 6.2.3: Ratio of the cluster energy spectrum in EMCal data to that in MB data separated by supermodule

fully efficient. Then for each super module, these histograms (normalized to the straight line fit) provide *turn-on* curves for triggering, i.e. probability distributions for triggering as a function of energy in each super module. In this way the detector response is modeled with a data driven procedure. These probability distributions plateau at some energy and are assumed to plateau at a 100% trigger efficiency. To complete the modeling the trigger mask is then taken into account. For a given particle that impinges on the EMCal, the trigger mask is used to completely reject (not trigger) clusters that are generated within the trigger mask shadow and accept (trigger) clusters outside the trigger mask shadow with a probability given by the turn-on curves.

One objection to this methodology is the assumption that at high p_T the trigger is fully efficient. To determine if this is indeed accurate, a data driven approach is adopted. The idea is to exploit the 'excess' clusters in the EMCal triggered cluster spectra. Suppose that at high p_T there was some finite trigger efficiency, ϵ. Then in events with multiple clusters of energies greater than threshold, one would expect that some of the clusters would not possess trigger primitives (precisely $(1-\epsilon)N$ where N is the total number of clusters). This would manifest itself in a difference between the spectra of all clusters vs *triggering* clusters. In fact (see Appendix D.2), the trigger efficiency is given by:

$$\epsilon = \frac{R + RS - 1}{S} \tag{6.1}$$

where R is the ratio of the all cluster to triggering cluster spectra, and S quantifies the cluster probability distribution (what fraction of events have a certain number of clusters that could trigger). Due to the effect of the trigger mask, we know that the trigger is in fact less than 100% efficient at high p_T; the 'fully' efficient assumption refers to the trigger efficiency modulo the effect of the trigger mask. Hence one cannot test for 100% trigger efficiency by comparing R to 1 ($R = (\epsilon S + 1)/(S+1)$). However, since the simulation assumes a 100% trigger efficiency modulo the trigger mask, by comparing R in simulation and data we can determine if the trigger is fully efficient at high p_T modulo the trigger mask. Figure 6.2.4 shows the ratio R in data and simulation, and indeed they are consistent within statistical errors. Moreover, with S determined to be 0.228 ± 0.007, the high $p_T (> 5$ GeV) trigger efficiency is determined to be $\epsilon = 0.93 \pm 0.05$. As the trigger mask obscures 11% of the EMCal, this indicates that the trigger efficiency modulo the trigger mask is $\epsilon = 1.04 \pm 0.06$, again indicating that the trigger is fully efficient at high p_T modulo the trigger mask (this being a more data driven approach than solely by comparison to simulation).

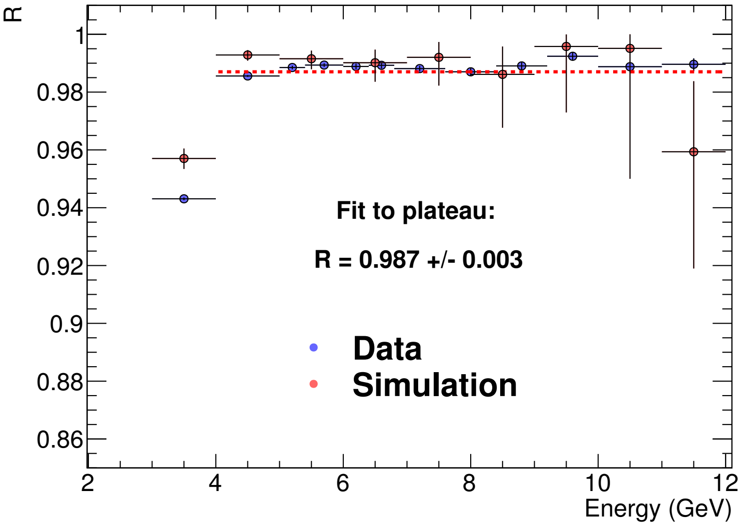

Figure 6.2.4: Ratio of the triggered cluster energy spectrum to the inclusive cluster energy spectrum in EMCal trigger data

6.2.3 Trigger Efficiency Correction

As has been indicated, the trigger efficiency comprises two components: the rejection factor, and the trigger efficiency. The simplest methodology, one that incorporates both the rejection factor and trigger efficiency, fails for electrons due to poor statistics. Using all clusters as opposed to electron clusters is one possibility to improve statistics, however this raises the question of potential differences between inclusive cluster and electron trigger efficiencies. A simulation that incorporates data driven effects (the trigger mask and regional variations in the trigger efficiency) was thus used to determine the trigger efficiency for all clusters and for electrons. In either case, the rejection factor is easily determined by examining the ratio of the triggered cluster energy spectrum in EMCal data to the inclusive cluster energy spectrum in MB data. Since the trigger was determined to be fully efficient at high p_T, the position of the plateau, P, is given by:

$$P = F_{rej}\epsilon_{mask}$$

where F_{rej} is the rejection factor and ϵ_{mask} is the trigger efficiency due to the trigger mask. Hence the rejection factor is given by:

$$F_{rej} = \frac{P}{\epsilon_{mask}} \tag{6.2}$$

Figure 6.2.5 shows the ratio of the triggered cluster energy spectrum in the EMCal triggered data

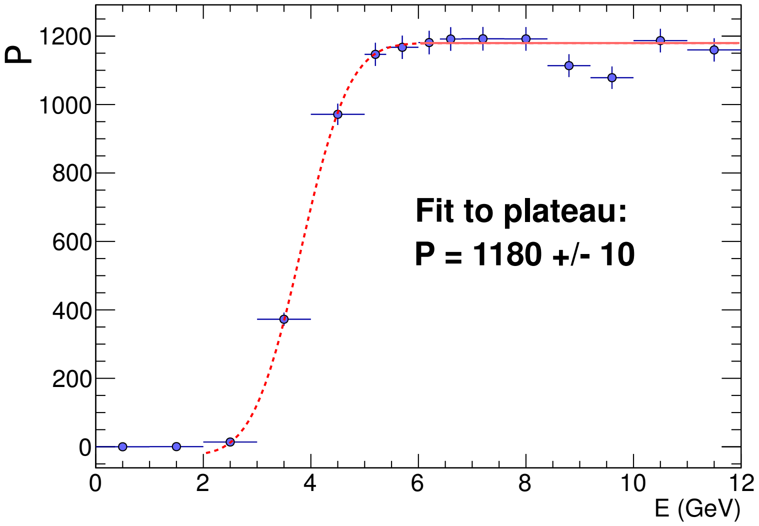

Figure 6.2.5: Ratio of the triggered cluster energy spectrum in EMCal data to the inclusive cluster energy spectrum in MB data

to the inclusive cluster energy spectrum in MB data, with a fit to the plateau. With $\epsilon_{mask} = 0.89$, P was determined to be 1180 ± 10 and hence the rejection factor was ascertained to be 1325 ± 11.

This method of determining the rejection factor also allows for a cross-check of the trigger simulation. By taking the ratio of the triggered cluster energy spectrum to the inclusive cluster spectrum in simulation, the trigger efficiency for all clusters was obtained. Dividing the triggered cluster energy spectrum in EMCal data by the rejection factor as given by equation (6.2), and subsequently dividing by the inclusive electron spectrum in MB data results in a data driven trigger efficiency. The simulated and data-driven trigger efficiencies are compared in Figure 6.2.6; they are consistent within error bars over the entire energy range considered.

In this analysis the final result is a track p_T spectrum of electrons. The difference between energy and p_T for electrons is the effect most likely to generate a difference between the trigger efficiency correction for a inclusive cluster energy spectrum and an electron track p_T spectrum. The trigger efficiency correction for electrons must be determined solely from simulations. Figure 6.2.7 shows the trigger efficiency for all clusters (in energy) compared to the trigger efficiency for electrons (in track p_T) as measured in simulations. As one would expect the turn-on for electrons in track p_T is broader and the plateau is slightly lower than for clusters in energy. Cases of high p_T electrons that deposit significantly lower or higher energy (either due to interactions in the material or poor clusterization) than their momenta are responsible for the slight difference in the position of the plateau.

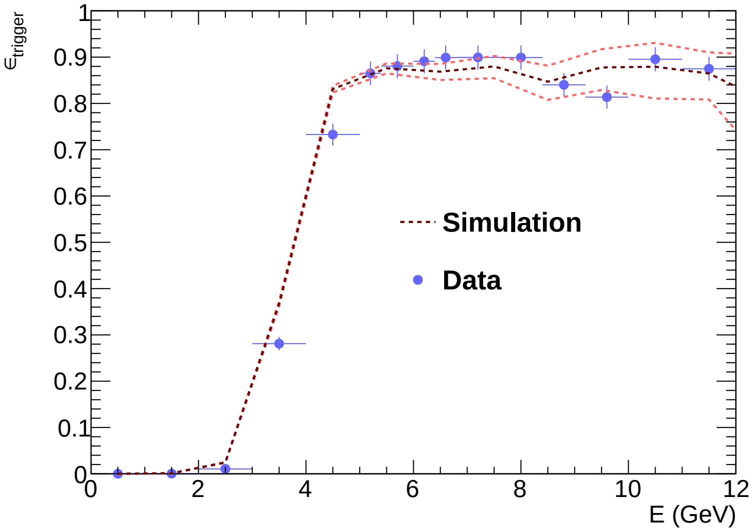

Figure 6.2.6: Comparison of the trigger efficiency for all clusters measured in data, to that obtained from the described trigger simulation. The red lines indicate the upper and lower uncertainty bands on the simulation

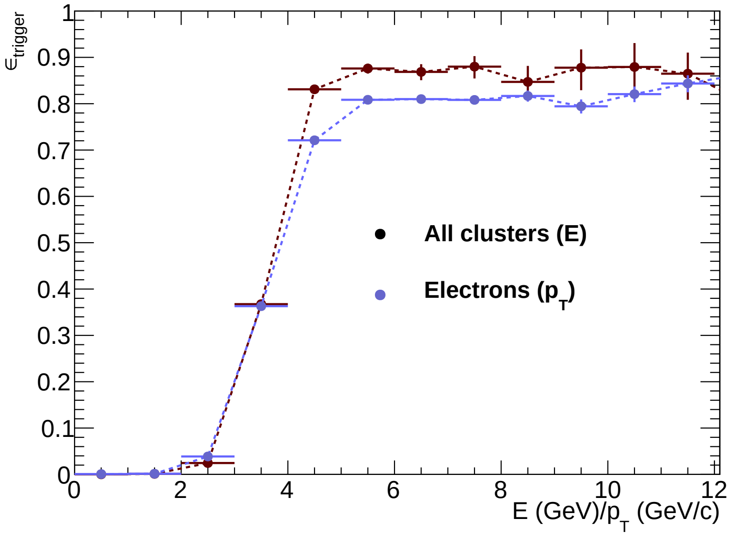

Figure 6.2.7: Comparison of the trigger efficiency for all clusters (in energy) to electrons (in track p_T)

The final spectrum must be corrected for both the rejection factor and the trigger efficiency. Since the rejection factor is determined from the inclusive cluster spectra via a measurement of P, one must divide the EMCal triggered raw spectrum by $\epsilon_{electron}P/\epsilon_{mask}$ (strictly speaking ϵ_{mask} should be $\lim\limits_{E\to\infty} \epsilon_{cluster}$, but we have seen that these numbers are identical since the trigger is fully efficient modulo the trigger mask at high p_T).

6.2.4 Systematic Uncertainty Associated with the Trigger Correction

The final trigger efficiency correction involves a multiplication by $\epsilon_{electron}P/\epsilon_{mask}$. The value of ϵ_{mask} is known with certainty, while P is a p_T independent constant whose uncertainty is taken as the error in the fit in Figure 6.2.5. The correction $\epsilon_{electron}$ is p_T dependent and is taken to be a fit to the simulated electron trigger efficiency in Figure 6.2.7. Specifically a straight line is fitted to the high p_T region, and an error function is fitted to the entire curve being constrained to reach the straight line fit at high p_T. This procedure is employed so as to avoid biasing the position of the plateau (which has lower statistics and higher degree of uncertainty) by the points around the turn-on. These points have greater statistics and it is not known whether the turn-on is well described by an error function. Figure 6.2.8 shows the result of this fitting procedure. The systematic error associated with this turn-on curve is determined by applying a similar fitting procedure to points defined by the upper and lower errors bars of the simulated trigger efficiency. The upper (lower) trigger curve is then applied with the largest (lowest) value of P (i.e $P - \delta P$ or $P + \delta P$) to obtain a

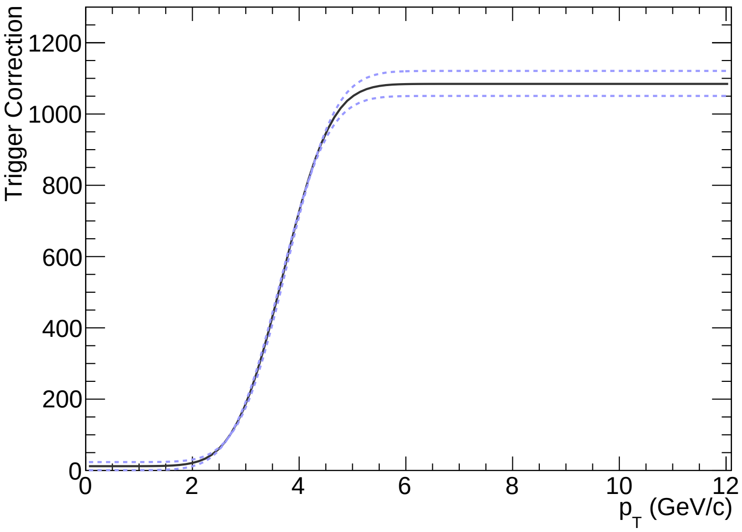

Figure 6.2.8: Applied trigger correction incorporating the trigger efficiency and the rejection factor. The blue lines indicate the error bounds used in assigning the systematic error

lower and upper corrected spectrum. The difference between these spectra is taken as the systematic error. Although the correction exhibits a slight p_T dependence, at high p_T the assigned systematic error is 3%.

7

Non-Heavy-Flavor Cocktail

The goal of this analysis is to extract the production cross-section of electrons from the decay of hadrons and mesons containing b and c quarks. The high masses of the b and c quarks indicate that their production is dominated by hard-scattering processes, and thus they can provide a probe for in-medium energy loss. By applying the corrections described in the previous chapters to the raw electron yield, the inclusive electron production cross-section can be obtained. There are two commonly used methods of obtaining a heavy-flavor electron production cross-section from an inclusive electron production cross-section: the 'cocktail subtraction' method and the 'photonic electron subtraction method'. The result of the latter method is often referred to as the cross-section for *non-photonic* electrons, which is not exactly the cross-section from heavy-flavor decays though it is sometimes used interchangeably. Non-photonic electrons are defined as electrons produced via a charged-current weak decay with the production of an (anti)neutrino. The spectrum of non-photonic electrons includes electrons from sources other than heavy-flavor decays (for instance charged pions, muons, kaons, etc). However, at high p_T the spectrum is dominated by electrons from heavy-flavor decays [276]. In a measurement of the cross-section of electrons from heavy-flavor decays, most of the background in the inclusive electron cross-section can often be removed by subtracting the *photonic* electrons (such as electrons from conversions, $J/\psi \to e^+e^-$ decays and Dalitz decays). This is exactly the procedure followed in the photonic electron subtraction method, and the non-photonic electron spectrum that results thus provides a proxy for the heavy-flavor electron cross-section. Hence the terminology 'non-photonic electrons' and 'heavy-flavor electrons' are somewhat interchangeable, though strictly speaking the former includes electrons from other sources that should in principle be subtracted.

In the photonic electron subtraction method, the background is subtracted in two components: the photonic background and the non-photonic background. Photonic electrons are identified by calculating the invariant mass of candidate electrons and all tracks which pass very loose electron identification criteria. A large fraction of photonic electrons (those from neutral pion Dalitz decays [$\pi^0 \rightarrow e^- e^+ \gamma$], and photon conversions) have low invariant mass. By placing an upper limit on the minimum invariant mass of a candidate track (minimum with respect to all track pairs formed), a large fraction of photonic electrons can be rejected. This procedure was followed by STAR [276, 289, 290] where $\gtrsim$ 95% of the background originated from photonic sources. In some analyses, the fact that the non-photonic electron spectrum is dominated by heavy-flavor electrons is used to identify the non-photonic electron spectrum with the heavy-flavor electron spectrum, or the result is simply quoted as the non-photonic electron spectrum acknowledging the presence of non-heavy-flavor electrons. To obtain a heavy-flavor electron spectrum from this procedure a simulated cocktail of background sources is generated and subtracted to remove any residual background.

In the cocktail subtraction method, no attempt is made to remove the photonic electron background as a separate background component, and the entire background is subtracted by generating a simulated background cocktail that includes all background sources. Both methods are equally valid, and the implementation of both analysis methods would provide a good cross-check of the results of any individual analysis. Which method is most appropriate is a quantitative question that depends on the nature of the detector being used, the statistics in the data sample, and the precision with which the background efficiency can be calculated. Ideally, one would like to subtract as much as the background as possible with a data driven approach like that used in the photonic subtraction method. However, if the fraction of background that can be identified with a data driven approach is very small, then a large simulated cocktail needs to be subtracted in any case, and it may not be worth the effort. Moreover, if the background efficiency cannot be determined with high precision, this fact may also limit the precision of the final result to such a large degree that the cocktail method would provide a more precise result despite relying on simulations to a greater extent. If the photonic background is very large, and the efficiency of the background identification can be determined with high precision, then the photonic subtraction method is certainly worthwhile as it relies less on a simulated cocktail. This was exactly the case for STAR where a high material budget resulted in a large background from photonic sources. PHENIX on the other hand, with a much lower material budget, did not employ the photonic subtraction method and instead implemented a complete cocktail.

Although a complete quantitative analysis of the relative merits of the two methods in the

ALICE detector was not undertaken, preliminary studies suggested that the measurement of the background identification efficiency could not be made with high precision due to the lack of statistics. Moreover, although the material budget of the ALICE detector is comparable to that of STAR, the track quality cuts utilized in this analysis reject a large fraction of the background from conversion electrons. Hence, in this analysis the cocktail methodology was employed to subtract the non-heavy-flavor electron background. This chapter describes the components of this cocktail, how they were generated, and the associated systematic uncertainty in the background non-heavy-flavor electron cross-section.

7.1 Cocktail Components

A variety of electrons from non-heavy-flavor sources are included in the inclusive electron spectrum. Broadly speaking, the inclusive electron spectrum consists of electrons from 5 components:

- Signal electrons from the decay of heavy-flavor quarks (more precisely, from the semi-leptonic decays of hadrons that contain charm and beauty quarks[1])
- Background electrons from Dalitz decays of light neutral mesons, and from the conversions in material of decay photons from light neutral mesons. These are subtracted based on measurements of the π^0 and η spectra as measured by ALICE, with the assumption of m_T scaling [76, 291] for mesons other than π^0 and η
- Background electrons from weak kaon decays (so called $\mathrm{K_{e3}}$ decays), $\mathrm{K}\rightarrow \mathrm{e}\pi\nu$. This contribution is estimated solely from simulations
- Background electrons from dielectron decays of heavy quarkonia (J/ψ, Υ), for instance J/$\psi \rightarrow e^-e^+$. An estimate of the contribution in $\sqrt{s} = 2.76$ TeV *pp* collisions is made from the measurement of the J/ψ cross-section in $\sqrt{s} = 7$ TeV *pp* collisions by ALICE, and the measurement of the Υ cross-section in $\sqrt{s} = 7$ TeV *pp* collisions by CMS
- Background electrons from both real and virtual direct photons originating from hard partonic scatterings. This contribution is yet to be measured in ALICE and is estimated from NLO perturbative QCD calculations

Table 7.1.1 explicitly delineates the various sources of electrons included in the cocktail and their respective branching ratios to electrons or daughters that can subsequently decay to electrons [48].

---

[1] Henceforth, this clarification is understood when referring to 'electrons from the decay of b/c quarks'

Decay	Branching Ratio (%)
$\pi^0 \to e^-e^+\gamma$	1.174 ± 0.035
$\eta \to e^-e^+\gamma$	$(7.0 \pm 0.7) \times 10^{-3}$
$\eta \to e^-e^+\pi^+\pi^-$	$(2.68 \pm 0.11) \times 10^{-4}$
$\rho^0 \to e^-e^+$	$(4.72 \pm 0.05) \times 10^{-5}$
$\rho^0 \to e^-e^+\pi^0$	$< 1.2 \times 10^{-5}$ (CL=90%)
$\omega \to e^-e^+$	$(7.28 \pm 0.14) \times 10^{-5}$
$\omega \to e^-e^+\pi^0$	$(7.7 \pm 0.6) \times 10^{-4}$
$\eta' \to e^-e^+\gamma$	$< 9 \times 10^{-4}$ (CL=90%)
$\eta' \to e^-e^+\pi^+\pi^-$	$(2.4^{+1.3}_{-1.0}) \times 10^{-4}$
$\phi \to e^-e^+$	$(2.954 \pm 0.030) \times 10^{-4}$
$\phi \to e^-e^+\pi^0$	$(1.12 \pm 0.28) \times 10^{-5}$
$\phi \to e^-e^+\eta$	$(15.32 \pm 0.32) \times 10^{-4}$
$\eta' \to \pi^0\pi^0\eta$	21.7 ± 0.8
$\eta' \to \pi^-\pi^+\eta$	43.2 ± 0.7
$\eta' \to \gamma\rho^0$	29.3 ± 0.5
$\eta' \to \gamma\omega$	2.75 ± 0.22
$\phi \to \pi^0\rho^0$	15.32 ± 0.32
$\phi \to \gamma\eta$	1.309 ± 0.024
$\pi^0 \to \gamma\gamma$	98.798 ± 0.032
$\eta \to \gamma\gamma$	39.31 ± 0.20
$\mathrm{K}^0_{\mathrm{e3}} \to \mathrm{e}^{+/-}\pi^{-/+}\nu$	40.55 ± 0.11 [1]
$\mathrm{K}^{+/-}_{\mathrm{e3}} \to \mathrm{e}^{+/-}\pi^{-/+}\nu$	5.07 ± 0.04
Direct $\gamma, \gamma*$	See text
$\Upsilon \to e^+e^-$	2.38 ± 0.11

Table 7.1.1: Sources of electrons included in the background cocktail simulation, their decay modes, and respective branching ratios [48]

Other possible sources of electrons, such as the Drell-Yan process, are assumed to be negligible. A discussion of these other possible sources is given the following section.

7.1.1 The Light Mesons

Background electrons from light mesons $(\rho, \omega, \eta, \eta', \phi, \pi^0)$ originate from either Dalitz decays (such as $\pi^0 \to e^-e^+\gamma$) or via two-photon production (such as $\eta \to \gamma\gamma$). To simulate the contributions to the total background cocktail from these sources, 10^7 of each particle were generated uniformly in full azimuth, p_T and a pseudorapidity range of $|\eta| < 0.6$. The particles were allowed to decay naturally (no decay channels were forced), producing spectra of various particle species. A spectrum of electrons from Dalitz decays is identified by selecting those electrons whose parent is one of the light mesons $(\rho, \omega, \eta, \eta', \phi, \pi^0)$. A realistic weighting of this resulting p_T spectra has to be applied to take into account the flat p_T spectrum of the generated parent particles. Such a weighting can be

---

[1] This refers to the K^0_L decay which is usually referred to as just $\mathrm{K}^0_{\mathrm{e3}}$. The contribution from similar K^0_S decays is essentially negligible

directly applied for both π^0 and η mesons, as in both cases ALICE has performed a measurement of the cross-section in $\sqrt{s} = 2.76$ TeV pp collisions. Although the final measurement is not yet published, a preliminary measurement of the cross-section of π^0 and η was used for the analysis in this thesis (see Figures 7.1.1 and 7.1.2 that show the preliminary measured cross-section of π^0 and η particles in $\sqrt{s} = 2.76$ TeV pp collisions). Both input cross-section measurements are fit with a

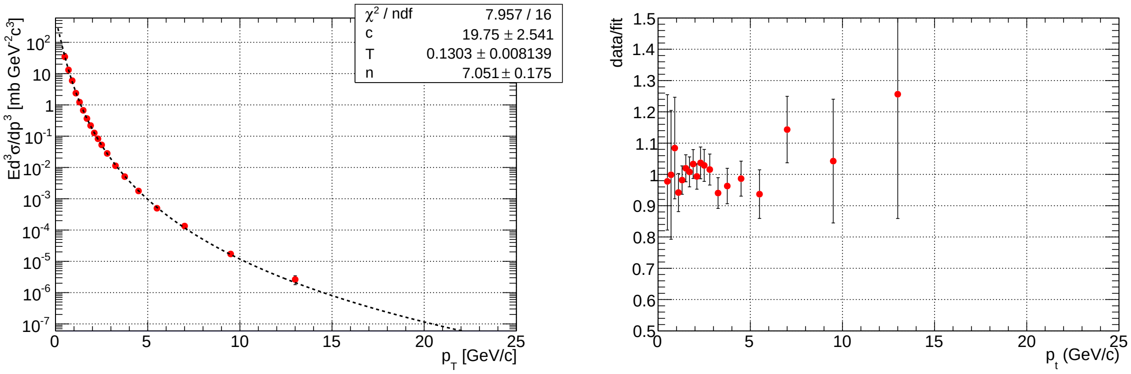

Figure 7.1.1: Invariant differential cross-section of π^0 production in $\sqrt{s} = 2.76$ TeV pp collisions as measured by ALICE. The left-hand size is the cross-section with a Tsallis fit, and the right-hand side is the ratio of the data points to the fit

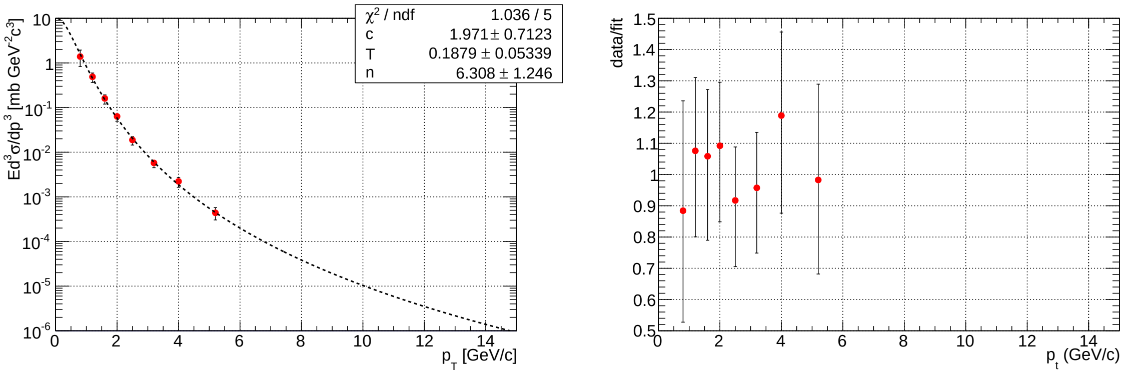

Figure 7.1.2: Invariant differential cross-section of η production in $\sqrt{s} = 2.76$ TeV pp collisions as measured by ALICE. The left-hand size is the cross-section with a Tsallis fit, and the right-hand side is the ratio of the data points to the fit

Tsallis function of the form [292]:

$$E\frac{d^3\sigma}{dp^3} = \frac{\sigma_{pp}}{2\pi}\frac{dN}{dy}\frac{(n-1)(n-2)}{nT(nT+m(n-2))}(1+(m_t-m)/(nT))^{-n} \tag{7.1}$$

where σ_{pp} is the inelastic pp cross section, m is the mass of the π^0 or η, m_t is the transverse mass ($m_t = \sqrt{m^2+p_T^2}$), and $\frac{dN}{dy}, T$ and n are parameters of the fit, the results of which are included

$\eta'/\pi^0 = 0.25 \pm 0.075$ [48]
$\omega/\pi^0 = 0.85 \pm 0.255$ [48, 294]
$\rho/\pi^0 = 1.0 \pm 0.3$ [48]
$\phi/\pi^0 = 0.40 \pm 0.12$ [48, 295]

Table 7.1.2: Ratio of various meson to π^0 yields at $p_T = 5$ GeV/c used in the m_T-scaling procedure

in the figures. The right hand side of each figure shows the ratio of the data to the fitted Tsallis function, and indicates that the fit is consistent with the data within the measured uncertainties. The fitted Tsallis functions are then used to weight the spectra of simulated electrons originating from Dalitz decays of the generated π^0 and η mesons.

Light mesons other than π^0 and η also contribute to the total electron background via Dalitz decays, but measurements of their respective cross-sections have not been performed by ALICE in $\sqrt{s} = 2.76$ TeV pp collisions. To estimate the contributions to the cocktail from these sources, m_T scaling was employed. m_T-scaling [76, 291] refers to the observation that when viewed as a function of the transverse mass, $m_T = \sqrt{m_2 + p_T^2}$, the yields of a large number of particle species appear to exhibit a similar *shape* (a common parameterization being $E\frac{d\sigma}{d^3p} = A\frac{e^{-m_T/T}}{m_T}$). Such m_T-scaling has hitherto been observed both at ISR ($\sqrt{s} \sim 23 - 63$ GeV) and RHIC ($\sqrt{s} = 200$ GeV) [291, 293]. Thus, the shape of the weighting functions for meson X are obtained from the shape of the π^0 weighting function via:

$$W_X\left(p_T^X\right) = W_{\pi^0}\left(\sqrt{(p_T^X)^2 + m_X^2 - m_{\pi^0}^2}\right)$$

where W_{X/π^0} is the weighting function for meson X/π^0, p_T^X the transverse momentum of meson X, and m_{X/π^0} is the mass of meson X/π^0. However, m_T-scaling does not hold in an absolute sense: although the shapes appear to follow an identical parameterization, the absolute values of the yields is species dependent. To determine the expected yields of other light mesons from the π^0 and η yields, measurements of the various yield ratios from other experiments were utilized to provide the appropriate absolute scaling; the values used are tabulated in Table 7.1.2.

The procedure hitherto described enables an estimate of the background contribution of electrons from Dalitz decays of light mesons. Photons are also produced in Dalitz decays, and some of the light mesons may decay via a $2-\gamma$ mode (e.g $\pi^0 \to \gamma\gamma$). Since the simulation does not incorporate elements of the ALICE detector (the process occurs in free space), the spectrum of electrons from the conversions of these photons is not directly available. However, with a precise knowledge of the material budget, an estimate of the electron yield from conversions can be deduced from the yield from Dalitz decays.

From the definition of the radiation length, the probability of a photon that passes through a material of thickness X interacting to produce a e^+e^- pair, $P(X)$, is given by:

$$P(X) = p(E)\left[1 - e^{-\frac{7}{9}\frac{X}{X_0}}\right]$$

where $p(E)$ takes into account the energy variation of this probability [48]. $p(E)$ assumes the form of an error function, and is dependent upon the material traversed. The precise shape was parameterized using a full Monte Carlo simulation. Hence the ratio of the yield of conversion electrons to the yield of Dalitz electrons is given by:

$$\frac{\text{Conversion}}{\text{Dalitz}} = \frac{BR_X^{\gamma\gamma} \times 2 \times p(E)(1 - -e^{-\frac{7}{9}\frac{X}{X_0}})}{BR_X^{\text{Dalitz}}} \tag{7.2}$$

where $BR_X^{\gamma\gamma}$ is the branching ratio of 2-γ decay modes for meson X, and BR_X^{Dalitz} is the branching ratio of Dalitz decay modes for meson X. The ratio $BR^{\gamma\gamma}/BR^{\text{Dalitz}}$ has a weak mass dependence so it is not a universal constant for each meson. Hence, from the expected yield of electrons from Dalitz decays of each meson, the corresponding expected yield from conversion electrons for each meson is obtained by multiplying by the ratio in equation (7.2).

7.1.2 $\mathrm{K_{e3}} \rightarrow \mathrm{e}^{+/-}\pi^{-/+}\nu$ decays

The yield of electrons from weak decays of charged and neutral Kaons, known as $\mathrm{K_{e3}}$ decays, is determined using a different simulation. In this case, a full simulation including a realistic GEANT modeling of the experimental geometry was utilized. By employing the same event, track quality cuts and reconstruction algorithms as applied to data, the contribution of electrons from $\mathrm{K_{e3}}$ decays was estimated. Only K_L^0 and $\mathrm{K}^{+/-}$ decays were considered, as the branching ratio of $\mathrm{K}_S^0 \rightarrow e^{+/-}\pi^{-/+}\nu$ is less than 10^{-3} [48], and thus its contribution was thus deemed negligible. Since tracks are required to possess 3 ITS hits in this analysis, the long lifetime of the pertinent Kaons (the decay length of $\mathrm{K}^{+/-}$ is 3.712 m, whereas the decay length of K_L^0 is 15.34 m [23]) indicates that the contribution from these decays should be negligible. Indeed, simulations confirm that the contribution is less than 0.5% for the entire p_T range (also see Figure 7.1.3).

7.1.3 Heavy Quarkonia

The contributions of electrons from J/ψ and Υ decays ($J/\psi \rightarrow e^+e^-$, $\Upsilon \rightarrow e^+e^-$) are estimated from data. Measurements of the production cross-section of J/ψ and Υ in $\sqrt{s} = 7$ TeV pp collisions have been performed by ALICE [22] and CMS [296]. Unfortunately, similar measurements were not yet performed in $\sqrt{s} = 2.76$ TeV pp collisions at the time of writing of this thesis. Hence, a pQCD based scaling was utilized to scale the cross-sections from $\sqrt{s} = 7$ TeV to $\sqrt{s} = 2.76$ TeV. The fact that pQCD calculations agree with a plethora of results both at $\sqrt{s} = 7$ TeV and $\sqrt{s} = 2.76$ TeV provides a basis for the suitability of this method. By dividing the FONLL pQCD predictions at $\sqrt{s} = 7$ TeV to those at $\sqrt{s} = 2.76$ TeV, and correctly propagating the systematic uncertainties in this process, a pQCD-based scaling factor is derived that is used to scale the measured cross-sections. These cross-sections were again fit with a Tsallis functions which provided an input weight for the cocktail generator. As for the case of the light mesons, 10^7 J/ψ and Υ particles were generated uniformly spatially and in p_T, and subsequently allowed to decay freely. The resulting electron yield is then weighted with the appropriate data-derived weighting function.

7.1.4 Direct Photons

Prompt photons from the initial hard scatterings can also contribute to the inclusive electron cross-section. Both real photons (which decay to electrons via conversion in the detector material) and virtual photons (which decay directly to $^{+}e^{-}$ pairs) provide contributions to the total electron yield. The prompt photon production cross-section has not yet been measured in ALICE, and thus NLO pQCD calculations were used to estimate this contribution [23, 297, 298]. The yield of real prompt photons from NLO pQCD calculations was parameterized and the corresponding electron spectrum from conversions was included in the cocktail. The yield of electrons from virtual prompt photons was estimated from the predicted yield of real prompt photons and the expected ratio of the real to prompt photon yields which exhibits a p_T dependence that had to be accounted for.

7.1.5 Other Possible Background Sources

All other potential background sources, such as Drell-Yan production, are assumed to be negligible in the background electron cocktail. The total background electron cocktail illustrating the magnitude of the various included components is illustrated in Figure 7.1.3:

7.2 Systematic Uncertainty

There are a number of sources of uncertainty in the background cocktail, the dominant source being the uncertainty in the pion input spectrum. The limited statistics in the $\sqrt{s} = 2.76$ TeV

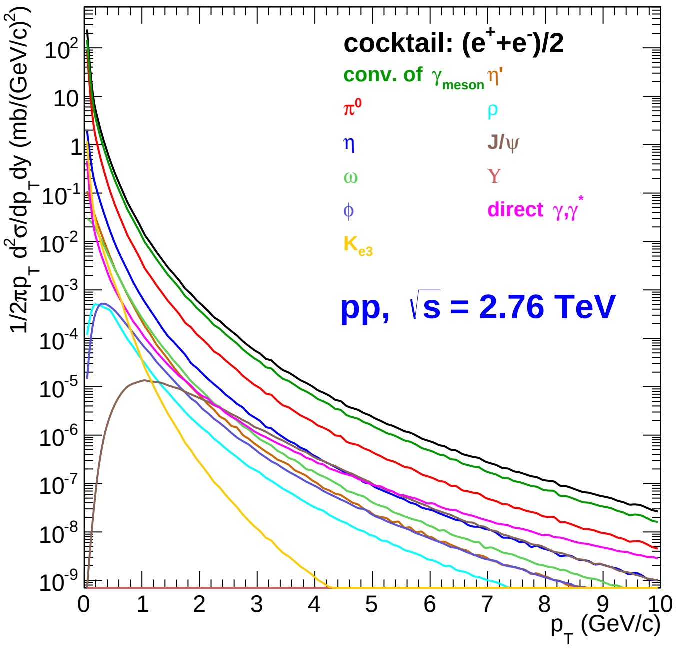

Figure 7.1.3: Invariant yield of background electrons from the various sources included in the background electron cocktail

pp sample limited the precision with which both the π and η production cross-sections could be measured. This uncertainty is subsequently propagated into the determination of the systematic uncertainty associated with the background electron cocktail. This uncertainty is also propagated to the weighting functions used to the other light mesons, in addition to the inclusion of the uncertainty in the measured ratios of the light meson yields. Finally, this uncertainty also has an impact on the yield of electrons from conversions of photons arising from the decays of the light mesons. In this case, the uncertainty incorporates both the uncertainty in the input spectrum, the uncertainty in any needed m_T scaling, the uncertainty in the relative 2-photon and Dalitz decay branching ratios, and the uncertainty in the material budget. For the $\mathrm{K_{e3}}$ decays, the yield of which relies completely on simulation, a conservative 100% uncertainty was assumed. For the electrons from prompt photons, again a conservative value of 50% was assumed. Finally, for J/ψ and Υ decays, the uncertainty in both the input spectrum, and the uncertainty associated the pQCD scaling factor was taken into account. The total systematic error is estimated to be between 7% and 30%, the p_T dependence and the relative magnitudes of the contribution from the various sources can be seen in Figure 7.2.1

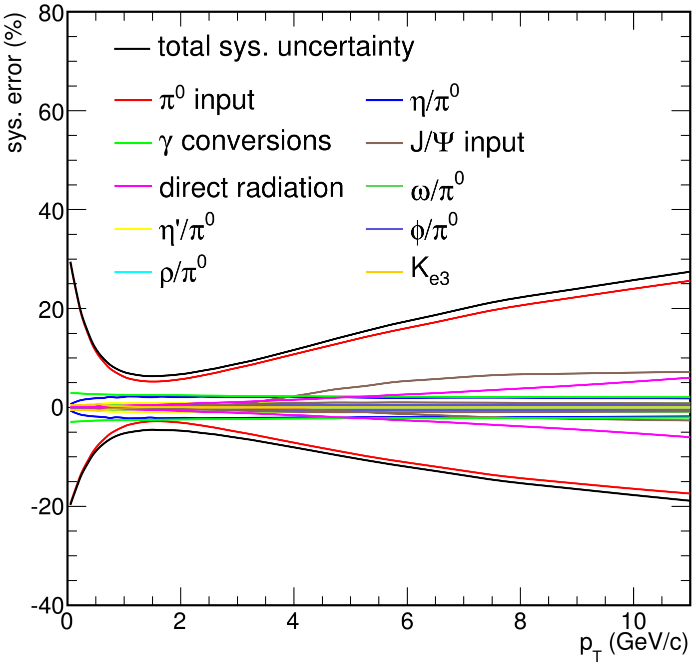

Figure 7.2.1: The magnitudes of the systematic error introduced in the background cocktail from various sources

8

Results

8.1 Inclusive Electron Cross-Section

Employing the event selection criteria described in Chapter 3, the track cut quality criteria of Chapter 4, and the particle identification methodology delineated in Chapter 5, a p_T spectrum of identified electrons is obtained. To convert this raw yield to a cross-section, multiple corrections need to be applied. Firstly, those corrections described in previous chapters have to be applied: the tracking efficiency correction, the corrections for the PID efficiency and purity, the trigger efficiency correction, and the p_T smearing and bremsstrahlung unfolding corrections. Secondly, the yield needs to be scaled against some reference cross-section, and also has to be divided by the region of phase space considered (to get a cross-section per unit rapidity and per unit ϕ). For the MB data set, the conversion from yield to cross-section follows from:

$$\frac{1}{2\pi p_T}\frac{d^2\sigma^e}{dp_T dy} = \frac{1}{2}\frac{1}{2p_T\Delta\phi}\frac{1}{\Delta y}\frac{1}{N_{evts}^{MB}}\frac{dN_{PID}^e}{dp_T}\frac{p_{PID}}{\epsilon_{PID}}\frac{1}{\epsilon_{trk}}\frac{\sigma_{MB}}{C} \tag{8.1}$$

where y is the pseudorapidity, Δy is the pseudorapidity acceptance, $\Delta\phi$ is the ϕ acceptance, N_{evts}^{MB} is the number of MB events that pass the event cuts, $\frac{dN_{PID}^e}{dp_T}$ is the raw yield (number of identified electrons per p_T without corrections), p_{PID} is the PID purity, ϵ_{PID} is the PID efficiency, and ϵ_{trk} is the tracking efficiency.

The factor $\Delta\phi\Delta y \sim (1.95)^*(2^*0.7)$ takes into account the acceptance of the EMCal detector. At the energies relevant for this measurement, the rapidity range is well approximated by the pseudorapidity range for electrons, and $\Delta y \approx \Delta\eta$. The fraction $\frac{1}{2}$ is inserted to account for the fact that the result includes both electrons and positrons; strictly speaking the measured yield is $\frac{1}{2}(N_{e^-} + N_{e^+})$, though it is referred to as the ‘electron yield’ throughout. The characteristic $\frac{1}{p_T}$ is included to generate a lorentz-invariant yield, and in this analysis, p_T is taken to be the midpoint of the p_T bin as per ALICE convention. The factors σ_{MB} and C pertain to the cross-section normalization. In order to convert to an electron cross-section, the total cross-section of a reference process that is simply related to the process under consideration has to be measured. In this case, the simplest measurement would be to measure the total cross-section, σ'_{MB}, for events that pass the event cuts used in this analysis. The conversion to a cross-section from the yield is then simply a multiplication by σ'_{MB}. However, the only cross-section measured at ALICE for $\sqrt{s} = 2.76$ TeV pp collisions, was the total cross-section with a slightly different set of event cuts than used in this analysis. Explicitly, the total cross-section was measured with the same event cuts as for this analysis but without the vertex existence requirement. Hence the measured cross-section has to be divided by $C = N_{evts}^{vtx}/N_{evts}^{\cancel{vtx}}$ where N_{evts}^{vtx} is the number of MB events that pass the vertex existence cut and $N_{evts}^{\cancel{vtx}}$ is the number of MB events that pass all cuts except the vertex existence requirement.

The total-cross section was measured by the ALICE collaboration with the Van-de-Meer scan technique [265]. The Van-de-Meer scan provides a method of luminosity monitoring, luminosity normalization and thus the measurement of reference cross-sections. In principle, the absolute luminosity can be determined solely from the properties of the beam (see section 2.1.1). However, a precise and non-destructive measurement of the relevant beam parameters poses difficulties. The Van-de-Meer scan method provides a precise way of measuring the absolute luminosity and thus (combined with the measured rate) normalization cross-sections. The principle of a Van-de-Meer scan is to measure the rate of a given process as a function of the beam position as the two beams are moved across one another in two directions in the plane perpendicular to the beam direction. The rate is approximately gaussian as a function of beam separation, with the maximum being the rate for head-on collisions. The luminosity is thus calculated as [265, 299]:

$$\mathcal{L} = nN_1N_2f_{rev}Q_XQ_Y \tag{8.2}$$

where n is the number of colliding bunches, $N_{1/2}$ is the number of protons per bunch in beam 1/2 and f_{rev} is the revolution frequency. $Q_{X/Y} = \frac{R(0,0)}{S_{X/Y}}$ where $R(0,0)$ is the maximum rate, and $S_{X/Y}$ is the scan area in the X/Y directions. The absolute luminosity enables a measurement of the cross-section of a particular process as $\sigma_R = R(0,0)/\mathcal{L}$ [265]. The resulting MB cross-section in $\sqrt{s} = 2.76$ TeV pp collisions was determined to be 47.7 ± 0.03 mb , with $C = 0.861 \pm 0.004$.

For the case of the EMCal triggered data, the conversion of the yield to cross-section also involves a correction for the trigger bias. As described in Chapter 6, this involves two elements: the rejection factor, F_{rej}, and the trigger efficiency, ϵ_{trig}. The conversion to cross-section is thus calculated as:

$$\frac{1}{2\pi p_T}\frac{d^2\sigma^e}{dp_T dy} = \frac{1}{2}\frac{1}{2p_T\Delta\phi}\frac{1}{\Delta y}\frac{1}{N^{HT}_{evts}}\frac{dN^e_{PID}}{dp_T}\frac{p_{PID}}{\epsilon_{PID}}\frac{1}{\epsilon_{trk}}\frac{\sigma_{MB}}{C}\frac{1}{\epsilon_{trig}}\frac{1}{F_{rej}} \tag{8.3}$$

where N^{HT}_{evts} is the number of EMCal triggered events that pass the event cuts. The p_T smearing and Bremsstrahlung correction can not easily be incorporated into these equations. Moreover, since the unfolding takes place after the spectra are merged, each individual spectrum is not really corrected exactly as in equations (8.1),(8.3). In fact, both spectra are first corrected with the $\frac{1}{N^{MB/HT}_{evts}}$ factor, and then the EMCal triggered spectrum is corrected for the trigger efficiency with the factor $\frac{1}{\epsilon_{trig}}\frac{1}{F_{rej}}$. The spectra are then combined, using the MB data for $p_T < 4$ GeV/c and using the HT trigger data for $p_T > 4$ GeV/c. At this stage the unfolding procedure is implemented, and the final merged spectrum is corrected in a similar way to equation (8.1) (modulo the $\frac{1}{N^{MB/HT}_{evts}}$ factor that was already applied).

One final comment applies to the application of the various efficiency and purity corrections to the spectrum as per equations (8.1),(8.3). Since the binning of the spectrum is not identical to the binning of the various calculated corrections, some interpolation needs to be employed. This problem is particularly acute for the PID efficiency and purity corrections where the binning is quite wide. In this context, the exponentially decaying form of the spectrum is particularly relevant. When the bins are wide with respect to the rate of change of the spectrum, it is not appropriate to take the center of the bin as a representation of average p_T of a particle in that bin [300]. In the case of an exponentially falling spectrum, the true p_T average will be shifted towards lower values of p_T. This effect had to be accounted for when employing these corrections. A sense of the magnitude of the correction can be seen in Figure 8.1.1 which shows the standard bin positions and correctly shifted bin positions for the inclusive cross-section.

In this analysis, the shifted bin positions were calculated assuming the spectrum follows that predicted by FONLL calculations. In theory, the shifted bin positions could be calculated without the use of FONLL by iteratively fitting a functional form to the measured cross-section, recalculating the bin positions from this measurement, and refitting a functional form to the new result with the new bin positions. However, since the final result was consistent with FONLL, and the bin-shifting correction is a small correction in any case, the smoother FONLL functional form was used. When a function is then fitted to the efficiency, the resulting curve thus provides the efficiency at the correctly shifted bin location. Note that this requires the calculation of several different bin shifted

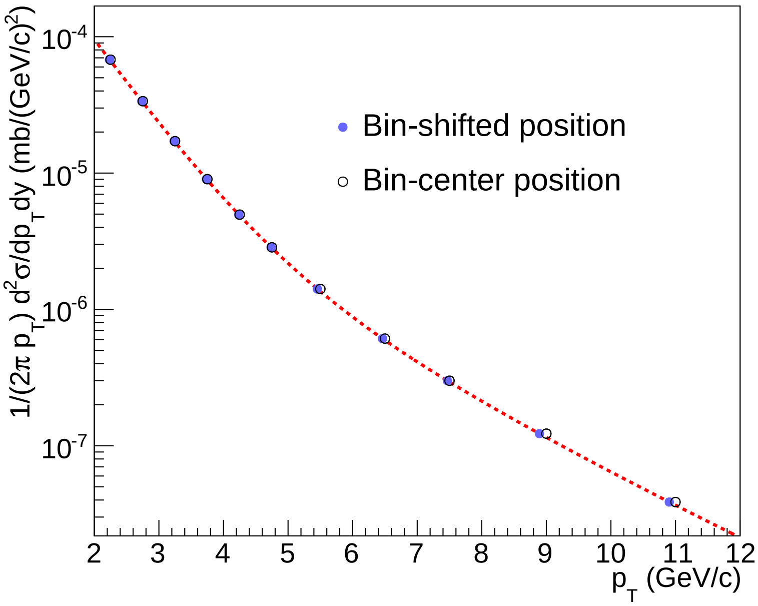

Figure 8.1.1: Illustration of the effect of an exponentially decaying spectrum on the average bin position. The FONLL prediction for the heavy-flavor cross-section was taken as the assumed functional form. This bin-shifting effect was incorporated into the application of the various efficiency and purity corrections

positions, one for the spectrum and one for each efficiency/purity correction (as the efficiencies and purities are calculated with different binnings than the spectrum).

Employing these various corrections results in the inclusive electron cross-section shown in Figure 8.1.2. In this figure, the unfolding correction is performed on the MB and EMCal spectra separately, and the resulting spectra are merged only in the final stage. The different colors make it clear where the MB data is utilized ($p_T < 4$ GeV), and where the EMCal triggered data is utilized ($p_T > 4$ GeV). That the points are consistent in the overlap region verifies that the trigger bias correction functions as expected. However, in Chapter 4 it was noted that the systematic uncertainty associated with the unfolding is reduced when the spectra are merged before the unfolding procedure is applied. Hence in this analysis, the spectra were merged before the unfolding correction was applied. The result of this method is shown in Figure 8.1.3. This result, and that in Figure 8.1.2 obtained by merging after unfolding, are consistent within the systematic uncertainty associated with the unfolding procedure.

The magnitude of the various sources of systematic uncertainty for both the inclusive electron and the heavy flavor cross-sections is shown in Figure 8.1.4. The largest contributions to the systematic uncertainty are the PID efficiency and purity (where a dearth of statistics limited the

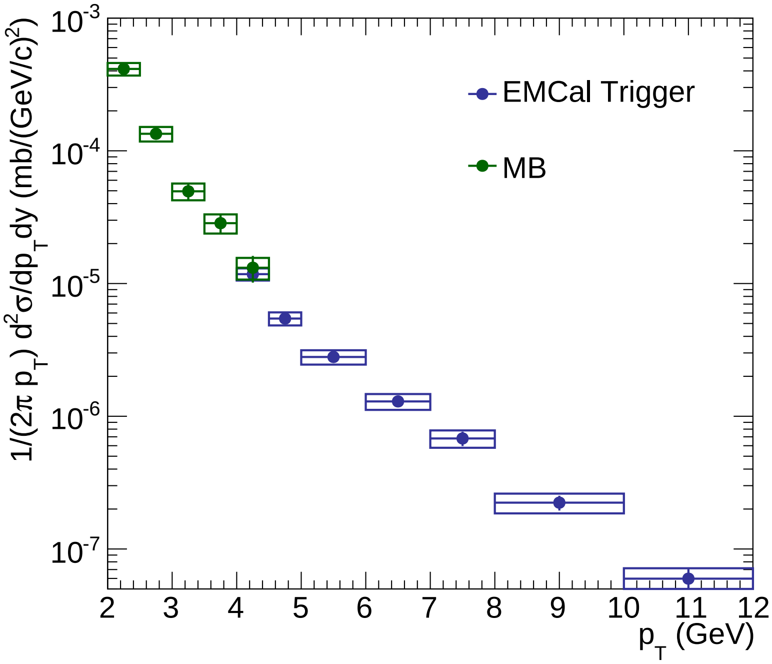

Figure 8.1.2: Inclusive electron cross-section obtained by unfolding the MB and EMCal separately and subsequently merging. The boxes present the systematic uncertainty and the error bars represent the statistical uncertainty

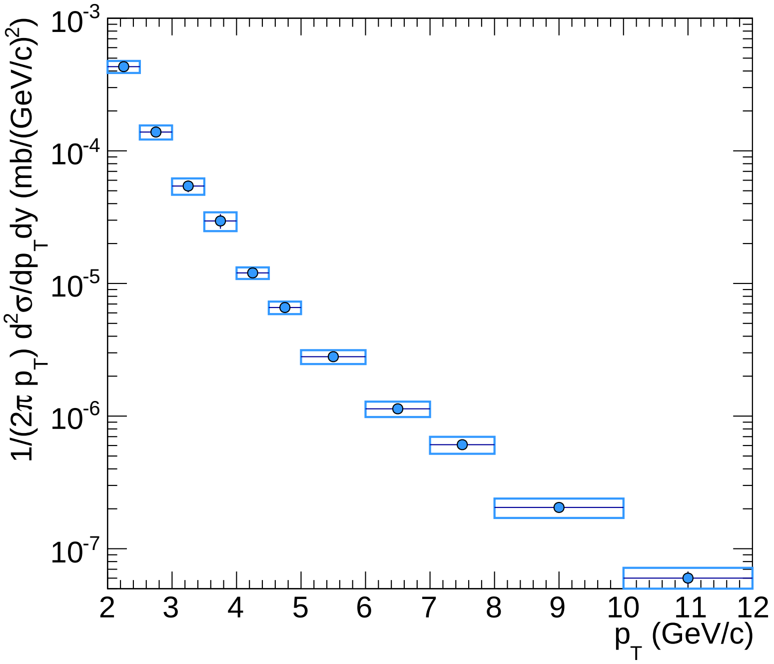

Figure 8.1.3: Inclusive electron cross-section obtained by merging the MB and EMCal trigger spectra before applying the unfolding procedure. The boxes present the systematic uncertainty and the error bars represent the statistical uncertainty

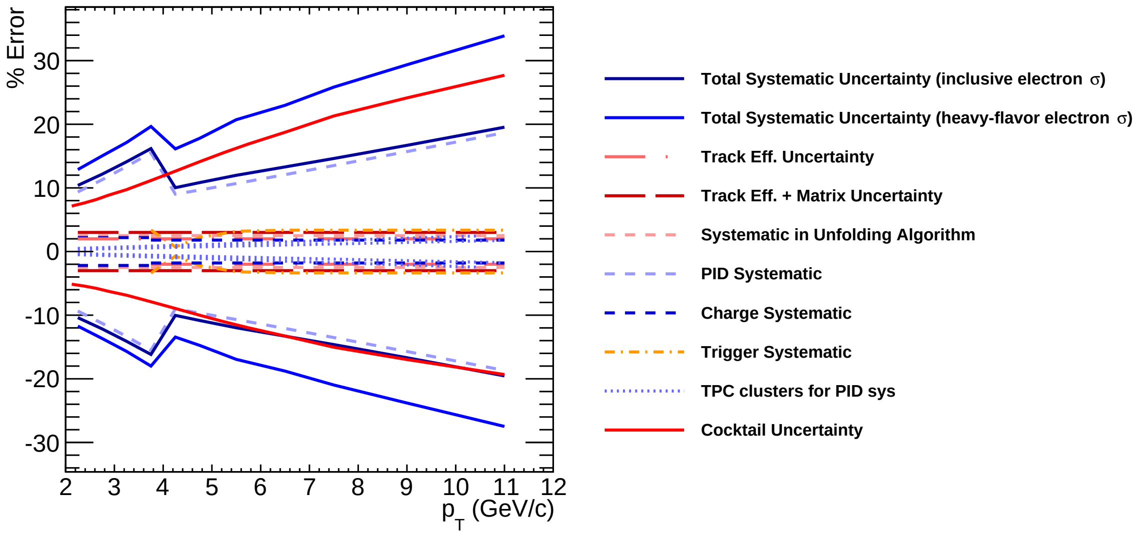

Figure 8.1.4: Systematic error from various source in the inclusive electron cross-section and the heavy-flavor electron cross-section. The heavy-flavor electron cross-section includes the systematic uncertainty associated with the cocktail

precision of the measurement), and the background cocktail used in the measurement of the heavy-flavor cross-section (where significant systematic and statistical uncertainties in the measurement of the π^0 and η spectra contributed to large uncertainty in the background cocktail, particularly at high p_T).

8.2 Heavy-Flavor Electron Cross-Section

The inclusive electron cross-section combines electrons from a multitude of sources. The goal of this analysis is to extract the heavy-flavor contribution, that is, electrons originating from the decays of b and c hadrons. The abundant electrons from other sources are assumed to be well described by the simulated cocktail described in Chapter 7. Although derived from simulations, the constructed cocktail is data-driven as far as possible; the spectra are weighted according to measurements from ALICE, and the only extra assumption is that of m_T−scaling. To determine the heavy-flavor electron cross-section, the generated background cocktail is subtracted from the inclusive electron cross-section. Figure 8.2.1 shows the result along with a comparison to a number of theoretical calculations. Since the b and c quarks have large masses, their production is dominated by the initial hard partonic scattering, and all three theoretical calculations are fundamentally based on perturbative QCD. The differences between the calculations largely arise from the chosen method of evaluating the hard-scattering partonic cross-section (see section 1.5.1).

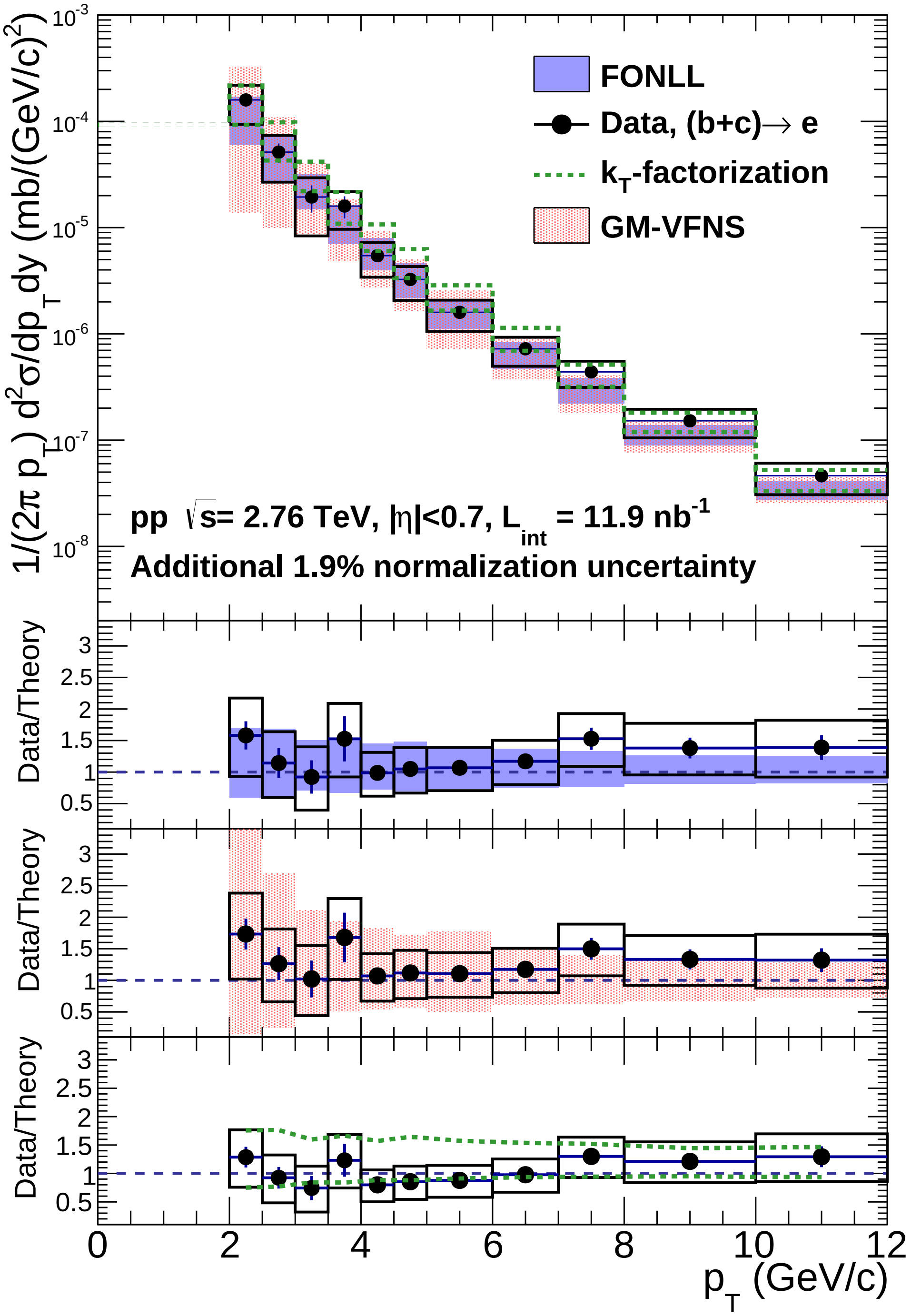

Figure 8.2.1: Heavy-flavor electron cross-section in $\sqrt{s} = 2.76$ TeV pp collisions compared to FONLL, GM-VFNS and k_T-factorization models

The bin-shifting effect that is necessary to properly apply the efficiency and purity corrections is also relevant when making comparisons to theoretical predictions. Theoretical predictions are continuous curves with a yield given at a precise value of p_T, while the measured cross-section is a histogram with finite bin widths. This can easily be resolved by plotting the measured cross-section in each bin not at the center of the bin, but at the correctly bin-shifted position. However, it is convention within ALICE to plot the bin position at the center of the bin. In order to make a fair comparison to theory, and to account for this bin-shifting effect, the theoretical prediction is binned in the same manner as the measurement (i.e the continuous curve is integrated over the bin width, and the average value is plotted at the center of the bin). The comparison shows that measured cross-section is consistent with all theoretical calculations considered. Improved precision in both theory and experiment would be required to distinguish between the models based on this measurement alone. However, this result is already an impressive outcome on both the theoretical and experimental ends. At the Tevatron it took many years between the apparent discrepancy between NLO pQCD predictions of and measurements of heavy-quark production cross-sections could be resolved.

The heavy-flavor electron cross-section is soon to be published in a paper which combines analyses using the TPC and TOF for PID, the TPC alone for PID, and this analysis using the TPC and EMCal for PID. The utilization of the TOF allows for improved particle identification at lower p_T. Moreover, the TPC-TOF and TPC-only analyses use data both with and without the SDD which results in a doubling of statistics. These two factors improve the precision of the cross-section measurement in the momentum range $0 \lesssim p_T \lesssim 6$ GeV/c.

The result is also an important piece of a number of other analyses that have been published and are yet to be published. In particular, the contributions to the heavy-flavor cross-section of electrons from the decay of b hadrons and from the decay of c hadrons has been disentangled using correlations. The measurement also provides a crucial reference for R_{AA} measurements. At present, preliminary results for 0-10% centrality have been presented within ALICE, and results for other centralities should soon follow. In the following sections, a short summary of the results of these other analysis is provided.

8.3 Disentanglement of b/c Contributions

The analysis conducted for this thesis provided a measurement of the cross-section of electrons originating from the decays of heavy-flavor hadrons in $\sqrt{s_{NN}} = 2.76$ TeV pp collisions. The unexpectedly large suppression of high p_T electrons from the semi-leptonic decays of charm and beauty hadrons in heavy-ion collisions observed in STAR makes the disentanglement of the relative b and c contributions imperative for understanding the energy loss mechanisms in the QGP [289, 290]. There are two approaches to this disentanglement currently employed in ALICE: the use of correlations, and the geometrical 'b-tagging' approach. In addition, CMS have measured the cross-section of b-electrons by measuring the transverse momentum of muons with respect to the closest jet [301].

In the 'b-tagging' approach, geometrical properties of beauty hadron decays are exploited to provide discrimination of electrons that originate from the decays of charm hadrons from those that originate from the decays of beauty hadrons. Leverage is in particular provided by the large decay length which can be of the order of 500 μm, leading to the generation of characteristic secondary vertices and large impact parameters from the primary vertex [302, 303, 304, 305]. The associated decay length is within the design resolution requirements of ALICE. Unfortunately, in practice the resolution has not been quite sufficient to provide easy identification of such *displaced vertices*, although discriminatory capabilities have already been demonstrated with measurement of the production cross section of electrons from the decay of beauty hadrons in $\sqrt{s}$ =7 TeV pp collisions [306]. The planned upgrade to the ALICE inner tracking system should provide enhanced secondary vertex identification capabilities [237]. Feasibility studies conducted by ALICE [307] concluded that geometrical 'b-tagging' was not feasible using the ALICE EMCal in $\sqrt{s_{NN}} = 2.76$ TeV pp collisions, so another approach needed to be employed.

The use of correlations provides an alternative approach to the disentanglement. Due to their large masses, heavy quarks are primarily produced in the initial hard scatterings. Flavor and momentum conservation then implies heavy quarks are produced in $q\bar{q}$ pairs back-to-back in azimuth. This azimuthal correlation in large part survives fragmentation. However, charm quarks tend to hadronize directly, whereas beauty quarks tend to do so via D^0 meson production. The differing fragmentation leads to azimuthally broader jets for b quark hadronization than c quark hadronization. Thus the initial state azimuthal correlation is less well preserved for b quarks, leading to broadened correlation distributions. By fitting $e-$hadron correlations with a weighted combination (the weighting being a parameter of the fit) of correlation distributions from b and c quarks generated from Monte Carlo simulations, the ratio of electron yield from b hadron decays to that of the heavy-flavor electron yield can be obtained. Figure 8.3.1 shows the result of this correlation analysis in $\sqrt{s}$ =2.76 TeV collisions. By combining this result with the cross-section of electrons from heavy-flavor decays, the cross-section of electrons from the decays of b and c hadrons can be extracted. Figure 8.3.2 shows the resulting disentangled cross-sections of electrons from b-hadron

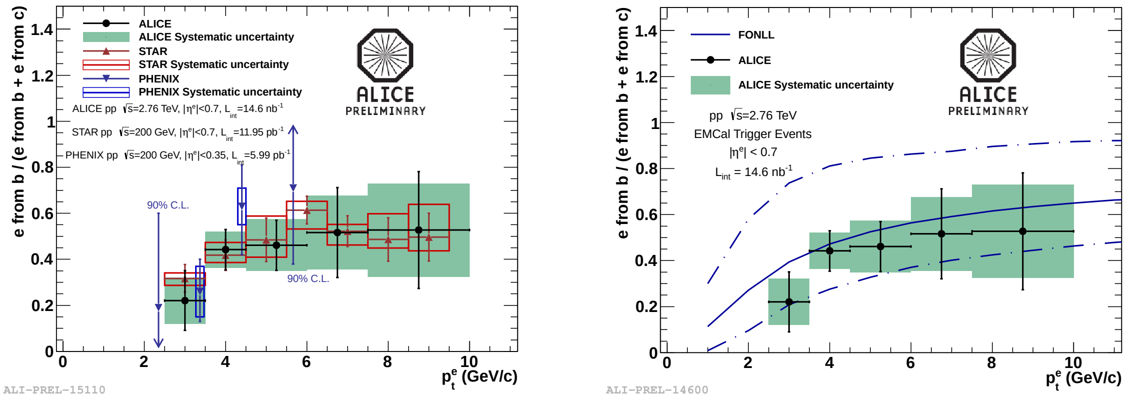

ALI-PREL-15110 ALI-PREL-14600

Figure 8.3.1: Measurement of the ratio of the yield of electrons from the decays of b-hadrons to the yield of electrons from heavy-flavor hadrons by ALICE, with comparison to other experiments (left) and FONLL (right) [41]

decays, and electrons from c-hadron decays. Since the statistics are limited for this data set, both

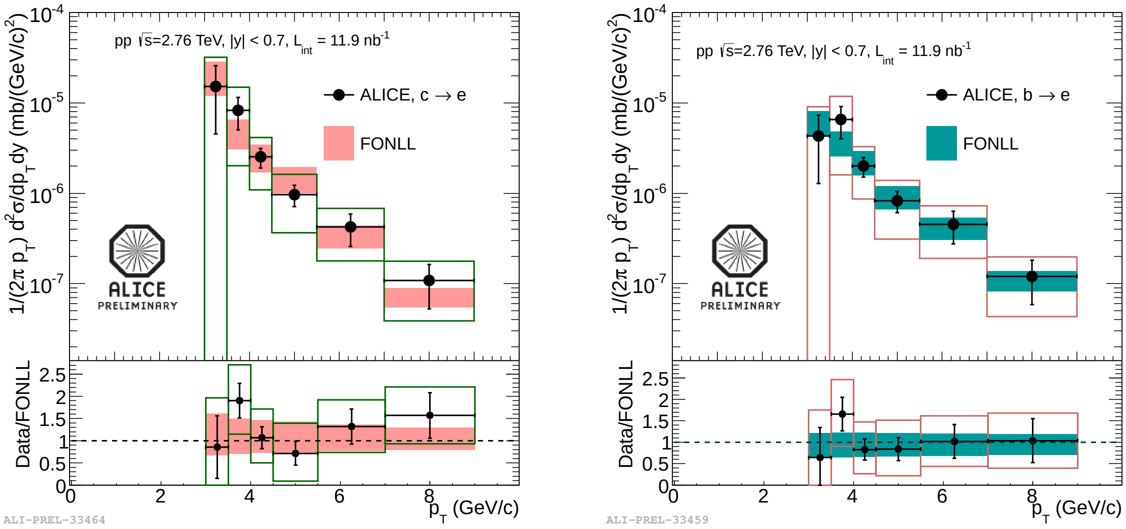

ALI-PREL-33464 ALI-PREL-33459

Figure 8.3.2: Measured of the charm and beauty electron cross-sections obtained by combining the result of this analysis with the result of a correlation analysis by ALICE [31]

analyses and have quite large associated systematic uncertainties. This results in large systematic uncertainties in the cross-section of electrons from b/c-hadron decays, but within the statistical and systematic uncertainties the results are consistent with FONLL predictions.

8.4 pQCD $\sqrt{s}$-Scaling of the Measurement at $\sqrt{s} = 7$ TeV

The cross-section of electrons from heavy-flavor decays has also been measured using ALICE in $\sqrt{s} = 7$ TeV *pp* collisions [23]. The measurement of the same quantity in $\sqrt{s} = 2.76$ TeV *pp* collisions provides the opportunity to test the $\sqrt{s}$-scaling of the cross-section as predicted by pQCD, in particular by FONLL. The uncertainty in a given prediction from pQCD is typically estimated with the variation of four sets of scales: the renormalization scale, μ_R, the factorization scale, μ_F, and the quark masses, m_c, m_b [308]. Like the running coupling constant, all measured quantities (including these parameters) vary with energy and thus there is some uncertainty in deciding exactly at what scale these parameters should be evaluated. The renormalization scale defines the energy scale at which renormalization is performed, and is typically set to one of the energy scales involved in the problem. The factorization scale is the scale that separates hard perturbative processes from soft non-perturbative processes, and the quark masses are self-explanatory. There is also uncertainty in the associated parton distribution functions and their evolution via the DGLAP equations [168]. The uncertainty in these parameters is commonly varied according to the following scheme [308, 309]:

- $0.5 < \mu_F/\mu_0 < 2$
- $0.5 < \mu_R/\mu_0 < 2$
- The above are imposed such that $0.5 < \mu_F/\mu_R < 2$
- $1.3 < m_c < 1.7$ GeV
- $4.5 < m_b < 5.0$ GeV

where $\mu_0 = \sqrt{m_Q^2 + p_{T,Q}^2} = m_{t,Q}$. The FONLL $\sqrt{s}$-scaling ratio is then obtained by taking the ratio of the FONLL prediction at $\sqrt{s} = 7$ TeV and the FONLL prediction at $\sqrt{s} = 2.76$ TeV, with the uncertainties estimated from the spread of the predictions resulting from the defined parameter variations. This scaling factor has already been applied to D-meson measurements performed by ALICE in $\sqrt{s} = 7$ TeV *pp* collisions, as well as the cross-section of electrons from heavy-flavor decays in $\sqrt{s} = 7$ TeV *pp* collisions [310]. Figure 8.4.1 shows the comparison of cross-section of heavy-flavor electron production measured in $\sqrt{s} = 2.76$ TeV *pp* collisions to the scaled $\sqrt{s} = 7$ TeV cross-section. The comparison demonstrates that in the region where the measurements overlap, the pQCD $\sqrt{s}$-scaling performs well. This is to be expected given that the measurements at both energies are consistent with FONLL predictions.

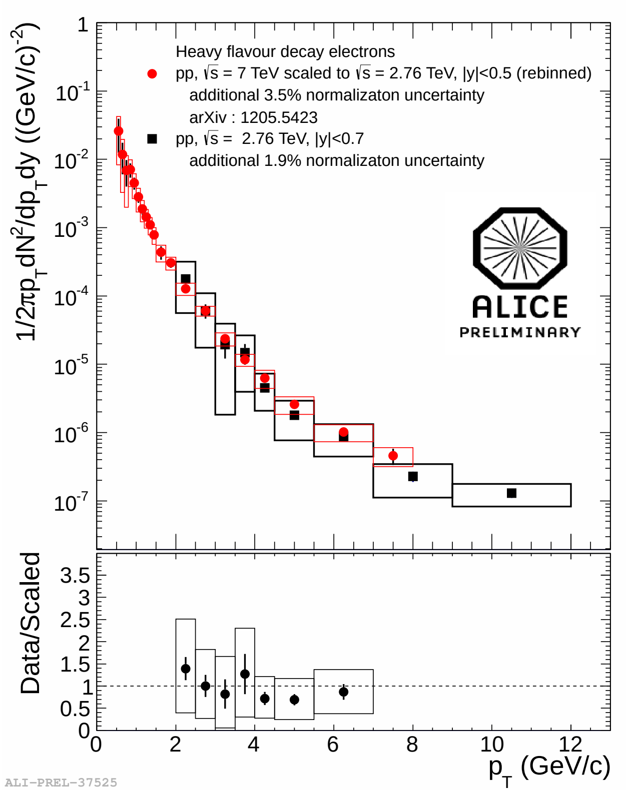

Figure 8.4.1: Comparison of the heavy-flavor electron production cross-section measured in $\sqrt{s} = 2.76$ TeV *pp* collisions for this thesis to the heavy-flavor electron production cross-section measured in $\sqrt{s} = 7$ TeV *pp* collisions scaled to $\sqrt{s} = 2.76$ TeV collision energies using a pQCD based scaling [31]

8.5 Measurement of Heavy-Flavor Electron R$_{AA}$

As described in Chapter 1, the measurement R$_{AA}$ provides a characterization of the in-medium energy loss in Pb-Pb collisions. The measurement performed in this analysis provided a necessary baseline for a determination of R$_{AA}$ in $\sqrt{s_{NN}} = 2.76$ TeV Pb-Pb collisions. A similar analysis to that undertaken for this thesis has been undertaken by ALICE in Pb-Pb collisions, that is, the heavy-flavor electron cross-section was also measured in $\sqrt{s_{NN}} = 2.76$ TeV Pb-Pb collisions [42]. At present, since the $\sqrt{s} = 2.76$ TeV result is not yet published, the result of the $\sqrt{s}$-scaling was used to justify utilization of the scaled $\sqrt{s} = 7$ TeV as a reference cross-section (latter results will directly utilize the measured cross-section at $\sqrt{s} = 2.76$ TeV as a reference). Moreover, the kinematic reach of the measurement in Pb-Pb collisions extends far beyond that in *pp* collisions, reaching almost 20 GeV/c. Hence the preliminary R_{AA} measurement utilizes the scaled $\sqrt{s} = 7$ TeV cross-section where possible, and since the FONLL prediction is consistent with measurement where statistics are sufficient, the FONLL prediction is used as a reference where the scaled measurement is statistics limited. Figure 8.5.1 shows the preliminary heavy-flavor electron R_{AA} measurement compared to results from PHENIX in $\sqrt{s} = 200$ GeV Au-Au collisions. This result is still in flux, and the measurement for different centralities is yet to be completed.

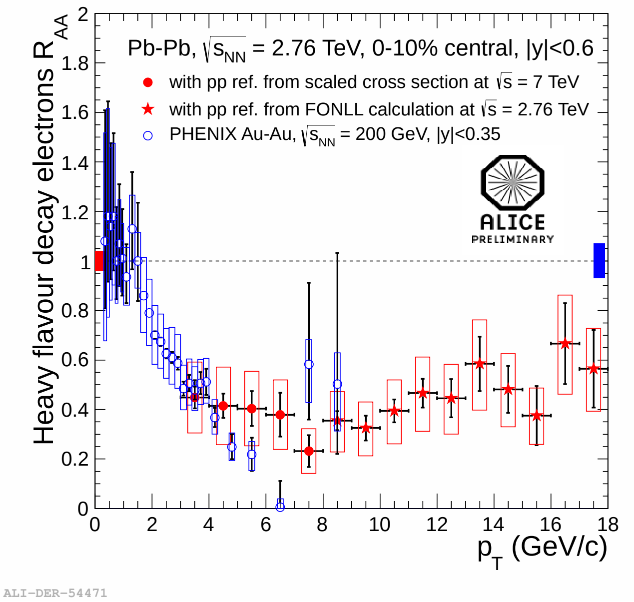

Figure 8.5.1: Heavy-flavor electron R_{AA} as measured by ALICE in $\sqrt{s} = 2.76$ TeV Pb-Pb collisions for most central events (0-10%) compared to the heavy-flavor electron R_{AA} measured by PHENIX in $\sqrt{s} = 200$ GeV Au-Au collisions [31, 42]. The results are consistent where they overlap. Note that for $p_T < 8$ GeV/c the the scaled $\sqrt{s} = 7$ TeV *pp* cross-section was used as a reference, while above $p_T = 8$ GeV/c the FONLL prediction for *pp* collisions was used as a reference

8.6 Looking Forward

Stemming from ideas in the early 1980's, the highest energy accelerator ever built, the LHC, finally began operation in 2008. The first operation of the LHC marks a new and exciting epoch for high energy physics that continues to the present day. Since it's inception, a plethora of interesting physics results have emerged from the LHC including the discovery of the long elusive Higgs boson [11, 311, 312, 313, 314]. The domain of heavy flavor physics is no exception to the success of the LHC thus far [315, 316, 317, 318, 319]. In this thesis, a measurement of the differential production cross-section of electrons from the decays of heavy-flavor hadrons in $\sqrt{s} = 2.76$ TeV *pp* collisions using the ALICE detector was presented. Like a plethora of other heavy-flavor results in *pp* collisions, the measurement is consistent with pQCD predictions of heavy-quark production. This conclusion is a success in it's own right, but the result also forms a crucial baseline for measurements in Pb-Pb collisions that aim to shed light on the energy loss mechanisms of quarks traversing the QGP.

Preliminary results of the production cross-section of electrons from the decays of charm and beauty hadrons measured by ALICE were also presented in this thesis, but in the future the precision of these preliminary results are expected to improve [320]. The first measurements of the R_{AA} of heavy-flavor electrons by ALICE have also recently emerged, with the full centrality dependence expected to soon follow [42]. In addition, geometrical b-tagging has allowed for measurement of the production cross-section of *b*-quarks on the particle level in ALICE, and on the jet-level in CMS in $\sqrt{s} = 7$ TeV *pp* collisions. CMS is expected to soon produce a measurement of the R_{AA} of b-jets [221], and ALICE has the capacity to do so with appropriate scaling. In addition to the forthcoming results based on the analysis of data already taken, the LHC is expected to have a long future ahead. In the 2017-2018 shutdown in particular, a number of improvement to the experiments will be undertaken. In the context of b-tagging, the improved ITS system that will be installed at ALICE should allow for significantly improved vertex resolution and the separation of charm and beauty decays based on displaced vertices [237, 238]. All in all, the present is a very exciting time for high energy physics. The measurement of heavy-flavor production and energy loss at the LHC in the coming years will continue to provide stringent tests of pQCD and hopefully shed light on the energy loss mechanism of in-medium heavy-quark energy loss.

Appendices

A The ALICE Coordinate System

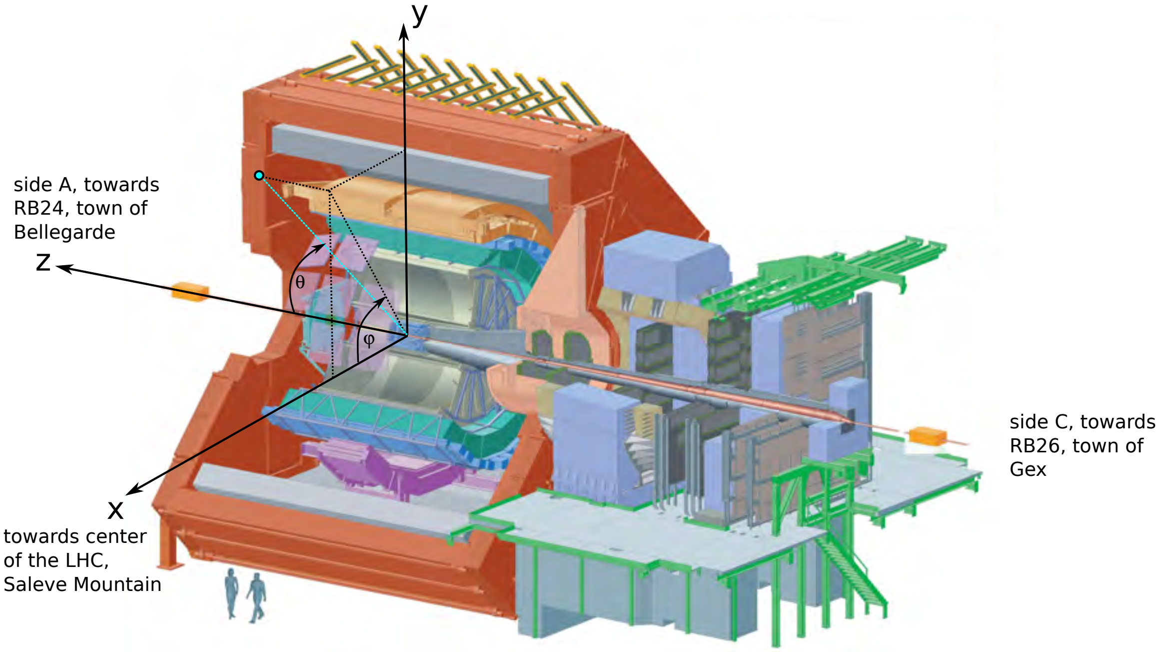

Figure A.1: The coordinate system of the ALICE detector. Adapted from [43, 44]

Figure A.1 illustrates the orthorgonal right-handed cartesian coordinate system of the ALICE detector[43]. The positive x-axis points towards the center of the LHC (see figure 2.1.3). Geographically this in the direction of the Saleve mountain, and the negative x-axis is in the direction of the Jura mountains. The positive z-axis points in the direction of counter-clockwise circulating beams. This side of the detector is know as *side A* (or RB24 after the name of the shielding plug installed at this side of the detector), and geographically is directed towards the town of Bellegarde. *Side C* of the detector is along the negative z-direction geographically directed towards Gex (this side is also referred to as the RB26 side, RB26 being the shielding installed on this side of the detector). The muon arm is installed on the C side of the detector. A polar coordinate system derived from this cartesian system in the usual way is also in use, with the azimuthal angle denoted ϕ and the polar angle denoted θ.

B The Effective Signal

The characterization and optimization of cut selection criteria is most easily accomplished with a quantitative measure of the 'effectiveness' of the cut(s). Often purity and efficiency are competing effects, and high levels of one is almost always at the expense of the other. Defining the optimial 'middle ground' can be a difficult task, and may depend critically on the exact measurement being made. In the context of the measurement of some signal over and above a background (for instance in the measurement of resonances), the *effective signal* can provide a useful quantitative measure of the cut quality, and allow for simple cut optimization algorithms [321].

Assume a measurement is made of some quantity that comprises a signal, S, and a background, B. Figure B.1 is an example of such a measurement with the background and signal highlighted.

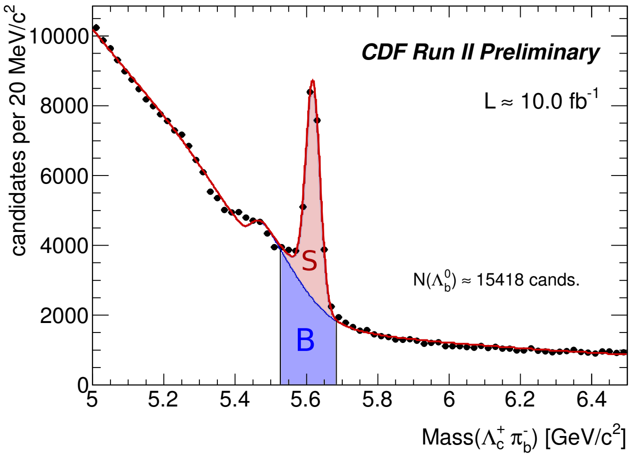

Figure B.1: A real-life example of the measurement that comprises some signal, S, and background B. In this case it is the measurement of the bottom baryon resonance, Λ_b^0, by the CDF collaboration [45]

The effective signal is defined as the signal strength *in the absence* of any background that has the same statistical significance as the measurement with background. The statistical significance is given by $S/\delta S$ and is thus expressed as multiples of σ; a 5σ signal being the accepted standard for claiming discovery. If the total number of counts observed is denoted T, then the significance is given by:

$$\begin{aligned}\frac{S}{\delta S} &= \frac{S}{\sqrt{(\delta T)^2 + (\delta B)^2}} \\ &= \frac{S}{\sqrt{S + 2B}}\end{aligned}$$

assuming poissionian statistics for T and B. With no background, the significance would be:

$$\frac{S}{\delta S} = \frac{S}{\sqrt{S}} = \sqrt{S}$$

Thus the defining relation of the effective signal, S_{eff} is:

$$\frac{S}{\sqrt{S+2B}} = \sqrt{S_{eff}}$$

and hence:

$$S_{eff} = \frac{S}{2\frac{B}{S}+1} \tag{4}$$

The effective signal is a background independent way of characterizing the significance. In the context of this analysis, it provided a convenient parameter for electron PID cut optimization. It was also used in the test beam analysis when studying the effectiveness of various shower parameters in providing electron/hadron separation.

C Additional PID plots

C.1 PID optimization

For completeness, figures C.1 and C.2 show the $\frac{dE}{dx}$ vs $\frac{E}{p}$ distributions in p_T slices for HT and MB data respectively.

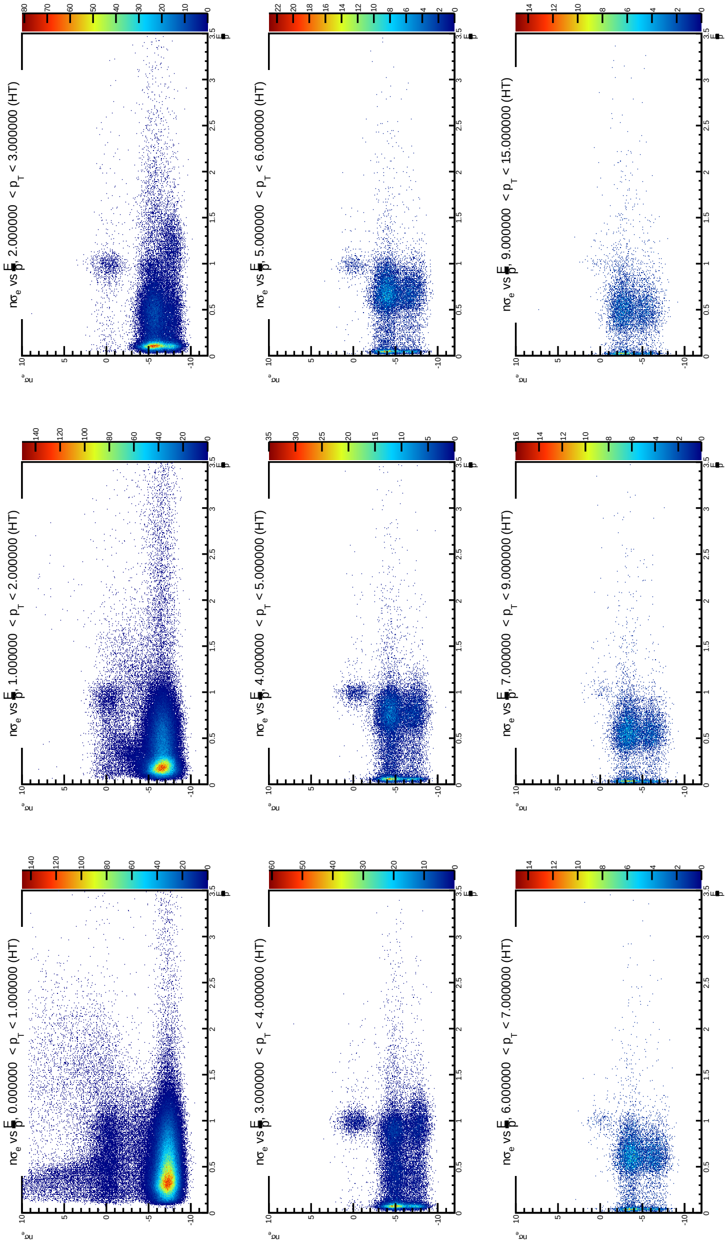

Figure C.1: $n\sigma_e$ vs $\frac{E}{p}$ distributions in p_T slices for HT data

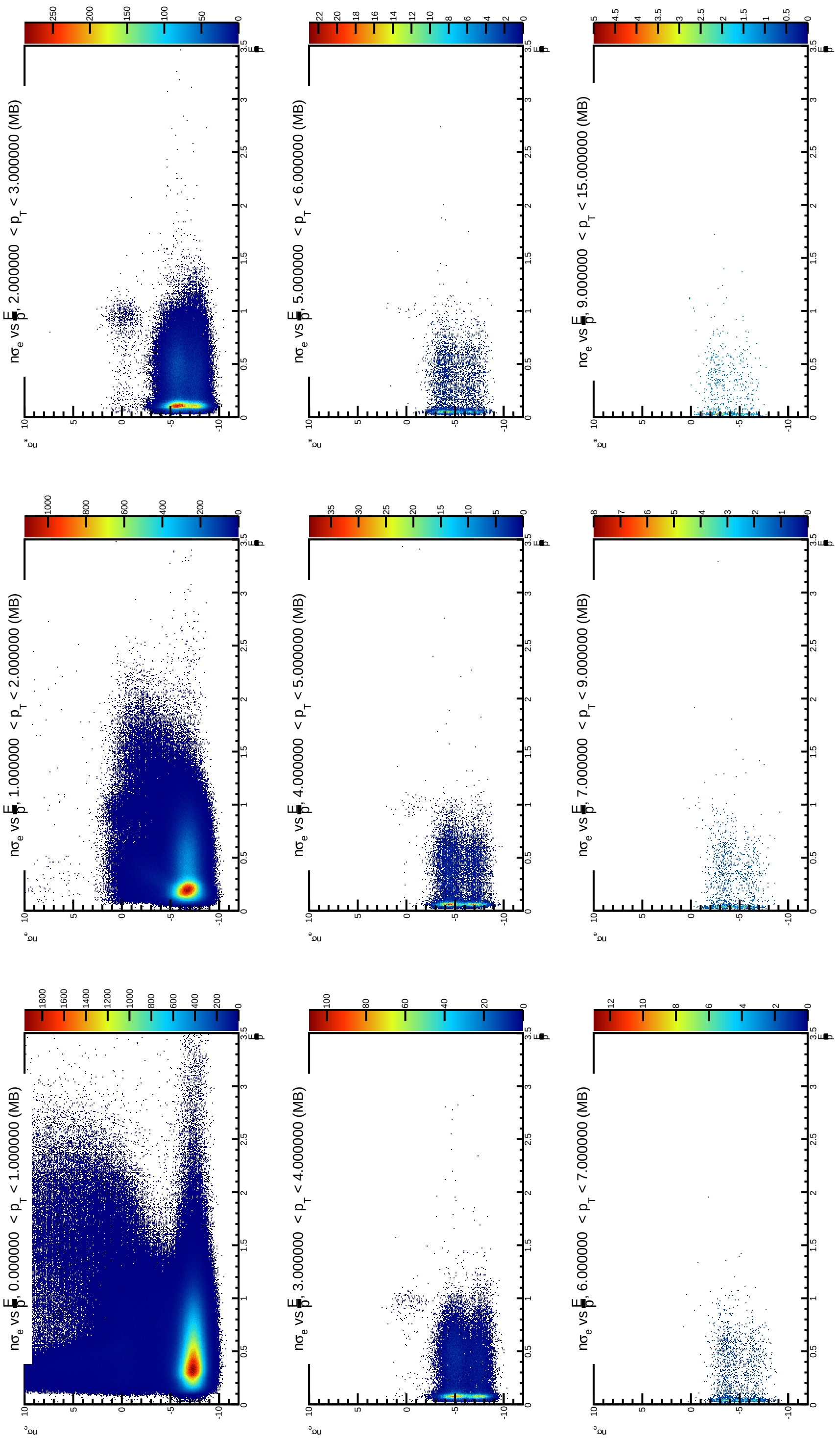

Figure C.2: $n\sigma_e$ vs $\frac{E}{p}$ distributions in p_T slices for MB data

C.2 High p_T PID Efficiency Toy Model

At high p_T the electron and pion dE/dx bands begin to overlap. This poses difficulties for the determination of the PID efficiency, since an estimate of the total number of electrons is needed. Traditionally this is estimated by assuming that all tracks with $n\sigma_e$ above the electron mean position are electrons, and that the total number of electrons in the sample is twice the number of such tracks. However, as the pion bands begin to encroach into the electron band, it is possible for the pion tail to extend beyond the electron band mean position and the assumption that all tracks with $n\sigma_e$ greater than this mean position fails. In this analysis, the approach taken was to vary the cut that defines a pure electron sample. In particular, the cut is moved far enough right that the pion tail does not contaminate the sample. To determine exactly at what position this 'purity cut' should be placed, a toy model was constructed to understand the behavior of the estimated efficiency as a function of this cut.

Figure C.3 illustrates the components of the toy model. An electron gaussian is drawn centered on zero, and four other curves which represent background (pions) are drawn. Three of these background curves are pion gaussians with varying means and correspond to cases of low, medium and high pion contamination of the electron sample defined as pure. A fourth background curve represents a gaussian with a slightly non-gaussian tail that extends beyond the defined purity cut. The effect of applying the E/p cut is replicated by shifting all background curves down by some fixed fraction, and not altering the electron gaussian in anyway. For each background case, the efficiency is estimated exactly as it is in data, however in this case the true efficiency is also known as well as

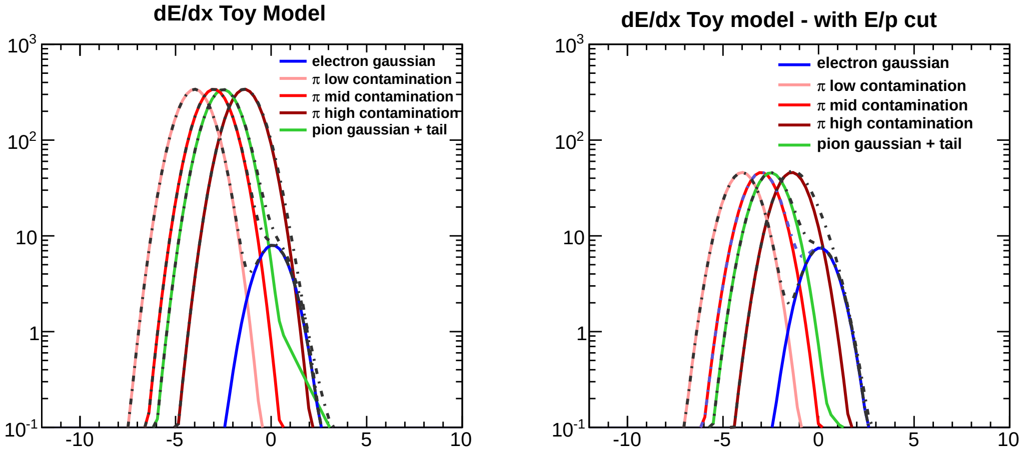

Figure C.3: Illustration of toy model employed to study the effects of varying the 'purity cut' on the determination of the PID efficiency this estimate. Figure C.4 shows the estimated efficiency as compared to the true efficiency for the various background scenarios as a function of the purity cut. The efficiencies exhibit the expected behavior: at low purity cuts where the pion tail easily contaminates the sample defined as pure electrons, the estimated efficiency is too low. As the purity cut is increased, the estimated efficiency eventually plateaus at the true efficiency. For the case with a non-gaussian tail the situation is more problematic: it is difficult to tell a priori how the true efficiency could be approximated at all. More modelling of the non-gaussian characteristics in data would be required. However, there is no evidence of non-gaussian distributions in the data sets used in this analysis so this possibility was ignored. By comparing the efficiency calculated in data as a function of the purity cut, the true efficiency can be determined by identifying the position of the plateau.

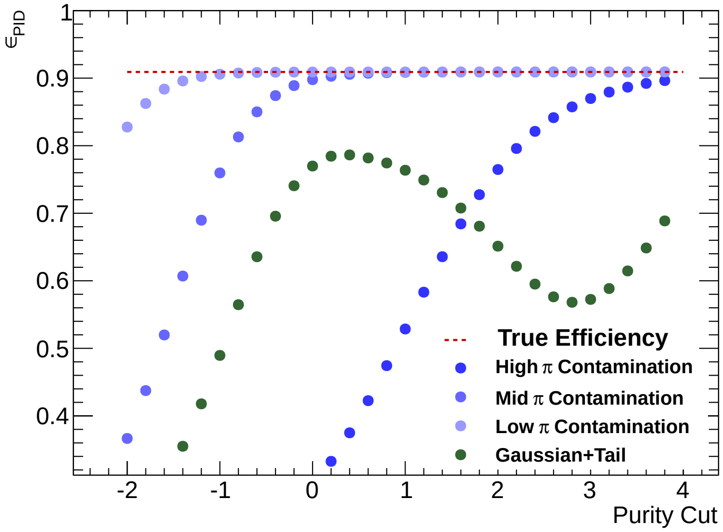

Figure C.4: Estimated PID efficiency in the toy model for various background scenarios as a function of the purity cut

D Trigger Efficiency Formulae

D.1 Trigger Efficiency from MB and EMCal Triggered Spectra

Suppose there are N MB events in a particular sample that could fire a trigger, that the rejection factor is unity, and there is a trigger efficiency of ϵ. Let f_i be the fraction of MB events with *at least* i clusters that could initiate a trigger. Then the number of clusters above the trigger threshold in the MB event (or in a particular bin above threshold) is:

$$\begin{aligned} N_{MB} &= f_1 N + f_2 N + f_3 N + \dots \\ &= N \sum_{i=0}^{\infty} f_i \end{aligned}$$

The corresponding number of clusters in the EMCal triggered spectrum will be:

$$\begin{aligned} N_{HT} &= f_1 N\epsilon + f_2 N\epsilon + f_3 N\epsilon + \dots \\ &= N\epsilon \sum_{i=0}^{\infty} f_i \end{aligned}$$

Hence the ratio of the MB and EMCal triggered spectra will be:

$$R = \frac{N_{HT}}{N_{MB}} = \frac{N\epsilon \sum_{i=0}^{\infty} f_i}{N \sum_{i=0}^{\infty} f_i} = \epsilon$$

which shows that the trigger efficiency can be obtained by simply taking the ratio of the EMCal triggered spectrum to the MB spectrum.

D.2 High p_T trigger efficiency

In this appendix an expression relating the trigger efficiency of the ALICE EMCal to the ratio of the cluster and triggered cluster energy spectra in triggered events is derived. In any particular event there may be multiple particles with an energy greater than the trigger threshold that could initiate a trigger, there being some finite trigger efficiency for doing so. In EMCal triggered events all clusters that could potentially have fired a trigger are labelled as such, and are referred to as *triggered* or *triggering* clusters. If the trigger efficiency were 100%, then one would expect that the inclusive cluster energy spectrum and the triggered cluster energy spectrum in triggered events would be identical. However, if there is some finite trigger efficiency then in some of the events with multiple clusters possessing an energy above the trigger threshold, one cluster will trigger (and hence the event is triggered) but one or more will not. Hence with a trigger efficiency less than 100%, the triggered cluster spectrum will always lie beneath the cluster spectrum. It is assumed that the trigger efficiency saturates at some constant level, ϵ, and we are interested in determining this value by examining the ratio of the triggered cluster to the inclusive cluster spectra. Clearly this ratio will depend on two factors: the trigger efficiency, ϵ, and the distribution of the number of particles that have energies exceeding the trigger threshold and could potentially fire a trigger (the greater the number of clusters that could potentially fire in an event, the greater the number that will not due to a finite trigger efficiency). Let M be the number of *triggered* events in a given sample. Let f_i be the fraction of events where there are at least i clusters above threshold that could initiate a trigger in that bin, and let g_i be the fraction of events that have *exactly* i clusters above threshold that could initiate a trigger in that bin. Then immediately:

$$\begin{aligned} f_1 &= 1 \\ \sum_{i=1}^{\infty} g_i &= 1 \end{aligned}$$

Moreover:

$$f_j = \sum_{i=j}^{\infty} g_i$$

and:

$$\begin{aligned} S = \sum_{i=1}^{\infty} f_i &= f_1 + f_2 + f_3 + \dots \\ &= (g_1 + g_2 + g_3 + g_4 + \dots) + (g_2 + g_3 + g_4 + g_5 + \dots) + (g_3 + g_4 + g_5 + \dots) + \dots \\ &= \sum_{i=1}^{\infty} i g_i \end{aligned}$$

Then the number of clusters appearing in the inclusive cluster energy spectrum is:

$$\begin{aligned} N_{all} &= g_1 N + 2g_2 N + 3g_3 N + \dots \\ &= (g_1 N + g_2 N + \dots) + (g_2 N + 2g_3 N + 3g_4 N + \dots) \\ &= N + N \sum_{i=2}^{\infty} g_i (i-1) \end{aligned}$$

For the triggered cluster spectrum we can imagine listing the events, and for each event ordering the clusters in some specified way such that the first cluster in the list is the one that trigggered the event. For instance:

Event 1: $\otimes$
Event 2: $\otimes \quad \otimes\otimes$
Event 3: $\otimes$
Event 4: $\otimes$
Event 5: $\otimes \quad \otimes$
$\ldots$

where $\bigotimes$ indicates a cluster. The number of clusters in the second column that will trigger is expected to be $f_2 N\epsilon$, the number that trigger in the third column $f_3 N\epsilon$, and so on. Hence in the triggered cluster spectrum, the number of clusters that appear is given by:

$$\begin{aligned}
N_{triggering} &= f_1 N + f_2 N\epsilon + f_3 N\epsilon + \ldots \\
&= f_1 N + N\epsilon \sum_{i=2}^{\infty} f_i \\
&= f_1 N + N\epsilon \left(\sum_{i=1}^{\infty} f_i - f_1 \right) \\
&= f_1 N + N\epsilon \left(\sum_{i=1}^{\infty} i g_i - \sum_{i=1}^{\infty} g_i \right) \\
&= N + N\epsilon \sum_{i=2}^{\infty} g_i (i-1)
\end{aligned}$$

Hence the ratio of the triggered cluster energy spectrum to the inclusive cluster energy spectrum, R, is given by:

$$R = \frac{N_{triggering}}{N_{all}} = \frac{N + N\epsilon \sum_{i=2}^{\infty} g_i (i-1)}{N + N \sum_{i=2}^{\infty} g_i (i-1)}$$

Now let $S = \sum_{i=2}^{\infty} g_i (i-1)$ which characterizes the distribution of number of clusters that could trigger, whereupon:

$$R = \frac{1 + \epsilon S}{1 + S}$$

and hence:

$$\epsilon = \frac{R + RS - 1}{S} \tag{5}$$

References

[1] HTTP://WWW2.SLAC.STANFORD.EDU/VVC/THEORY/FUNDAMENTAL.HTML. vi, 2

[2] SIEGFRIED BETHKE. **The World Average of α_s**. *arXiv:0908.1135v2*, 2006. vi, 1, 4

[3] F. KARSCH. **Deconfinement and chiral symmetry restoration in QCD with fundamental and adjoint fermions**. *6th Hellenic School and Workshop on Elementary Particle Physics*, 1998. vi, 6, 7

[4] KENJI FUKUSHIMA. **Chiral Symmetry and Heavy-Ion Collisions**. *J.Phys.*, **G35**:104020, 2008. vi, 6, 7

[5] A. BAZAVOV, T. BHATTACHARYA, M. CHENG, N. H. CHRIST, C. DETAR, S. EJIRI, STEVEN GOTTLIEB, R. GUPTA, U. M. HELLER, K. HUEBNER, C. JUNG, F. KARSCH, E. LAERMANN, L. LEVKOVA, C. MIAO, R. D. MAWHINNEY, P. PETRECZKY, C. SCHMIDT, R. A. SOLTZ, W. SOELDNER, R. SUGAR, D. TOUSSAINT, AND P. VRANAS. **Equation of state and QCD transition at finite temperature**. *Phys. Rev. D*, **80**:014504, Jul 2009. vi, 7

[6] T. ULLRICH. **RHIC experimental overview - what we have learned**. *Colliders to Cosmic Rays conference*, 2007. vi, 9

[7] PETER PETRECZKY. **Quarkonium in Hot Medium**. *J.Phys.*, **G37**:094009, 2010. vi, 13

[8] P BRAUN-MUNZINGER, D MAGESTRO, K REDLICH, AND J STACHEL. **Hadron production in Au-Au collisions at RHIC**. *Physics Letters B*, **518**(12):41 – 46, 2001. vi, 13, 14

[9] N. HERRMANN, J.P. WESSELS, AND T. WIENOLD. **Collective flow in heavy ion collisions**. *Ann. Rev. Nucl. Part. Sci.*, **49**:581–632, 1999. vii, 11, 14, 15, 16

[10] SERGEI A. VOLOSHIN, ARTHUR M. POSKANZER, AND RAIMOND SNELLINGS. **Collective phenomena in non-central nuclear collisions**. *arXiv:0809.2949*, 2008. vii, 17

[11] RANBIR SINGH, LOKESH KUMAR, PAWAN KUMAR NETRAKANTI, AND BEDANGADAS MOHANTY. **Experimental Results from Heavy Ion Collisions at LHC**. *arXiv:1304.2969*, 2013. vii, 17, 164

[12] J. Adams et al. **Experimental and theoretical challenges in the search for the quarkgluon plasma: The STAR Collaboration's critical assessment of the evidence from RHIC collisions**. *Nuclear Physics A*, **757**(12):102 – 183, 2005. vii, 11, 12, 14, 18, 19, 22

[13] K. Aamodt et al. **Two-pion Bose-Einstein correlations in central Pb-Pb collisions at $\sqrt{s_{NN}}$ = 2.76 TeV**. *Phys. Lett.*, **B696**:328–337, 2011. vii, 18, 19

[14] R. Averbeck. **Heavy-flavor production in heavy-ion collisions and implications for the properties of hot QCD matter**. *Progress in Particle and Nuclear Physics*, **70**(0):159 – 209, 2013. vii, 20, 24, 25, 28, 32, 33, 34, 35

[15] K. Aamodt et. al. **Harmonic decomposition of two particle angular correlations in PbPb collisions at**. *Physics Letters B*, **708**(35):249 – 264, 2012. vii, 22

[16] J. Adams et al. **Evidence from d+Au Measurements for Final-State Suppression of High-p_T Hadrons in Au-Au Collisions at RHIC**. *Phys. Rev. Lett.*, **91**:072304, Aug 2003. viii, 23

[17] Jacek Otwinowski. **High-p_T Processes Measured with ALICE at the LHC**. *Acta Phys. Polon.*, **B43**:713, 2012. viii, 23

[18] D. et.al. Acosta. **Measurement of the J/ψ meson and b-hadron production cross sections in $p\overline{p}$ collisions at $\sqrt{s} = 1960$ GeV**. *Phys. Rev. D*, **71**:032001, Feb 2005. viii, 28

[19] A. Adare et al. **Measurement of High-p_T Single Electrons from Heavy-Flavor Decays in $p+p$ Collisions at $\sqrt{s} = 200$ GeV**. viii, 28, 29

[20] H. Agakishiev et al. **High p_T non-photonic electron production in $p+p$ collisions at $\sqrt{s} = 200$ GeV**. *Phys. Rev. D*, **83**:052006, Mar 2011. viii, 28, 29

[21] B. Abelev et al. **Inclusive J/ψ production in pp collisions at $\sqrt{s} = 2.76$ TeV**. *Phys. Lett.*, **B718**:295–306, 2012. viii, 30

[22] K. Aamodt et al. **Rapidity and transverse momentum dependence of inclusive J/ψ production in pp collisions at $\sqrt{s} = 7$ TeV**. *Phys. Lett.*, **B704**:442–455, 2011. viii, 30, 148

[23] ALICE Collaboration. **Measurement of electrons from semileptonic heavy-flavour hadron decays in pp collisions at $\sqrt{s} = 7$ TeV**. *arXiv:1205.5423 [hep-ex]*, 2012. viii, 30, 58, 62, 65, 109, 147, 148, 161

[24] Betty Abelev et al. **Measurement of charm production at central rapidity in proton-proton collisions at $\sqrt{s} = 2.76$ TeV**. *JHEP*, **1207**:191, 2012. viii, 30, 31

[25] Steffen A. Bass, Charles Gale, Abhijit Majumder, Chiho Nonaka, Guang-You Qin, Thorsten Renk, and Ruppert. **Systematic comparison of jet energy-loss schemes in a realistic hydrodynamic medium**. *Phys. Rev. C*, **79**:024901, Feb 2009. ix, 32, 33

[26] A. Adare et al. **Heavy Quark Production in $p+p$ and Energy Loss and Flow of Heavy Quarks in Au+Au Collisions at $\sqrt{s_{NN}} = 200$ GeV**. *Phys. Rev.*, **C84**:044905, 2011. ix, 34

[27] M.M. Aggarwal et al. **Measurement of the Bottom contribution to non-photonic electron production in $p+p$ collisions at $\sqrt{s}$=200 GeV**. *Phys. Rev. Lett.*, **105**:202301, 2010. ix, 35

[28] Betty Abelev et al. **Suppression of high transverse momentum D mesons in central Pb-Pb collisions at $\sqrt{s_{NN}} = 2.76$ TeV**. *JHEP*, **1209**:112, 2012. ix, 35

[29] Wolfgang K. H. Panofsky. **The Evolution of Particle Accelerators and Colliders**. *SLAC Beamline, Spring 1997, Volume 27, No.1.* ix, 37, 38

[30] Various. **Various CERN Figures**. *CERN Document Server*, 2013. ix, 39, 41

[31] ALICE Collaboration. **Various ALICE Figures**. *ALICE Figure Repository*, 2013. ix, x, xvi, 48, 53, 54, 57, 59, 160, 162, 163

[32] M. Hoch. **Trends and new developments in gaseous detectors**. *Nuclear Instruments and Methods in Physics Research Section A: Accelerators, Spectrometers, Detectors and Associated Equipment*, **535**(12):1 – 15, 2004. ix, 49

[33] L. Musa. **The Time Projection Chamber for the ALICE experiment**. *The European Physical Journal C - Particles and Fields, Topical Volume 4 (S1), 2002. III International Symposium on LHC Physics and Detectors*, **26**(1):153–162, 2002. x, 50

[34] R. Ma. **p_T resolution of tracking system in $\sqrt{s} = 2.76$ TeV pp collisions**. *Private Communication*, 2013. x, 52

[35] The ALICE Collaboration. **The ALICE experiment at the CERN LHC**. *Journal of Instrumentation*, **3**(08):S08002, 2008. x, 30, 49, 51, 52, 54, 79, 91, 96

[36] Rene Bellwied for the ALICE EMCal Collaboration. **ALICE EMCal Physics Performance Report**. *arXiv:1008.0413*, 2010. x, 62, 63, 65

[37] F Ronchetti and the ALICE collaboration. **The ALICE electromagnetic calorimeter project**. *Journal of Physics: Conference Series*, **160**(1):012012, 2009. x, 64

[38] P. Cortese et al. **ALICE forward detectors: FMD, TO and VO: Technical Design Report**. *Technical Design Report ALICE, CERN, Geneva*, 2004. x, 69

[39] M. Ivanov, K. Safarik, Y. Belikov, and J. Bracinik. **TPC tracking and particle identification in high-density environment**. *arXiv:physics/00306108*, jun 2003. xii, 79, 90

[40] O. Bourrion, N. Arbor, G. Conesa-Balbastre, C. Furget, R. Guernane, and G. Marcotte. **The ALICE EMCal L1 trigger first year of operation experience**. *arXiv:1210.8078 [hep-ex]*, October 2012. xiv, 130, 131

[41] Deepa Thomas. **Azimuthal angular correlations between heavy-flavour decay electrons and charged hadrons in pp collisions at $\sqrt{s} = 2.76$ TeV in ALICE**. *arXiv:1208.1181*, 2012. xvi, 160

[42] Shingo Sakai. **Heavy-flavor electron R_{AA} analysis status**. *Private Communication*, 2013. xvi, 163, 164

[43] L.Betev and P.Chochula. **Definition of the ALICE Coordinate System and Basic Rules for Sub-detector Components Numbering**. *ALICE Project Document No. ALICE-INT-2003-038*, 2003. xvi, 166

[44] ALICE Figure Repository. **3D ALICE Schematic**, August 2012. xvi, 166

[45] The CDF Collaboration. **Observation of the bottom baryon resonance state Λ_b^{*0} with the CDF II Detector**. *CDF Public Note 10900*, 2012. xvi, 167

[46] Lyndon Evans and Philip Bryant. **LHC Machine**. *Journal of Instrumentation*, **3**(08):S08001, 2008. xvii, 44, 45

[47] A. Rossi. **Alice Alignment, Tracking and Physics Performance Results**. *arXiv:1101.3491*, 2011. xvii, 54, 56

[48] K. Nakamura et al. (Particle Data Group). **The Review Of Particle Physics**. *J. Phys. G 37, 075021*, 2010. xvii, 2, 5, 23, 26, 53, 67, 99, 143, 144, 146, 147

[49] J. Ellis. **Beyond the Standard Model with the LHC**. *Nature 448, 297-301*, 2007. 1

[50] F. Sciulli M. Gaillard, P. Grannis. **The Standard Model of Particle Physics**. *Rev. Mod. Phys. 71, S96-S111*, 1999. 1

[51] Paul Langacker. **Grand Unified Theories and Proton Decay**. *Phys. Rept.*, **72**:185, 1981. 1

[52] B. D'Urso B. Odom, D. Hanneke and G. Gabrielse. **New Measurement of the Electron Magnetic Moment Using a One-Electron Quantum Cyclotron**. *Phys. Rev. Lett. 97, 030801 (2006)*, 2006. 1

[53] A. Pich. **The Standard Model of Particle Physics: Status & Low-Energy Tests**. *arXiv:hep-ph/0206011v1*, 2006. 1

[54] L. Nodulman. **Experimental Tests of the Standard Model**. *arXiv:hep-ex/9810035v1*, 1998. 1

[55] Schroeder Peskin. **An Introduction to Quantum Field Theory**. *Westview Press*, 1995. 1, 3, 20

[56] S. Pokorski. **Gauge Field Theories (Cambridge Monographs on Mathematical Physics)**. *Cambridge University Press; 2nd edition*, 2000. 1, 3

[57] J. Polchinski. **String Theory, Volume 1: An Introduction to the Bosonic String**. *Cambridge University Press*, 2005. 1

[58] Y. Ne'eman M. Gell-Mann. **The Eightfold Way**. *New York:Benjamin*, 1964. 2

[59] O.W.Greenberg. **Resource Letter Q-1: Quarks**. *Am. J. Phys. 50, 1074*, 1982. 2

[60] S.P.Rosen D.B.Lichtenberg. **Developments in the quark theory of hadrons**. *Nonantum: Hadronic Press*, 1980. 2

[61] P.N.Burrows. **Precise Tests of QCD in e^+e^-annihilation**. *SLAC-PUB-7434, MIT-LNS-97-267*, 1997. 2

[62] A.J.G.Hey I.J.R.Aitchison. **Gauge Theories in Particle Physics, Volume II**. *Taylor and Francis Group*, 2003. 2

[63] J. Collins. **Renormalization**. *Cambrdige University Press*. 3

[64] G Altarelli. **Experimental Tests of Perturbative QCD**. *Annual Review of Nuclear and Particle Science*, **39**(1):357–406, 1989. 4

[65] Siegfried Bethke. **Experimental tests of asymptotic freedom**. *Prog. Part. Nucl. Phys.*, **58**:351–386, 2007. 4

[66] K. Yagi, T. Hatsuda, and Y. Miake. **Quark-gluon plasma: From big bang to little bang**. *Camb. Monogr. Part. Phys. Nucl. Phys. Cosmol.*, **23**:1–446, 2005. 5

[67] M. Creutz. **Quarks, Gluons and Lattices**. 1984. 5

[68] Thomas DeGrand and Carleton E. Detar. **Lattice methods for quantum chromodynamics**. *World Scientific*, 2006. 5

[69] Steven Weinberg. **The Discovery of Subatomic Particles**. *Cambridge University Press*. 5, 37

[70] Frank Close. **The New Cosmic Onion: Quarks and the Nature of the Universe**. *Taylor + Francis*. 5, 37

[71] John C. Collins and M.J. Perry. **Superdense Matter: Neutrons Or Asymptotically Free Quarks?** *Phys. Rev. Lett.*, **34**:1353, 1975. 5

[72] N. Cabibbo and G. Parisi. **Exponential Hadronic Spectrum and Quark Liberation**. *Phys. Lett.*, **B59**:67–69, 1975. 5

[73] R. Hagedorn. **Statistical thermodynamics of strong interactions at high-energies**. *Nuovo Cim. Suppl.*, **3**:147–186, 1965. 5

[74] C E DeTar and J F Donoghue. **Bag Models of Hadrons**. *Annual Review of Nuclear and Particle Science*, **33**(1):235–264, 1983. 6

[75] K. Yagi, T. Hatsuda, and Y. Miake. **Quark-gluon plasma: From big bang to little bang**. *Camb. Monogr. Part. Phys. Nucl. Phys. Cosmol.*, **23**:1–446, 2005. 6, 8, 11, 12, 13, 14, 18, 19, 20, 22

[76] C.Y. Wong. **Introduction to High-Energy Heavy-Ion Collisions**. *World Scientific Publishing Company Incorporated*, 1994. 6, 11, 12, 143, 146

[77] E. Laermann and O. Philipsen. **Lattice QCD at Finite Temperature**. *Annual Review of Nuclear and Particle Science*, **53**(1):163–198, 2003. 7

[78] Rajan Gupta. **Equation of State from Lattice QCD Calculations**. *Nucl. Phys.*, **A862-863**:111–117, 2011. 7

[79] Owe Philipsen. **The QCD equation of state from the lattice**. *Prog. Part. Nucl. Phys.*, **70**:55–107, 2013. 7

[80] Szabolcs Borsanyi et al. **Transition temperature and the equation of state from lattice QCD, Wuppertal-Budapest results**. *Acta Phys. Polon. Supp.*, **4**:593–602, 2011. 7

[81] Dirk H. Rischke. **The Quark gluon plasma in equilibrium**. *Prog. Part. Nucl. Phys.*, **52**:197–296, 2004. 7

[82] Z. Fodor and S. D. Katz. **Finite T/μ Lattice QCD and the Critical Point**. *Progress of Theoretical Physics Supplement*, **153**:86–92, 2004. 7

[83] C. R. Allton, S. Ejiri, S. J. Hands, O. Kaczmarek, F. Karsch, E. Laermann, Ch. Schmidt, and L. Scorzato. **QCD thermal phase transition in the presence of a small chemical potential**. *Phys. Rev. D*, **66**:074507, Oct 2002. 7

[84] Mark G. Alford. **Color superconducting quark matter**. *Ann. Rev. Nucl. Part. Sci.*, **51**:131–160, 2001. 8

[85] Y. Nambu and G. Jona-Lasinio. **Dynamical Model of Elementary Particles Based on an Analogy with Superconductivity. I**. *Phys. Rev.*, **122**:345–358, Apr 1961. 8

[86] Jerzy Bartke. **Introduction to relativistic heavy ion physics**. 2009. 8, 18, 22

[87] Ulrich W. Heinz. **From SPS to RHIC: Breaking the barrier to the quark gluon plasma**. *AIP Conf. Proc.*, **602**:281–292, 2001. 8

[88] J Stachel and G. R. Young. **Relativistic Heavy ION Physics at Cern and BNL**. *Annual Review of Nuclear and Particle Science*, **42**(1):537–597, 1992. 8

[89] Richard M. Weiner. **Surprises from the search for quark-gluon plasma? When was quark-gluon plasma seen?** *Int. J. Mod. Phys.*, **E15**:37–70, 2006. 8

[90] H R Schmidt and J Schukraft. **The physics of ultra-relativistic heavy-ion collisions**. *Journal of Physics G: Nuclear and Particle Physics*, **19**(11):1705, 1993. 8

[91] A. Dainese. **Review on Heavy-Ion Physics**. *arXiv:1012.4038*, 2010. 8

[92] Berndt Muller and James L. Nagle. **Results from the relativistic heavy ion collider**. *Ann. Rev. Nucl. Part. Sci.*, **56**:93–135, 2006. 8

[93] Ranbir Singh, Lokesh Kumar, Pawan Kumar Netrakanti, and Bedangadas Mohanty. **Experimental Results from Heavy Ion Collisions at LHC**. *arXiv:1304.2969*, 2013. 8

[94] Michael L. Miller, Klaus Reygers, Stephen J. Sanders, and Peter Steinberg. **Glauber modeling in high energy nuclear collisions**. *Ann. Rev. Nucl. Part. Sci.*, **57**:205–243, 2007. 10

[95] R.J Glauber. **Lectures in Theoretical Physics**. *Lectures in Theoretical Physics: Lectures Delivered at the Summer Institute for Theoretical Physics, University of Colorado, Boulder*, 1959. 10

[96] H. De Vries, C.W. De Jager, and C. De Vries. **Nuclear charge-density-distribution parameters from elastic electron scattering**. *Atomic Data and Nuclear Data Tables*, **36**(3):495 – 536, 1987. 10

[97] Betty Abelev et al. **Centrality determination of Pb-Pb collisions at $\sqrt{s_{NN}} = 2.76$ TeV with ALICE**. *arXiv:1301.4361*, 2013. 10

[98] K.J. Eskola. **Mini - jets in ultrarelativistic heavy ion collisions at future colliders**. *Comments Nucl. Part. Phys.*, **22**:185–203, 1998. 11

[99] Francois Gelis, Edmond Iancu, Jamal Jalilian-Marian, and Raju Venugopalan. **The Color Glass Condensate**. *Ann. Rev. Nucl. Part. Sci.*, **60**:463–489, 2010. 11

[100] Larry D. McLerran. **The Color glass condensate and small x physics: Four lectures**. *Lect. Notes Phys.*, **583**:291–334, 2002. 11

[101] Raju Venugopalan. **From many body wee parton dynamics to perfect fluid: a standard model for heavy ion collisions**. *PoS*, **ICHEP2010**:567, 2010. 11

[102] Raju Venugopalan. **From Glasma to Quark Gluon Plasma in heavy ion collisions**. *J.Phys.*, **G35**:104003, 2008. 11

[103] Kevin Dusling and Raju Venugopalan. **Comparison of the Color Glass Condensate to dihadron correlations in proton-proton and proton-nucleus collisions**. *arXiv:1302.7018*, 2013. 11

[104] F. Gelis. **Color Glass Condensate and Glasma**. *Int. J. Mod. Phys.*, **A28**:1330001, 2013. 11

[105] Wojciech Florkowski. **The Early thermalization and HBT puzzles at RHIC**. *Acta Phys. Polon.*, **B41**:2747–2761, 2010. 11

[106] U. Heinz and P. Kolb. **Early thermalization at RHIC**. *Nuclear Physics A*, **702**(14):269 – 280, 2002. 11, 15

[107] Ulrich W Heinz and Raimond Snellings. **Collective flow and viscosity in relativistic heavy-ion collisions**. *arXiv:1301.2826*, 2013. 11

[108] Tetsufumi Hirano, Ulrich W. Heinz, Dmitri Kharzeev, Roy Lacey, and Yasushi Nara. **Hadronic dissipative effects on elliptic flow in ultrarelativistic heavy-ion collisions**. *Phys. Lett.*, **B636**:299–304, 2006. 11

[109] Huichao Song. **VISHNU hybrid model for the viscous QCD matter at RHIC and LHC energies**. *Central European Journal of Physics*, **10**(6):1242–1244, 2012. 11, 15

[110] F. Becattini. **An Introduction to the Statistical Hadronization Model**. *arXiv:0901.3643*, 2009. 12

[111] K. Kajantie and L. McLerran. **Probes of the Quark Gluon Plasma in High-Energy Collisions**. *Annual Review of Nuclear and Particle Science*, **37**:293–323, 1987. 12

[112] T. Matsui and H. Satz. **J/ suppression by quark-gluon plasma formation**. *Physics Letters B*, **178**(4):416 – 422, 1986. 12

[113] B. Alessandro et al. **A New measurement of J/psi suppression in Pb-Pb collisions at 158-GeV per nucleon**. *Eur. Phys. J.*, **C39**:335–345, 2005. 12

[114] A.D. Frawley, T. Ullrich, and R. Vogt. **Heavy flavor in heavy-ion collisions at RHIC and RHIC II**. *Physics Reports*, **462**:125 – 175, 2008. 12

[115] L. Kluberg. **20 years of J/ ψ suppression at the CERN SPS.** *European Physical Journal C – Particles & Fields*, **43**(1-4):145 – 156, 2005. 12

[116] A. Adare et al. **J/ψ suppression at forward rapidity in Au+Au collisions at $\sqrt{s_{NN}} = 200$ GeV**. *Phys. Rev.*, **C84**:054912, 2011. 12

[117] G. Aad et al. **Measurement of the centrality dependence of J/ψ yields and observation of Z production in lead-lead collisions with the ATLAS detector at the LHC**. *Phys. Lett.*, **B697**:294–312, 2011. 12

[118] R.L. Thews and M.L. Mangano. **Momentum spectra of charmonium produced in a quark-gluon plasma**. *Phys. Rev.*, **C73**:014904, 2006. 12

[119] A. Wroblewski. **On the strange quark supperssion factor in high energy collisions**. *Acta. Phys. Pol. B*, **16**:379, 1985. 13

[120] P Koch, B Mller, and J Rafelski. **Strangeness in relativistic heavy ion collisions**. *Physics Reports*, **142**(4):167 – 262, 1986. 13

[121] Johann Rafelski and Berndt Muller. **Strangeness Production in the Quark-Gluon Plasma**. *Phys. Rev. Lett.*, **48**:1066–1069, Apr 1982. 13

[122] K. Kajantie. **From QCD to heavy ion collisions**. *Nucl. Phys.*, **A663**:191–198, 2000. 13

[123] P Koch, B Mller, and J Rafelski. **Strangeness in relativistic heavy ion collisions**. *Physics Reports*, **142**(4):167 – 262, 1986. 13

[124] C. Adler et al. **Kaon production and kaon to pion ratio in Au + Au collisions at $\sqrt{s_{NN}}$=130 GeV**. *Physics Letters B*, **595**(14):143 – 150, 2004. 13

[125] J. Adams et al. **Multistrange Baryon Production in Au-Au Collisions at $\sqrt{s_{NN}} = 130$ GeV**. 13, 14

[126] P. Braun-Munzinger, I. Heppe, and J. Stachel. **Chemical equilibration in Pb+Pb collisions at the SPS**. *Physics Letters B*, **465**(14):15 – 20, 1999. 13, 14

[127] Raimond Snellings. **Elliptic Flow: A Brief Review**. *New J.Phys.*, **13**:055008, 2011. 14, 15

[128] Wojciech Broniowski, Piotr Bożek, and Maciej Rybczyński. **Fluctuating initial conditions in heavy ion collisions from the Glauber approach**. *Phys. Rev. C*, **76**:054905, Nov 2007. 15

[129] Alice Ohlson. **Calculating jet v_n and the event plane in the presence of a jet**. *Phys. Rev. C*, **87**:034909, Mar 2013. 15

[130] Gregory Kestin and Ulrich Heinz. **Hydrodynamic radial and elliptic flow in heavy-ion collisions fromAGStoLHC energies**. *The European Physical Journal C*, **61**(4):545–552, 2009. 15

[131] Eugene Hecht. **Optics (4th Edition)**. *Addison Wesley*, August 2001. 16

[132] Claude Cohen-Tannoudji, Bernard Diu, Frank Laloe, and Bernard Dui. **Quantum Mechanics (2 vol. set)**. *Wiley-Interscience*, October 2006. 16

[133] Ulrich W. Heinz and Barbara V. Jacak. **Two particle correlations in relativistic heavy ion collisions**. *Ann. Rev. Nucl. Part. Sci.*, **49**:529–579, 1999. 16, 18, 19

[134] R. Hanbury Brown and R.Q. Twiss. **A Test of a new type of stellar interferometer on Sirius**. *Nature*, **178**:1046–1048, 1956. 16

[135] Dirk H. Rischke and Miklos Gyulassy. **The Time delay signature of quark - gluon plasma formation in relativistic nuclear collisions**. *Nucl. Phys.*, **A608**:479–512, 1996. 18, 19

[136] Michael Annan Lisa, Scott Pratt, Ron Soltz, and Urs Wiedemann. **Femtoscopy in relativistic heavy ion collisions**. *Ann. Rev. Nucl. Part. Sci.*, **55**:357–402, 2005. 19

[137] Scott Pratt. **Resolving the HBT Puzzle in Relativistic Heavy Ion Collision**. *Phys. Rev. Lett.*, **102**:232301, 2009. 19

[138] Gavin P. Salam. **Towards Jetography**. *Eur. Phys. J.*, **C67**:637–686, 2010. 20

[139] Gavin P. Salam and Gregory Soyez. **A Practical Seedless Infrared-Safe Cone jet algorithm**. *JHEP*, **0705**:086, 2007. 20

[140] Stephen D. Ellis and Davison E. Soper. **Successive combination jet algorithm for hadron collisions**. *Phys. Rev.*, **D48**:3160–3166, 1993. 20

[141] Matteo Cacciari, Gavin P. Salam, and Gregory Soyez. **The Anti-k(t) jet clustering algorithm**. *JHEP*, **0804**:063, 2008. 20

[142] J.D. Bjorken. **Energy Loss of Energetic Partons in Quark Gluon Plasma: Possible Extinction of High p(t) Jets in Hadron - Hadron Collisions**. *Fermilab Report: FERMILAB-PUB-82-059-THY*, 1982. 20

[143] J. W. Cronin, H. J. Frisch, M. J. Shochet, J. P. Boymond, P. A. Piroué, and R. L. Sumner. **Production of hadrons at large transverse momentum at 200, 300, and 400 GeV**. *Phys. Rev. D*, **11**:3105–3123, Jun 1975. 22

[144] A Accardi and M Gyulassy. **Cronin effect vs. geometrical shadowing in d+Au collisions at RHIC**. *Physics Letters B*, **586**(34):244 – 253, 2004. 22

[145] W. Florkowski. **Phenomenology of Ultra-relativistic Heavy-ion Collisions**. *World Scientific*, 2010. 22

[146] Tim Gershon. **Flavour physics in the LHC era**. *arXiv:1306.4588*, 2013. 23, 24

[147] Frank-Peter Schilling. **Top Quark Physics at the LHC: A Review of the First Two Years**. *Int. J. Mod. Phys.*, **A27**:1230016, 2012. 23

[148] Robert W. Lambert. **Heavy Flavour in a Nutshell**. *arXiv:1105.1061*, 2011. 24

[149] Andrzej J. Buras. **Flavour Theory: 2009**. *PoS*, **EPS-HEP2009**:024, 2009. 24

[150] Gino Isidori. **B Physics in the LHC Era**. *arXiv:1001.3431*, pages 69–109, 2010. 24

[151] Laurent Canetti, Marco Drewes, and Mikhail Shaposhnikov. **Matter and Antimatter in the Universe**. *New J.Phys.*, **14**:095012, 2012. 24

[152] Matteo Cacciari, Stefano Frixione, Nicolas Houdeau, Michelangelo L. Mangano, Paolo Nason, et al. **Theoretical predictions for charm and bottom production at the LHC**. *JHEP*, **1210**:137, 2012. 24, 25

[153] Gines Martinez. **Advances in Quark Gluon Plasma**. *arXiv:1304.1452*, 2013. 24

[154] Ralf Rapp and Hendrik van Hees. **Heavy Quarks in the Quark-Gluon Plasma**. *arXiv:0903.1096*, 2009. 24

[155] Hendrik van Hees and Ralf Rapp. **Thermalization of heavy quarks in the quark-gluon plasma**. *Phys. Rev.*, **C71**:034907, 2005. 24

[156] R. Thomas, Burkhard Kampfer, and G. Soff. **Gluon emission of heavy quarks: Dead cone effect**. *Acta Phys. Hung.*, **A22**:83–91, 2005. 24

[157] Matteo Cacciari. **Rise and fall of the bottom quark production excess**. *arXiv:hep-ph/0407187*, pages 41–46, 2004. 24, 28

[158] P. Nason, S. Dawson, and R. Keith Ellis. **The Total Cross-Section for the Production of Heavy Quarks in Hadronic Collisions**. *Nucl. Phys.*, **B303**:607, 1988. 24, 28

[159] C. Albajar et al. **Beauty Production at the CERN Proton - anti-Proton Collider. 1.** *Phys. Lett.*, **B186**:237–246, 1987. 24

[160] D. Acosta et al. **Measurement of the B^+ total cross section and B^+ differential cross section $d\sigma/dp_T$ in $p\bar{p}$ collisions at $\sqrt{s} =$ 1.8-TeV**. *Phys. Rev.*, **D65**:052005, 2002. 24

[161] D. Acosta et al. **Measurement of the ratio of b quark production cross sections in $\bar{p}p$ collisions at $\sqrt{s} = 630$ GeV and $\sqrt{s} = 1800$ GeV**. *Phys. Rev.*, **D66**:032002, 2002. 24

[162] B. Abbott et al. **Small angle muon and bottom quark production in $p\bar{p}$ collisions at $\sqrt{s} = 1.8$ TeV**. *Phys. Rev. Lett.*, **84**:5478–5483, 2000. 24

[163] A. Majumder and M. Van Leeuwen. **The Theory and Phenomenology of Perturbative QCD Based Jet Quenching**. *Prog. Part. Nucl. Phys.*, **A66**:41–92, 2011. 25, 32

[164] P.A Nason. **Recent Developments in POWHEG**. *PoS*, **RADCOR2009**:018, 2010. 25

[165] Torbjorn Sjostrand, Stephen Mrenna, and Peter Z. Skands. **PYTHIA 6.4 Physics and Manual**. *JHEP*, **0605**:026, 2006. 25, 76

[166] G. Corcella, I.G. Knowles, G. Marchesini, S. Moretti, K. Odagiri, et al. **HERWIG 6: An Event generator for hadron emission reactions with interfering gluons (including supersymmetric processes)**. *JHEP*, **0101**:010, 2001. 25

[167] Stefano Frixione, Fabian Stoeckli, Paolo Torrielli, Bryan R. Webber, and Chris D. White. **The MCaNLO 4.0 Event Generator**. *arXiv:1010.0819*, 2010. 25

[168] Richard Keith Ellis, William James Stirling, and Bryan R Webber. **QCD and Collider Physics**. *Cambridge Univ. Press*, 2003. Photography by S. Vascotto. 25, 161

[169] M Cacciari, S P Baranov, S Diglio, T O Eynck, H Jung, Bernd A Kniehl, S Kretzer, A V Lipatov, Eric Laenen, F Maltoni, F Petrucci, O I Piskounova, I Schienbein, J Smith, A Tonazzo, M Verducci, and N P Zotov. **Theoretical review of various approaches in heavy quark production**. *HERA and the LHC : A Workshop on the Implications of HERA for LHC Physics, CERN, Geneva, Switzerland*, 2005. 25

[170] Matteo Cacciari, Mario Greco, and Paolo Nason. **The p_T spectrum in heavy-flavour hadroproduction**. *Journal of High Energy Physics*, **1998**(05):007, 1998. 25

[171] Matteo Cacciari, Stefano Frixione, and Paolo Nason. **The p T spectrum in heavy-flavour photoproduction**. *Journal of High Energy Physics*, **2001**(03):006, 2001. 25

[172] Matteo Cacciari, Stefano Frixione, Nicolas Houdeau, Michelangelo L. Mangano, Paolo Nason, et al. **Theoretical predictions for charm and bottom production at the LHC**. *JHEP*, **1210**:137, 2012. 25

[173] B.A. Kniehl, G. Kramer, I. Schienbein, and H. Spiesberger. **Collinear subtractions in hadroproduction of heavy quarks**. *Eur. Phys. J.*, **C41**:199–212, 2005. 26

[174] BerndA. Kniehl, Gustav Kramer, Ingo Schienbein, and Hubert Spiesberger. **Inclusive charmed-meson production at the CERN LHC**. *The European Physical Journal C*, **72**(7):1–10, 2012. 26

[175] B.A. Kniehl, G. Kramer, I. Schienbein, and H. Spiesberger. **Inclusive D*+- production in p anti-p collisions with massive charm quarks**. *Phys. Rev.*, **D71**:014018, 2005. 26

[176] Bernd A. Kniehl. **Inclusive production of heavy-flavored hadrons at NLO in the GM-VFNS**. *arXiv:0807.2215*, page 195, 2008. 26

[177] Paolo Bolzoni and Gustav Kramer. **Inclusive lepton production from heavy-hadron decay in pp collisions at the LHC**. *Nucl. Phys.*, **B872**:253–264, 2013. 26

[178] H. Jung, M. Kraemer, A.V. Lipatov, and N.P. Zotov. **Investigation of beauty production and parton shower effects at LHC**. *Phys. Rev.*, **D85**:034035, 2012. 26

[179] Philipp Hagler, Roland Kirschner, Andreas Schafer, Lech Szymanowski, and Oleg Teryaev. **Heavy quark production as sensitive test for an improved description of high-energy hadron collisions**. *Phys. Rev.*, **D62**:071502, 2000. 26

[180] S.P. Baranov, N.P. Zotov, and A.V. Lipatov. **Production of heavy quarks on protons within the semihard QCD approach**. *Physics of Atomic Nuclei*, **67**(4):837–845, 2004. 26

[181] S.P. Baranov, A.V. Lipatov, and N.P. Zotov. **B meson production in $p\bar{p}$ collisions at Tevatron with k_T factorization**. *Yad. Fiz.*, **67**:856, 2004. 26

[182] H. Jung, M. Kraemer, A.V. Lipatov, and N.P. Zotov. **Heavy Flavour Production at Tevatron and Parton Shower Effects**. *JHEP*, **1101**:085, 2011. 26

[183] Rafal Maciula and Antoni Szczurek. **Open charm production at the LHC - k_t-factorization approach**. *arXiv:1301.3033*, 2013. 26

[184] MinJung Kweon. **Measurement of electrons from heavy-flavour decays in pp and Pb-Pb collisions with ALICE at the LHC**. *arXiv:1208.5411*, 2012. 26

[185] Betty Abelev et al. **Measurement of electrons from beauty hadron decays in pp collisions at $\sqrt{s} = 7$ TeV**. *Phys. Lett.*, **B721**:13–23, 2013. 26, 31

[186] Vardan Khachatryan et al. **Inclusive b-hadron production cross section with muons in pp collisions at $\sqrt{s} = 7$ TeV**. *JHEP*, **1103**:090, 2011. 26, 31

[187] F.W. Busser et al. **Observation of high transverse momentum electrons at the CERN ISR**. *Physics Letters B*, **53**(2):212 – 216, 1974. 26

[188] W. Beenakker, W.L. Van Neerven, R. Meng, G.A. Schuler, and J. Smith. **QCD corrections to heavy quark production in hadron-hadron collisions**. *Nuclear Physics B*, **351**(3):507 – 560, 1991. 26

[189] David Tlusty. **Open charm hadron production via hadronic decays at STAR**. *arXiv:1208.0057*, 2012. 28

[190] Anthony D. Frawley, T. Ullrich, and R. Vogt. **Heavy flavor in heavy-ion collisions at RHIC and RHIC II**. *Phys. Rept.*, **462**:125–175, 2008. 28

[191] Jaroslav Bielcik. **Heavy flavor physics at STAR**. *arXiv:nucl-ex/0606010*, 2006. 28

[192] Gang Wang. **Measurements of Heavy Flavor and Di-electron Production at STAR**. *Central Eur. J.Phys.*, **10**:1230–1233, 2012. 28

[193] Zebo Tang. **J/ψ production and correlation in p+p and Au+Au collisions at STAR**. *J.Phys.*, **G38**:124107, 2011. 28

[194] Bertrand Biritz. **Non-photonic electron-hadron azimuthal correlation for Au Au, Cu Cu and pp collisions at $\sqrt{s_{NN}} = 200$ GeV**. *Nucl. Phys.*, **A830**:849C–852C, 2009. 28

[195] The LHCb Collaboration. **The LHCb Detector at the LHC**. *Journal of Instrumentation*, **3**(08):S08005, 2008. 28

[196] R Aaij et al. **First Evidence for the Decay $B_s^0 \to \mu^+\mu^-$**. *Phys. Rev. Lett.*, **110**:021801, 2013. 30

[197] The CMS Collaboration. **The CMS experiment at the CERN LHC**. *Journal of Instrumentation*, **3**(08):S08004, 2008. 30

[198] Roberto Covarelli and on behalf of the CMS. **Measurement of Heavy-Flavor Properties at CMS and ATLAS**. *arXiv:1306.0790*, 2013. 30, 31

[199] J. Schieck on behalf of the ATLAS. **Heavy Flavor Measurements in ATLAS and CMS**. *arXiv:1205.4153*, 2012. 30, 31

[200] Keith Ulmer. **Heavy-Flavor Results from CMS**. *arXiv:1301.4690*, 2013. 30, 31

[201] The ATLAS Collaboration. **The ATLAS Experiment at the CERN Large Hadron Collider**. *Journal of Instrumentation*, **3**(08):S08003, 2008. 30

[202] Vardan Khachatryan et al. **Prompt and non-prompt J/ψ production in pp collisions at $\sqrt{s} = 7$ TeV**. *Eur. Phys. J.*, **C71**:1575, 2011. 30

[203] Dong Ho Moon. **Measurement of charmonium production in PbPb collisions at 2.76 TeV with CMS**. *arXiv:1209.1084*, 2012. 30

[204] Georges Aad et al. **Measurement of the differential cross-sections of inclusive, prompt and non-prompt J/ψ production in proton-proton collisions at $\sqrt{s} = 7$ TeV**. *Nucl. Phys.*, **B850**:387–444, 2011. 30

[205] G. Aad et al. **Measurement of the centrality dependence of J/ψ yields and observation of Z production in lead-lead collisions with the ATLAS detector at the LHC**. *Phys. Lett.*, **B697**:294–312, 2011. 30

[206] Georges Aad et al. **Measurement of Upsilon production in 7 TeV pp collisions at ATLAS**. *Phys. Rev.*, **D87**:052004, 2013. 30

[207] Serguei Chatrchyan et al. **Measurement of the Strange B Meson Production Cross Section with J/Psi ϕ Decays in pp Collisions at $\sqrt{s} = 7$ TeV**. *Phys. Rev.*, **D84**:052008, 2011. 30

[208] Christian Finck and Alice Muon Spectrometer collaboration. **The Muon Spectrometer of the ALICE**. *Journal of Physics: Conference Series*, **50**(1):397, 2006. 31

[209] B. Abelev et al. **Production of Muons from Heavy Flavor Decays at Forward Rapidity in pp and Pb-Pb Collisions at $\sqrt{s_{NN}}$=2.76 TeV**. *Phys. Rev. Lett.*, **109**:112301, Sep 2012. 31

[210] Paolo Bellan. **Heavy flavor physics with CMS**. *arXiv:1109.0945*, 2011. 31

[211] Ralf Averbeck. **Heavy-flavour measurements in pp and Pb-Pb collisions with the ALICE experiment at the CERN LHC**. *PoS*, **IHEP-LHC-2011**:014, 2012. 31

[212] Giuseppe Eugenio Bruno. **Heavy flavour measurements in the ALICE experiment at the LHC**. *PoS*, **BEAUTY2011**:007, 2011. 31

[213] Alessandro Grelli and the ALICE Collaboration. **Heavy Flavour Physics with the ALICE detector at the CERN-LHC**. *Journal of Physics: Conference Series*, **316**(1):012025, 2011. 31

[214] Yuri L. Dokshitzer and D.E. Kharzeev. **Heavy quark colorimetry of QCD matter**. *Phys. Lett.*, **B519**:199–206, 2001. 32

[215] R. Baier, Yu.L. Dokshitzer, A.H. Mueller, S. Peign, and D. Schiff. **Radiative energy loss and p-broadening of high energy partons in nuclei**. *Nuclear Physics B*, **484**(12):265 – 282, 1997. 32

[216] Magdalena Djordjevic and Miklos Gyulassy. **Heavy quark radiative energy loss in QCD matter**. *Nucl. Phys.*, **A733**:265–298, 2004. 32

[217] P. B. Gossiaux and J. Aichelin. **Toward an understanding of the single electron data measured at the BNL Relativistic Heavy Ion Collider (RHIC)**. *Phys. Rev. C*, **78**:014904, Jul 2008. 33

[218] Guy D. Moore and Derek Teaney. **How much do heavy quarks thermalize in a heavy ion collision?** *Phys. Rev. C*, **71**:064904, Jun 2005. 33

[219] Azfar Adil and Ivan Vitev. **Collisional dissociation of heavy mesons in dense {QCD} matter**. *Physics Letters B*, **649**(23):139 – 146, 2007. 33

[220] K. Kovtun, P. D. T. Son, and A. O. Starinets. **Viscosity in Strongly Interacting Quantum Field Theories from Black Hole Physics**. *Phys. Rev. Lett.*, **94**:111601, Mar 2005. 33

[221] The CMS Collaboration. **Measurement of the b-jet to inclusive jet ratio in Pb-Pb and** pp **collisions at** $\sqrt{s_{NN}} = 2.76$ **TeV with the CMS detector**. *CMS Analysis note: CMS PAS HIN-12-003*, 2013. 36, 164

[222] The ALICE Collaboration. **The nuclear modification factor of electrons from heavy-flavour decays in Pb-Pb collisions at** $\sqrt{s_{\mathrm{NN}}} = 2.76$ **TeV in semi-central collisions**. *ALICE Analysis note: ANA-918*, 2013. 36

[223] Edmund Wilson. **An Introduction to Particle Accelerators**. *Oxford Univetsiry Press.* 37

[224] G E. Moore. **Cramming More Components into Integrated Circuits**. *Electronics, Volume 38, Number 8.* 37

[225] Simon van Meer. **The Long-Term Future of Particle Accelerators**. *Springer Netherlands*, 2008. 37

[226] L. Evans et al. **The Large Hadron Collider: A Marvel of Technology**. *EPFL Press*, 2009. 40, 42, 46

[227] P. Bagnaia et al. **Evidence for** $Z^0 \to e^+e^-$ **at the CERN** pp **collider**. *Physics Letters B*, **129**(12):130 – 140, 1983. 40

[228] G. Arnison et.al. **Experimental observation of isolated large transverse energy electrons with associated missing energy at** $\sqrt{s} = 540$ **GeV**. *Physics Letters B*, **122**(1):103 – 116, 1983. 40

[229] M. Banner et al. **Observation of single isolated electrons of high transverse momentum in events with missing transverse energy at the CERN pp collider**. *Physics Letters B*, **122**(56):476 – 485, 1983. 40

[230] A.I.Drozhdin et al. **The Very Large Hadron Collider Beam Collimation System**. *Talk at the VLHC Workshop on Accelerator Physics,* `http://vlhc.org/vlhc/AP_prog.html`, 2000. 42

[231] R.Assmann et al. **The Very Large Hadron Collider**. *Proceedings of EPAC 2002, Paris, France*, 2002. 42

[232] D.Boussard. **RF Power Requirements for a High Intensity Proton Collider**. *PAC, San Francisco*, 1991. 42

[233] T.Linnecard D.Boussard. **The LHC Superconducting RF System**. *LHC Project Report 316*, 1999. 42

[234] M.A.Furman. **The Moller Luminosity Factor**. *LBNL-53553, CBP Note-543*, 2003. 43

[235] R.Assmann et al. **Measurement of the Relative Luminosity at the LHC**. *LHC-B-ES-0008 rev 0.4*, 2003. 44

[236] W.Herr and B.Muratori. **The Concept of Luminosity**. *Yellow Report (CERN 2006-002)*, 2006. 44

[237] The ALICE Collaboration. **Upgrade of the Inner Tracking System Conceptual Design Report**. *CERN-LHCC-2012-013 (LHCC-P-005)*, 2012. 46, 57, 159, 164

[238] The ALICE Collaboration. **Upgrade of the ALICE Experiment Letter of Intent**. *CERN-LHCC-2012-013 (LHCC-P-005)*, 2012. 46, 164

[239] J.Allen et al. **ALICE DCal: An Addendum to the EMCal Technical Design Report Di-Jet and Hadron-Jet correlation measurements in ALICE**. *CERN-LHCC-2010-011 ; ALICE-TDR-014-ADD-1*, 2010. 47

[240] The ALICE Collaboration. **Charged-Particle Multiplicity Density at Midrapidity in Central Pb-Pb Collisions at $\sqrt{s}_{NN} = 2.76$ TeV**. *Phys. Rev. Lett.*, **105**:252301, Dec 2010. 49

[241] H J Hilke. **Time projection chambers**. *Reports on Progress in Physics*, **73**(11):116201, 2010. 49

[242] J. Alme et al. **The ALICE TPC, a large 3-dimensional tracking device with fast readout for ultra-high multiplicity events**. *Nuclear Instruments and Methods in Physics Research Section A: Accelerators, Spectrometers, Detectors and Associated Equipment*, **622**(1):316 – 367, 2010. 50

[243] L.Betev and P.Chochula. **Definition of the ALICE Coordinate System and Basic Rules for Sub-detector Components Numbering**. *ALICE Project Document No. ALICE-INT-2003-038*, 2003. 50

[244] I. Lehraus. **Progress in particle identification by ionization sampling**. *Nuclear Instruments and Methods in Physics Research*, **217**(12):43 – 55, 1983. 50

[245] J. Alme et al. **The ALICE TPC, a large 3-dimensional tracking device with fast readout for ultra-high multiplicity events**. *Nuclear Instruments and Methods in Physics Research Section A: Accelerators, Spectrometers, Detectors and Associated Equipment*, **622**(1):316 – 367, 2010. 51

[246] Alexander Kalweit. *PRIVATE COMMUNICATION and soon to be available phD thesis*, 2012. 52

[247] The ALICE Collaboration. **Alignment of the ALICE Inner Tracking System with cosmic-ray tracks**. *Journal of Instrumentation*, **5**(03):P03003, 2010. 55, 56

[248] S. Beol. **The ALICE Inner Tracking System: Performance with Proton and Lead Beams**. *Physics Procedia*, **37**(0):1062 – 1069, 2012. ¡ce:title¿Proceedings of the 2nd International Conference on Technology and Instrumentation in Particle Physics (TIPP 2011)¡/ce:title¿. 56

[249] ALICE Collaboration. **ALICE: Physics Performance Report, Volume II**. *Journal of Physics G: Nuclear and Particle Physics*, **32**(10):1295, 2006. 56

[250] Renu Bala. **Study of D-mesons using hadronic decay channels with the ALICE detector**. *Nuclear Physics B - Proceedings Supplements*, **210**(0):33 – 36, 2011. 56

[251] Vitalii L Ginzburg. **Radiation by uniformly moving sources (VavilovCherenkov effect, transition radiation, and other phenomena)**. *Physics-Uspekhi*, **39**(10):973, 1996. 58

[252] Jackson. **Classical Electrodynamics, 3rd Ed.** *Wiley*, 1999. 58

[253] Christoph Blume. **Commissioning and performance of the ALICE-TRD**. *Nuclear Instruments and Methods in Physics Research Section A: Accelerators, Spectrometers, Detectors and Associated Equipment*, (0):–, 2012. 58

[254] Yvonne Pachmayer. **Physics with the ALICE Transition Radiation Detector**. *arXiv:1112.2098 [nucl-ex]*, 2011. 58

[255] **Jet and Photon Physics with ALICE: First Results from the pp Runs**. *Nuclear Physics A*, **862**(0):160 – 167, 2011. 60

[256] The ALICE Collaboration. **Technical design report of the photon spectrometer**. *CERN-LHCC-99-004*, 1999. 60

[257] **Neutral pion and meson production in protonproton collisions at and**. *Physics Letters B*, **717**:162 – 172, 2012. 62

[258] Sevil Salur. **Reconstructed jets at RHIC**. *Journal of Physics: Conference Series*, **230**(1):012008, 2010. 62

[259] Jorn Putschke. **First fragmentation function measurements from full jet reconstruction in heavy-ion collisions at $\sqrt{s_{NN}}$ = 200 GeV by STAR**. *The European Physical Journal C - Particles and Fields*, **61**:629–635, 2009. 10.1140/epjc/s10052-009-0904-7. 62

[260] Sevil Salur. **First direct measurement of jets in$\sqrt{s_{NN}}$ = 200 GeV heavy ion collisions by STAR**. *The European Physical Journal C - Particles and Fields*, **61**:761–767, 2009. 10.1140/epjc/s10052-009-0880-y. 62

[261] Rongrong Ma for the ALICE collaboration. **Measurements of the inclusive jet cross section and jet fragmentation in pp collisions with the ALICE experiment at the LHC**. *arXiv:1208.4537 [nucl-ex]*, 2012. 62, 65, 131

[262] L. Aphecetche et al. **PHENIX calorimeter**. *Nuclear Instruments and Methods in Physics Research Section A: Accelerators, Spectrometers, Detectors and Associated Equipment*, **499**:521 – 536, 2003. 63

[263] ALICE collaboration. **The ALICE Electromagnetic Calorimeter Conceptual Design Report**. *For Submission to DOE.* 63

[264] Rene Bellwied for the ALICE Collaboration. **ALICE EMCal Physics Performance Report**. *arXiv:1008.0413v1.* 66

[265] The ALICE Collaboration. **Cross section normalization in proton-proton collisions at $\sqrt{s}$ = 2.76 TeV and 7 TeV, with ALICE at LHC**. *arXiv:1107.0692 [physics.ins-det]*, 2011. 70, 75, 152

[266] The ALICE Collaboration. **Measurement of inelastic, single- and double-diffraction cross sections in proton–proton collisions at the LHC with ALICE**. *arXiv:1208.4968 [hep-ex]*, 2012. 70

[267] R. Brun, R. Hagelberg, M. Hansroul, and J.C. Lassalle. **Geant: Simulation Program for Particle Physics Experiments. User Guide and Reference Manual**. *CERN report: CERN-DD-78-2-REV, CERN-DD-78-2*, 1978. 76

[268] S. Agostinelli et al. **GEANT4: a simulation toolkit**. *Nuclear Instruments and Methods in Physics Research Section A: Accelerators, Spectrometers, Detectors and Associated Equipment*, **506**(3):250 – 303, 2003. 76

[269] F. W. Bopp, R. Engel, and J. Ranft. **Rapidity gaps and the PHOJET Monte Carlo**. *ArXiv High Energy Physics - Phenomenology e-prints*, mar 1998. 76

[270] D.Elia et al. **The pixel detector based tracklet reconstruction algorithm in ALICE**. *ALICE Project Document No. ALICE-INT-2009-021*, 2009. 79

[271] Dan Simon. **Optimal State Estimation: Kalman, H Infinity, and Nonlinear Approaches**. *Wiley-Interscience*, 2006. 89

[272] A. Gelb. **Applied Optimal Estimation**. *Mit Press*, 1974. 89

[273] R. Fruhwirth. **Application of Kalman filtering to track and vertex fitting**. *Nucl. Instrum. Meth.*, **A262**:444–450, 1987. 89

[274] A.Francescon et.a. **Performance of the ALICE SPD cooling system**. *Journal of Physics: Conference Series*, **395**(1):012063, 2012. 92

[275] **Measurement of Tracking Efficiency**. Technical Report CMS-PAS-TRK-10-002, CERN, 2010. Geneva, 2010. 98

[276] A. Knospe. **Yield and suppression of electrons from open heavy-flavor decays in heavy-ion collisions**. *Ph. D thesis, Yale University*, 2011. 98, 141, 142

[277] Richard Aster, Brian Borchers, and Clifford Thurber. **Parameter Estimation and Inverse Problems (International Geophysics)**. *Academic Press*, January 2005. 101, 102

[278] Volker Blobel. **An Unfolding method for high-energy physics experiments**. *arXiv:hep-ex/0208022*, pages 258–267, 2002. 102

[279] G. Cowan. **A Survey of Unfolding Methods for Particle Physics**. *Advanced Statistical Techniques in Particle Physics Grey College, Durham 18 22 March 2002*. 102

[280] Andreas Hocker and Vakhtang Kartvelishvili. **SVD approach to data unfolding**. *Nucl. Instrum. Meth.*, **A372**:469–481, 1996. 103, 107

[281] G. D'Agostini. **A multidimensional unfolding method based on Bayes' theorem**. *Nuclear Instruments and Methods in Physics Research A*, **362**:487–498, February 1995. 103

[282] Tim Adye. **Unfolding algorithms and tests using RooUnfold**. *arXiv:1105.1160*, May 2011. 103

[283] The ALICE Collaboration. **Soon to be published paper**. 2013. 109, 131

[284] D. Larsen. **Monitoring and calibration of the ALICE time projection chamber**. *phD thesis, http://hdl.handle.net/1956/4103*. 110

[285] W. Riegler W. Blum and L. Rolandi. **Particle Detection with Drift Chambers, 2nd ed.** *Springer-Verlag.* 110

[286] M. Oreglia. **A Study of the Reactions $\psi' \to \gamma\gamma\psi$.** *SLACE report: SLAC-0236, UMI-81-08973, SLAC-R-0236, SLAC-R-236*, 1980. 122

[287] R. Wigmans. **Calorimetry: Energy Measurement in Particle Physics**. *Oxford University Press*, 2001. 129

[288] F. Moreau. **The low noise L1 trigger of the H1 lead/scintillating-fibre electromagnetic calorimeter**. *Nuclear Physics B - Proceedings Supplements*, **61**(3):132 – 136, 1998. Proceedings of the Fifth International Conference on Advanced Technology and Particle Physics. 129

[289] B. I. Abelev et al. **Transverse Momentum and Centrality Dependence of High-p_T Nonphotonic Electron Suppression in** $\mathrm{Au}+\mathrm{Au}$ **Collisions at** $\sqrt{s_{\mathrm{NN}}} = 200$ GeV. *Phys. Rev. Lett.*, **98**:192301, May 2007. 142, 159

[290] B. I. Abelev et al. **Erratum: Transverse Momentum and Centrality Dependence of High-p_T Nonphotonic Electron Suppression in** Au+Au **Collisions at** $\sqrt{s_{NN}} = 200$ GeV [**Phys. Rev. Lett. 98, 192301 (2007)**]. *Phys. Rev. Lett.*, **106**:159902, Apr 2011. 142, 159

[291] Richard Witt. $< p_T >$ **Systematics and m_T-Scaling**. *arXiv:nucl-ex/0403021*, 2004. 143, 146

[292] Constantino Tsallis. **Possible generalization of Boltzmann-Gibbs statistics**. *Journal of Statistical Physics*, **52**(1-2):479–487, 1988. 145

[293] B. Alper et al. **Production spectra of , K, p at large angles in proton-proton collisions in the CERN intersecting storage rings**. *Nuclear Physics B*, **100**(2):237 – 290, 1975. 146

[294] A. Adare et al. **Production of ω mesons in $p+p$, $d+$ Au, Cu + Cu, and Au + Au collisions at $\sqrt{s_{NN}} = 200$ GeV**. *Phys. Rev. C*, **84**:044902, Oct 2011. 146

[295] J Bielcikova and the STAR Collaboration. **Azimuthal and pseudo-rapidity correlations with strange particles at intermediate-p_T at RHIC**. *Journal of Physics G: Nuclear and Particle Physics*, **34**(8):S929, 2007. 146

[296] Serguei Chatrchyan et al. **Suppression of non-prompt J/ψ, prompt J/ψ, and Y(1S) in PbPb collisions at $\sqrt{s_{NN}} = 2.76$ TeV**. *JHEP*, **1205**:063, 2012. 148

[297] L.E. Gordon and W. Vogelsang. **Polarized and unpolarized prompt photon production beyond the leading order**. *Phys. Rev.*, **D48**:3136–3159, 1993. 148

[298] L.E. Gordon and W. Vogelsang. **Polarized and unpolarized isolated prompt photon production beyond the leading order**. *Phys. Rev.*, **D50**:1901–1916, 1994. 148

[299] Simon White. **Determination of the Absolute Luminosity at the LHC**. *CERN-THESIS-2010-139*, 2010. 152

[300] G.D. Lafferty and T.R. Wyatt. **Where to stick your data points: The treatment of measurements within wide bins**. *Nuclear Instruments and Methods in Physics Research Section A: Accelerators, Spectrometers, Detectors and Associated Equipment*, **355**(23):541 – 547, 1995. 153

[301] Khachatryan V. et al. **Inclusive b-hadron production cross section with muons in pp collisions at $\sqrt{s} = 7$ TeV**. *Journal of High Energy Physics*, **2011**(3), 2011. 159

[302] Cristina Ferro. **B-tagging in CMS**. *EPJ Web Conf.*, **28**:12055, 2012. 159

[303] Marc Lehmacher. **b-Tagging Algorithms and their Performance at ATLAS**. *arXiv:0809.4896*, 2008. 159

[304] Thomas Wright. ***B*-Tagging at CDF and D0, lessons for LHC**. *arXiv:0707.1712*, 2006. 159

[305] Mouthuy T., Rozanov A., and Vacavant L. **b-tagging at LHC**. *Nuclear Instruments and Methods in Physics Research Section A: Accelerators, Spectrometers, Detectors and Associated Equipment*, **386**(1):100–108, 1997. 159

[306] Betty Abelev et al. **Measurement of electrons from beauty hadron decays in *pp* collisions at $\sqrt{s} = 7$ TeV**. *Phys. Lett.*, **B721**:13–23, 2013. 159

[307] Tomas Aronsson. **Feasibility of b-tagging in $\sqrt{s} = 2.76$ TeV *pp* collisions**. *Private Communication.* 159

[308] J. Baines, S.P. Baranov, O. Behnke, J. Bracinik, M. Cacciari, et al. **Heavy quarks (Working Group 3): Summary Report for the HERA-LHC Workshop Proceedings**. *arXivhep-ph/0601164*, 2006. 161

[309] Matteo Cacciari, Paolo Nason, and Ramona Vogt. **QCD Predictions for Charm and Bottom Quark Production at RHIC**. *Phys. Rev. Lett.*, **95**:122001, Sep 2005. 161

[310] R. Averbeck, N. Bastid, Z. Conesa del Valle, P. Crochet, A. Dainese, et al. **Reference Heavy Flavour Cross Sections in pp Collisions at $\sqrt{s} = 2.76$ TeV, using a pQCD-Driven $\sqrt{s}$-Scaling of ALICE Measurements at $\sqrt{s} = 7$ TeV**. *arXiv:1107.3243*, 2011. 161

[311] Tommaso Dorigo. **Recent CMS Results**. *arXiv:1210.6809*, 2012. 164

[312] Roberto Preghenella. **ALICE Physics Summary**. *EPJ Web Conf.*, **49**:02003, 2013. 164

[313] Paolo Spagnolo. **Physics results from CMS**. *Journal of Physics: Conference Series*, **347**(1):012002. 164

[314] Krzysztof Sliwa. **ATLAS Overview and Main Results**. *arXiv:1305.4551*, 2013. 164

[315] S Spagnolo. **Heavy Flavor Measurements at LHC**. 2013. 164

[316] Francesco Prino. **ALICE results on heavy-flavour and quarkonium production at the LHC**. *EPJ Web of Conferences*, **49**:16010, 2013. 164

[317] Roberto Covarelli and on behalf of the CMS. **Measurement of Heavy-Flavor Properties at CMS and ATLAS**. *arXiv:1306.0790*, 2013. 164

[318] Keith Ulmer. **Heavy-Flavor Results from CMS**. *arXiv:1301.4690*, 2013. 164

[319] Alessandro Grelli and the ALICE Collaboration. **Heavy Flavour Physics with the ALICE detector at the CERN-LHC**. *Journal of Physics: Conference Series*, **316**(1):012025, 2011. 164

[320] Deepa Thomas. $e - h$ **correlations analysis status**. *Private Communication*, 2013. 164

[321] Thomas Ullrich. **What is the Effective Signal and what is it good for?** *Private Communication*, 2009. 167